BYBEE, CHARLES RANDALL. Fourier Transform as Signature of Chaos in Nuclei and Data Acquisition for Compton-Suppressed Spectrometer. (Under the direction of Dr. Gary Mitchell and Dr. John Shriner, Jr.)

The first part of this thesis investigates the use of the Fourier Transform as a signature of chaos in nuclei. Although the Fourier Transform has been used to analyze atomic and molecular data sets, specific application has not been made to nuclear data. In this work a systematic modeling of the behavior of the Fourier Transform as a function of both experimental and analysis-related variables has been performed. The data for the modeling consist of sets of eigenvalues. Two quantities were defined to characterize the power spectrum that results from an application of the Fourier Transform to these data sets. The parameter which has the most significant impact on the utility of the Fourier Transform is the number of eigenvalues which comprise the data set. The modeling results indicate that the Fourier Transform can be a useful analysis tool even if the data are of poor quality. However, if the number of levels is smaller than $\approx$ 200, the Fourier Transform is unable to clearly distinguish chaotic and regular behavior.

The second part of this thesis describes the design of a data acquisition system for a Compton-suppressed γ-ray detector system. The detector system consists of two High Purity Germanium detectors and a Compton-suppression shield for one of them. Used in conjunction with the accelerator system at the High Resolution Laboratory at the Triangle Universities Nuclear Laboratory, the detector system

will be used to study nuclear structure via capture reactions. The immediate goal is the establishment of a complete level scheme for ^{30}P in order to search for chaotic behavior. The data acquisition system functions well; as an illustration, data for five ^{30}P resonances are shown and discussed. Constraints for J, π, and T have been placed or verified on these five resonance states and several other bound and unbound final states.

FOURIER TRANSFORM AS SIGNATURE OF CHAOS IN NUCLEI AND DATA ACQUISITION FOR COMPTON-SUPPRESSED SPECTROMETER

by

CHARLES RANDALL BYBEE

A dissertation submitted to the Graduate Faculty of
North Carolina State University
in partial fulfillment of the
requirements for the Degree of
Doctor of Philosophy

Department of Physics

Raleigh
1995

APPROVED BY:

Larry K. Norris
Co-chair of Advisory Committee

D. Randall Tilley
John F. Shriner, Jr.
Co-chair of Advisory Committee

Dedication

I dedicate this thesis to my family. The strength and endurance necessary for the completion of this work comes solely from them. I cannot duly express my gratitude for the constant support and encouragement that I have received from Dad and Mom, Steve and his family, and my grandparents. I would not have finished this work without them.

A constant sense of the presence of God is a continuing encouragement. He has blessed me beyond measure, and I trust that this thesis is a glory to Him.

> Make a joyful noise unto the LORD,
> all ye lands.
>
> Serve the LORD with gladness: come
> before his presence with singing.
>
> Know ye that the LORD he is God: it
> is he that hath made us, and not we ourselves:
> we are his people, and the sheep of his pasture.
>
> Enter into his gates with thanksgiving,
> and into his courts with praise: be thankful
> unto him, and bless his name.
>
> For the LORD is good; his mercy is everlasting;
> and his truth endureth to all generations.
>
> Psalm 100

Biography

Charles Randall Bybee

Personal: Born October 25, 1966, Gainesboro, TN

Education: B.S. in Physics, Tennessee Technological University, 1988

Positions:

Research Assistant, 1991 – present

Teaching Assistant, 1989 – 1991

Membership: American Physical Society

Publications:

"Tests of Time Reversal Invariance and Parity with Charged Particles", G. E. Mitchell, E. G. Bilpuch, C. R. Bybee, J. M. Drake, J. F. Shriner, Jr., *Time Reversal Invariance and Parity Violation in Neutron Resonances*, C. R. Gould, J. D. Bowman, Y. P. Popov, editors, World Scientific, Singapore, 167 (1994).

"Detailed Balance Test of Time Reversal Invariance with Interfering Resonances", G. E. Mitchell, E. G. Bilpuch, C. R. Bybee, J. M. Drake, J. F. Shriner, Jr., Nucl. Phys. **A560**, 483 (1993).

"Detailed Balance Study of Time Reversal Invariance with Interfering Resonances", G. E. Mitchell, E. G. Bilpuch, C. R. Bybee, J. M. Drake, J. F. Shriner, Jr., Nucl. Instrum. Methods **B79**, 290 (1993).

"Yrast Decays in ^{43}K", R. L. Kozub, C. R. Bybee, M. M. Hindi, J. F. Shriner, Jr., R. Holzmann, R. V. Janssens, T.-L. Khoo, W. C. Ma, M. W. Drigert, U. Garg, J. J. Kolata, Phys. Rev. **C46**, 1671 (1992).

Abstracts Published:

"A Compton-Suppressed Spectrometer for the Study of ^{29}Si(p,γ)", G. A. Vavrina, E. G. Bilpuch, C. R. Bybee, J. M. Drake, G. E. Mitchell, E. F. Moore, J. F. Shriner, Jr., P. M. Wallace, C. R. Westerfeldt, Bull. Am. Phys. Soc. **39**, 8 (1994).

"A High Resolution Study of ^{29}Si(p,γ)", P. M. Wallace, E. G. Bilpuch, C. R. Bybee, J. M. Drake, G. E. Mitchell, E. F. Moore, J. F. Shriner, Jr., G. A. Vavrina, C. R. Westerfeldt, Bull. Am. Phys. Soc. **39**, 8 (1994).

"Possible Tests of Detailed Balance with Interfering Proton Resonances", J. M. Drake, E. G. Bilpuch, C. R. Bybee, G. E. Mitchell, J. F. Shriner, Jr., Bull. Am. Phys. Soc. **38**, 9 (1993).

"Application of Fourier Transform Techniques to Quantum Chaos Studies in Nuclear Physics", C. R. Bybee, E. G. Bilpuch, G. E. Mitchell, J. F. Shriner, Jr., Bull. Am. Phys. Soc. **37**, 7 (1992).

"A Detailed Balance Study of Time Reversal Invariance with Interfering Resonances", J. M. Drake, E. G. Bilpuch, C. R. Bybee, G. E. Mitchell, J. F. Shriner, Jr., Bull. Am. Phys. Soc. **37**, 7 (1992).

"A Compton-suppression Spectrometer for the Study of ^{29}Si(p,γ)", C. R. Bybee, E. G. Bilpuch, J. M. Drake, G. E. Mitchell, S. S. Patterson, J. F. Shriner, Jr., C. R. Westerfeldt, Bull. Am. Phys. Soc. **36**, 10 (1991).

"A Search for Proton Resonances Suitable for Tests of Detailed Balance Violation", J. M. Drake, E. G. Bilpuch, C. R. Bybee, G. E. Mitchell, J. F. Shriner, Jr., Bull. Am. Phys. Soc. **36**, 10 (1991).

Acknowledgements

The work represented by this thesis has been accomplished with the assistance of many people, either directly or indirectly.

I express my sincere thanks to my co-advisors, Dr. Gary Mitchell and Dr. John Shriner, Jr., for their guidance and direction throughout my graduate career. I consider myself fortunate to have worked with them; I especially appreciate the professional manner in which they have advised me. I suspect that they do not realize how much I have learned from them.

I thank Dr. Russell Roberson and Dr. Edward Bilpuch for their continuing interest in and support of the experiments performed at the High Resolution Laboratory.

I thank Mr. Chris Westerfeldt, Mr. Paul Carter, and Mr. Richard O'Quinn for their labors in diagnosing and repairing the many accelerator troubles. I especially thank Chris for his outstanding work in the day-to-day maintenance and operation of the HRL.

I express a deep thanks to the electronics shop personnel, Mr. Sidney Edwards and Mr. Patrick Mulkey. Their constant efforts in repairing electronics modules and diagnosing computer difficulties is greatly appreciated.

The work of the Duke University Instrument Shop in helping to setup the CSS system is appreciated.

To my colleagues in the HRL group, Joann Shriner, Jerry Vavrina, Paul Wallace, Amzie Adams, Matt LaBonte, Lisa Lowie, and Sharon Stephenson, I express a sincere thanks for the assistance in collecting the data and for many helpful discussions. I have benefited greatly from working and interacting with each one of them. I can hardly imagine a better atmosphere in which to work. I also thank Mr. Gu for his assistance in collecting the data during my first data run.

I thank Dr. Frank Moore for his assistance with the γ-ray spectroscopy part of this thesis. His previous experience with accumulating and analyzing γ-ray data made this work much easier. The set of computer programs that he made available has expedited this work greatly.

I thank my church family for their unending encouragement throughout this work. I especially owe many thanks to the Cole Mill Road Church of Christ.

This work was supported by the United States Department of Energy.

Table of Contents

List of Tables

List of Figures

Preface

This thesis is composed of two distinct parts. The first part presents a modeling calculation to determine the usefulness of the Fourier Transform as a tool to analyze nuclear data sets for signs of chaos. The second part describes the data acquisition system for a Compton-suppression spectrometer and presents ^{30}P data taken with the detector system.

The modeling calculations were undertaken to determine the extent to which the Fourier Transform could be used as an additional eigenvalue statistic for the analysis of nuclear spectra. The results indicate that the Fourier Transform is a useful signature of chaos in nuclei if the data set consists of a sufficient number of levels, independent of the quality of the data. Chapters 1 through 6 describe the modeling calculations.

The Compton-suppression spectrometer will be used to establish a pure and compiete level scheme for ^{30}P via the capture reaction ^{29}Si(p,γ). The ultimate goal is to study the fluctuation properties of the energy levels in ^{30}P. Chapters 7 through 10 include a discussion of the data acquisition system. ^{30}P data accumulated using the system, and the analysis to determine the quantum numbers of the resonance and final states.

Part I

Fourier Transform as Signature of Chaos in Nuclei

Chapter 1

Introduction

The study of energy level fluctuations has a long and distinguished history in nuclear physics, dating back to Wigner [Wig57a]. The use of energy level fluctuations in the nuclear resonance regime has led to increased understanding of the nucleus in terms of the statistical description of level spacings [Lio72], reduced widths ([Shr89] and [Mit85]), and reduced width amplitudes [Shr87]. A relatively recent conjecture by Bohigas *et al.* has given added incentive to such studies [Boh84]. This conjecture — that quantum analogs of classically chaotic systems obey Gaussian orthogonal ensemble (GOE) statistics [Bro81] — has suggested a connection between the statistics of energy level fluctuations and the dynamics of the corresponding physical system. Exploration of this connection and its resulting consequences has been ongoing for several years; much work, both experimental and analytical, has been devoted to a detailed study of the dynamics of many systems and the statistics which a spectrum from the system obeys (see, for example, [Del87],[Ble94],[Wel89], [Iu89],[Hol87]). It is now generally accepted that the conjecture of Bohigas *et al.* is true for generic systems and, further, that quantum analogs of classically regular systems obey Poisson statistics.

In general, GOE statistics are expected to be applicable only to a set of energy

levels all of which have the same set of good quantum numbers; we shall use the term *sequence* to denote such a set of levels. Several statistics have been defined and used to characterize to what degree a sequence has behavior consistent with Poisson or GOE statistics [Bro81]. However, a severe restriction is well known in the application of these traditional statistics to GOE spectra; namely, the data set must be of extremely high quality — being both pure (having few levels with misassigned quantum numbers) and complete (having few missing levels). In particular, for GOE sequences, impurity or incompleteness, even if present to a small degree, may strongly bias the statistical analysis. Since it is difficult to acquire experimental data of such high quality, it is desirable to have an eigenvalue statistic which is less sensitive to data quality.

Leviandier *et al.* proposed that the Fourier transform (FT) might be used to characterize the statistical behavior of impure or incomplete spectra [Lev86]. Early applications of the FT to spectrum analysis were primarily to molecular data sets. These studies, some of which are discussed in Section 2.4, showed significant promise for the utility of the FT as an eigenvalue statistic, particularly for molecular data sets. However, nuclear data sets generally contain many fewer members than molecular data sets, and therefore it cannot be guaranteed that the technique will work as well when applied to sets of nuclear levels.

Since no systematic study has been performed on the application of the FT to nuclear data, we have modeled the behavior of the FT to evaluate this approach for characterizing the statistics of nuclear spectra. Specifically, in this modeling, we have considered the effects of relevant experimental as well as analysis-related variables on the use of the FT as an eigenvalue statistic.

A brief theoretical background to the statistical theory of energy levels is presented in chapter 2, including a discussion of two of the more common eigenvalue statistics. In addition, a sampling of the past uses of the FT as an eigenvalue statistic is presented. The quantitative aspects of our implementation of the FT as

an eigenvalue statistic are discussed in chapter 3. The results of our modeling are presented and discussed in chapter 4. Finally, in chapter 5, applications of the FT are made to some experimental nuclear data sets. Results are shown and compared with other eigenvalue statistics. Chapter 6 consists of a summary of our modeling of the behavior of the FT.

Chapter 2

Statistical Spectroscopy

2.1 Introduction

A nucleus is a collection of protons and neutrons which move in a complicated effective potential well that results from the interactions among all the nucleons. Formally, the method of solution for all states of the nuclear system is straightforward: (1) construct the Hamiltonian function $\mathcal{H}$ for the system of interest, and (2) solve the Schrödinger equation (for the non-relativistic solution) for the corresponding eigenvalues and eigenfunctions. There are formidable difficulties in the implementation of this procedure. Firstly, $\mathcal{H}$ in specific form is unknown for a nuclear system. Secondly, even if $\mathcal{H}$ were known, the computational requirements, involving many coupled nonlinear partial differential equations with complicated boundary conditions, for such a calculation would be extreme. It appears that a complete and exact solution for the nuclear many-body problem is unrealizable in the near future.

Since it is hopeless to calculate the detailed properties of a nuclear many-particle system based on the dynamics of its constituent particles, nuclear models have been

used successfully to describe relatively low-lying nuclear states [Boh69]. In particular, the nuclear shell model is quite successful, explaining many observed nuclear properties for states of low excitation energy. The algorithm used by the shell model is to construct a given state wave function as a sum of antisymmetrized products of single-particle wave functions. The totality of single-particle wave functions which are used in the construction of a state is called a basis. A basis should be composed of those single-particle wave functions which could contribute to the final state configuration. At low excitation energies, a relatively small number of single-particle configurations contribute to the final state configuration, and the required computations in the shell model are tractable. However as the excitation energy increases, the size of the basis needed to construct all possible state combinations grows exponentially [Won86], rendering the computation intractable. Thus, detailed information on the properties of highly excited states is not attainable from model calculations, and statistical approaches must be employed.

The subject of statistical spectroscopy has an extensive history [Bro81] and has found considerable application in many areas of research. Rather than producing a detailed description of individual levels, a statistical approach to spectroscopy seeks to describe the general features of the level structure; no exact results for specific levels are expected. An analogy may be made with classical statistical mechanics [Meh91]. In the case of statistical mechanics, it is impossible to calculate the state function for a macroscopic system from its constituent particles (which may number $\approx 10^{23}$). Rather, a statistical approach is adopted in which one considers an ensemble of states of the system that are compatible with a given Hamiltonian, obtaining macroscopic quantities such as temperature and entropy as appropriate averages over the ensemble of states. In statistical spectroscopy, one considers an ensemble of Hamiltonians consistent with the general symmetry properties of the physical system, obtaining such macroscopic quantities as the form for the level spacing.

Wigner was the first to surmise that the local statistical properties of levels in a sequence are identical with the eigenvalues of a random matrix, i.e., a matrix whose elements are random variables [Wig57a]. An entire field of study, named random matrix theory (RMT), was begun with the early work of Wigner, Dyson, and others and has continued to flourish. GOE statistics, referred to earlier in connection with the conjecture of Bohigas *et al.*, are but one type of statistics that emerge from RMT. A brief discussion of RMT is given in section 2, followed by a short consideration of some common eigenvalue statistics in section 3. Some applications of the use of the FT as an eigenvalue statistic will be presented in section 4.

2.2 Random Matrix Theory

In RMT, one introduces an ensemble of Hamiltonian random matrices, each of which is a possible Hamiltonian for the system. Since $\mathcal{H}$ is unknown, all possible Hamiltonians (and therefore all possible laws of interaction) must be represented in the ensemble. The goal is then to determine the joint probability density function (jpdf) of the matrix elements that permits maximum statistical independence, subject only to the constraints imposed by the symmetries of the system. Numerous ensembles with different properties and varying uses have been defined and used; for some of these ensembles, there is currently no known physical system for which the ensemble is appropriate for its description [Meh91]. For any particular ensemble, quantities of interest can then be calculated, in accord with a statistical approach, by averaging contributions from its constituent members. Comparison of the results of RMT with a given experimental sequence rests on the assumption of ergodicity in the matrix ensembles; i.e., that the average of a specific quantity over many nuclear states is equal to the corresponding average over the ensemble. Pandey has shown that the Gaussian ensembles, of which the GOE is a member,

demonstrate ergodicity [Pan79]. A discussion of RMT, including its history and its mathematical details, is given elsewhere [Meh91]; only a brief discussion of the general features is presented here.

As alluded to in the previous section, symmetries play a fundamental role in RMT. The principle which describes the importance of symmetries in RMT is as follows: throughout the considered range of excitation energies there are certain good quantum numbers [such as angular momentum (J) and parity (π)]. The corresponding symmetries [spatial isotropy and spatial reflection, in this case] determine the general features of the level structure in this region. Although there may be other good quantum numbers over various subintervals of the energy range considered, their effect on the properties of the entire sequence is limited. Moreover, the symmetries of the system that result in the good quantum numbers completely determine the jpdf of the elements of the $\mathcal{H}$ matrix and therefore the spectral statistics obeyed by the system. Two special classes of statistics — Poisson and GOE statistics — are most common in the analysis of nuclear sequences and will be discussed further.

In general, $\mathcal{H}$ is a complex hermitian matrix. The presence of symmetries may, however, simplify the form of $\mathcal{H}$. The total absence of symmetries places no additional constraints on the form of $\mathcal{H}$ and results in Poisson statistics for the spectrum. In this case, the level positions are completely uncorrelated, independent random variables. However, if a system is rotationally symmetric and invariant under the operation of time reversal, the elements of $\mathcal{H}$ can be taken to be real, the $\mathcal{H}$ matrix can be taken to be symmetric, and any orthogonal similarity transformation must leave the ensemble invariant. Statistical independence of the elements of $\mathcal{H}$ then restricts the jpdf of the matrix elements to be Gaussian in form. Invariance under orthogonal transformations is imposed to insure that all appropriate interaction types are equally represented. This ensemble is termed the Gaussian orthogonal ensemble (GOE), and its statistical properties are well known [Rei92]. Since many

systems have been found which have spectra that agree with the predictions of the GOE, the GOE is the most studied and most familiar of the ensembles.

Explicit expressions for an n-level system that obeys Poisson or GOE statistics are now presented. A quantity that is useful in characterizing the classes of statistics is the probability density function (pdf) P for the set of $n-1$ spacings between adjacent levels. For GOE statistics, the pdf for the nearest-neighbor spacing distribution can only be determined numerically but is closely approximated by the Wigner surmise [Wig57a],

$$P_{GOE}(x) = \frac{\pi}{2} x e^{-\frac{\pi x^2}{4}}, \tag{2.1}$$

where $x \equiv S/D > 0$ is the spacing S divided by the average spacing D. P_{GOE} is normalized and unimodal with maximum value $\sqrt{\pi/2e}$ at $x = \sqrt{2/\pi}$. As can be seen from Equation 2.1, there is a small probability of observing both small spacings and large spacings since

$$\lim_{x \to 0} P_{GOE} = \lim_{x \to \infty} P_{GOE} = 0. \tag{2.2}$$

A lack of small spacings is termed level repulsion. In addition to level repulsion, a GOE sequence possesses a long-range order termed spectral rigidity. Basically, a series of eigenvalues from a GOE sequence display spacings with "an extremely high degree of regularity" [Dys63] — the eigenvalues tend to be regularly spaced. An example of a perfectly rigid spectrum is the set of eigenvalues from a 1D harmonic oscillator [$E_n = \hbar\omega(n + 1/2)$], in which the level spacing is always $\hbar\omega$. Though a GOE sequence is not perfectly rigid, the levels of such a sequence tend to be regularly spaced on average. A second quantity that is of interest for GOE statistics is the level density ρ. The level density ρ_{GOE} for GOE statistics, though known only as a series expansion, is closely approximated by a "semicircular law" [Wig57b]:

$$\rho_{GOE}(y) \approx \begin{cases} \frac{1}{\pi}\sqrt{2n - y^2} & |y| < \sqrt{2n} \\ 0 & |y| \geq \sqrt{2n}. \end{cases} \tag{2.3}$$

The nuclear level density is approximately exponential as a function of energy. However, Equation 2.3 indicates that the level density for the GOE is semicircular. Thus, Equation 2.3 cannot be correct globally over the entire energy range. Rather, the semicircular prediction for the level density has been shown to be valid in the neighborhood of $x = 0$ for large n and to be inappropriate near the endpoints $\pm\sqrt{2n}$.

An n-level sequence that obeys Poisson statistics has very different properties than those just mentioned for GOE sequences. Specifically, the nearest-neighbor spacing pdf for Poisson statistics P_P is given by [Ber77]

$$P_P(x) = e^{-x} \tag{2.4}$$

where x is defined as in Equation 2.1. P_P is monotonically decreasing from a maximum value of 1 at $x = 0$. Thus, the probability of small spacings is large for Poisson statistics: there is no level repulsion. Moreover, a Poisson spectrum does not display spectral rigidity. Since GOE statistics and Poisson statistics have such different properties, it is not surprising that many statistics exist that might identify a spectrum as being GOE-like or Poisson-like; two of the more common ones are discussed in the next section.

2.3 Eigenvalue Statistics

An implicit assumption of RMT is that the statistical behavior of a sequence is identical with that of the eigenvalues of a random matrix whose elements are averaged over an appropriate ensemble. Since the predictions of RMT are in accord with experiment, this assumption is accepted as true. Given this assumption, it is then reasonable to compare the statistical behavior of a sequence with the statistical behavior of a set of numbers which are derived from the set of eigenvalues of an appropriately generated random matrix. Identifying a single experimental sequence

as being Poisson-like or GOE-like is extremely revealing, in light of the conjecture by Bohigas *et al.* which suggests a connection between spectral statistics and system dynamics. Several statistics exist to characterize the behavior of a given sequence; an excellent review article describing not only the theoretical basis but also the relative merits of various spectral statistics is available [Bro81]. Of the existing statistics, two have become most used — the nearest neighbor spacing (NNS) distribution and the Dyson-Mehta Δ_3 statistic.

The NNS distribution is the simplest and most straightforward of the eigenvalue statistics. One compares the NNS distribution for the data under study with the theoretical NNS pdf for the GOE and Poisson extremes given by Equations 2.1 and 2.4. The NNS distribution reveals short-range order, indicating the extent to which nearest neighboring levels are correlated. As will be shown more completely in Section 3.3, the existence of correlations among a set of energy levels is the key consequential difference between Poisson and GOE statistics. A Poisson sequence has levels that are completely uncorrelated while the levels in a GOE sequence are strongly correlated. An interpolation formula between the Poisson and GOE extremes is useful. Brody proposed a one-parameter interpolation formula between the Poisson and GOE extremes [Bro73]:

$$P(x;\omega) = a(\omega+1)x^{\omega}e^{-ax^{\omega+1}} \tag{2.5}$$

with

$$a = \left[\Gamma\left(\frac{\omega+2}{\omega+1}\right)\right]^{\omega+1} \tag{2.6}$$

where $\omega = 0(1)$ corresponds to Poisson (GOE) behavior and Γ is the complete gamma function. As with the Poisson distribution and the Wigner surmise, the Brody formula is normalized to 1 and has average value 1. In Figure 2.1 is shown a plot of the Brody formula for ω values in the interval [0,1] with individual curves differing by $\omega = 0.2$. The curve for $\omega = 1$ is given by Equation 2.1, and the curve

for $\omega = 0$ is given by Equation 2.4. A value for ω thus identifies the degree to which a sequence is Poisson-like or GOE-like. Though ω is a convenient parameter for specifying spectrum behavior, as yet it has no physical interpretation.

A statistic which measures long-range correlations among levels is expected to be more suited to identifying the dynamics of the system from which a given spectrum is accumulated [Del91]. A function which is used in the definition of most long-range order statistics is the number density $N(E)$, where E represents energy. For a sequence of n levels, $N(E)$ is defined as the number of levels having energy less than or equal to E. The Dyson-Mehta Δ_3 statistic is then defined as

$$\Delta_3(L) = \min_{A,B} \left\{ \frac{1}{E_{max} - E_{min}} \int_{E_{min}}^{E_{max}} \left[N(E) - (AE + B) \right]^2 dE \right\} \tag{2.7}$$

where the n levels have energies in the interval $[E_{min}, E_{max}]$ and L is the number of spacings in the interval $[E_{min}, E_{max}]$. This statistic, Δ_3, is a least-squares measure of the deviations of $N(E)$ about the best linear fit to the data and is an indicator of the long-range order in a sequence.

For a sequence that obeys Poisson statistics, $\Delta_3(L) = \Delta_{3P}(L) = L/15$. The expected result for a sequence which obeys GOE statistics cannot be expressed in a simple closed form, but, for large N, is approximated by

$$\Delta_3(L) = \Delta_{3G}(L) \approx \frac{1}{\pi^2} \left(\ln L - .0686 \right). \tag{2.8}$$

Seligman and Verbaarschot proposed an interpolation formula for Δ_3 between Poisson and GOE statistics [Sel85]:

$$\Delta_3(L; \mu) = \Delta_{3G}(\mu L) + \Delta_{3P}[(1 - \mu)]L. \tag{2.9}$$

Hence, $\mu = 0(1)$ corresponds to pure Poisson (GOE) statistics. The interpolation formula of Seligman and Verbaarschot is plotted in Figure 2.2 for μ in the interval $[0, 1]$ with adjacent curves differing by $\mu = 0.2$. The $\mu = 1$ curve is given by

Figure 2.1 NNS probability density function. The NNS distribution given by the Brody interpolation formula for $\omega = 0$ to 1 in increments of 0.2.

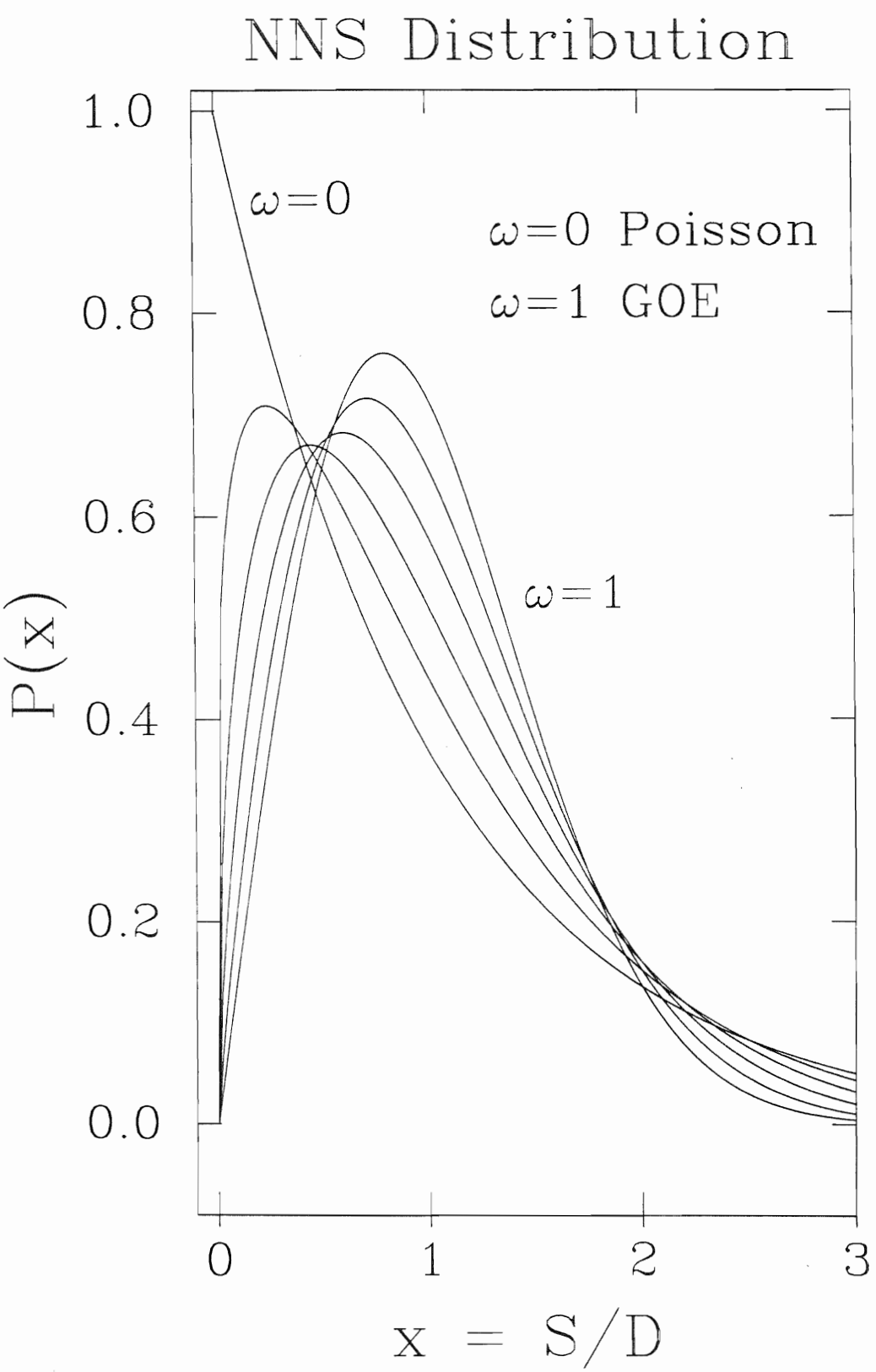
NNS Distribution
1.0
0.8
0.6
0.4
0.2
0.0
P(x)
ω=0
ω=0 Poisson
ω=1 GOE
ω=1
0
1
2
3
x = S/D

Figure 2.2 $\Delta_3(L)$ statistic. The Δ_3 interpolation formula for $\mu = 0$ to 1 in increments of 0.2.

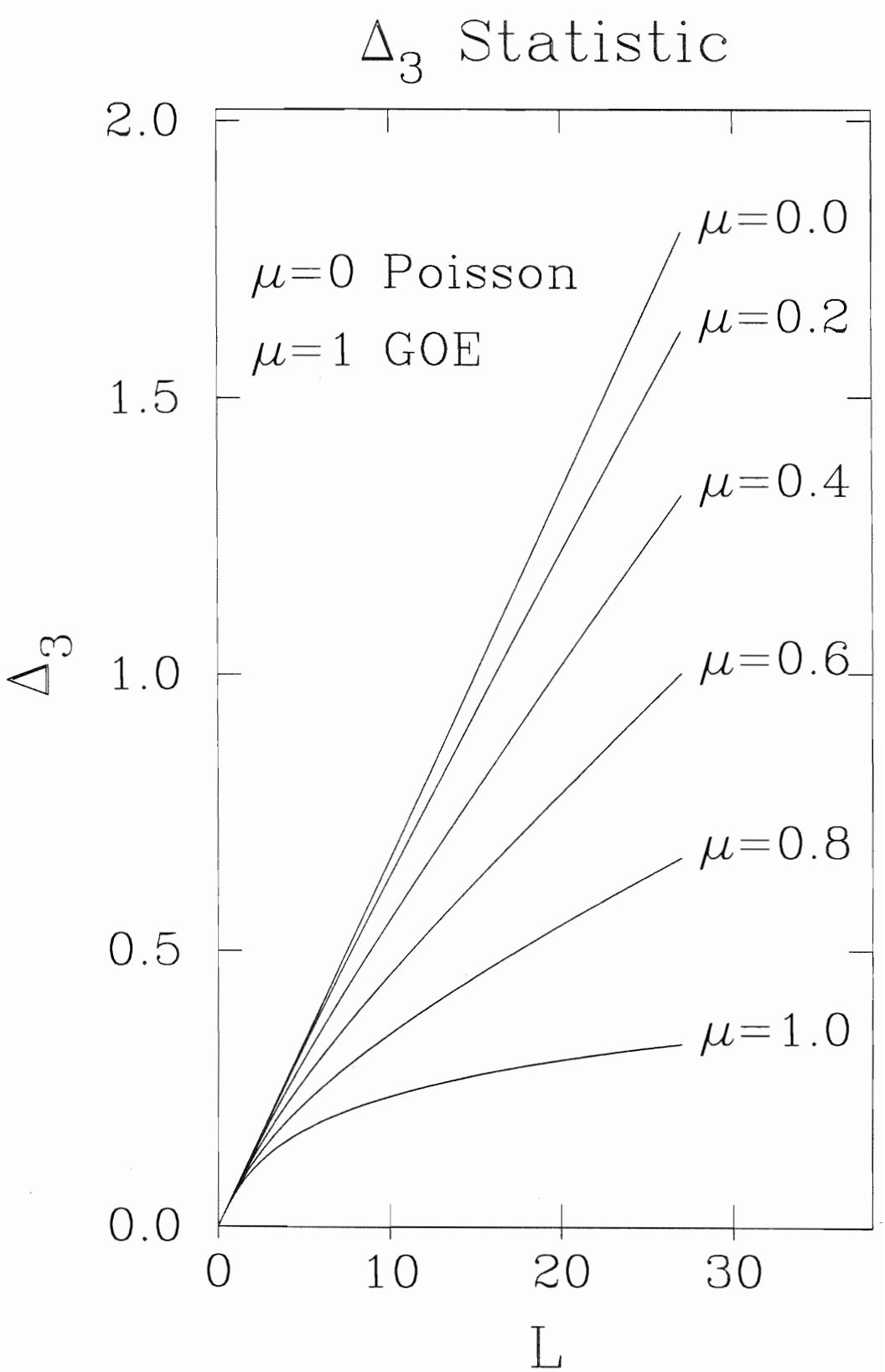
Δ_3 Statistic
2.0
1.5
1.0
0.5
0.0
Δ_3
0
10
20
30
L
μ=0 Poisson
μ=1 GOE
μ=0.0
μ=0.2
μ=0.4
μ=0.6
μ=0.8
μ=1.0

Equation 2.8, and the $\mu = 0$ curve is given by $\Delta_{3P} = L/15$. Thus, the parameter μ indicates the agreement between Δ_3 for a given data set and Δ_3 for the Poisson/GOE extremes.

Both the NNS distribution and the Δ_3 statistic can be used as reliable eigenvalue statistics, even for sequences which contain few levels [Shr92] — which is the case for nuclear sequences. However, as the degree of impurity or incompleteness in GOE sequences increases, the above eigenvalue statistics become unreliable [Shr92]. It is desirable to have an eigenvalue statistic that is reliable both for a wide range of sample sizes and for incomplete/impure spectra.

2.4 Fourier Transform as an Eigenvalue Statistic

Leviandier *et al.* suggested that "the Fourier transform of very complex spectra gives a sound measurement of long-range statistical properties of levels even in cases of badly resolved, poorly correlated spectra" [Lev86]. The FT was thus potentially an extremely useful tool for characterizing spectrum behavior since the experimental limitations of resolution and weakly observed levels would have little effect on the results of an FT analysis.

The FT was used by Leviandier *et al.* to confirm the presence of strong correlations in the vibrational spectrum of acetylene [Lev86]. Pique *et al.* also used-based analysis to study the vibrationally excited states of acetylene, particularly the transition regime from regular to chaotic motion [Piq87]. Sitja and Pique explicitly confirmed a transition from regular to soft chaotic dynamics in the vibrational spectrum of the CS_2 molecule [Sit94]. Their analysis made use of both the NNS distribution (for short range correlations) and the FT (for long-range correlations). These analyses of molecular spectra are representative of the utility that the FT has found as a tool to distinguish spectrum behavior.

Much work has been invested in the characterization of nuclear spectra as

well [Rei92]. However, the FT has not been extensively used in these analyses. One primary reason for this lack of usage of the FT for nuclear spectra is the uncertainty involved in the application. In molecular spectra, it is not uncommon to experimentally acquire data sets of several hundred levels. For example, in the citations involving molecular spectra mentioned above, the analysis of Leviandier *et al.* involved approximately 1000 levels, and that of Sitja *et al.* involved 966 levels. For nuclear spectra, the largest known sequences contain approximately 100 levels; the vast majority of currently available nuclear sequences contain many fewer levels [Shr92]. A critical question is then whether the FT is equally useful as an eigenvalue statistic when applied to spectra of smaller size.

The application of an FT algorithm to a spectrum is presented in the following chapter. Also included is a discussion of our modeling, not only as a function of the number of levels in a sequence but also as a function of other relevant variables.

Chapter 3

Fourier Transform Algorithm

3.1 Introduction

The Fourier transform (FT) was developed by Fourier prior to 1822 to solve analytical problems involving the conduction of heat in solid objects of specific geometries. In particular, the equation to be solved was a linear, second-order, partial differential equation containing the Laplacian operator, ∇^2. Equations of this type are common in physics and mathematical analysis, some notable examples being the Laplace equation, the wave equation, and the diffusion equation. Thus, the method Fourier devised to solve heat conduction equations was of great utility for solving many other equations as well. Fourier theory has since developed into an extensive field of mathematical endeavor.

Let f be a function of one independent variable x. When applied to f, the FT yields a different function S of a different independent variable, which we label q. The unit of q is reciprocal to that of x. One definition of the FT is

$$S(q) = \int_{-\infty}^{\infty} f(x) e^{-2\pi i q x}\, dx. \tag{3.1}$$

From its definition, S is a normalized, linear integral transform with kernel $e^{-2\pi i q x}$.

S has an inverse given by

$$f(x) = \int_{-\infty}^{\infty} S(q) e^{2\pi i q x} \, dq. \tag{3.2}$$

(Other definitions of the FT and its inverse differ only in the normalization, not the kernel [Bri74].) The FT provides a means of representing a given function in terms of its sinusoidal components (of which there may be infinitely many). The domain in which a function is represented by S as a function of q is termed the transform domain. One common use of the FT is to represent a function of time (t) in terms of frequency (ω) [which has reciprocal units to t]. In this way, a function may be defined equally as magnitudes of some quantity f at values of time or as amplitudes of a different quantity S at values of frequency. To switch from one representation to the other, Equations 3.1 and 3.2 are used.

In experimental applications, one is often forced to deal with functions of discrete variables since sampled quantities are generally determined at finitely separated points. The FT of such a discrete function is closely related to the FT for a corresponding function of a continuously defined variable. Not surprisingly, the FT and its inverse for a function of a discrete variable are obtained as approximations of Equations 3.1 and 3.2.

Consider a set of N samples $\{f_i | i = 0, N-1\}$ of some quantity f determined at equi-spaced points $\{x_i | i = 0, N-1\}$ with $x_{i+1} - x_i = \Delta$. In the transform domain, the independent variable q assumes $N+1$ discrete values at which S is determined. (The transform values at the extremum values of q are not independent, reducing the number of independent transform values to N, as expected.) The interval in which values of q are specified is determined as a consequence of the sampling theorem.

The sampling theorem states that a continuous function that is sampled at a rate Δ is completely determined by the set of samples if the function contains no frequencies larger than the Nyquist frequency $\nu_c = \frac{1}{2\Delta}$. Such a function is termed

a band-limited function. Two immediate possibilities in the application of the sampling theorem are apparent: cases where the sampled function is and is not band-limited to frequencies less than ν_c. If the sampled function is band-limited to frequencies less than ν_c, the original function is completely determined by its transform values specified in the interval $(-\frac{1}{2\Delta}, \frac{1}{2\Delta})$. On the other hand, if the sampled function is not band-limited to frequencies less than ν_c, the FT of the original function contains high-frequency components (frequencies higher than ν_c) which are spuriously placed in the interval $(-\frac{1}{2\Delta}, \frac{1}{2\Delta})$. This undesirable effect is termed aliasing and results physically from an undersampling of the original function. In either case the interval of obtainable frequencies is restricted to $(-\frac{1}{2\Delta}, \frac{1}{2\Delta})$ [Pre92].

In practice, level correlations manifest themselves in the FT at low frequencies (See Section 3.2). To insure that aliasing effects are minimized, the FT has been modeled as a function of Δ. Thus, any spurious affects due to aliasing can be identified. In light of the sampling theorem, one thus obtains N independent transform values at $N+1$ values of q given by

$$q_j = \frac{j}{N\Delta}: \quad j = -\frac{N}{2}, -\frac{N}{2}+1, \ldots, \frac{N}{2}-1, \frac{N}{2}. \tag{3.3}$$

Having specified the values of q, the remaining task is to approximate Equation 3.1 for application to discrete data. Conversion of 3.1 to a form appropriate for discretely sampled data yields for a particular element of the discrete FT, $\hat{S}_{q_j}$.

$$\hat{S}_{q_j} \cong \Delta \sum_{k=0}^{N-1} f_k e^{-2\pi i q_j x_k} \tag{3.4}$$

where j ranges over the same indices as described for q in Equation 3.3.

Evaluation of Equation 3.4 can be time-consuming, particularly if N is large. A method of significantly reducing the computation time (by 4-5 orders of magnitude) for the evaluation of Equation 3.4 became widely known in 1965 [Bra78]. This algorithm, known as the Fast Fourier Transform (FFT), makes use of efficient, recursive grouping of terms in the sum and is responsible for the common use of

the FT as an analysis tool. One restriction of all FFT algorithms is that N must be at worst factorable into a set of small prime numbers and at best be an integral power of two (so that all prime factors are 2). Many FFT algorithms assume the best situation. To satisfy this requirement, a common suggestion for applying FFT algorithms to arrays of length not a power of two is to pad the array with zeroes to make N a power of two. This procedure of padding an array with zeroes cannot be applied in this work (see Section 3.2), and, therefore, use of an FFT algorithm is questionable. An extensive literature is available on the FFT, its history, its uses, and its wide applications ([Bri74] and [Pre92]).

3.2 Application of the Fourier Transform

The input to a discrete FT routine must be some quantity sampled at regular intervals so that the spacing between consecutive elements is a constant Δ. In modeling, we have generated sequences of N eigenvalues whose spacing pdf is either Poisson or GOE. In either case, consecutive spacings throughout the sequence are not equal and thus not appropriate for input into a FT code. The manner in which we have produced data sets for input into a FT algorithm is discussed next.

Generation of sets of eigenvalues with appropriate statistical behavior is crucial for this modeling calculation. The eigenvalue sets obeying Poisson statistics were produced by first generating a set of spacings by randomly sampling from a Poisson pdf. From the set of spacings, a set of eigenvalues was iteratively constructed; the first eigenvalue was chosen to be zero, and each succeeding eigenvalue was produced by adding the value of the next spacing to the previous eigenvalue. The GOE eigenvalue sets were more complicated to produce; they were generated by an inverse procedure to that described in Section 2.2 and summarized here. A symmetric $N \times N$ matrix whose N^2 elements are Gaussian random variables was formed and diagonalized. (Since the GOE is defined in the space of real, symmetric matrices,

only $N(N+1)/2$ of the matrix elements are independent.) The resulting diagonal elements (which are the eigenvalues of the original matrix and are invariant under similarity transformations) have a GOE spacing pdf. Since the set of eigenvalues has a semicircular level density (see Section 2.2) but should have a constant level density for further analysis (see Section 3.3), the subset consisting of the central quarter was chosen for further analysis. A computer code that implements this procedure was obtained and used [Guh90a].

From a set of eigenvalues having an appropriate pdf, an array suitable for input into a FT algorithm was formed in the following manner. Let the set of eigenvalues, either Poisson or GOE, be denoted by $\{E_i | i = 1, N\}$. The eigenvalues are arranged in ascending order by construction. A value of Δ was chosen; usually $\Delta = 0.01$. An initially zeroed array, Z, was then formed by incrementing by one those array locations with indices $\{\mathcal{R}\left(\frac{E_i}{\Delta}\right)\}$ where $\mathcal{R}$ indicates rounding to the nearest integer. This resulting array, Z, is composed mostly of zeroes and is of size $\frac{E_N}{\Delta}$. As mentioned in the previous section, it is common practice in FT analysis to pad an array with zeroes until its dimension is the next power of two; such an array is then suitable for input into a FFT routine. It should be emphasized that Z should not be padded with zeroes to the next power of two, since padding with zeroes garbles S for small values of the independent variable [Lom90].

There are many available routines that calculate the FT of a data set. We have used a set of FORTRAN subroutines that were written by Paul Swartztrauber and that are available from a public software library at the AT&T Bell Labs Research Center in Murray Hill, New Jersey. The principal routine, RFFTF, accepts as input a one dimensional array of size 2N and returns the N complex FT values of the data set in the same array. If N is a product of small prime numbers, the code utilizes an FFT algorithm; otherwise, it utilizes a less efficient FT algorithm. Availability of the code and its flexibility in handling arrays of variable dimension were the principle reasons for using this particular set of routines.

In general, the FT, $\hat{S}$, is a complex-valued function. Following Leviandier *et al.* [Lev86] and Jost *et al.* [Jos86], we have considered the absolute square of $\hat{S}$, $|\hat{S}|^2$, which is the associated, real power spectrum. Since the FT of a real function is even, $\hat{S}_\nu = \hat{S}_{-\nu}$, and the power spectrum array is calculated via

$$|\hat{S}|^2{}_\nu = |\hat{S}_\nu|^2 + |\hat{S}_{-\nu}|^2 = 2\,|\hat{S}_\nu|^2 \tag{3.5}$$

where the ν subscript refers to a given value of frequency. Also following the references above, it is convenient to express the abscissa variable in the dimensionless unit q/ρ, where ρ is the average level density. In all subsequent plots and discussion, $|\hat{S}|^2$ is considered a function of q/ρ, unless otherwise noted. Two distinct but related applications of the FT to spectra have been investigated.

If a number of spectra have identical behavior, one can compute the FT of each spectrum and then arithmetically average the resulting $|\hat{S}|^2$ functions to produce an ensemble averaged FT curve, $<|\hat{S}|^2>$. As more spectra are included in the calculation, $<|\hat{S}|^2>$ becomes smoother and more well-defined, regardless of the particular spectrum type.

The key fact which has led to the use of the FT as an eigenvalue statistic is the difference in functional form of $<|\hat{S}|^2>$ for a GOE spectrum versus a Poisson spectrum. In Figure 3.1 is displayed a plot of $<|\hat{S}|^2>$ for 500 spectra of 100 levels each, the top portion for GOE spectra and the bottom portion for Poisson spectra. Both curves display some small fluctuations about a well-defined average, have a spike roughly two orders of magnitude off scale at $q/\rho = 0$, and individually approach a constant value for large q/ρ. However, at small q/ρ, there is a noticeable decrease in $<|\hat{S}|^2>$ for GOE sequences compared to Poisson sequences. This general shape of $<|\hat{S}|^2>$ for GOE sequences at small q/ρ is termed a correlation hole; the appearance of a correlation hole in the $<|\hat{S}|^2>$ spectrum signals GOE behavior and thus could be used as an eigenvalue statistic. As will be shown in the next section, the presence of a correlation hole is directly related to the presence of correlations

Figure 3.1 Ensemble-averaged power spectra. (Top) An ensemble-averaged power spectrum for 500 GOE sequences of 100 levels each. (Bottom) An ensemble-averaged power spectrum for 500 Poisson sequences of 100 levels each.

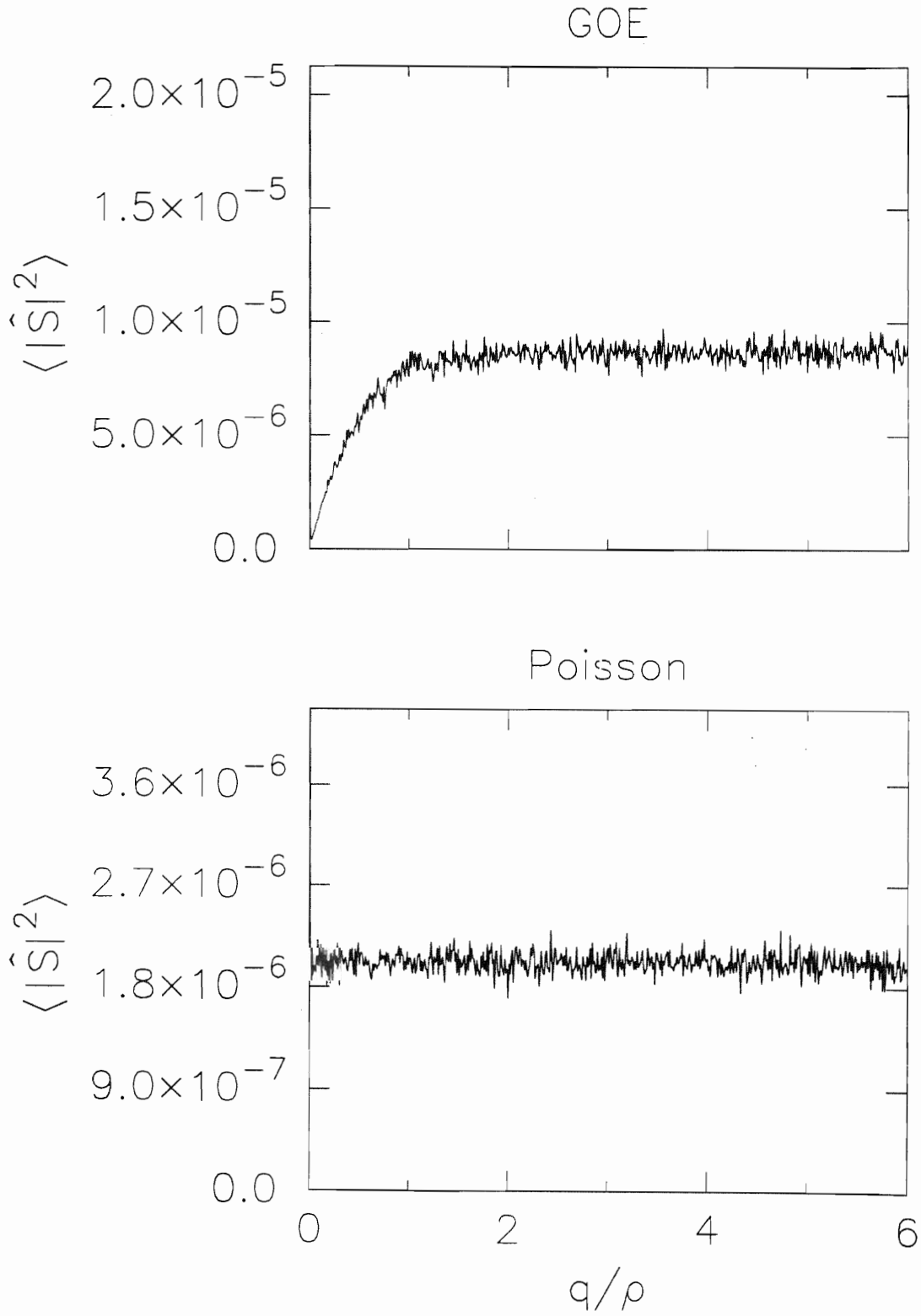
GOE
2.0×10^{-5}
1.5×10^{-5}
1.0×10^{-5}
5.0×10^{-6}
0.0
$\langle|\hat{S}|^2\rangle$
Poisson
3.6×10^{-6}
2.7×10^{-6}
1.8×10^{-6}
9.0×10^{-7}
0.0
$\langle|\hat{S}|^2\rangle$
0
2
4
6
q/ρ

in the spectrum.

The situation with which one is presented in practice, however, is the identification of the behavior of a single sequence, not a number of sequences from which an ensemble average could be computed. The FT of a single spectrum is much noisier [Del91], as illustrated in Figure 3.2 in which $|\hat{S}|^2$ is shown for a single GOE sequence (top) and for a single Poisson sequence (bottom). In this case, the presence of a correlation hole is no longer obvious, and therefore the suitability of the FT as an eigenvalue statistic is questionable. One of the goals of this work is to investigate the behavior of the FT when applied to individual nuclear sequences.

One technique that has been suggested as an aid to analyzing single sequences via a FT algorithm is to smooth $|\hat{S}|^2$ before applying any tests related to the presence of a correlation hole [Del91]. We have implemented nine different methods of smoothing $|\hat{S}|^2$ — one-point, one-point weighted, two point, two-point weighted, four-point, four-point weighted, median (with $r = 1$ and 2), and a dichotomic convoluted windows (DCW) average method. Each of the methods of k-point smoothing (1, 2, and 4) replaces an array element with the average of the array element and its k nearest neighbors on each side. Each of the methods of k-point weighted smoothing (1, 2, and 4) replaces an array element with the gaussian weighted average of the array element and its k nearest neighbors on each side. The weighting coefficients of the terms in the weighted average are the binomial coefficients. Specifically, a given element $\overline{|\hat{S}|^2}_i$ of an array that has been smoothed by k-point weighted smoothing is given by

$$\overline{|\hat{S}|^2}_i = \sum_{j=-k}^{k} C(2k, k+j)|\hat{S}|^2_j \tag{3.6}$$

where

$$C(n, r) = \frac{n!}{r!(n-r)!}. \tag{3.7}$$

Median smoothing of r points replaces each element $|\hat{S}|^2_i$ of an array with the median of the $2r + 1$ elements nearest to $|\hat{S}|^2_i$, one point being $|\hat{S}|^2_i$ itself.

Figure 3.2 Individual power spectra. (Top) An individual power spectrum for a GOE sequence of 100 levels. (Bottom) An individual power spectrum for a Poisson sequence of 100 levels.

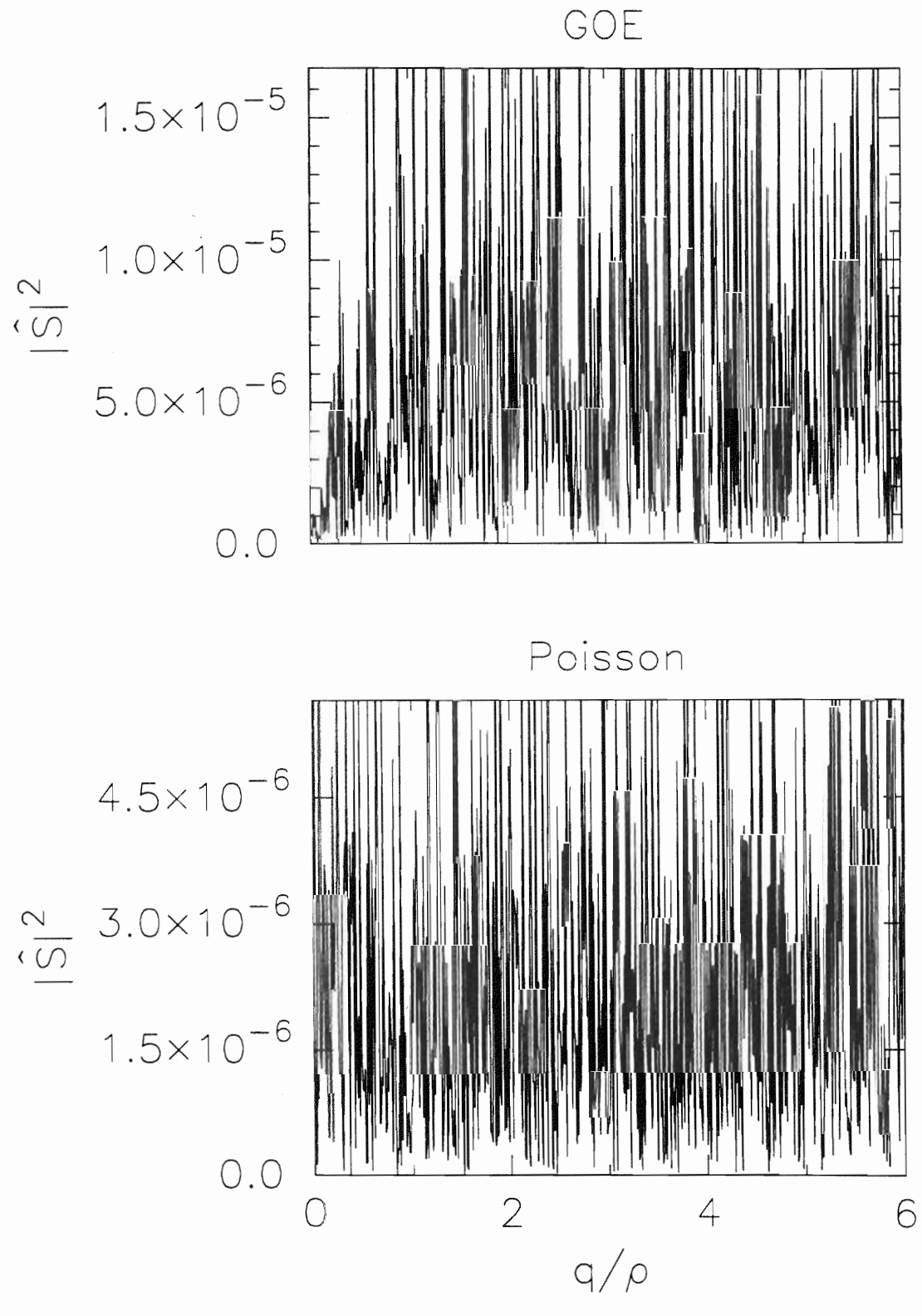
GOE
1.5×10⁻⁵
1.0×10⁻⁵
5.0×10⁻⁶
0.0
|Ŝ|²
Poisson
4.5×10⁻⁶
3.0×10⁻⁶
1.5×10⁻⁶
0.0
|Ŝ|²
0
2
4
6
q/ρ

Finally, the DCW's average method of smoothing is that method used and recommended for this type of analysis ([Piq90] and [Lom90]). It is accomplished by performing three successive smoothing procedures: a four-point weighted smoothing, a two-point weighted smoothing, and a one-point weighted smoothing in that order. The rationale for the DCW's average is due to the consequences of each k-point weighted smoothing. A k-point weighted smoothing results in a high-frequency noise since this type of smoothing effectively convolves the function with a square function which produces an oscillating curve superimposed on the smoothed result. A $\frac{k}{2}$-point weighted smoothing also results in a high-frequency noise but with minima which are located at the maxima of the k-point weighted smoothing. After three applications the high-frequency noise disappears almost completely.

In Figures 3.3, 3.4, and 3.5 are displayed smoothed versions of the power spectrum displayed in the top portion of Figure 3.2. Though each of these smoothing techniques produces a less noisy spectrum for $|\hat{S}|^2$, none of them results in a spectrum smooth enough to liken it to the top portion of Figure 3.1. A summary of the results of the nine smoothing algorithms is presented in tabular form in Section 4.1, after our choice of quantification of the behavior of the FT has been discussed.

3.3 Spectral Correlations

The effects of spectral correlations on the FT can be calculated directly using the approach of Mehta [Meh91]. Let $\{E_i | i = 1, N\}$ be a sequence of N energy eigenvalues in the interval [-L, L], and let $\mathcal{P}(E_1, E_2, \ldots, E_N)$ be the probability density function for observing one eigenvalue at E_1, a second eigenvalue at E_2, ..., and the N^{th} eigenvalue at E_N. All statistical properties of the sequence can be described in terms of the set of n-level correlation functions, R_n [Meh91],

$$R_n(E_1, E_2, \ldots, E_N) = \frac{N!}{(N-n)!} \int_{\infty}^{\infty} \cdots \int_{\infty}^{\infty} \mathcal{P}(E_1, E_2, \ldots, E_N) dE_{n+1} \cdots dE_N. \quad (3.8)$$

Figure 3.3 Smoothed power spectra I. (Top) An individual power spectrum smoothed by one-point smoothing for a GOE sequence of 100 levels. (Center) An individual power spectrum smoothed by one-point weighting for a GOE sequence of 100 levels. (Bottom) An individual power spectrum smoothed by two-point smoothing for a GOE sequence of 100 levels.

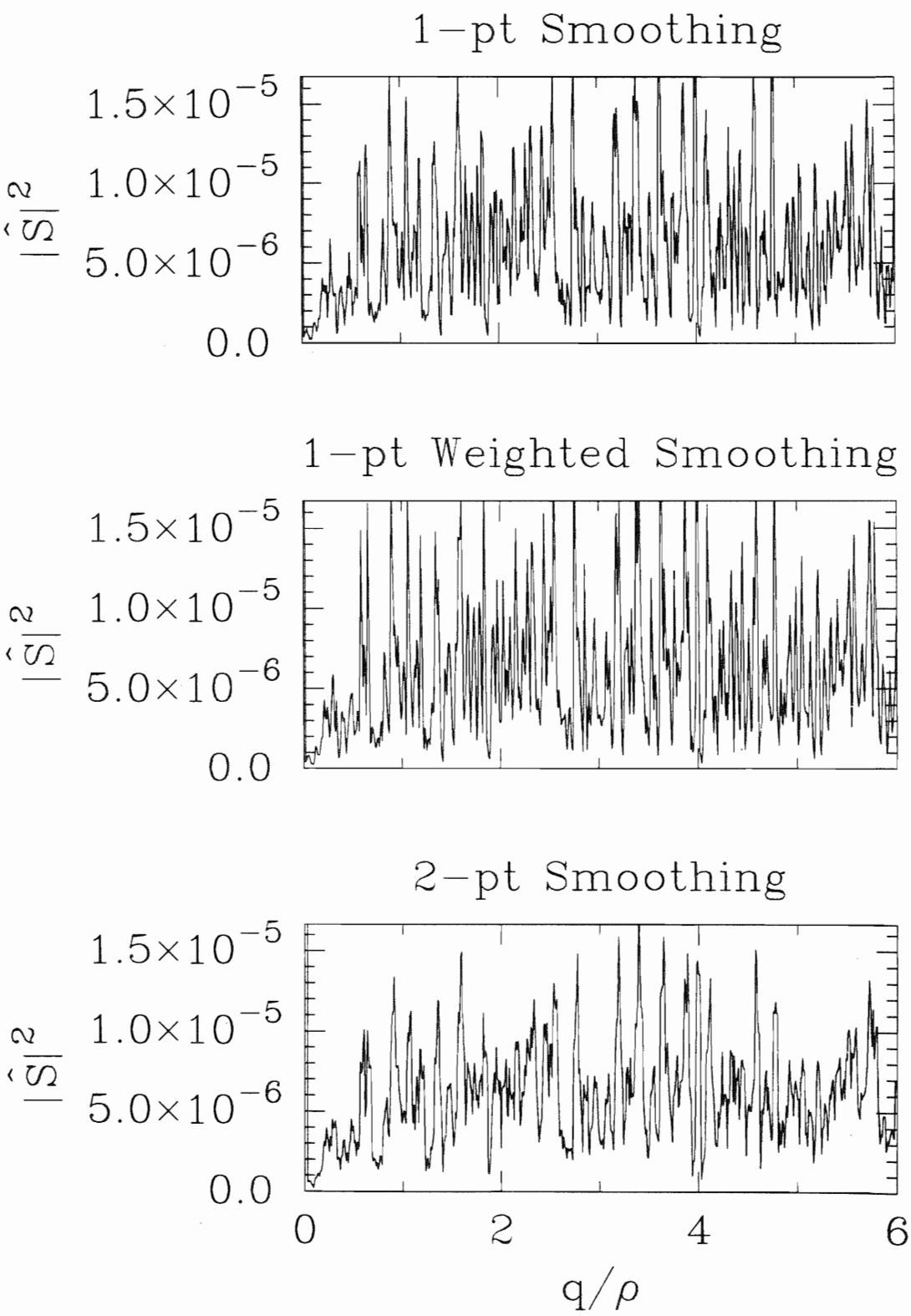
1−pt Smoothing
1.5×10^−5
1.0×10^−5
5.0×10^−6
0.0
⟨|S|^2⟩
1−pt Weighted Smoothing
1.5×10^−5
1.0×10^−5
5.0×10^−6
0.0
⟨|S|^2⟩
2−pt Smoothing
1.5×10^−5
1.0×10^−5
5.0×10^−6
0.0
⟨|S|^2⟩
0
2
4
6
q/ρ

Figure 3.4 Smoothed power spectra II. (Top) An individual power spectrum smoothed by two-point weighting for a GOE sequence of 100 levels. (Center) An individual power spectrum smoothed by four-point smoothing for a GOE sequence of 100 levels. (Bottom) An individual power spectrum smoothed by four-point weighting for a GOE sequence of 100 levels.

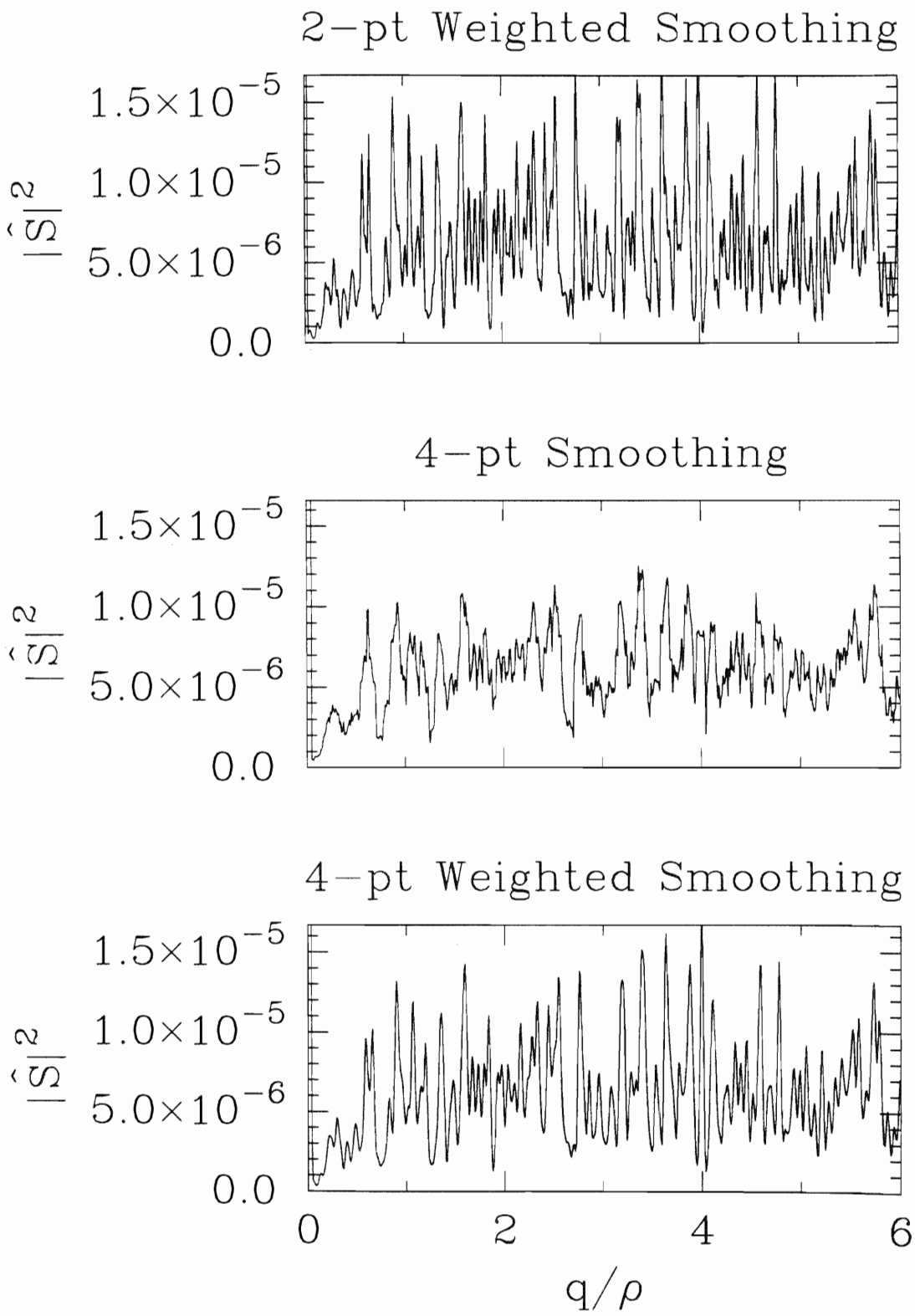
2−pt Weighted Smoothing
4−pt Smoothing
4−pt Weighted Smoothing
$\langle \overline{\Omega}^2 \rangle$
1.5×10⁻⁵
1.0×10⁻⁵
5.0×10⁻⁶
0.0
0
2
4
6
q/ρ

Figure 3.5 Smoothed power spectra III. (Top) An individual power spectrum smoothed by one-point median smoothing for a GOE sequence of 100 levels. (Center) An individual power spectrum smoothed by two-point median smoothing for a GOE sequence of 100 levels. (Bottom) An individual power spectrum smoothed by DCW's average smoothing for a GOE sequence of 100 levels.

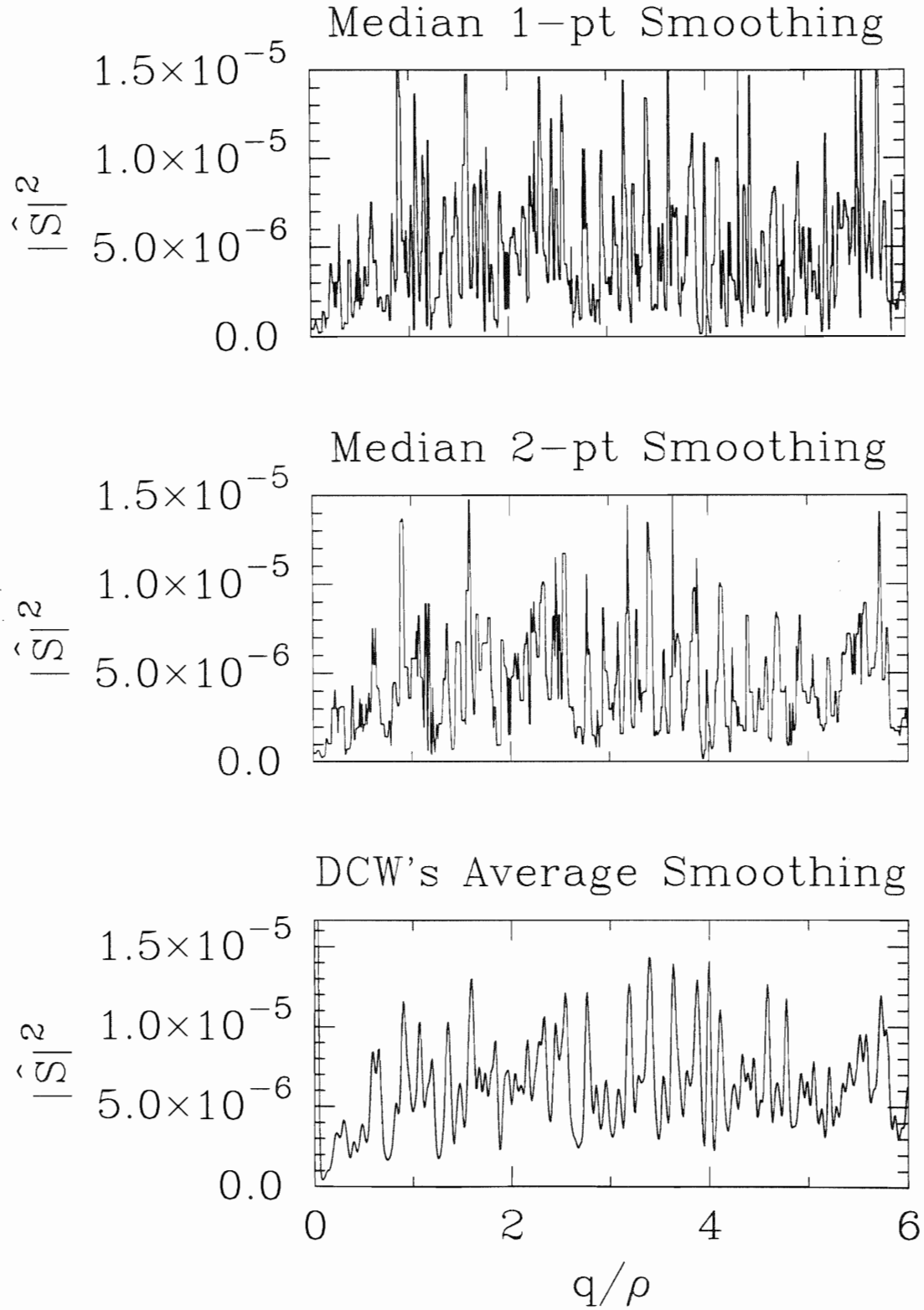
Median 1−pt Smoothing
Median 2−pt Smoothing
DCW's Average Smoothing
$\widehat{|S|^2}$
1.5×10^{-5}
1.0×10^{-5}
5.0×10^{-6}
0.0
0
2
4
6
q/ρ

It is convenient to work with the set of n-level cluster functions, T_n, [Meh91]

$$T_n(E_1, E_2, \ldots, E_N) = \sum_G (-1)^{n-m}(m-1)! \prod_{j=1}^{m} R_{G_j}(E_k, with\ k\ in\ G_j) \qquad (3.9)$$

where G is any division of the n indices into m subgroups. Each set of functions — R_n and T_n — is expressible in terms of the other. In particular,

$$T_1(E) = R_1(E) = \rho(E), \qquad (3.10)$$

and

$$T_2(E_1, E_2) = -R_2(E_1, E_2) + R_1(E_1)R_1(E_2). \qquad (3.11)$$

where ρ is the level density. The function T_n describes completely the correlation properties of a single cluster of n levels, without considering the effects of correlations of order less than n. Another useful quantity is the n-level form factor which is defined as the FT of T_n. In particular, the two-level form factor, labeled b_2, occurs frequently (since several spectrum characteristics depend only on it) and is well known for the Gaussian ensembles [Meh91].

The effect of level correlations on the FT of a sequence of discrete energy eigenvalues is now shown. The sequence defined above, $\{E_i | i = 1, N\}$, can be represented by the function f,

$$f(E) = \sum_{i=1}^{N} \delta(E - E_i) \qquad (3.12)$$

where δ is the Dirac delta function. Substitution of Equation 3.12 into Equation 3.1 yields

$$S(\tfrac{q}{\rho}) = \int_{-\infty}^{\infty} \sum_{i=1}^{N} \delta(E - E_i) e^{-2\pi i \frac{q}{\rho} E} dE = \sum_{i=1}^{N} e^{-2\pi i \frac{q}{\rho} E_i}. \qquad (3.13)$$

Therefore, the power spectrum, $|S(\frac{q}{\rho})|^2$, is

$$|S(\tfrac{q}{\rho})|^2 = \sum_{i=1}^{N} \sum_{j=1}^{N} e^{-2\pi i \frac{q}{\rho}(E_i - E_j)} = N + \sum_{i=1}^{N} \sum_{j \neq i}^{N} e^{-2\pi i \frac{q}{\rho}(E_i - E_j)}. \qquad (3.14)$$

Equation 3.14 is the continuous power spectrum for the function defined by Equation 3.12. The discrete FT approximates this behavior and can illuminate the effect

of level correlations. The manner in which level correlations manifest themselves is seen using Equation 3.14 and the results of Section 2.2.

In practice, there are two kinds of energy fluctuations present in a spectrum — the smooth exponential dependence of level density on energy (slow fluctuations) and the fast fluctuations about the smooth exponential average. Usually, the slow fluctuations are of little interest; therefore, the spectrum is unfolded to remove the exponential energy dependence. The fluctuations of interest are the fast fluctuations that are present, and these remain even when the spectrum is unfolded. When this unfolding is done, the level density is constant over the interval [-L , L]; in complete generality, one can choose

$$\rho(E) = R_1(E) = \frac{1}{D} = \frac{N}{2L}, \tag{3.15}$$

where D is the average level spacing. Furthermore, the energy range can be easily rescaled to an interval $[-L, L]$ once the unfolding procedure has been performed.

The operation of ensemble averaging, needed for comparison of Figure 3.1 with the prediction of Equation 3.14, is performed by averaging over a probability distribution (rather than discretely summing over the levels). Using the level density function ρ to rewrite Equation 3.14 in terms of continuous variables, one has, for the ensemble averaged power spectrum,

$$<|\hat{S}(\tfrac{q}{\rho})|^2> = N + \int_{-L}^{L}\int_{-L}^{L}\rho(E)\rho(E')e^{-2\pi i\frac{q}{\rho}(E-E')}dE\,dE'. \tag{3.16}$$

If no correlations exist among the levels, the integrals can be performed separately, and Equation 3.16 becomes

$$<|\hat{S}(\tfrac{q}{\rho})|^2> = N + \left|\int_{-L}^{L} R_1(E)e^{-2\pi i\frac{q}{\rho}E}dE\right|^2. \tag{3.17}$$

If two point correlations exist among the levels, one must consider the integral obtained by replacing $\rho(E)\rho(E')$ with $R_2(E, E')$ in the second term of Equation 3.16; one then has

$$<|\hat{S}(\tfrac{q}{\rho})|^2> = N + \int_{-L}^{L}\int_{-L}^{L} R_2(E, E')e^{-2\pi i\frac{q}{\rho}(E-E')}dE\,dE'. \tag{3.18}$$

Using Equation 3.11 in Equation 3.18 results in

$$<|\hat{S}(\tfrac{q}{\rho})|^2> = N + \int_{-L}^{L}\int_{-L}^{L}[R_1(E)R_1(E') - T_2(E,E')]\, e^{-2\pi i\frac{q}{\rho}(E-E')}dE\, dE'. \quad (3.19)$$

The first term in the double integral is the same as the integral of Equation 3.16 and is given by the second term of Equation 3.17. Thus,

$$<|\hat{S}(\tfrac{q}{\rho})|^2> = N + \left|\int_{-L}^{L} R_1(E)e^{-2\pi i\frac{q}{\rho}E}dE\right|^2 - \int_{-L}^{L}\int_{-L}^{L} T_2(E,E')e^{-2\pi i\frac{q}{\rho}(E-E')}dE\, dE'. \quad (3.20)$$

The effect of level correlations is in the third term of Equation 3.20. Using Equation 3.10, term 2 of Equation 3.20 becomes

$$\left|\int_{-L}^{L} R_1(E)e^{-2\pi i\frac{q}{\rho}E}dE\right|^2 = \left|\int_{-L}^{L} De^{-2\pi i\frac{q}{\rho}E}dE\right|^2 = D^2\left|\frac{\sin 2\pi\frac{q}{\rho}L}{\pi\frac{q}{\rho}}\right|^2. \quad (3.21)$$

Rewriting the last term of Equation 3.21 and using Equation 3.15 implies that

$$\left|\int_{-L}^{L} R_1(E)e^{-2\pi i\frac{q}{\rho}E}dE\right|^2 = N^2\left|\frac{\sin 2\pi\frac{q}{\rho}L}{2\pi\frac{q}{\rho}L}\right|^2. \quad (3.22)$$

If $T_2(E,E') = T_2(E-E')$, which is the case as long as ρ is constant over the interval [-L, L] [Meh91], the third term in Equation 3.20 becomes $-Nb_2$, where b_2 is the two-level form factor. Therefore, in simplified form, Equation 3.20 is

$$<|\hat{S}(\tfrac{q}{\rho})|^2> = N + N^2\left|\frac{\sin 2\pi\frac{q}{\rho}L}{2\pi\frac{q}{\rho}L}\right|^2 - Nb_2. \quad (3.23)$$

Grouping terms yields

$$<|\hat{S}(\tfrac{q}{\rho})|^2> = N^2\left|\frac{\sin 2\pi\frac{q}{\rho}L}{2\pi\frac{q}{\rho}L}\right|^2 + N(1-b_2). \quad (3.24)$$

The case of no correlations, for which Equation 3.17 is valid, is obtained if $b_2 = 0$. The FT of a sequence is thus a measure of b_2, which in turn reflects the existence of correlations among levels in the sequence. The first term on the right-hand side of Equation 3.24 is reminiscent of the expression which describes the intensity pattern

for Fraunhofer diffraction from a single slit; since $\frac{q}{\rho} \geq 0$, it has a central envelope extending from $\frac{q}{\rho} = 0$ to $\frac{q}{\rho} = \frac{1}{2L}$. This term depends only on the level density function, and results in a so-called fast component to $<|\hat{S}(\frac{q}{\rho})|^2>$ of N^2 at $\frac{q}{\rho} = 0$. This is the origin of the spike at $q/\rho = 0$ in Figure 3.1. For $\frac{q}{\rho} \neq 0$, this term has negligible effect. The second term on the right-hand side of Equation 3.24 is proportional to N, is the so-called slow component to $<|\hat{S}(\frac{q}{\rho})|^2>$, and contains the effects of two-point correlations between levels.

For GOE statistics, b_2 is given by [Meh91]

$$b_2(\xi) = \begin{cases} 1 - 2|\xi| + |\xi| \ln(1 + 2|\xi|) & |\xi| \leq 1 \\ -1 + |\xi| \ln\left(\frac{2|\xi|+1}{2|\xi|-1}\right) & |\xi| \geq 1 \end{cases} \tag{3.25}$$

The quantity $1 - b_2$ is indicative of a correlation hole and is plotted in Figure 3.6. The similarity of this form to that of Figure 3.1 is apparent.

The qualitative appearance of a correlation hole is thus indicative of GOE statistics and therefore of chaotic behavior. It is important, however, to derive a quantitative measure of the behavior of $<|\hat{S}(\frac{q}{\rho})|^2>$ similar to ω and μ discussed in Section 2.3. The methods we have used to quantify the behavior of $<|\hat{S}(\frac{q}{\rho})|^2>$ are discussed in the next section.

3.4 Quantification of the Fourier Transform

Two methods of quantifying the behavior of the FT have been investigated in this work. Both methods make specific use of the fact that, at small $\frac{q}{\rho}$, $<|\hat{S}(\frac{q}{\rho})|^2>$ for a GOE spectrum takes on a different functional form than does $<|\hat{S}(\frac{q}{\rho})|^2>$ for a Poisson spectrum, as was shown in Figure 3.1. The first measure that we have used to quantify the behavior of the FT is the area of the correlation hole ($\mathcal{A}$), and the second is the set of parameters obtained by fitting a specified function of certain parameters to the $<|\hat{S}(\frac{q}{\rho})|^2>$ curve. Each of these techniques is discussed in detail.

Figure 3.6 Two-level form factor for GOE statistics.

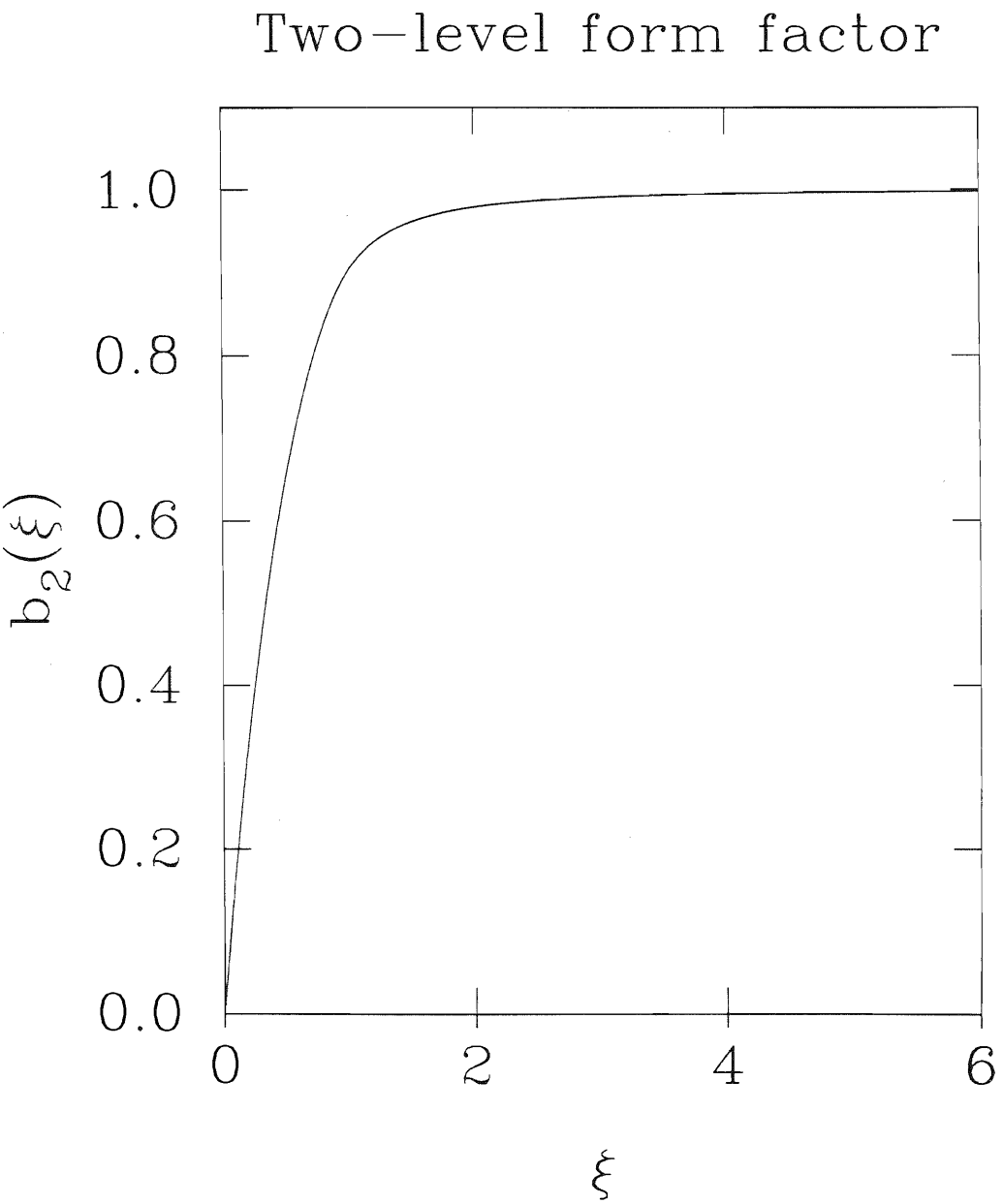
Two-level form factor
1.0
0.8
0.6
0.4
0.2
0.0
$b_2(\xi)$
0
2
4
6
ξ

The first task in calculating $\mathcal{A}$ is to specify the region of the correlation hole. One feature of $<|\hat{S}(\frac{q}{\rho})|^2>$ which is present for both GOE spectra and for Poisson spectra is a constant value of the FT (which we term a background) at large $\frac{q}{\rho}$; we denote this constant value of $<|\hat{S}(\frac{q}{\rho})|^2>$ by β. We chose the background region to be those values of $<|\hat{S}(\frac{q}{\rho})|^2>$ for which $\frac{q}{\rho} \geq 2.5 = q_{min}$. This value of q_{min} was selected after it became apparent that in all cases $<|\hat{S}(\frac{q}{\rho})|^2>$ had achieved a constant value for $\frac{q}{\rho} \geq q_{min}$. (We also fit a line to the background region, but in all cases the slope within error was consistent with zero.) Although the background is fixed for a given spectrum, it varies from spectrum to spectrum as the modeling parameters are changed. A second feature of $<|\hat{S}(\frac{q}{\rho})|^2>$ that is present for both GOE and for Poisson spectra is a spike $\approx$ 2 orders of magnitude off the two scales of Figure 3.1. We have specified the correlation hole as that region enclosed by the following boundaries: (1) the horizontal line $<|\hat{S}(\frac{q}{\rho})|^2> = \beta$, (2) the vertical line $q = \lambda$, where λ is the $\frac{q}{\rho}$ value of the first point in the sequence of $|\hat{S}|^2$ values for which the value of $|\hat{S}|^2 \leq \beta$, and (3) the $|\hat{S}|^2$ curve. For the power spectrum shown in the top portion of Figure 3.7, the correlation hole region is shown shaded.

It is analytically straightforward to calculate the area of the correlation hole once the boundaries of the correlation hole region are well-defined. An array of values (A_i) is formed by subtracting each element of the $<|\hat{S}(\frac{q}{\rho})|^2>$ array for which $q \leq q_{min}$ from β. The set of J numbers (A_i) is then numerically integrated to determine $\mathcal{A}$. The particular algorithm used in these calculations to perform the numerical integration is an alternative extended Simpson's rule. An estimate of the error in the integration calculation can be analytically derived and is of order J^{-4}. In all cases, we have specified the normalized area, obtained as $\frac{\mathcal{A}}{\beta}$.

The second quantification procedure determines the set of coefficients obtained by fitting a specified function via a least-squares algorithm to the $<|\hat{S}(\frac{q}{\rho})|^2>$ curve. It is necessary that the fitting function have at least one undetermined parameter which distinguishes between GOE-like and Poisson-like behavior. As displayed

Figure 3.7 Fourier Transform eigenvalue statistics. (Top) A plot showing an ensemble-averaged power spectrum with the correlation hole region shaded. (Bottom) A plot showing an ensemble-averaged power spectrum with the functional fit overlayed.

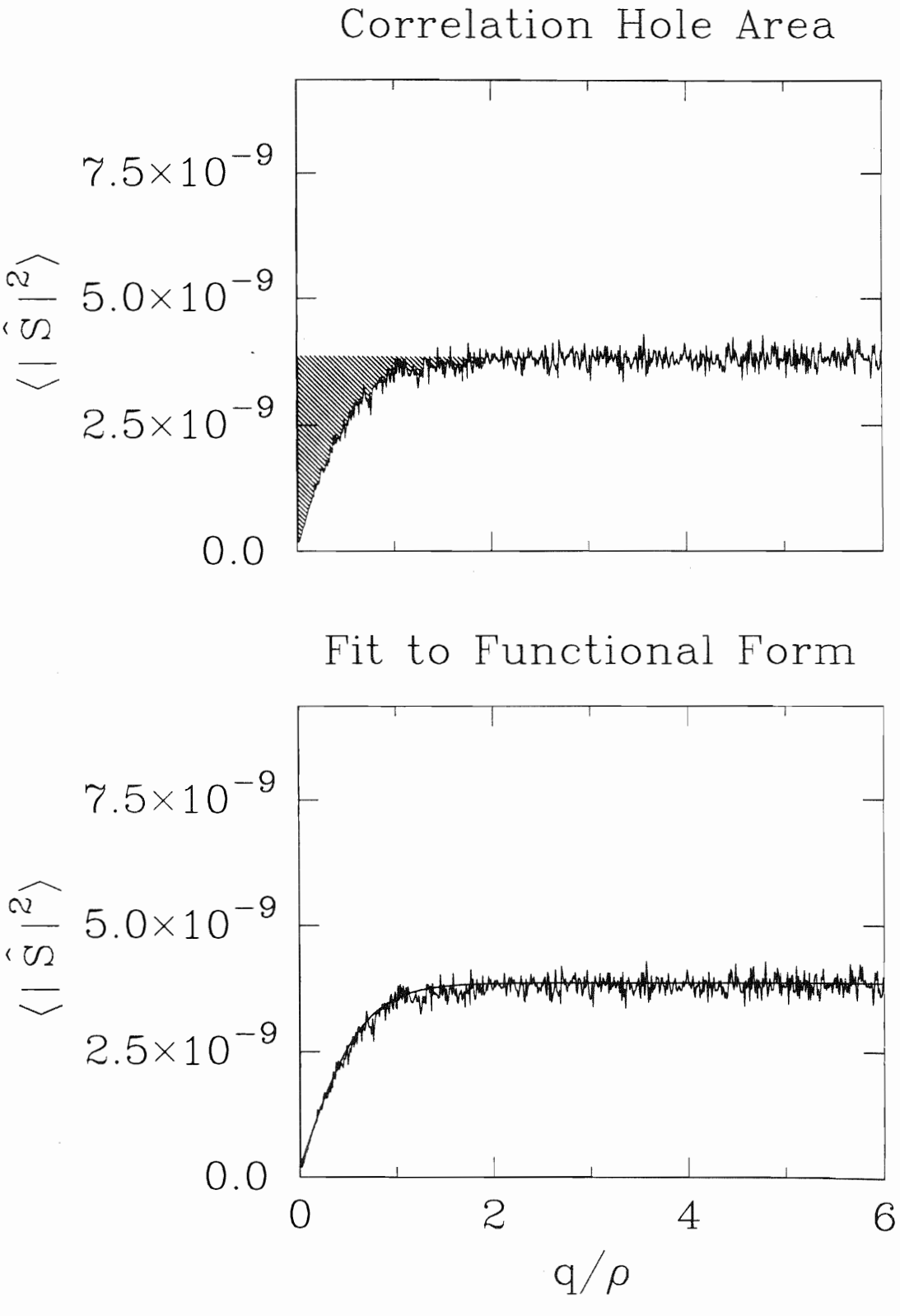
Correlation Hole Area
7.5×10⁻⁹
5.0×10⁻⁹
2.5×10⁻⁹
0.0
⟨|Ŝ|²⟩
Fit to Functional Form
7.5×10⁻⁹
5.0×10⁻⁹
2.5×10⁻⁹
0.0
⟨|Ŝ|²⟩
0
2
4
6
q/ρ

in Figure 3.1, the shape of $<|\hat{S}(\frac{q}{\rho})|^2>$ for GOE spectra, apart from the spike at $\frac{q}{\rho} = 0$, is reminiscent of a hyperbolic tangent curve. The $<|\hat{S}(\frac{q}{\rho})|^2>$ curve for Poisson spectra, on the other hand, has a constant value, once again apart from a spike at $\frac{q}{\rho} = 0$. Let the $<|\hat{S}(\frac{q}{\rho})|^2>$ function be represented by y. A functional form that might incorporate both possibilities is

$$y\left(\frac{q}{\rho}\right) = a_1 \tanh\left(\frac{q/\rho}{a_2}\right) + a_3. \tag{3.26}$$

In Equation 3.26, a_1 and a_3 are measures of the relative strengths of the GOE and Poisson components of $<|\hat{S}(\frac{q}{\rho})|^2>$ respectively. The parameter a_2 measures the width of the correlation hole. Rearranging Equation 3.26 and redefining the coefficient a_1 yields

$$y\left(\frac{q}{\rho}\right) = a_3\left[a_1 \tanh\left(\frac{q/\rho}{a_2}\right) + 1\right]. \tag{3.27}$$

In Equation 3.27, a_3 is a normalization factor for the entire function, a_2 measures the width of the correlation hole, and a_1 is a measure of the relative importance of GOE versus Poisson components in $<|\hat{S}(\frac{q}{\rho})|^2>$. This form, Equation 3.27, is the form that we have used in our fitting procedure, and the fit obtained for the power spectrum displayed in Figure 3.1 is shown in the bottom portion of Figure 3.7.

Fitting a specified function to a number of data points is a standard problem in numerical analysis. A significant division in approach occurs, however, depending on whether the fitting function is linear or nonlinear in the parameters. There are a number of efficient routines available to perform a fit to a function that is linear in the parameters. However, the available methods for fitting to a nonlinear function are much less in number. More difficult yet to obtain is a routine that permits the specification of limits on the fitting coefficients. The form, Equation 3.27, is nonlinear in a_2 and, therefore, a nonlinear fitting routine must be used. Furthermore, it is desirable to impose limits on the range of permitted values returned for the fitting coefficients. In particular, we have imposed the following limits on the coefficients:

$$0 \leq a_1 \leq 100000,$$

$$0.15 \leq a_2 \leq 5.0, \quad \text{and} \tag{3.28}$$
$$0 \leq a_3 \leq 1000.$$

The values of a_2 are limited since very large or very small values of a_2 give the shape of a Poisson curve, and a fit that produces such values of a_2 for a GOE curve would be meaningless. The upper bounds on a_1 and a_3 are merely for termination; if the fitting routine increases a_1 and a_3 to these limits, the fit is not improving, and an alternate approach to improving the fit by varying a different coefficient is appropriate. The fitting code we have used in this work is DN2GB — a double precision, nonlinear, FORTRAN subroutine that we obtained from the public-access PORT library maintained at the AT&T Bell Labs Research Center in Murray Hill, New Jersey.

A FORTRAN program was written to incorporate the calculations described in this chapter. Using the generated sets of eigenvalues, each of which has a known spacing pdf, statistics related to the correlation hole area and the fitting coefficients were determined. The results for the modeling are presented in the following chapter.

Chapter 4

Modeling Results

4.1 Modeling Variables

There are a number of variables which affect the final form of $|\hat{S}|^2$ for a single spectrum or $<|\hat{S}|^2>$ for an ensemble of spectra. Some of the variables are determined by the data set being analyzed; others are chosen in the process of calculating the power spectrum. It is important to understand any limitations or caveats of a FT-based analysis and to interpret the results accordingly. Therefore, we have modeled the behavior of the FT as a function of several relevant variables, and those results are presented in this chapter. First, results of the FT procedure applied to ensemble-averaged spectra are presented in Section 4.2, followed by the results for individual spectra in Section 4.3. To study the behavior of ensemble-averaged spectra, we have generated 500 spectra of each type, calculated the FT for each spectrum, formed the corresponding power spectrum, averaged the power spectra, and determined the quantities of interest from the ensemble-averaged curve. Each of the original 500 spectra have identical defining parameters — N, D, Δ, and ζ — all to be discussed presently.

Those variables that are determined by the data set are strictly fixed, and their

value may thus place restrictions on what sequences are properly analyzable with a FT technique. One variable that is determined by the data set is the number of levels (N) which compose a given sequence. The importance of the value of N in our modeling has been previously discussed in Section 2.4. We have studied the behavior of the FT for eigenvalue sets having $N = 20, 50, 100, 150$, and 300 members. A second data-related parameter is the average level spacing (D) for a sequence. The level spacing values for a sequence may cover a wide range (an order of magnitude or more if the sequence spans low excitation and high excitation energies) since the nuclear level density is approximately exponential as a function of excitation energy. The average level spacing for a sequence having spacing values $\{S_i | i = 1, N-1\}$ is calculated using the expression,

$$D = \frac{1}{N-1} \sum_{k=1}^{N-1} S_i. \tag{4.1}$$

In our modeling, a given spectrum is scaled so that its average spacing is given by the desired value of D. We have considered the behavior of the power spectrum for $D = 0.1, 0.2, 0.3, 0.4$, and 0.5. With N fixed, a larger (smaller) value of D implies that the sequence spans a larger (smaller) energy range.

One parameter that is chosen in the calculation of the power spectrum for a sequence is Δ, the sampling interval. For a given data set, a wide range in possible values of Δ exists; however, unfavorable consequences may result from some choices of Δ. For example, if Δ is on the order of D, the elements of the array that results from sampling (denoted by Z in Section 3.2) are determined by a number of the eigenvalues, i.e., many eigenvalues may be lumped together to form a given element of Z. This situation may be undesirable, depending on the particular application. A value of Δ that is too small may also present problems. A smaller (larger) value of Δ physically means that the array to be Fourier transformed (Z of Section 3.2) is more (less) sparse, i.e., has more (less) elements equal to zero. Additionally, as Δ is chosen smaller, the dimension of Z becomes larger, necessitating more computer

memory and longer computation times. Values of Δ of 0.002, 0.005, 0.01, 0.02, and 0.03 have been considered in our modeling.

The approach that we have employed in modeling is to vary each parameter individually to determine what effects such variation may have on the resulting power spectrum. In one instance, however, two parameters, N and D, were varied simultaneously so that a fixed energy range was spanned. Since the energy range spanned by an eigenvalue set is proportional to both N and D, holding all other variables fixed, a fixed energy range may be spanned by increasing N (D) while decreasing D (N). In our modeling, N and D were chosen such that $(N-1)D = 20$.

In the modeling of the FT as a function of N, D, and Δ, only pure and complete spectra were used. However, a nuclear data set may be incomplete and/or impure, and the effects are significant. In particular, the NNS distribution and value of Δ_3 for a GOE spectrum tends toward more Poisson-like behavior as the degree of impurity or incompleteness increases. Physically, this means that levels actually belonging to the sequence have not been included in it (missing levels) or that levels not belonging to a sequence have been erroneously included with it (spurious levels). Two possible reasons for incompleteness and/or impurity may derive from experimental limitations on the acquisition of the data or incorrect assignment of quantum numbers. As discussed previously, it is hoped that the FT will reveal useful information even under these circumstances. For convenience in studying the effects of impurity and incompleteness, we shall denote the percentage of spurious/missing levels in a sequence by ζ; for a sequence with spurious levels, $\zeta > 0$, and for a sequence with missing levels, $\zeta < 0$. In modeling, we have considered sequences for which 10%, 20%, 30%, 40%, and 50% of the levels are spurious and sequences for which 10%, 20%, 30%, 40%, 50%, 60%, and 70% of the levels are missing. In the modeling of x % missing levels for a set of N eigenvalues, we have generated a set of eigenvalues composed of $N/(1 - \frac{x}{100})$ levels. Then, we randomly remove x % of the levels before calculation of the power spectrum. Conversely, in

the modeling of x % spurious levels for a set of N eigenvalues, we have generated two sets of eigenvalues, each set of which has $N(1 - \frac{x}{100})$ levels and identical N, D, Δ, and spectrum type. Then, we include a random subset of x levels of one sequence into the other sequence.

It may be the case experimentally that two or more sequences are mistakenly considered as one. Such a circumstance may occur, for example, in a data set for which there are more good quantum numbers than previously thought. Thus, one supposed sequence may actually be composed of two or more smaller sequences. Such a situation has observable consequences in the associated power spectrum for a GOE sequence. If m independent GOE spectra are superimposed, the width of the correlation hole is reduced by a factor of m, while the depth of the correlation hole remains independent of m [Lev86]. Superposition of Poisson spectra is expected to remain Poisson. We have chosen $m = 1, 2, 3, 4, 5$, and 6 for specific modeling. In each case of modeling m superimposed GOE spectra, we chose $N = 300$ as the case for study (300 is evenly divisible by 2, 3, 4, 5, and 6) and generated $500m$ sets of eigenvalues with each set containing $\frac{300}{m}$ levels. Subsequently, m sequences are merged and placed in ascending order to form 500 sequences of 300 levels each. From these merged sequences, the previously mentioned FT calculations involving $\mathcal{A}, a_1$, and a_2 are performed.

The computer program that we use to generate sets of eigenvalues having a GOE spacing pdf arbitrarily assigns the first eigenvalue to be zero. Therefore, the straightforward superposition of m GOE spectra would result in the value zero being m-fold degenerate. To avoid this circumstance, when superimposing m spectra, we select the single spectrum (of the set of m) that spans the largest energy range (denote the upper energy limit as E_N), calculate the corresponding central value of energy ($\frac{E_N}{2}$), center the remaining $m - 1$ eigenvalue sets about this largest central value, and finally superimpose the m spectra.

4.2 Ensemble Average Results

The effect of varying N, D, Δ, ζ, and m are first considered on ensemble-averaged spectra. In each case, the quantities that are tabulated are the normalized correlation hole area ($\mathcal{A}$), the background value (β), the spike-to-background ratio ($R_{sb} = <|\hat{S}(q=0)|^2> / \beta$), and the fitting coefficients a_1 and a_2.

The modeling results for $\mathcal{A}$ as a function of N are presented in Table 4.1. In this case both D and Δ remain fixed, and $\zeta = 0$. The normalized correlation hole area ($\mathcal{A}$) is distinctly different for GOE spectra than for Poisson spectra. In all cases, $0.40 \leq \mathcal{A} \leq 0.45$ for GOE spectra, while $\mathcal{A}$ is closely scattered around zero for Poisson spectra. The smallest values for $\mathcal{A}$ occur for the smallest values of N, but, even in that case, a clear distinction between GOE behavior and Poisson behavior exists. For both GOE and Poisson spectra, β is independent of N, and R_{sb} differs from N by no more than one.

Previously, it has been suggested [Lev86] that $\beta \propto N$ and that $<|\hat{S}(q=0)|^2> \propto N^2$; however, we do not observe that $\beta \propto N$. The definitions of certain quantities may be sufficiently different to cause this discrepancy. In Appendix A, R_{sb} is evaluated for a function composed of a sequence of delta functions and shown to equal N. This behavior for R_{sb} is seen to occur in all subsequent tables showing modeling results for unsmoothed spectra. We conclude that $\mathcal{A}$ distinguishes GOE and Poisson behavior, independent of the value of N.

The results for the determination of the fitting coefficients as a function of N are shown in Table 4.2. The values for a_1 are spread closely around 20 for GOE spectra while they are near zero for Poisson spectra. The values for a_2 are also separate for the two extremes, being ≈ 0.67 for GOE spectra and near the lower limit of 0.15 for Poisson spectra. Thus, a_1 and a_2 also clearly distinguish GOE and Poisson behavior, independent of the value of N.

The results of the modeling of the FT as a function of D are shown in Tables 4.3

TABLE 4.1. Correlation hole properties as a function of N for ensemble-averaged spectra: $D = 0.3$, $\Delta = 0.01$.

Spectrum Type	N	β	R_{sb}	$\mathcal{A}$
GOE	20	6.7×10^{-6}	19	0.41
GOE	50	6.7×10^{-6}	49	0.44
GOE	100	6.7×10^{-6}	99	0.45
GOE	150	6.7×10^{-6}	149	0.45
GOE	300	6.7×10^{-6}	300	0.46
Poisson	20	6.7×10^{-6}	19	0.00
Poisson	50	6.7×10^{-6}	49	0.00
Poisson	100	6.7×10^{-6}	99	0.00
Poisson	150	6.7×10^{-6}	149	0.00
Poisson	300	6.7×10^{-6}	299	0.00

TABLE 4.2. Fitting coefficients as a function of N for ensemble-averaged spectra; $D = 0.3$, $\Delta = 0.01$.

Spectrum Type	N	a_1	a_2
GOE	20	15	0.68
GOE	50	23	0.66
GOE	100	19	0.67
GOE	150	20	0.67
GOE	300	19	0.67
Poisson	20	0.080	0.15[a]
Poisson	50	0.00[a]	N/A[b]
Poisson	100	0.030	0.15[a]
Poisson	150	0.021	0.17
Poisson	300	0.00[a]	N/A[b]

[a]Limiting value of coefficient imposed in fitting routine.

[b]Value of a_2 is meaningless if $a_1 = 0$.

and 4.4. Both Δ and N remain fixed, and $\zeta = 0$. As in the variation with N, $\mathcal{A} \approx 0.45$ in each case for GOE spectra and about zero for Poisson spectra. The background appears to vary approximately inversely with D ($\beta \approx 1.97 \times 10^{-6}/D$). The fitting coefficients display similar behavior as in the variation with N: $a_1 \approx 20$ for GOE spectra and $a_1 \approx 0$ for Poisson spectra; $a_2 \approx 0.67$ for GOE spectra, and $a_2 = 0.15$, which is the lower limit of the coefficient imposed in the fitting routine. Therefore, $\mathcal{A}, a_1$, and a_2 distinguish GOE and Poisson behavior, regardless of the value of N.

In Tables 4.5 and 4.6 are shown the results for modeling the behavior of the FT as a function of Δ. Both N and D remain fixed, and $\zeta = 0$. The three statistics, $\mathcal{A}$, a_1, and a_2, again assume very distinct and consistent values: $\mathcal{A} \approx 0.45$, $a_1 \approx 20$, and $a_2 \approx 0.67$ for GOE spectra while $\mathcal{A}$ and a_1 are approximately zero and a_2 is equal to the lower limit for Poisson spectra. The background roughly follows a power relation: $\beta \approx 6.7\Delta^3$.

The results for the modeling when N and D are simultaneously varied to achieve a constant energy range are presented in Tables 4.7 and 4.8 and reflect the individual variations of N and D. The values of $\mathcal{A}$ are in the range [0.41 , 0.45] with smaller values of $\mathcal{A}$ occurring for smaller values of N, just as in the results with only N varied. Also, the background varies inversely with D (and proportionally to N), as in the cases where only D is varied. The fitting coefficients display behavior similar to previous cases — $a_1 \approx 20$ (except at the smallest values of N) for GOE spectra and $a_1 \approx 0.0$ for Poisson spectra. The width parameter, a_2, assumes values near 0.66 for GOE spectra and near 0.15 for Poisson spectra, the lower limit imposed in the fitting routine.

The values of the three statistical parameters — $\mathcal{A}$, a_1, and a_2 — for ensemble-averaged spectra are shown graphically in Figures 4.1, 4.2, and 4.3. On these graphs are displayed the variations of $\mathcal{A}$, a_1, and a_2 singly as a function of N, D, Δ, and jointly as a function of N and D. In each case, $<|\hat{S}|^2>$ is well-defined, as is each of

TABLE 4.3. Correlation hole properties as a function of D for ensemble-averaged spectra: N = 100. $\Delta = 0.01$.

Spectrum Type	D	β	R_{sb}	$\mathcal{A}$
GOE	0.1	2.0×10^{-5}	100	0.44
GOE	0.2	1.0×10^{-5}	99	0.45
GOE	0.3	6.7×10^{-6}	99	0.45
GOE	0.4	5.0×10^{-6}	99	0.45
GOE	0.5	4.0×10^{-6}	99	0.45
Poisson	0.1	2.0×10^{-5}	99	0.00
Poisson	0.2	1.0×10^{-5}	99	0.00
Poisson	0.3	6.7×10^{-6}	99	0.00
Poisson	0.4	5.0×10^{-6}	99	0.00
Poisson	0.5	4.0×10^{-6}	99	0.00

TABLE 4.4. Fitting coefficients as a function of D for ensemble-averaged spectra; N = 100, $\Delta = 0.01$.

Spectrum Type	D	a_1	a_2
GOE	0.1	21	0.65
GOE	0.2	19	0.66
GOE	0.3	19	0.67
GOE	0.4	18	0.67
GOE	0.5	18	0.67
Poisson	0.1	0.03	0.15[a]
Poisson	0.2	0.03	0.15[a]
Poisson	0.3	0.03	0.15[a]
Poisson	0.4	0.03	0.15[a]
Poisson	0.5	0.03	0.15[a]

[a]Limiting value of coefficient imposed in fitting routine.

TABLE 4.5. Correlation hole properties as a function of Δ for ensemble-averaged spectra; N = 100. $D = 0.3$.

Spectrum Type	Δ	β	R_{sb}	$\mathcal{A}$
GOE	0.002	5.3×10^{-8}	99	0.45
GOE	0.005	8.3×10^{-7}	99	0.45
GOE	0.01	6.7×10^{-6}	99	0.45
GOE	0.02	5.3×10^{-5}	99	0.44
GOE	0.03	1.8×10^{-4}	100	0.44
Poisson	0.002	5.3×10^{-8}	99	0.00
Poisson	0.005	8.3×10^{-7}	99	0.00
Poisson	0.01	6.7×10^{-6}	99	0.00
Poisson	0.02	5.3×10^{-5}	99	0.00
Poisson	0.03	1.8×10^{-4}	99	0.00

TABLE 4.6. Fitting coefficients as a function of Δ for ensemble-averaged spectra; N = 100, $D = 0.3$.

Spectrum Type	Δ	a_1	a_2
GOE	0.002	18	0.68
GOE	0.005	18	0.67
GOE	0.01	19	0.67
GOE	0.02	20	0.66
GOE	0.03	21	0.65
Poisson	0.002	0.03	0.15[a]
Poisson	0.005	0.03	0.15[a]
Poisson	0.01	0.03	0.15[a]
Poisson	0.02	0.03	0.15[a]
Poisson	0.03	0.03	0.15[a]

[a]Limiting value of coefficient imposed in fitting routine.

TABLE 4.7. Correlation hole properties as a function of N and D for ensemble-averaged spectra; $(N-1)D = 20$, $\Delta = 0.01$.

Spectrum Type	N	β	R_{sb}	$\mathcal{A}$
GOE	20	1.9×10^{-6}	19	0.41
GOE	50	4.9×10^{-6}	49	0.44
GOE	100	9.9×10^{-6}	99	0.45
GOE	150	1.5×10^{-5}	150	0.44
GOE	300	3.0×10^{-5}	301	0.44
Poisson	20	1.9×10^{-6}	19	0.00
Poisson	50	4.9×10^{-6}	49	0.00
Poisson	100	9.9×10^{-6}	99	0.00
Poisson	150	1.5×10^{-5}	149	0.00
Poisson	300	3.0×10^{-5}	299	0.00

TABLE 4.8. Fitting coefficients as a function of N and D for ensemble-averaged spectra; $(N-1)D = 100$, $\Delta = 0.01$.

Spectrum Type	N	a_1	a_2
GOE	20	14	0.69
GOE	50	23	0.66
GOE	100	19	0.66
GOE	150	22	0.66
GOE	300	26	0.64
Poisson	20	0.07	0.15[a]
Poisson	50	0.00[a]	N/A[b]
Poisson	100	0.03	0.15[a]
Poisson	150	0.02	0.17
Poisson	300	0.00[a]	N/A[b]

[a]Limiting value of coefficient imposed in fitting routine.

[b]Value of a_2 is meaningless if $a_1 = 0$.

Figure 4.1 Variation of $\mathcal{A}$ for ensemble-averaged spectra. (First) The variation of $\mathcal{A}$ with N [D = 0.3, $\Delta = 0.01$]. (Second) The variation of $\mathcal{A}$ with D [N = 100, $\Delta = 0.01$]. (Third) The variation of $\mathcal{A}$ with Δ [N = 100, D = 0.3]. (Fourth) The variation of $\mathcal{A}$ with N and D [$(N-1)D = 20$, $\Delta = 0.01$]. Values for GOE (Poisson) spectra are denoted by a $\bullet$ ($\times$) symbol.

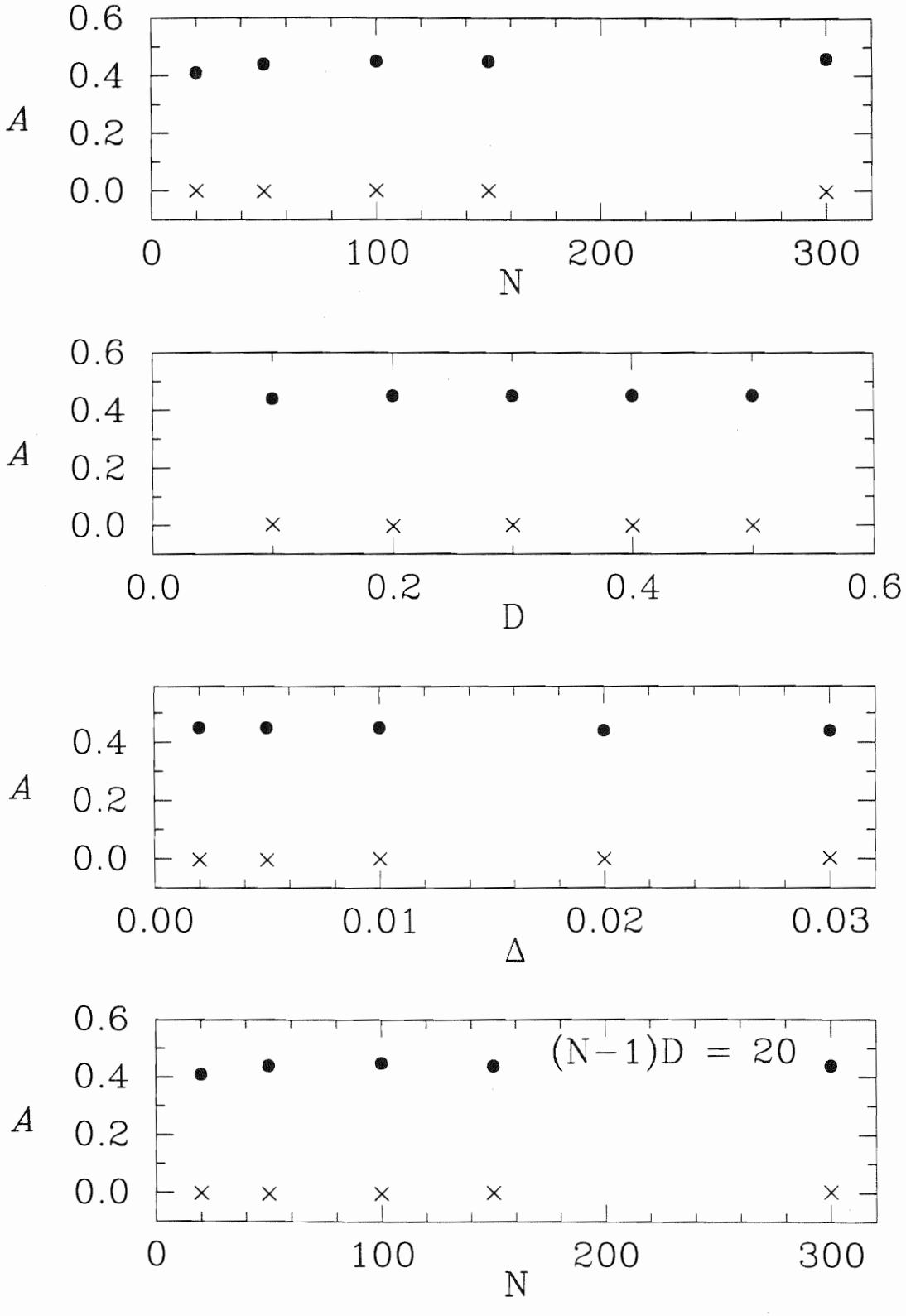
0.6
0.4
0.2
0.0
A
0
100
200
300
N
0.6
0.4
0.2
0.0
A
0.0
0.2
0.4
0.6
D
0.4
0.2
0.0
A
0.00
0.01
0.02
0.03
Δ
0.6
0.4
0.2
0.0
A
(N−1)D = 20
0
100
200
300
N

Figure 4.2 Variation of a_1 for ensemble-averaged spectra. (First) The variation of a_1 with N [D = 0.3, Δ = 0.01]. (Second) The variation of a_1 with D [N = 100, Δ = 0.01]. (Third) The variation of a_1 with Δ [N = 100, D = 0.3]. (Fourth) The variation of a_1 with N and D [$(N-1)D = 20$, Δ = 0.01]. Values for GOE (Poisson) spectra are denoted by a $\bullet$ ($\times$) symbol.

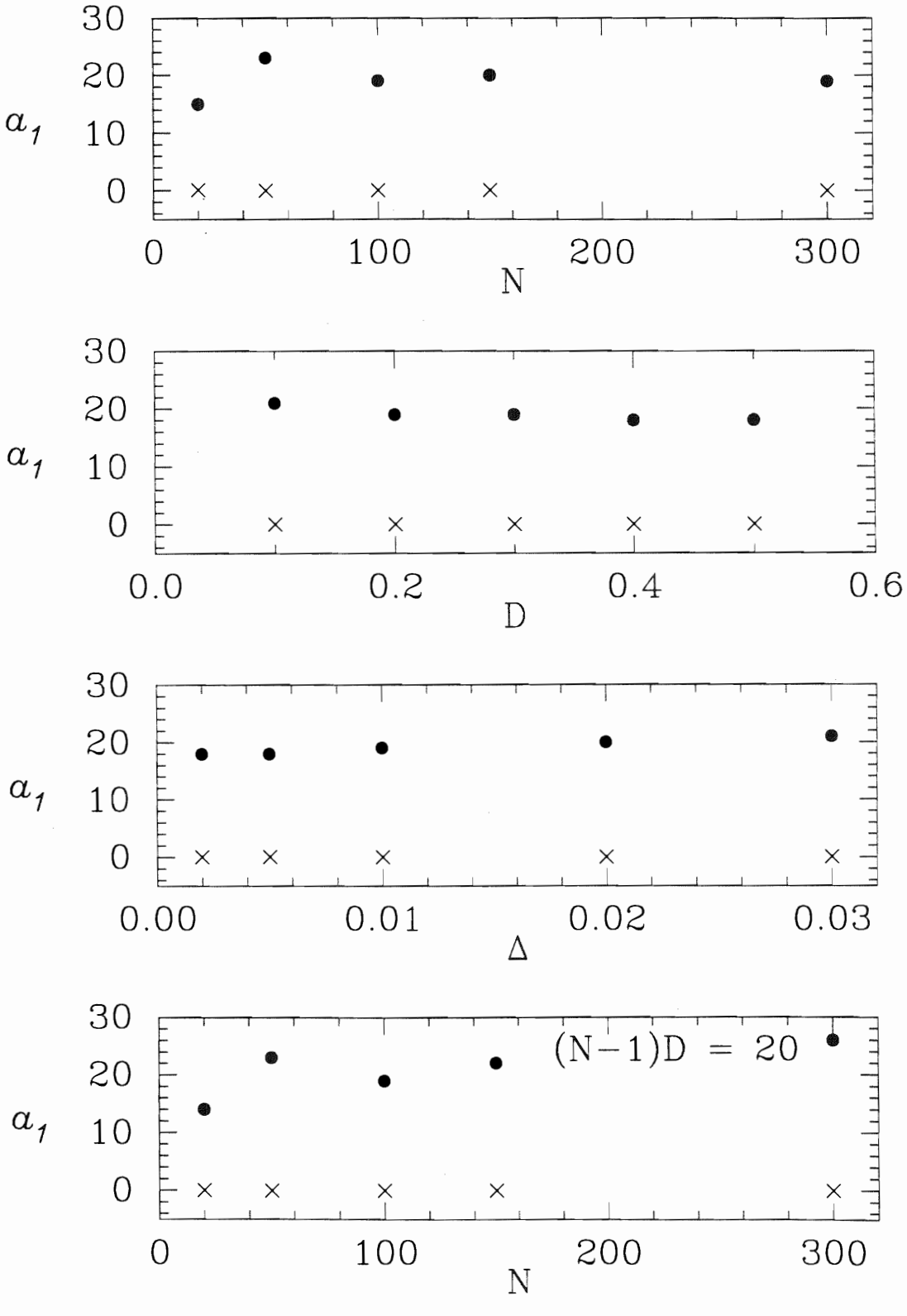
30
20
10
0
a_1
0
100
200
300
N
0.0
0.2
0.4
0.6
D
0.00
0.01
0.02
0.03
Δ
(N−1)D = 20

Figure 4.3 Variation of a_2 for ensemble-averaged spectra. (First) The variation of a_2 with N [D = 0.3, $\Delta = 0.01$]. Values for which $a_1 = 0$ are denoted by a $\square$ at $a_2 = 0$. (Second) The variation of a_2 with D [N = 100, $\Delta = 0.01$]. (Third) The variation of a_2 with Δ [N = 100, D = 0.3]. (Fourth) The variation of a_2 with N and D [$(N-1)D = 20$, $\Delta = 0.01$]. Values for which $a_1 = 0$ are denoted by a $\square$ at $a_2 = 0$. Values for GOE (Poisson) spectra are denoted by a $\bullet$ ($\times$) symbol.

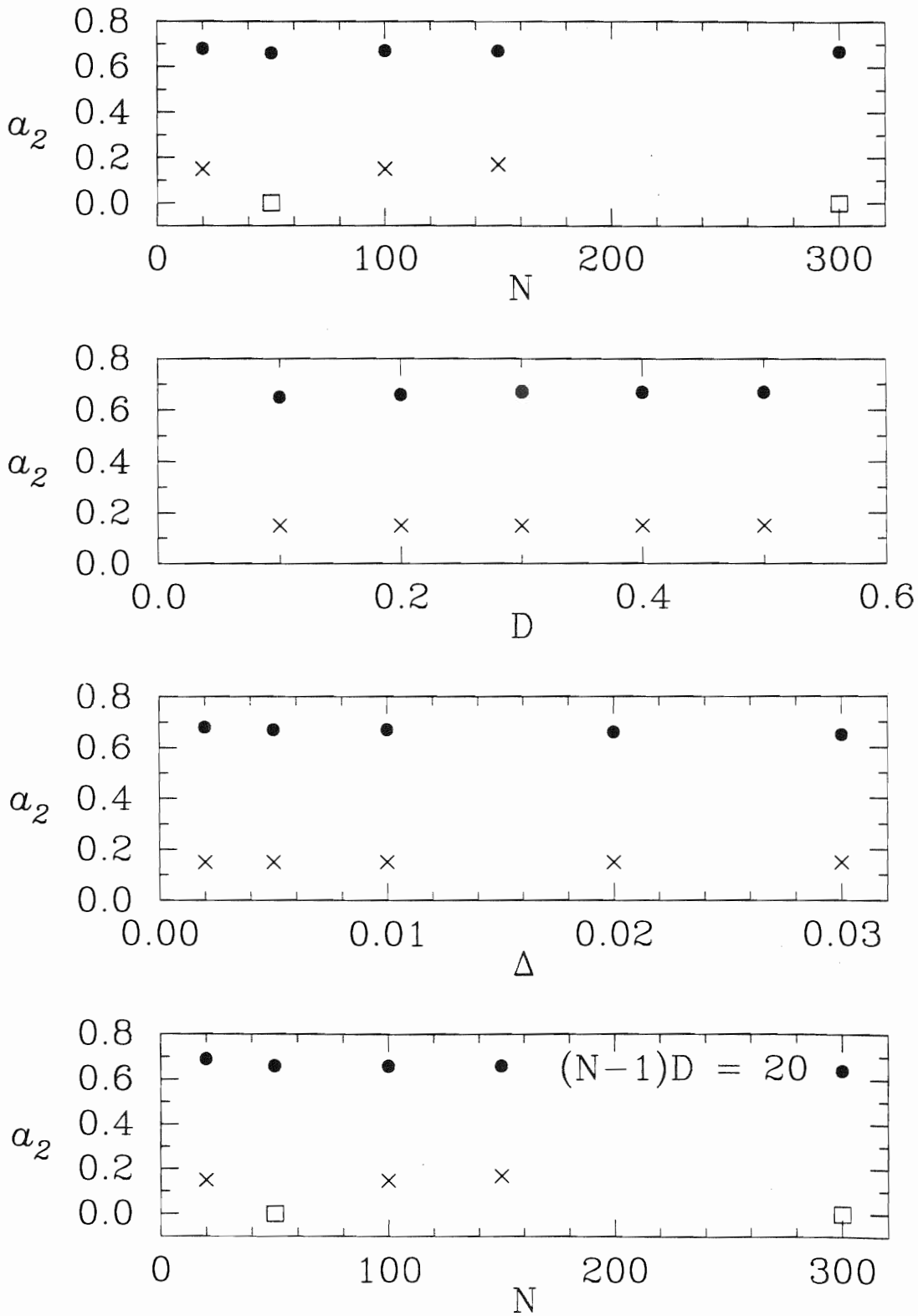
0.8
0.6
0.4
0.2
0.0
a_2
0
100
200
300
N
0.0
0.2
0.4
0.6
D
0.00
0.01
0.02
0.03
Δ
(N−1)D = 20

the three parameters. Accordingly, $\mathcal{A}$, a_1, and a_2 may be used to quantitatively characterize the $<|\hat{S}|^2>$ curve. Furthermore, there is an unambiguous distinction in parameter values for GOE versus Poisson spectra. The parameter values are consistent with the surmise:

$$\begin{aligned} &\mathcal{A} \approx 0.45, \quad a_1 \approx 20, \text{ and } \quad a_2 \approx 0.67 \quad \text{indicate GOE statistics;} \\ &\mathcal{A} \approx 0.0, \quad a_1 \approx 0.0, \text{ and } \quad a_2 \approx 0.15 \quad \text{indicate Poisson statistics.} \end{aligned} \tag{4.2}$$

The next question to address is how the parameters are affected by incompleteness and/or impurity, for which the relevant variable is ζ.

The variation of $\mathcal{A}$, a_1, and a_2 as a function of ζ is shown in Tables 4.9 - 4.12. From Tables 4.9 and 4.10, both β and R_{sb} are independent of ζ, having values $\beta \approx 6.6 \times 10^{-6}$ and $R_{sb} \approx N$. This behavior is observed for both GOE and Poisson spectra. However, in the case of GOE spectra, $\mathcal{A}$ is sharply affected by varying ζ: $\mathcal{A}$ is significantly reduced with increasing positive values of ζ, and $\mathcal{A}$ is reduced (more slowly) with increasing negative values of ζ. The behavior of $\mathcal{A}$ as a function of ζ is shown in the top portion of Figure 4.4. Of note is the fact that, for GOE spectra, the effect on $\mathcal{A}$ is not symmetric in ζ: missing levels has a less severe impact than does spurious levels.

In Tables 4.11 and 4.12 are shown the values of a_1 and a_2 as a function of ζ. The response of a_1 to varying ζ is not as clear as the response of $\mathcal{A}$ to varying ζ. For GOE spectra, a_1 initially decreases and then increases with increasing positive ζ. For $\zeta < 0$, a_1 decreases monotonically with decreasing ζ. More simply, a_2 is monotonically decreasing with ζ. The variations in a_1 and a_2 for the monotonic cases are given approximately by:

$$\begin{aligned} a_1 &\approx 8.2e^{0.044\zeta} && \zeta < 0 \\ a_2 &\approx 0.74e^{-0.016\zeta} && \zeta > 0 \\ a_2 &\approx 0.57e^{-0.018\zeta} && \zeta < 0. \end{aligned} \tag{4.3}$$

TABLE 4.9. Correlation hole properties as a function of ζ for ensemble-averaged Poisson spectra; N = 100, $\Delta = 0.01$, $D = 0.3$.

Spectrum Type	ζ	β	R_{sb}	$\mathcal{A}$
GOE	+50%	6.7×10^{-6}	99	0.22
GOE	+40%	6.7×10^{-6}	99	0.23
GOE	+30%	6.7×10^{-6}	99	0.26
GOE	+20%	6.7×10^{-6}	99	0.32
GOE	+10%	6.7×10^{-6}	99	0.37
GOE	0%	6.7×10^{-6}	99	0.45
GOE	-10%	6.6×10^{-6}	99	0.44
GOE	-20%	6.6×10^{-6}	99	0.44
GOE	-30%	6.6×10^{-6}	99	0.43
GOE	-40%	6.6×10^{-6}	99	0.43
GOE	-50%	6.6×10^{-6}	99	0.41
GOE	-60%	6.6×10^{-6}	100	0.40
GOE	-70%	6.6×10^{-6}	100	0.36

TABLE 4.10. Correlation hole properties as a function of ζ for ensemble-averaged Poisson spectra; N = 100, $\Delta = 0.01$, $D = 0.3$.

Spectrum Type	ζ	β	R_{sb}	$\mathcal{A}$
Poisson	+50%	6.7×10^{-6}	99	0.00
Poisson	+40%	6.7×10^{-6}	99	0.00
Poisson	+30%	6.7×10^{-6}	99	−0.01
Poisson	+20%	6.7×10^{-6}	99	−0.01
Poisson	+10%	6.7×10^{-6}	99	−0.01
Poisson	0%	6.7×10^{-6}	99	0.00
Poisson	-10%	6.7×10^{-6}	99	0.00
Poisson	-20%	6.7×10^{-6}	99	−0.02
Poisson	-30%	6.7×10^{-6}	99	0.00
Poisson	-40%	6.7×10^{-6}	99	0.01
Poisson	-50%	6.7×10^{-6}	99	0.01
Poisson	-60%	6.7×10^{-6}	99	0.00
Poisson	-70%	6.7×10^{-6}	99	0.00

TABLE 4.11. Fitting coefficients as a function of ζ for ensemble-averaged GOE spectra; N = 100, $\Delta = 0.01$, $D = 0.3$.

Spectrum Type	ζ	a_1	a_2
GOE	+50%	28	0.33
GOE	+40%	4.8	0.40
GOE	+30%	3.7	0.47
GOE	+20%	4.0	0.55
GOE	+10%	6.2	0.62
GOE	0%	19	0.67
GOE	-10%	6.5	0.72
GOE	-20%	3.0	0.84
GOE	-30%	2.0	0.93
GOE	-40%	1.3	1.1
GOE	-50%	0.89	1.3
GOE	-60%	0.60	1.7
GOE	-70%	0.40	2.2

TABLE 4.12. Fitting coefficients as a function of ζ for ensemble-averaged Poisson spectra; N = 100, $\Delta = 0.01$, $D = 0.3$.

Spectrum Type	ζ	a_1	a_2
Poisson	+50%	0.00[a]	N/A[b]
Poisson	+40%	0.00[a]	N/A[b]
Poisson	+30%	0.00[a]	N/A[b]
Poisson	+20%	0.00[a]	N/A[b]
Poisson	+10%	0.00[a]	N/A[b]
Poisson	0%	0.030	0.15[a]
Poisson	-10%	0.00[a]	N/A[b]
Poisson	-20%	0.00[a]	N/A[b]
Poisson	-30%	0.02	0.47
Poisson	-40%	0.01	0.34
Poisson	-50%	0.01	0.55
Poisson	-60%	0.00[a]	N/A[b]
Poisson	-70%	0.03	0.15[a]

[a]Limiting value of coefficient imposed in fitting routine.

[b]Value of a_2 is meaningless if $a_1 = 0$.

Figure 4.4 Variation of statistics with ζ for ensemble-averaged spectra. GOE (Poisson) spectra are denoted by a $\bullet$ ($\times$) symbol. (Top) The variation of $\mathcal{A}$ with ζ. (Center) The variation of a_1 with ζ. Those Poisson values with $a_1 = 0$ are marked with a $\square$ at $a_1 = 10^{-3}$. (Bottom) The variation of a_2 with ζ. Those points with $a_1 = 0$ are marked with a $\square$. In each figure, D = 0.3, $\Delta = 0.01$, and N = 100.

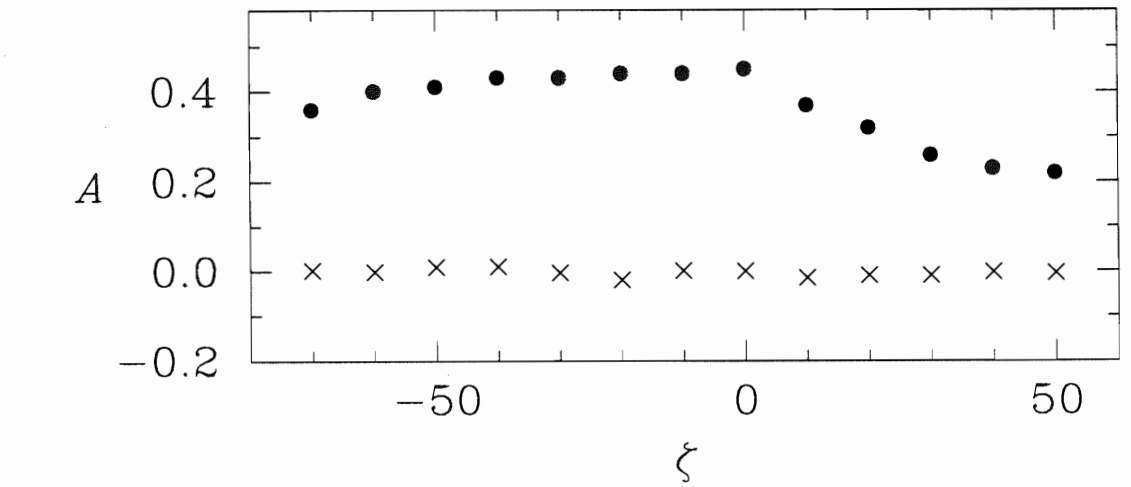
0.4
A 0.2
0.0
−0.2
−50
0
50
ζ

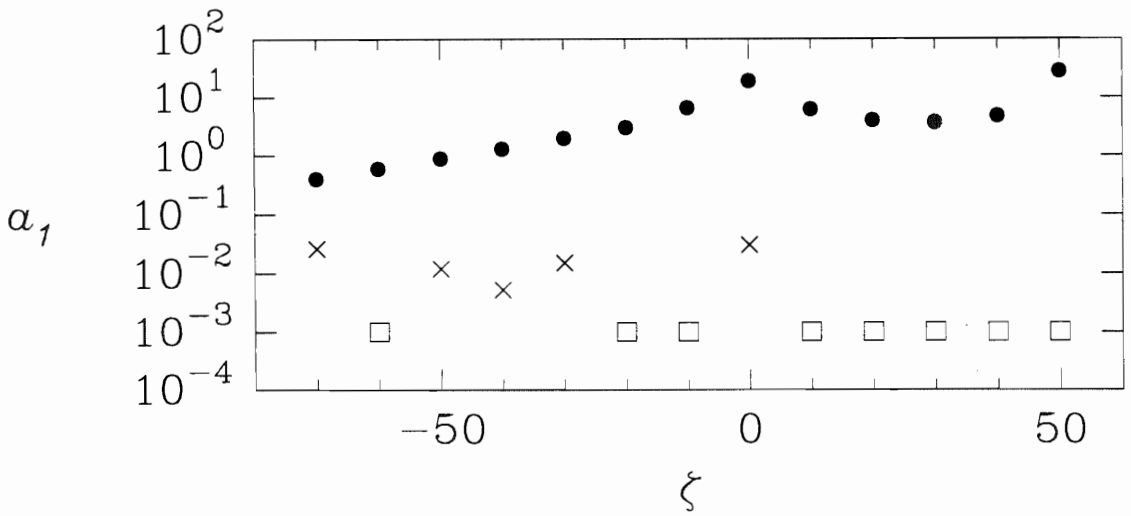
10^2
10^1
10^0
10^{-1}
10^{-2}
10^{-3}
10^{-4}
a_1
−50
0
50
ζ

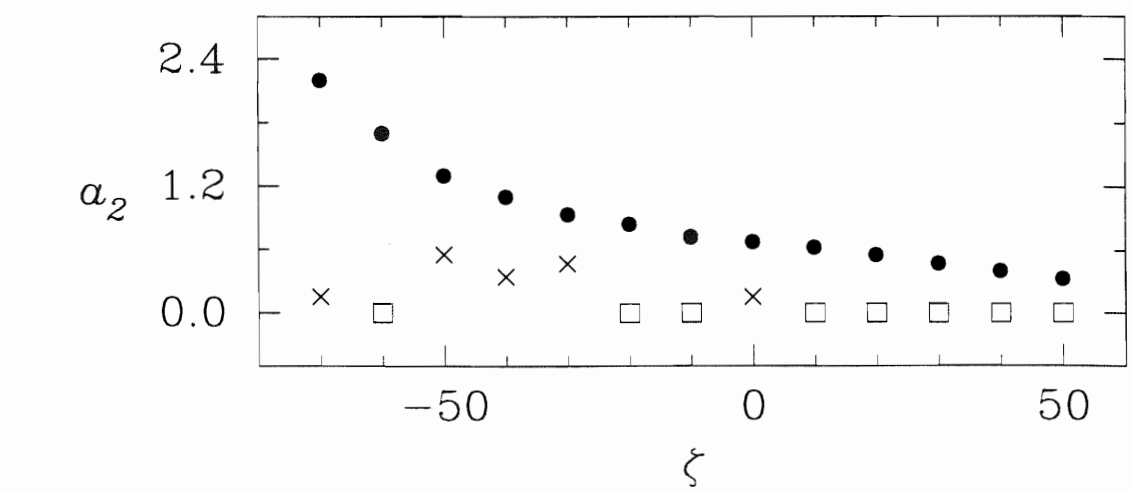
2.4
a_2 1.2
0.0
−50
0
50
ζ

The values of a_1 and a_2 are shown as a function of ζ in the center and bottom portions of Figure 4.4, where the behavior is clear. Even though the values of $\mathcal{A}$, a_1, and a_2 are different for $\zeta \neq 0$ than for $\zeta = 0$, the GOE and Poisson limits are clearly identified for ensemble-averaged spectra, even when 70% of the levels are missing.

The final type of modeling concerns the superposition of m GOE sequences. The results for this modeling are listed in Tables 4.13 and 4.14. Since the surmise of superimposed spectra applies only to GOE spectra, all results in these tables are for GOE spectra. The relevant parameters in this modeling are $\mathcal{A}$ and a_2, since the claim is that the width of the correlation hole varies inversely with m (Section 4.1). The data in Tables 4.13 and 4.14 were fit by a linear least-squares algorithm to the functional form

$$c_1 m^{c_2}. \tag{4.4}$$

The best-fit coefficients are

$$\begin{aligned} c_1 &= 0.455 \pm 0.011 \quad c_2 = -1.01 \pm 0.02 \quad \text{for } \mathcal{A} \\ c_1 &= 0.613 \pm 0.054 \quad c_2 = -0.87 \pm 0.07 \quad \text{for } a_2. \end{aligned} \tag{4.5}$$

For both $\mathcal{A}$ and a_2, there is a strong inverse dependence on m. The value of c_2 indicates that, for ensemble-averaged spectra, the behavior of $\mathcal{A}$ is in clear agreement with the expectation enunciated in Section 4.1. The value of c_2 for a_2 does not as clearly agree with the expectation. The results for $\mathcal{A}$ and a_2 (Equation 4.4 with coefficients given by Equation 4.5) are plotted in Figure 4.5, where the inverse relationship is clearly evident. The dashed line is the best-fit equation.

TABLE 4.13. Correlation hole properties as a function of m for ensemble-averaged spectra: $N = 300$, $\Delta = 0.01$, $D = 0.3$.

m	β	R_{sb}	$\mathcal{A}$
1	1.5×10^{-5}	300	0.45
2	3.1×10^{-5}	300	0.23
3	3.7×10^{-5}	301	0.14
4	4.3×10^{-5}	301	0.11
5	4.8×10^{-5}	300	0.09
6	5.2×10^{-5}	302	0.07

TABLE 4.14. Fitting coefficients as a function of m for ensemble-averaged spectra; $N = 300$, $\Delta = 0.01$, $D = 0.3$.

m	a_1	a_2
1	20	0.67
2	115	0.32
3	16	0.22
4	14	0.17
5	8	0.15[a]
6	4	0.15[a]

[a]Limiting value of coefficient imposed in fitting routine.

Figure 4.5 Ensemble-averaged results for the superposition of m GOE sequences. (Top) The variation of $\mathcal{A}$ with m. (Bottom) The variation of a_2 with m. In each case the dashed curve is the best-fit equation.

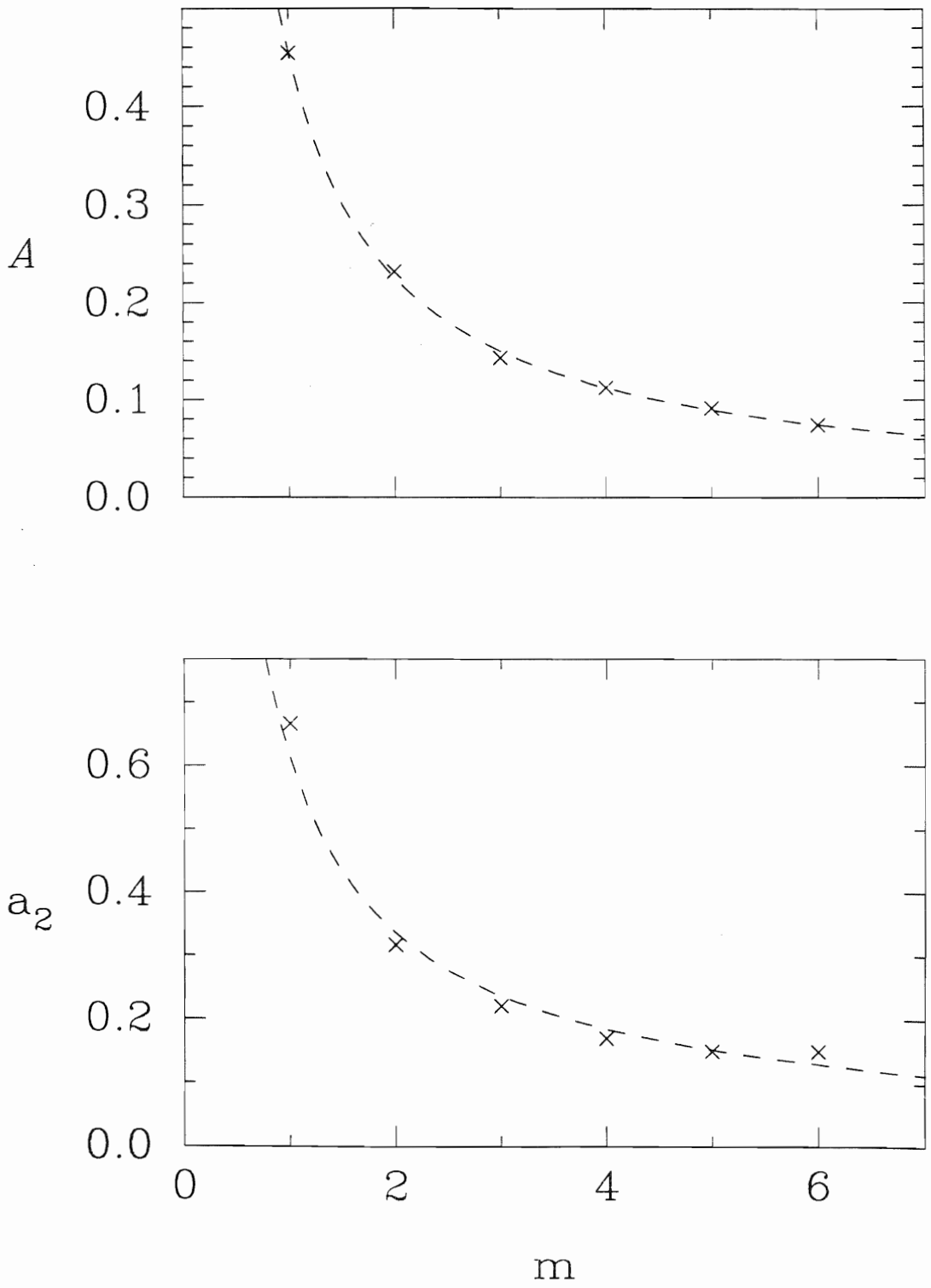
A
0.4
0.3
0.2
0.1
0.0
a2
0.6
0.4
0.2
0.0
0
2
4
6
m

4.3 Individual Spectrum Results

The same quantities — $\mathcal{A}$, a_1, and a_2 — are of interest for both a single spectrum and an ensemble-averaged spectrum. As discussed in Section 3.2, the power spectrum for a single spectrum is substantially noisier than an ensemble-averaged power spectrum. It is not surprising that a range of values of the relevant parameters will be observed for a single spectrum. To study the behavior of the FT for a single spectrum, we calculated $|\hat{S}|^2$ for each of 500 individual spectra and performed the same type of analysis on each $|\hat{S}|^2$ curve that is done on $<|\hat{S}|^2>$. This process results in a set of 500 values each of $\mathcal{A}$, a_1, and a_2. We have chosen to quantify the set of values of $\mathcal{A}$ by specifying the mean and sample standard deviation, both of which are readily calculable. The mean and sample standard deviation of the set of R_{sb} values are also quoted.

For the fitting coefficients a_1 and a_2, quoting a single number that is meaningful and representative of the entire set of values is nontrivial. This is because the distribution of fitting coefficients is severely skewed. For a_1, the skewness is a result of a long-tailed distribution toward large values of a_1 in the GOE case and a result of the imposed limits on a_1 in the Poisson case (Equation 3.29). For a_2, a similar situation exists due to the limits imposed on a_2. Also, if $a_1 = 0$, then the value of a_2 is meaningless. The skewed distributions of fitting coefficients make the common measures of central tendency — the mean, median, and mode — inappropriate descriptive measures of the distributions. What is quoted instead is the central 68% interval and the central 95% interval of the resulting pdf. For example, the 68% confidence interval is calculated by placing the set of 500 values in question in ascending order and choosing the lower bound of the confidence interval as element 80 [= (500)(.16)] and the upper bound of the confidence interval as element 420 [= (500)(.84)].

The smoothing procedures discussed in Section 3.2 do not recover a curve similar

to Figure 3.1 from the power spectrum from a single spectrum. To demonstrate the effect of smoothing $|\hat{S}|^2$, the nine smoothing procedures were applied to 500 individual spectra. For each of the smoothing procedures, the standard deviation of the set of $\mathcal{A}$ values is listed in column two of Table 4.15, and the length of the 68% confidence interval for a_1 (a_2) is shown in column three (four) of Table 4.15. All methods of smoothing, except both types of median smoothing, decrease σ, the standard deviation of the set of $\mathcal{A}$ values. Moreover, the length of the 68% confidence intervals for a_1 and a_2 is increased in median smoothing. Both two-point and four-point smoothing yield unacceptable results, removing significant structures from the spectrum so that the best fit is a horizontal line. Both two-point weighted and four-point weighted smoothing significantly reduce the length (by two orders of magnitude) of the intervals on the fitting coefficients. These algorithms force a similarity on the spectra, making each resulting power spectrum likely to produce very similar sets of fitting coefficients and $\mathcal{A}$. When used in succession in the DCW's average method, the smoothed power spectra all yield the same set of fitting coefficients, a_1 and a_2. Some methods of smoothing seem more appropriate for reducing the variability in the fitting coefficients, and all methods of smoothing reduce σ to roughly the same value (0.06).

The modeling results for a single spectrum as a function of N are shown in Tables 4.16 and 4.17. For small N, $\mathcal{A}$ decreases slightly but remains near the ensemble-averaged value of $\mathcal{A} = 0.45$. For Poisson spectra, $\mathcal{A} = 0.0$ for each N within the sample standard deviation. The main effect, however, is seen in the sample standard deviation on $\mathcal{A}$, which increases by a factor of 4 in passing from $N = 300$ to $N = 20$ in the case of both GOE and Poisson spectra. A consequence of this increase in the standard deviation of the set of values of $\mathcal{A}$ as N increases is that GOE and Poisson behavior are clearly distinguishable if N is large enough, but becomes increasingly less so as N decreases. However, even for $N = 50$, it is possible to distinguish GOE and Poisson behavior to one standard deviation. The

TABLE 4.15. Effects of Spectrum Smoothing on $\mathcal{A}, a_1$, and a_2. For each spectrum, $N = 100, D = 0.3$, and $\Delta = 0.01$

Type of Smoothing	σ	Length of 68% Confidence Interval	Length of 68% Confidence Interval
No smoothing	0.07	82	0.22
1 point	0.05	69	0.159
1 point weighted	0.07	82	0.22
2 point	0.06	0.0[a]	0.0[a]
2 point weighted	0.07	0.81	0.34
4 point	0.01	0.0[a]	0.0[a]
4 point weighted	0.07	0.23	0.69
1 point median	0.11	98	0.32
2 point median	0.13	97	0.37
DCW's average	0.07	0.0[a]	0.0[a]

[a]All separate fits yielded the same values for a_1 and a_2.

TABLE 4.16. Correlation hole properties as a function of N for individual spectra; $D = 0.3$, $\Delta = 0.01$.

		R_{sb}		$\mathcal{A}$	
Spectrum Type	N	μ	σ	μ	σ
GOE	20	19.0	0.3	0.41	0.16
GOE	50	49.1	0.5	0.44	0.10
GOE	100	99.2	0.6	0.45	0.07
GOE	150	149.4	0.7	0.45	0.06
GOE	300	299.6	1.0	0.46	0.04
Poisson	20	19.1	1.2	0.00	0.41
Poisson	50	49.0	1.9	0.00	0.24
Poisson	100	99.1	2.7	0.00	0.18
Poisson	150	149.1	3.4	0.00	0.14
Poisson	300	299.0	4.9	0.00	0.10

TABLE 4.17. Fitting coefficients as a function of N for individual spectra; $D = 0.3$, $\Delta = 0.01$.

Spectrum Type	N	a_1		a_2	
		68% Confidence Interval	95% Confidence Interval	68% Confidence Interval	95% Confidence Interval
GOE	20	[2.4 , 99]	[0.66 , 190]	[0.53 , 1.1]	[0.35 , 1.9]
GOE	50	[4.9 , 95]	[1.7 , 260]	[0.55 , 0.86]	[0.42 , 1.2]
GOE	100	[6.7 , 86]	[3.1 , 250]	[0.57 , 0.79]	[0.46 , 0.95]
GOE	150	[8.1 , 87]	[4.1 , 320]	[0.59 , 0.77]	[0.51 , 0.88]
GOE	300	[9.5 , 66]	[5.6 , 300]	[0.61 , 0.75]	[0.56 , 0.81]
Poisson	20	[0.0[a] , 4.6]	[0.0[a] , 73]	N/A[b]	N/A[b]
Poisson	50	[0.0[a] , 0.86]	[0.0[a] , 37]	N/A[b]	N/A[b]
Poisson	100	[0.0[a] , 0.52]	[0.0[a] , 2.0]	N/A[b]	N/A[b]
Poisson	150	[0.0[a] , 0.40]	[0.0[a] , 1.3]	N/A[b]	N/A[b]
Poisson	300	[0.0[a] , 0.23]	[0.0[a] , 0.69]	N/A[b]	N/A[b]

[a]Limiting value of coefficient imposed in fitting routine.

[b]Value of a_2 is meaningless if $a_1 = 0$.

fitting coefficients display a similar pattern. The 68% confidence interval for a_1 is disjoint for GOE and Poisson limits for $N \geq 50$. A 95% confidence interval, however, for a_1 is disjoint only for $N \geq 100$. While the confidence intervals are well-defined for a_2 in the GOE cases, comparison with the corresponding Poisson case is difficult since $a_1 = 0$ in many of the cases (and therefore a_2 is meaningless). Hence, for small sequences, it is difficult to distinguish GOE and Poisson behavior from the eigenvalue statistics related to $\mathcal{A}$ or the fitting coefficients a_1 and a_2.

In Tables 4.18 and 4.19 the modeling results for single spectra are shown as a function of D. For GOE spectra. $\mathcal{A} \approx 0.45$. while $\mathcal{A} \approx 0.0$ for Poisson spectra. In each case, the GOE and Poisson limits are distinguishable at the 1σ level for $\mathcal{A}$, and the 95% confidence interval is nonoverlapping for a_1. Clearly, within the range of D which we considered, variation in D has little effect on $\mathcal{A}$ or a_1.

Similar remarks may be made concerning the modeling results for single spectra as a function of Δ, which are listed in Tables 4.20 and 4.21. The normalized area $\mathcal{A} \approx 0.45$ for GOE spectra, and $\mathcal{A} \approx 0$ for Poisson spectra. As in the variation with D. the GOE and Poisson limits for $\mathcal{A}$ are distinguishable for each Δ at the 1σ level. Moreover, the 95% confidence intervals for a_1 are disjoint for each Δ. Therefore, variation in Δ over the range we considered also has little effect on $\mathcal{A}$ or a_1.

As both N and D are varied, the results reflect the individual variations of N and D separately. The results for the simultaneous variation of N and D are listed in Tables 4.22 and 4.23. Although $\mathcal{A} \approx 0.45$ for GOE spectra and $\mathcal{A} \approx 0.0$ for Poisson spectra, the uncertainties on $\mathcal{A}$ increase with decreasing N. In fact, the GOE and Poisson limits for $\mathcal{A}$ are not distinct for $N = 20$, just as in the case of variation of N alone (Table 4.16). Furthermore, the standard deviation of R_{sb} increases with decreasing N, duplicating the behavior observed in the variation of D alone (Table 4.18). The 68% (95%) confidence interval for a_1 is such as to distinguish GOE and Poisson behavior only for $N \geq 50(100)$.

TABLE 4.18. Correlation hole properties as a function of D for individual spectra; N = 100, $\Delta = 0.01$.

		R_{sb}		$\mathcal{A}$	
Spectrum Type	D	μ	σ	μ	σ
GOE	0.1	99.6	2.7	0.44	0.11
GOE	0.2	99.3	1.0	0.45	0.08
GOE	0.3	99.2	0.6	0.45	0.07
GOE	0.4	99.2	0.4	0.45	0.07
GOE	0.5	99.1	0.4	0.45	0.07
Poisson	0.1	99.2	6.2	0.00	0.23
Poisson	0.2	99.2	3.4	0.00	0.18
Poisson	0.3	99.1	2.7	0.00	0.18
Poisson	0.4	99.1	2.2	0.00	0.17
Poisson	0.5	99.1	2.0	0.00	0.17

TABLE 4.19. Fitting coefficients as a function of D for individual spectra; N = 100, $\Delta = 0.01$

Spectrum Type	D	a_1		a_2	
		68% Confidence Interval	95% Confidence Interval	68% Confidence Interval	95% Confidence Interval
GOE	0.1	[7.4 , 130]	[3.2 , 320]	[0.55 , 0.80]	[0.45 , 0.98]
GOE	0.2	[6.8 , 110]	[2.8 , 430]	[0.56 , 0.79]	[0.47 , 0.97]
GOE	0.3	[6.7 , 86]	[3.1 , 250]	[0.57 , 0.79]	[0.46 , 0.95]
GOE	0.4	[6.8 , 80]	[3.0 , 230]	[0.57 , 0.80]	[0.47 , 0.95]
GOE	0.5	[6.5 , 76]	[3.0 , 240]	[0.58 , 0.80]	[0.48 , 0.95]
Poisson	0.1	[0.0[a] , 0.51]	[0.0[a] , 2.1]	N/A[b]	N/A[b]
Poisson	0.2	[0.0[a] , 0.50]	[0.0[a] , 1.9]	N/A[b]	N/A[b]
Poisson	0.3	[0.0[a] , 0.52]	[0.0[a] , 2.0]	N/A[b]	N/A[b]
Poisson	0.4	[0.0[a] , 0.47]	[0.0[a] , 1.9]	N/A[b]	N/A[b]
Poisson	0.5	[0.0[a] , 0.41]	[0.0[a] , 2.0]	N/A[b]	N/A[b]

[a]Limiting value of coefficient imposed in fitting routine.

[b]Value of a_2 is meaningless if $a_1 = 0$.

TABLE 4.20. Correlation hole properties as a function of Δ for individual spectra; N = 100, $D = 0.3$.

		R_{sb}		$\mathcal{A}$	
Spectrum Type	Δ	μ	σ	μ	σ
GOE	0.002	99.1	0.1	0.45	0.06
GOE	0.005	99.1	0.2	0.45	0.07
GOE	0.01	99.2	0.6	0.45	0.07
GOE	0.02	99.4	1.4	0.44	0.09
GOE	0.03	99.6	2.7	0.44	0.11
Poisson	0.002	99.1	1.0	0.00	0.16
Poisson	0.005	99.2	1.8	0.00	0.17
Poisson	0.01	99.1	2.7	0.00	0.18
Poisson	0.02	99.3	4.5	0.00	0.20
Poisson	0.03	99.2	6.2	0.00	0.23

TABLE 4.21. Fitting coefficients as a function of Δ for individual spectra; N = 100, $D = 0.3$.

Spectrum Type	Δ	a_1		a_2	
		68% Confidence Interval	95% Confidence Interval	68% Confidence Interval	95% Confidence Interval
GOE	0.002	[6.3 , 54]	[3.0 , 180]	[0.59 , 0.80]	[0.49 , 0.95]
GOE	0.005	[6.5 , 68]	[2.9 , 300]	[0.58 , 0.80]	[0.49 , 0.95]
GOE	0.01	[6.7 , 86]	[3.1 , 250]	[0.57 , 0.79]	[0.46 , 0.95]
GOE	0.02	[7.0 , 120]	[2.9 , 350]	[0.56 , 0.80]	[0.46 , 0.97]
GOE	0.03	[7.4 , 130]	[3.2 , 320]	[0.55 , 0.80]	[0.45 , 0.98]
Poisson	0.002	[0.0[a] , 0.45]	[0.0[a] , 1.9]	N/A[b]	N/A[b]
Poisson	0.005	[0.0[a] , 0.41]	[0.0[a] , 1.9]	N/A[b]	N/A[b]
Poisson	0.01	[0.0[a] , 0.52]	[0.0[a] , 2.0]	N/A[b]	N/A[b]
Poisson	0.02	[0.0[a] , 0.46]	[0.0[a] , 2.1]	N/A[b]	N/A[b]
Poisson	0.03	[0.0[a] , 0.51]	[0.0[a] , 2.1]	N/A[b]	N/A[b]

[a]Limiting value of coefficient imposed in fitting routine.

[b]Value of a_2 is meaningless if $a_1 = 0$.

TABLE 4.22. Correlation hole properties as a function of N and D for individual spectra; $(N-1)D = 20$, $\Delta = 0.01$.

		R_{sb}		$\mathcal{A}$	
Spectrum Type	N	μ	σ	μ	σ
GOE	20	19.0	0.1	0.41	0.14
GOE	50	49.1	0.3	0.44	0.10
GOE	100	99.3	1.0	0.45	0.08
GOE	150	149.8	1.9	0.44	0.07
GOE	300	301.0	10.5	0.44	0.10
Poisson	20	19.0	0.5	0.01	0.37
Poisson	50	49.1	1.6	0.00	0.25
Poisson	100	99.1	3.4	0.00	0.18
Poisson	150	149.4	6.1	0.00	0.17
Poisson	300	300.2	19.1	−0.01	0.19

TABLE 4.23. Fitting coefficients as a function of N and D for individual spectra; $(N-1)D = 20.\ \Delta = 0.01$.

Spectrum Type	N	a_1		a_2	
		68% Confidence Interval	95% Confidence Interval	68% Confidence Interval	95% Confidence Interval
GOE	20	[2.1 , 59]	[0.61 , 110]	[0.55 , 1.1]	[0.39 , 1.9]
GOE	50	[4.6 , 83]	[1.7 , 170]	[0.55 , 0.86]	[0.43 , 1.2]
GOE	100	[6.4 , 99]	[3.0 , 360]	[0.57 , 0.79]	[0.46 , 0.98]
GOE	150	[8.4 , 100]	[4.4 , 310]	[0.58 , 0.77]	[0.50 , 0.89]
GOE	300	[11 , 140]	[6.4 , 400]	[0.57 , 0.73]	[0.51 , 0.82]
Poisson	20	[0.0[a] , 3.8]	[0.0[a] , 45]	N/A[b]	N/A[b]
Poisson	50	[0.0[a] , 0.91]	[0.0[a] , 21]	N/A[b]	N/A[b]
Poisson	100	[0.0[a] , 0.50]	[0.0[a] , 2.0]	N/A[b]	N/A[b]
Poisson	150	[0.0[a] , 0.41]	[0.0[a] , 1.4]	N/A[b]	N/A[b]
Poisson	300	[0.0[a] , 0.29]	[0.0[a] , 0.75]	N/A[b]	N/A[b]

[a]Limiting value of coefficient imposed in fitting routine.

[b]Value of a_2 is meaningless if $a_1 = 0$.

In summary, the power spectrum for single pure and complete spectra are described well by $\mathcal{A}$, a_1, and a_2 for $N \gtrsim 100$. Neither $\mathcal{A}$ nor a_1 are significantly affected by variations in D or Δ. However, for small N, both $\mathcal{A}$ and a_1 may not distinguish GOE and Poisson behavior. In Figures 4.6 and 4.7 the variations in $\mathcal{A}$ and a_1 are displayed singly as functions of N, D, and Δ and jointly as a function of N and D. The marked points in Figure 4.6 are the mean values of $\mathcal{A}$, and the error limits span the range $(\mathcal{A} - \sigma\ , \mathcal{A} + \sigma)$. The interval in Figure 4.7 is the 68% confidence interval for a_1. A GOE (Poisson) interval is symbolized by a $\bullet$ $(\times)$ at the midpoint of the a_1 interval. The lower limit of the Poisson interval, if equal to zero, has been drawn at the bottom of the plot.

In Tables 4.24 and 4.25 the results for $\mathcal{A}$ from single spectra are listed when ζ is varied. As in the ensemble-averaged case (Tables 4.9 and 4.10), spurious levels have a more severe effect on $\mathcal{A}$ than do missing levels. The standard deviation of $\mathcal{A}$, however, is relatively independent of ζ, while $\mathcal{A}$ decreases significantly for GOE spectra as ζ increases from zero. All Poisson cases have $\mathcal{A} \approx 0.0$ and $\sigma \approx 0.18$. Consequently, Poisson and GOE limits become indistinguishable for $\zeta > +30\%$. However, even for $\zeta = -70\%$, the GOE and Poisson limits are distinguishable. In Figure 4.8, which graphically displays the contents of Tables 4.24 and 4.25, these properties are clearly evident as ζ is varied. The top portion, center portion, and bottom portion show, respectively, the variation with ζ of $\mathcal{A}, a_1$, and a_2. The top portion of the figure shows the mean value of $\mathcal{A}$ with error limits of 1 standard deviation as ζ is varied. The center portion displays the 68% confidence intervals for both GOE and Poisson intervals as ζ is varied. For graphical purposes, if the lower limit of a Poisson interval equals zero, it has been drawn at the bottom scale. The Poisson results for a_2, which would have been in the bottom portion of the figure, are not graphed since $a_1 = 0$ most of the time for the Poisson cases; therefore, a_2 is meaningless.

Figure 4.6 Variation of $\mathcal{A}$ for individual spectra: (First) The variation of $\mathcal{A}$ with N for individual spectra [D = 0.3, Δ = 0.01]. (Second) The variation of $\mathcal{A}$ with D [N = 100, Δ = 0.01]. (Third) The variation of $\mathcal{A}$ with Δ [N = 100, D = 0.3]. (Fourth) The variation of $\mathcal{A}$ with N and D [$(N-1)D = 20$, Δ = 0.01]. Values for GOE (Poisson) spectra are denoted by a $\bullet$ ($\times$) symbol.

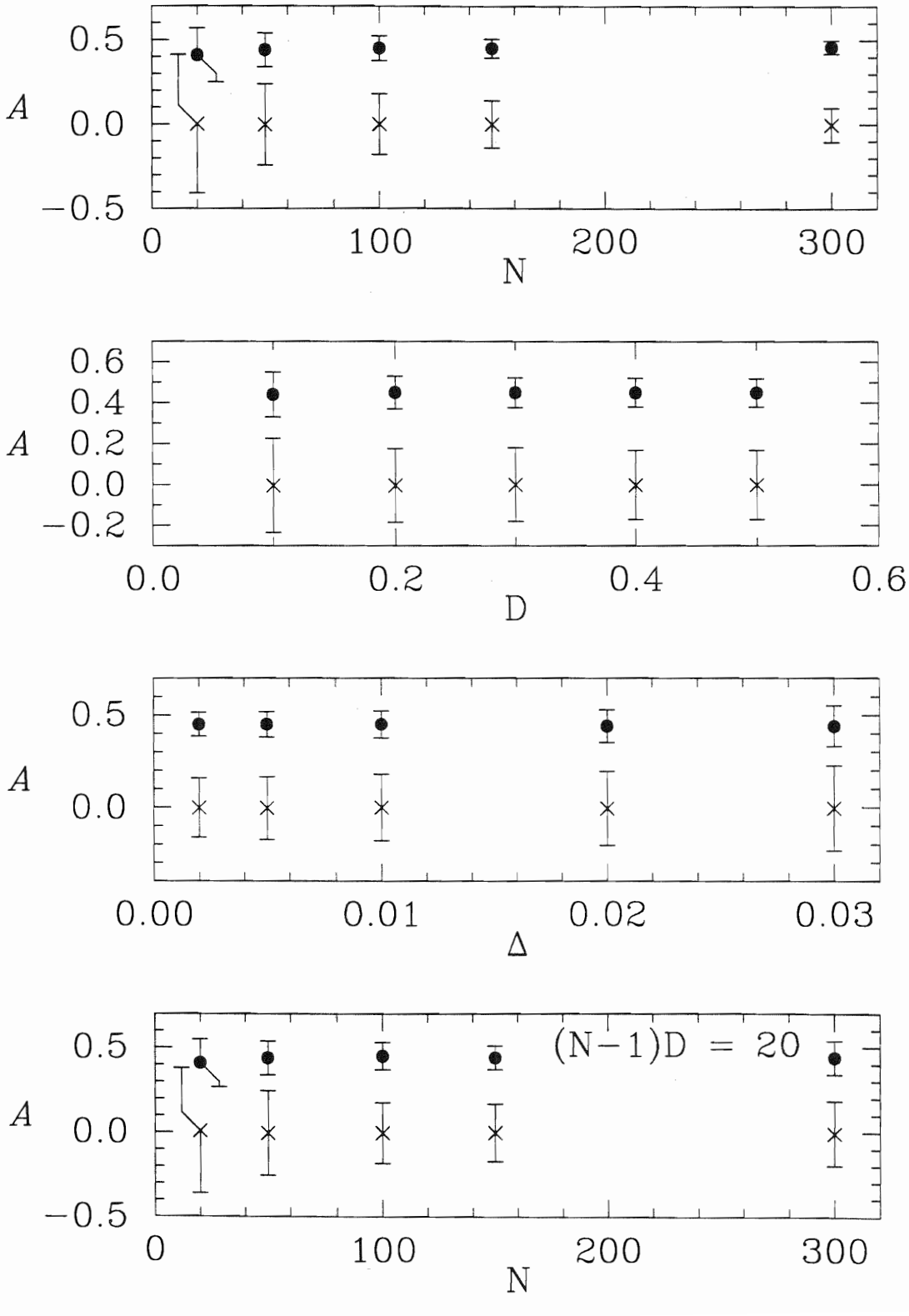
0.5
A
0.0
−0.5
0
100
200
300
N
0.6
0.4
A
0.2
0.0
−0.2
0.0
0.2
0.4
0.6
D
0.5
A
0.0
0.00
0.01
0.02
0.03
Δ
0.5
A
0.0
−0.5
(N−1)D = 20
0
100
200
300
N

Figure 4.7 Variation of a_1 for individual spectra. GOE (Poisson) 68% intervals are symbolized by a $\bullet$ ($\times$) placed at the midpoint of the interval. (First) The variation of a_1 with N [D = 0.3, $\Delta = 0.01$]. (Second) The variation of a_1 with D [N = 100, $\Delta = 0.01$]. (Third) The variation of a_1 with Δ [N = 100, D = 0.3]. (Fourth) The variation of a_1 with N and D. For each figure, $(N-1)D = 20$, $\Delta = 0.01$.

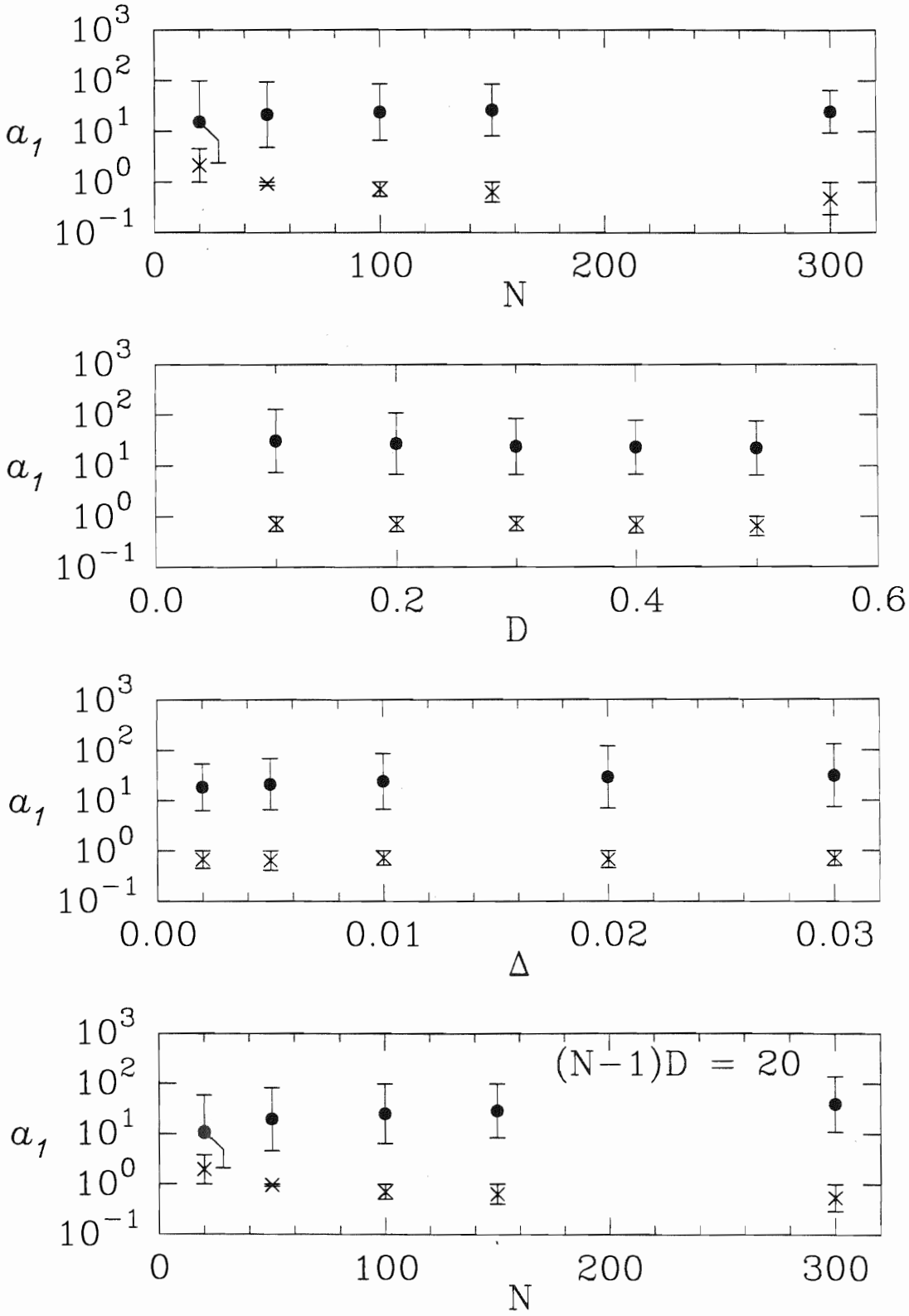
10^3
10^2
10^1
10^0
10^{-1}
a_1
0
100
200
300
N
0.0
0.2
0.4
0.6
D
0.00
0.01
0.02
0.03
Δ
(N−1)D = 20

TABLE 4.24. Correlation hole properties as a function of ζ for individual GOE spectra; N = 100, $\Delta = 0.01$, $D = 0.3$.

		R_{sb}		$\mathcal{A}$	
Spectrum Type	ζ	μ	σ	μ	σ
GOE	+50%	99.2	1.9	0.22	0.12
GOE	+40%	99.1	1.9	0.23	0.12
GOE	+30%	99.3	1.8	0.26	0.11
GOE	+20%	99.2	1.5	0.31	0.10
GOE	+10%	99.0	1.4	0.38	0.09
GOE	0%	99.2	0.6	0.45	0.07
GOE	-10%	99.3	0.6	0.44	0.07
GOE	-20%	99.3	0.7	0.44	0.08
GOE	-30%	99.3	0.7	0.43	0.08
GOE	-40%	99.4	0.7	0.43	0.08
GOE	-50%	99.4	0.8	0.41	0.09
GOE	-60%	99.5	0.8	0.40	0.09
GOE	-70%	99.8	0.9	0.35	0.10

TABLE 4.25. Correlation hole properties as a function of ζ for individual Poisson spectra; N = 100, $\Delta = 0.01$, $D = 0.3$.

		R_{sb}		$\mathcal{A}$	
Spectrum Type	ζ	μ	σ	μ	σ
Poisson	+50%	99.0	2.8	−0.01	0.18
Poisson	+40%	99.1	2.9	−0.01	0.18
Poisson	+30%	99.5	2.8	−0.02	0.18
Poisson	+20%	99.3	2.8	−0.01	0.18
Poisson	+10%	99.1	2.8	−0.02	0.17
Poisson	0%	99.1	2.7	0.00	0.18
Poisson	-10%	99.1	2.9	0.00	0.18
Poisson	-20%	99.1	2.7	−0.02	0.17
Poisson	-30%	98.9	2.8	0.00	0.18
Poisson	-40%	99.3	2.6	0.01	0.17
Poisson	-50%	99.2	2.8	0.01	0.16
Poisson	-60%	99.1	2.8	0.00	0.17
Poisson	-70%	99.2	2.8	0.00	0.17

Figure 4.8 Variation of statistics with ζ for individual spectra. (Top) The variation of $\mathcal{A}$ with ζ. GOE (Poisson) spectra are symbolized by $\bullet$ ($\times$). (Center) The variation of a_1 with ζ. GOE (Poisson) 68% confidence intervals are denoted with a $\bullet$ ($\times$) at the midpoint of the interval. If the lower limit of the Poisson interval is zero, it has been given a value of $a_1 = 0.01$. (Bottom) The variation of a_2 with ζ. Poisson values are not shown for a_2. In each figure, D = 0.3, $\Delta = 0.01$, and N = 100.

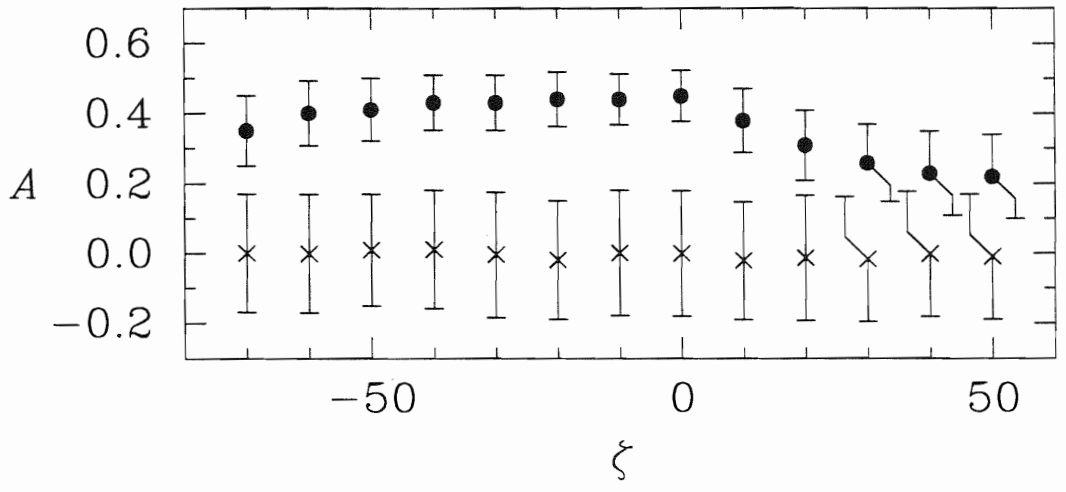
0.6
0.4
A 0.2
0.0
−0.2
−50
0
50
ζ

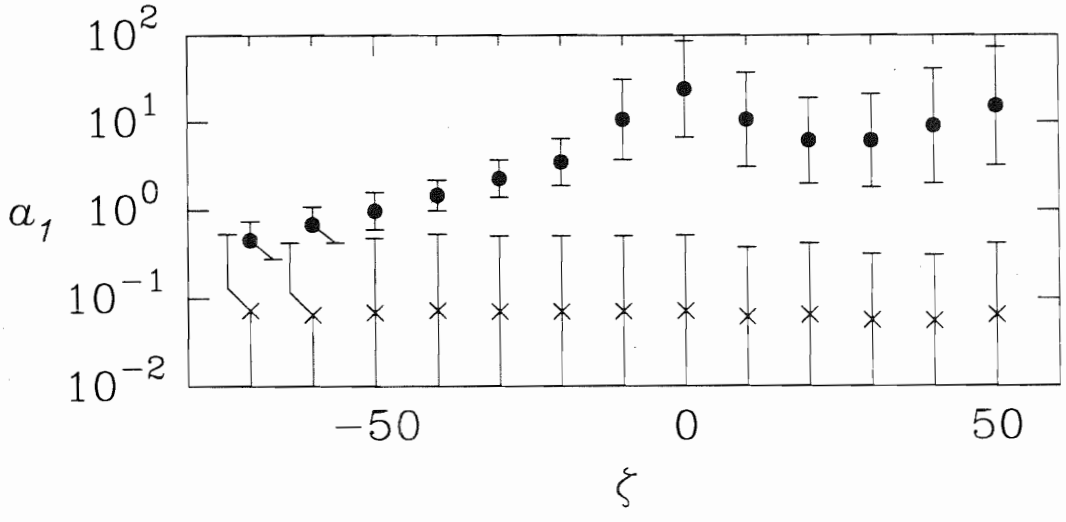
10^2
10^1
a_1 10^0
10^{-1}
10^{-2}
−50
0
50
ζ

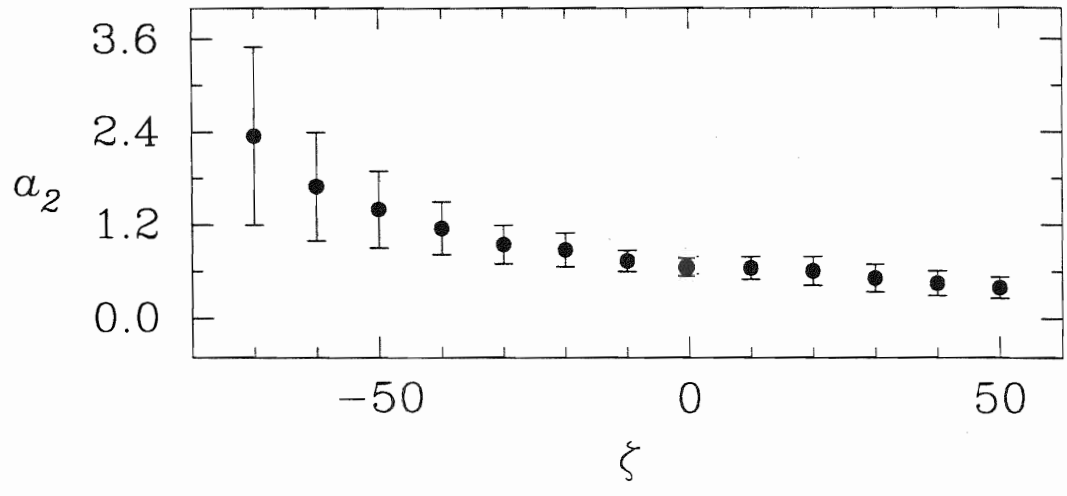
3.6
2.4
a_2 1.2
0.0
−50
0
50
ζ

The tabulated confidence intervals for variation of $\mathcal{A}$ as a function of ζ in individual spectrum modeling are listed in Tables 4.26 and 4.27. With 68% confidence, the confidence interval for a_1 distinguishes GOE and Poisson behavior up to at least 50% spurious levels. However, with 95% confidence, the confidence interval for a_1 distinguishes GOE and Poisson behavior up to only $\zeta = 10\%$. Interestingly, this behavior is exactly opposite to the behavior for $\mathcal{A}$ when ζ is varied. Whereas $\mathcal{A}$ distinguishes GOE and Poisson limits even for large negative ζ but not effectively for positive ζ, the coefficient a_1 (at the 68% level of confidence) distinguishes GOE and Poisson behavior quite effectively for positive ζ but not for negative ζ.

The single spectrum results that are obtained when multiple GOE sequences are superimposed are similar to the corresponding ensemble-averaged results. In Tables 4.28 and 4.29 the single spectrum results for $\mathcal{A}$ and a_1 are displayed as a function of m, the number of superimposed GOE sequences. For $\mathcal{A}$ the sample standard deviation increases rapidly up to $m = 3$, then decreases again. Performing a weighted fit of these data to a function of the form of Equation 4.4 yields

$$c_1 = 0.454 \pm 0.002 \quad \text{and} \quad c_2 = -1.01 \pm 0.01. \tag{4.6}$$

The value of c_2 indicates that $\mathcal{A} \propto \frac{1}{m}$, in agreement with the proposal of Leviandier *et al.* A weighted fit of the values in Table 4.29 to an equation of the form of Equation 4.4 for a_2 yields

$$c_1 = 0.663 \pm 0.003 \quad \text{and} \quad c_2 = -1.01 \pm 0.01. \tag{4.7}$$

The value of c_2 indicates that $a_2 \propto \frac{1}{m}$. Therefore, the two statistics, $\mathcal{A}$ and a_2, are measures of $|\hat{S}|^2$ that have the proper dependence on m. In Figure 4.9 the data and the best-fit curve (Equation 4.4 with coefficients given by Equation 4.7) are shown. Whereas $\mathcal{A} \propto \frac{1}{m}$ for $m = 1, 2, \cdots, 6$, a_2 deviates considerably from such a form for $m > 4$.

TABLE 4.26. Fitting coefficients as a function of ζ for individual GOE spectra; N = 100, $\Delta = 0.01$, $D = 0.3$.

Spectrum Type	ζ	a_1		a_2	
		68% Confidence Interval	95% Confidence Interval	68% Confidence Interval	95% Confidence Interval
GOE	+50%	[3.2 , 73]	[0.98 , 190]	[0.26 , 0.53]	[0.20 , 1.0]
GOE	+40%	[2.0 , 41]	[0.98 , 120]	[0.29 , 0.61]	[0.21 , 1.1]
GOE	+30%	[1.8 , 21]	[0.97 , 130]	[0.34 , 0.69]	[0.24 , 1.1]
GOE	+20%	[2.0 , 19]	[1.0 , 120]	[0.42 , 0.79]	[0.28 , 1.2]
GOE	+10%	[3.1 , 37]	[1.9 , 180]	[0.50 , 0.79]	[0.39 , 1.0]
GOE	0%	[6.7 , 86]	[3.1 , 250]	[0.57 , 0.79]	[0.46 , 0.95]
GOE	-10%	[3.7 , 31]	[2.0 , 120]	[0.60 , .87]	[0.48 , 1.1]
GOE	-20%	[1.9 , 6.5]	[1.3 , 33]	[0.66 , 1.1]	[0.52 , 1.3]
GOE	-30%	[1.4 , 3.7]	[0.95 , 7.1]	[0.70 , 1.2]	[0.53 , 1.6]
GOE	-40%	[.99 , 2.2]	[0.58 , 4.7]	[0.82 , 1.5]	[0.61 , 1.9]
GOE	-50%	[.61 , 1.6]	[0.40 , 2.9]	[0.91 , 1.9]	[0.55 , 2.8]
GOE	-60%	[.43 , 1.1]	[0.27 , 2.0]	[1.0 , 2.4]	[0.52 , 3.8]
GOE	-70%	[.28 , .75]	[.20 , 1.8]	[1.2 , 3.5]	[0.48 , 5.0[a]]

TABLE 4.27. Fitting coefficients as a function of ζ for individual Poisson spectra; N = 100, $\Delta = 0.01$, $D = 0.3$.

Spectrum Type	ζ	a_1		a_2	
		68% Confidence Interval	95% Confidence Interval	68% Confidence Interval	95% Confidence Interval
Poisson	+50%	[0.0[a] , 0.42]	[0.0[a] , 1.9]	N/A[b]	N/A[b]
Poisson	+40%	[0.0[a] , 0.31]	[0.0[a] , 1.5]	N/A[b]	N/A[b]
Poisson	+30%	[0.0[a] , 0.32]	[0.0[a] , 1.6]	N/A[b]	N/A[b]
Poisson	+20%	[0.0[a] , 0.42]	[0.0[a] , 1.8]	N/A[b]	N/A[b]
Poisson	+10%	[0.0[a] , 0.38]	[0.0[a] , 1.5]	N/A[b]	N/A[b]
Poisson	0%	[0.0[a] , 0.52]	[0.0[a] , 2.0]	N/A[b]	N/A[b]
Poisson	-10%	[0.0[a] , 0.51]	[0.0[a] , 1.5]	N/A[b]	N/A[b]
Poisson	-20%	[0.0[a] , 0.51]	[0.0[a] , 3.1]	N/A[b]	N/A[b]
Poisson	-30%	[0.0[a] , 0.51]	[0.0[a] , 2.0]	N/A[b]	N/A[b]
Poisson	-40%	[0.0[a] , 0.54]	[0.0[a] , 2.3]	N/A[b]	N/A[b]
Poisson	-50%	[0.0[a] , 0.48]	[0.0[a] , 1.9]	N/A[b]	N/A[b]
Poisson	-60%	[0.0[a] , 0.43]	[0.0[a] , 2.0]	N/A[b]	N/A[b]
Poisson	-70%	[0.0[a] , 0.54]	[0.0[a] , 2.8]	N/A[b]	N/A[b]

[a]Limiting value of coefficient imposed in fitting routine.

[b]Value of a_2 is meaningless if $a_1 = 0$.

TABLE 4.28. Correlation hole properties as a function of m for individual spectra; $N = 300$, $\Delta = 0.01$, $D = 0.3$.

	R_{sb}		$\mathcal{A}$	
m	μ	σ	μ	σ
1	299.6	5.0	0.45	0.06
2	300.3	16.4	0.23	0.14
3	302.7	41.5	0.13	0.34
4	300.7	17.2	0.11	0.10
5	300.1	15.3	0.09	0.07
6	301.0	16.7	0.08	0.07

TABLE 4.29. Fitting coefficients as a function of m for individual spectra; $N = 300$, $\Delta = 0.01$, $D = 0.3$.

	a_1		a_2	
m	68% Confidence Interval	95% Confidence Interval	68% Confidence Interval	95% Confidence Interval
1	[9.6 , 101]	[5.8 , 422]	[.60 , .74]	[.53 , .84]
2	[7.0 , 137]	[3.5 , 625]	[.27 , .42]	[.23 , .53]
3	[4.9 , 125]	[2.1 , 334]	[.17 , .30]	[.15[a] , .48]
4	[3.5 , 91.2]	[1.5 , 300]	[.15[a] , .25]	[.15[a] , .42]
5	[2.1 , 18.5]	[1.0 , 171]	[.15[a] , .23]	[.15[a] , .67]
6	[1.5 , 6.2]	[0.7 , 22.9]	[.150[a] , .22]	[.15[a] , .96]

[a]Limiting value of coefficient imposed in fitting routine.

Figure 4.9 Individual spectrum results for the superposition of m GOE sequences. (Top) The variation of $\mathcal{A}$ with m. (Bottom) The variation of a_2 with m. In each case the dashed curve is the best-fit equation.

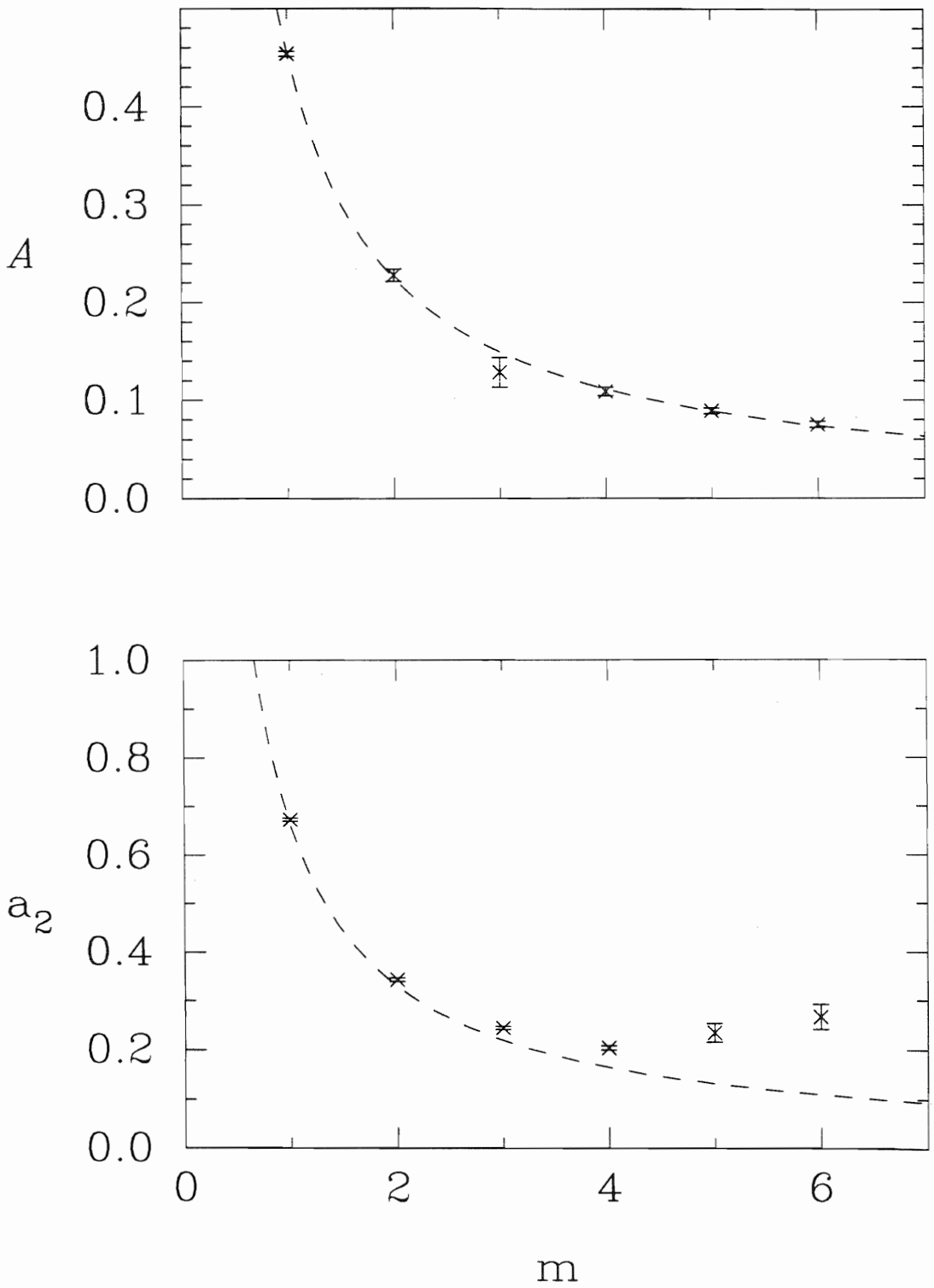
A
0.4
0.3
0.2
0.1
0.0
a2
1.0
0.8
0.6
0.4
0.2
0.0
0
2
4
6
m

Chapter 5

Applications to Nuclear Data

The modeling results presented in the preceding chapter characterize the behavior of the FT when applied to computer-generated data sets. Although we attempted to mimic experimental data in modeling, a more realistic test would use appropriate nuclear data. High-quality data sets, possessing a high degree of purity and completeness, are particularly desirable for initial application since such "ideal" cases permit a test of the FT algorithm under the best conditions. For such data sets direct comparison with the results for pure and complete sequences is possible. There are three data sets to which we have applied the FT algorithm.

The first data set that we have used is the set of 56 resonances with $J^\pi = \frac{1}{2}^+$ in the energy range $E_p = 3.1 - 4.0$ MeV in ^{57}Co ([Wat80] and [Wat81]). (E_p is the incident proton energy.) Based on comparison with predictions of models, this set of resonances is thought to be quite pure and complete. It was established from an analysis of excitation functions arising from proton elastic and inelastic scattering from an ^{56}Fe target. The data are listed by incident proton energy in column one of Table 5.1. As expected, the level density for ^{57}Co varies approximately exponentially with energy. To remove this exponential dependence, an unfolding similar to

that discussed in Section 3.3 is performed. (A more detailed discussion of the unfolding procedure is given by Shriner *et al.* [Shr90].) The resulting set of resonance energies, though possessing a constant level density over the range of included energies, possesses the fast fluctuations that are indicative of the statistics of the data set. A histogram plot of the NNS distribution for the set of ^{57}Co eigenvalues is shown in the top portion of Figure 5.1. The solid (dashed) curve represents the GOE (Poisson) NNS distribution pdf given by Equation 2.1 (Equation 2.4). The Brody parameter, obtained by fitting the histogrammed data to Equation 2.5 via a least-squares algorithm, for this data set is $\omega = 1.11 \pm 0.24$, consistent with a GOE description. The Dyson-Mehta Δ_3 statistic is shown in the center portion of Figure 5.1; the solid curve represents the GOE limit for $\Delta_3(L)$, given by Equation 2.8, and the dashed curve represents the Poisson limit, given by $\Delta_3(L) = L/15$. The shaded region represents Δ_3 for this sequence; for a given value of L, the upper and lower limits of the shaded region are the mean value of Δ_3 plus and minus the associated uncertainty. The best-fit interpolation value is $\mu = 1.04$, also consistent with GOE. These statistics indicate that the sequence has nearly pure GOE behavior. The following parameters are obtained for the corresponding FT analysis of the ^{57}Co data:

$$\begin{aligned} \mathcal{A} &= 0.33, \\ R_{sb} &= 56.1, \quad \text{and} \\ a_1 &= 0.0, \end{aligned} \tag{5.1}$$

The value for a_1 is the lower limit and makes the corresponding value of a_2 meaningless. These parameters were obtained with no smoothing of the power spectrum. The bottom portion of Figure 5.1 displays the power spectrum and the functional fit to Equation 3.27. Although there is visual evidence for a correlation hole, the best fit has $a_1 = 0$. As expected, $R_{sb} \approx 56$, the number of levels in the sequence. The correlation-hole area, $\mathcal{A}$, falls between the GOE and Poisson limits, but lying

Figure 5.1 Corrected resonance energies for ^{57}Co $\frac{1}{2}^+$ levels. The energies are listed in Table 5.1. See text for an explanation of the correction procedure. (Top) The NNS distribution for the data set. The solid (dashed) curve represents the GOE (Poisson) limits. (Center) A plot of Δ_3 for the data set. See text for explanation. The solid (dashed) curve represents the GOE (Poisson) limits. (Bottom) The scaled power spectrum, $|\hat{S}|^2$, for the same data set. The dashed curve is the best fit to Equation 3.27.

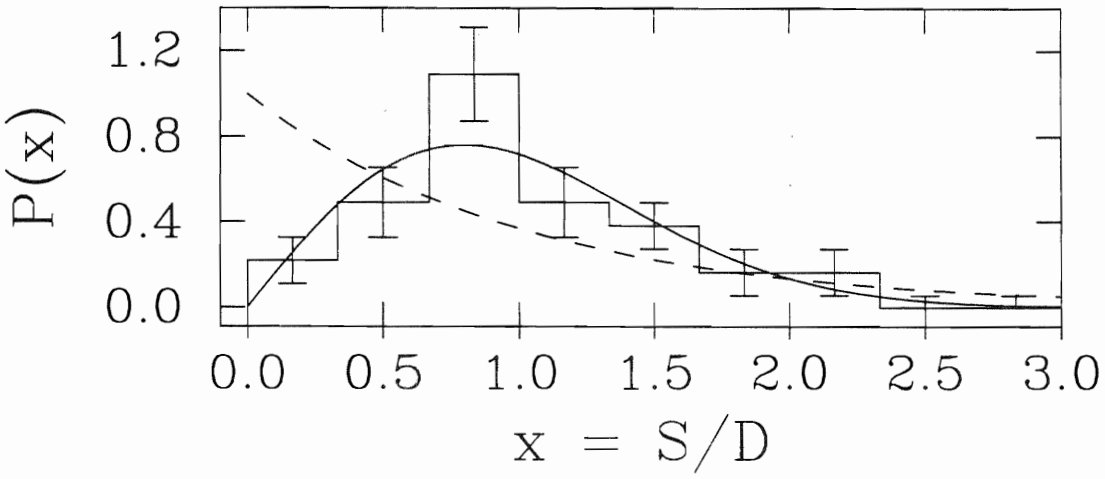
P(x)
1.2
0.8
0.4
0.0
0.0
0.5
1.0
1.5
2.0
2.5
3.0
x = S/D

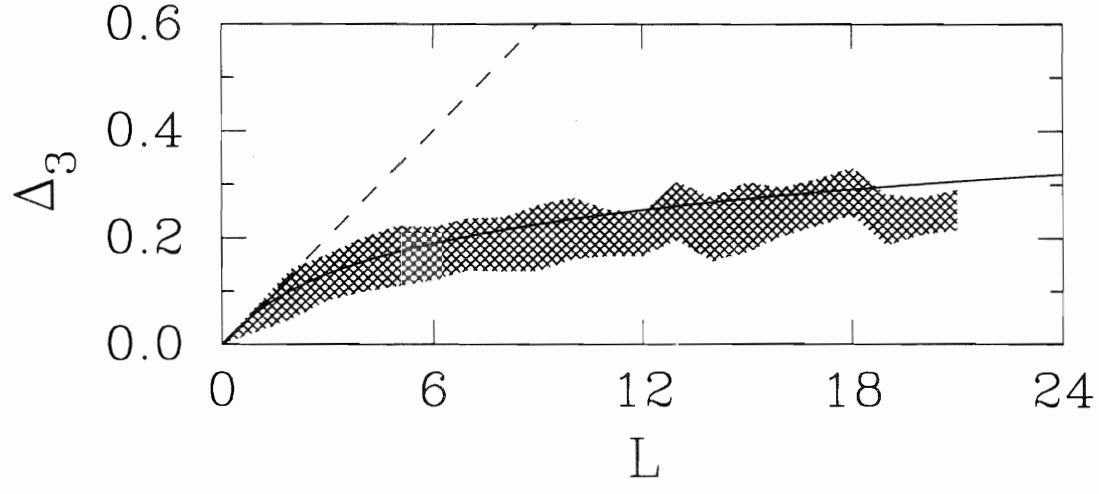
Δ_3
0.6
0.4
0.2
0.0
0
6
12
18
24
L

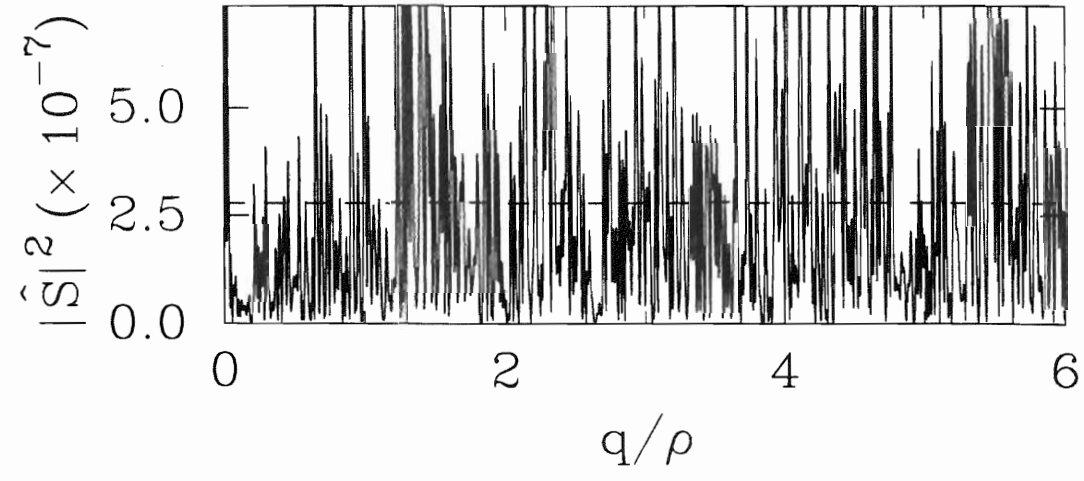
$|\hat{S}|^2 (\times 10^{-7})$
5.0
2.5
0.0
0
2
4
6
q/ρ

closer to the GOE expected value. For a single GOE sequence of 50 levels that is assumed pure and complete ($\zeta = 0$), the expected range of $\mathcal{A}$, from Table 4.16, is $(0.34, 0.54)$. The upper limit on the corresponding interval for $\mathcal{A}$ for a pure and complete Poisson sequence of 50 levels, also from Table 4.16, is approximately 0.24. Thus, for the ^{57}Co sequence, $\mathcal{A}$ lies considerably outside the Poisson interval and just outside one sample standard deviation of the GOE interval. Both fitting statistics, a_1 and a_2, are consistent with complete Poisson behavior. Thus, one would conclude that the FT results of an analysis on the ^{57}Co sequence appear much more ambiguous than do the NNS distribution and Δ_3. This conclusion is not in close agreement with the conclusion that would be reached based on the values of ω and μ.

A second data set to which we applied our FT algorithm is the set of 102 resonances with $J^\pi = \frac{1}{2}^+$ in the energy range $E_p = 3.08 - 3.86$ MeV in ^{49}V([Li90] and [Li91]). This set of resonances is believed to be relatively pure and complete, as evidenced by the statistical analyses performed on the data set. This data set is the result of the analysis of excitation functions arising from proton elastic and inelastic scattering from a ^{48}Ti target. The data are listed by incident proton energy in column two of Table 5.1. As with the ^{57}Co data set discussed above, the set of ^{49}V resonance energies has been unfolded to remove the approximate exponential dependence on energy. The NNS distribution for the ^{49}V sequence is shown in the top portion of Figure 5.2. The GOE and Poisson NNS distribution pdf curves are shown solid and dashed, respectively. There is a clear similarity in the NNS pdf from the data to the GOE NNS pdf, but less so than in the case of ^{57}Co. For the ^{49}V data set, $\omega = 0.62 \pm 0.11$. The corresponding interpolation value for Δ_3 is $\mu = 0.77$. A graph of Δ_3 is shown in the center portion of Figure 5.2. Both statistics, ω and μ, indicate behavior between the GOE and Poisson extremes, but favoring GOE. Our FT analysis performed on the ^{49}V data set yields the power spectrum curve shown in the bottom portion of Figure 5.2. The best-fit equation to the form of

Figure 5.2 Corrected resonance energies for ^{49}V $\frac{1}{2}^+$ levels. The energies are listed in Table 5.1. See text for an explanation for the correction procedure. (Top) The NNS distribution for the data set. The solid (dashed) curve represents the GOE (Poisson) limits. (Center) A plot of Δ_3 for the data set. See text for explanation. The solid (dashed) curve represents the GOE (Poisson) limits. (Bottom) The scaled power spectrum, $|\hat{S}|^2$, for the same data set. The dashed curve is the best fit to Equation 3.27.

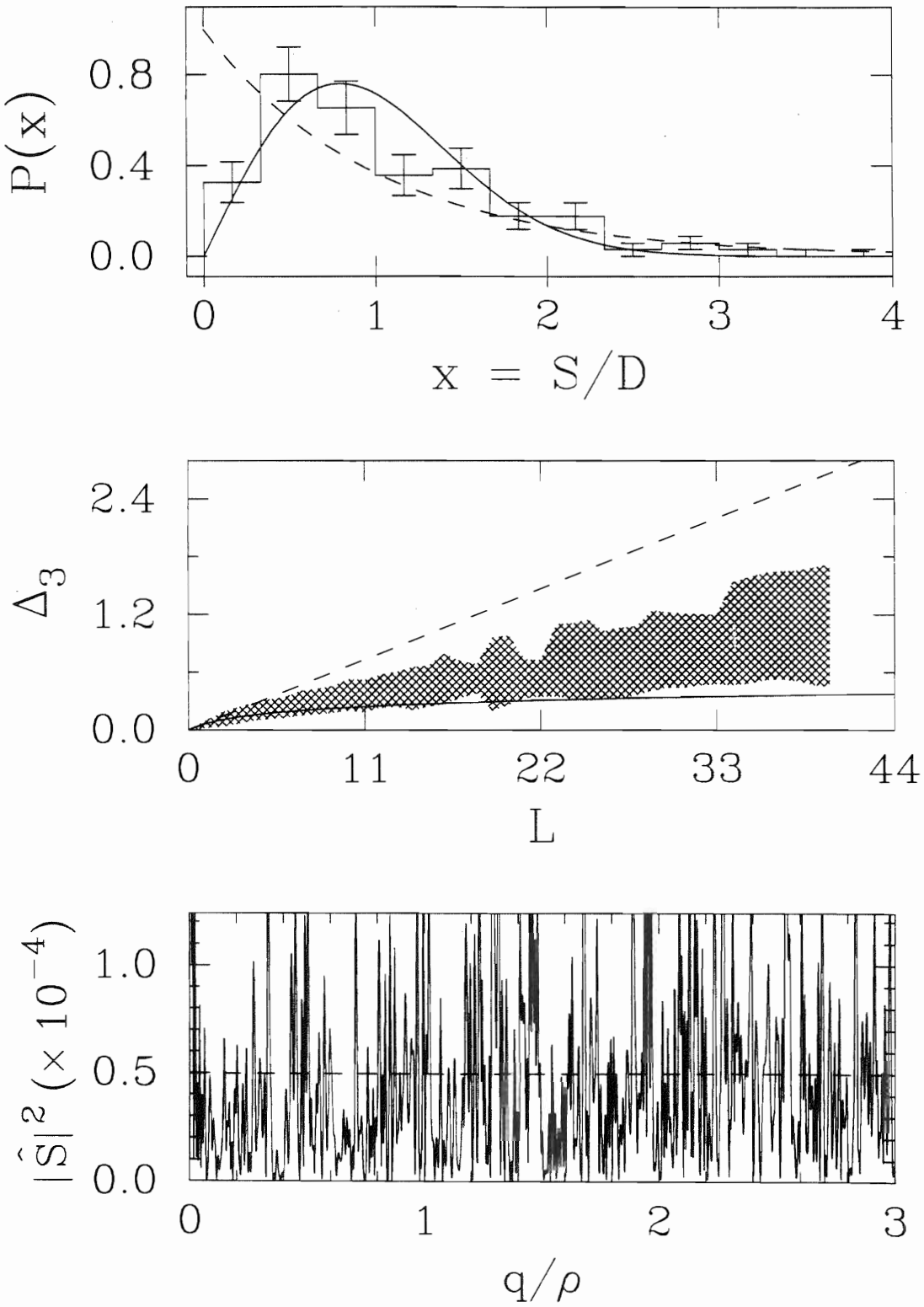
P(x)
0.8
0.4
0.0
0
1
2
3
4
x = S/D
Δ_3
2.4
1.2
0.0
0
11
22
33
44
L
$|\hat{S}|^2 (\times 10^{-4})$
1.0
0.5
0.0
0
1
2
3
q/ρ

Equation 3.27 is shown dashed. The values obtained in our FT analysis are

$$\begin{aligned} \mathcal{A} &= 0.30, \\ R_{sb} &= 102.4, \quad \text{and} \\ a_1 &= 0.0, \end{aligned} \tag{5.2}$$

As expected, $R_{sb} \approx 102$. For a 100-member GOE sequence for which $\zeta = 0$, the one sigma range for $\mathcal{A}$ is $(0.38, 0.52)$, while the upper limit of the interval for a corresponding Poisson sequence is 0.18. Thus, the value of $\mathcal{A}$ is well outside both the GOE and Poisson one sigma limits. Based solely upon $\mathcal{A}$, one would conclude intermediate behavior between GOE and Poisson for this sequence. The values of the a_1 fitting coefficient is zero, making a_2 undefined. This value for a_1 is consistent with Poisson behavior. Thus, the general impression based on a FT analysis is of behavior intermediate to GOE and Poisson, in contrast to the earlier analysis of Li *et al.*

The final data set used for comparison was the set of 109 s-wave resonances in the energy range $E_n = 15.56$ to $E_n = 1686.4$ eV in ^{166}Er [Lio72]. (E_n is the incident neutron energy.) Comparison with predictions of RMT suggest that this data set is nearly pure and complete. This sequence results from an analysis of the reaction, ^{166}Er(n ,n)^{166}Er. The data are listed by incident neutron energy in column three of Table 5.1. The NNS pdf for the ^{166}Er data is shown in the top portion of Figure 5.3. There is good agreement between the histogram curve and the GOE curve (the solid curve). The Brody parameter is 0.98 ± 0.13, which reinforces the conclusion drawn from the figure that the sequence displays strong GOE behavior. Correspondingly, one would conclude from the center portion of Figure 5.3, which displays the results of a calculation of Δ_3 for the ^{166}Er data set, that Δ_3 also is in strong agreement with GOE statistics: the interpolation parameter is $\mu = 0.99$. In the bottom portion of Figure 5.3 is shown the power spectrum and best fit to Equation 3.27 — shown as a dashed curve — for the ^{166}Er sequence. There is

Figure 5.3 Resonance energies for ^{166}Er s-wave resonances. The energies are listed in Table 5.1. (Top) The NNS distribution for the data set. The solid (dashed) curve represents the GOE (Poisson) limits. (Center) A plot of Δ_3 for the data set. See text for explanation. The solid (dashed) curve represents the GOE (Poisson) limits. (Bottom) The scaled power spectrum, $|\hat{S}|^2$, for the same data set. The dashed curve is the best fit to Equation 3.27.

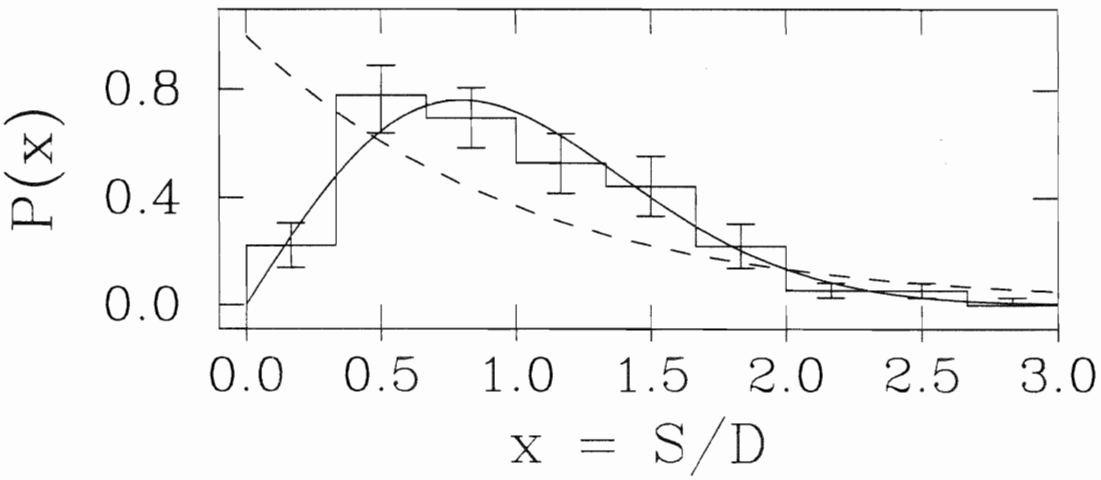
P(x)
0.8
0.4
0.0
0.0
0.5
1.0
1.5
2.0
2.5
3.0
x = S/D

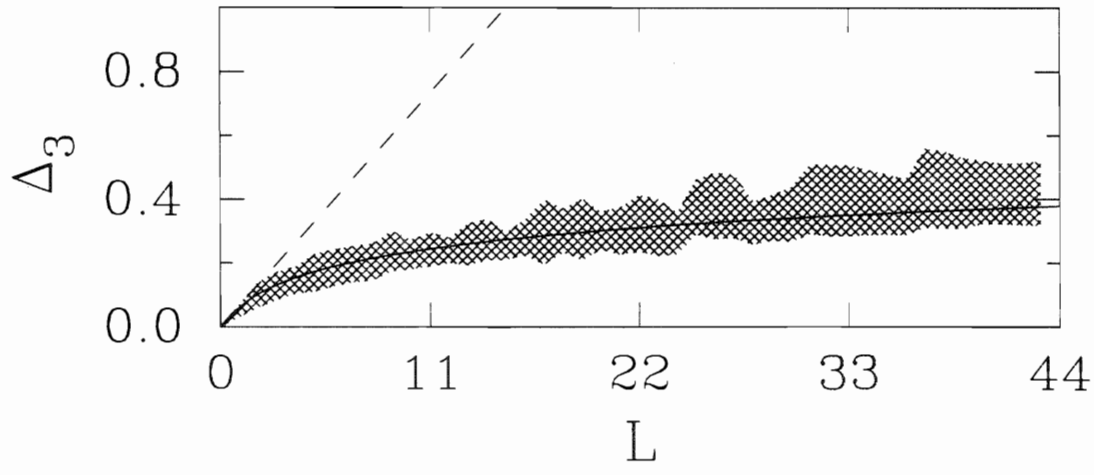
Δ_3
0.8
0.4
0.0
0
11
22
33
44
L

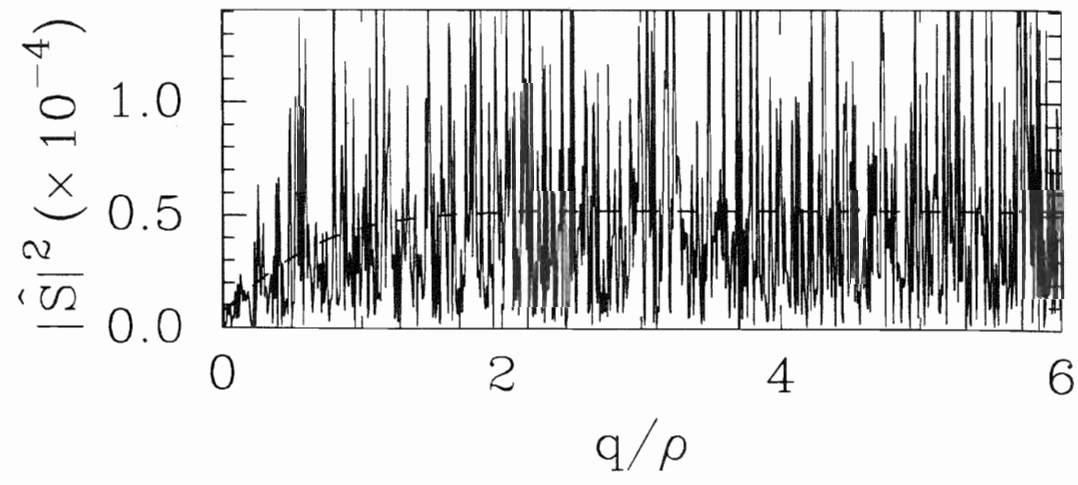
$|\tilde{S}|^2$ ($\times 10^{-4}$)
1.0
0.5
0.0
0
2
4
6
q/ρ

a visible correlation hole which the best fit reflects. The statistics from our FT analysis are

$$\begin{aligned} \mathcal{A} &= 0.52, \\ R_{sb} &= 109.0, \\ a_1 &= 6.4, \quad \text{and} \\ a_2 &= 0.84. \end{aligned} \tag{5.3}$$

In this case, $\mathcal{A}$ lies at the upper end of the one sigma GOE interval $(0.38\,,0.52)$ that is appropriate for a 100-member GOE sequence that is pure and complete (See Table 4.16). The value of a_1 is just outside the corresponding 68% GOE interval $(6.7\,,86)$ and well outside the corresponding 68% Poisson interval $(0.0\,,0.52)$. Thus, our FT analysis also indicates GOE behavior for the ^{166}Er sequence, in agreement with the NNS distribution and with Δ_3.

TABLE 5.1. Resonance Energies[a] for ^{57}Co, ^{49}V, and ^{166}Er

#	^{57}Co	^{49}V	^{166}Er
	E_p (keV)	E_p (keV)	E_n (eV)
1	3121.20	3085.00	15.50
2	3144.20	3089.62	73.70
3	3175.40	3094.25	81.70
4	3185.20	3099.32	110.60
5	3196.00	3109.49	154.10
6	3213.50	3115.28	170.90
7	3235.50	3121.34	243.50
8	3251.10	3124.77	301.10
9	3262.90	3136.28	315.70
10	3285.90	3146.31	352.20
11	3295.50	3161.09	388.40
12	3300.60	3175.01	457.80
13	3319.70	3182.76	509.00
14	3332.00	3200.57	535.30
15	3339.90	3203.51	594.80
16	3347.10	3227.73	601.00
17	3367.20	3231.07	642.10
18	3394.50	3244.03	708.20
19	3409.30	3255.70	747.30
20	3423.60	3260.37	772.80
21	3444.20	3265.78	794.40
22	3458.80	3271.30	848.90
23	3469.60	3277.39	873.00
24	3491.20	3288.51	905.00
25	3502.90	3303.70	923.90

Table 5.1 (continued)

#	^{57}Co	^{49}V	^{166}Er
	E_p (keV)	E_p (keV)	E_n (eV)
26	3511.00	3313.26	973.90
27	3534.80	3319.38	1025.10
28	3562.20	3324.57	1036.90
29	3564.10	3331.57	1056.80
30	3584.30	3351.85	1137.20
31	3599.10	3357.21	1171.00
32	3632.90	3369.72	1183.70
33	3653.90	3370.20	1259.50
34	3668.70	3386.56	1325.00
35	3681.00	3392.60	1339.70
36	3701.30	3400.90	1367.30
37	3712.70	3413.45	1431.30
38	3721.50	3416.01	1468.60
39	3742.50	3418.87	1502.30
40	3756.50	3421.83	1545.60
41	3779.00	3425.68	1556.20
42	3781.80	3432.02	1618.10
43	3801.90	3437.19	1640.50
44	3813.00	3441.96	1678.90
45	3825.30	3444.45	1757.80
46	3859.40	3444.85	1785.70
47	3865.70	3460.97	1809.60
48	3877.20	3468.52	1831.90
49	3887.80	3469.12	1846.40

Table 5.1 (continued)

#	^{57}Co	^{49}V	^{166}Er
	E_p (keV)	E_p (keV)	E_n (eV)
50	3901.60	3478.72	1906.50
51	3928.00	3494.77	1940.20
52	3936.00	3496.30	1987.70
53	3949.40	3505.71	2027.50
54	3953.00	3509.19	2069.00
55	3987.60	3519.57	2121.60
56	4000.50	3522.15	2128.90
57		3529.38	2174.50
58		3532.18	2197.50
59		3535.91	2245.40
60		3537.15	2269.50
61		3550.90	2364.50
62		3551.21	2401.40
63		3573.03	2463.20
64		3578.73	2476.20
65		3585.71	2514.00
66		3589.10	2548.50
67		3596.43	2569.00
68		3606.67	2594.90
69		3621.79	2656.40
70		3624.58	2669.60
71		3629.11	2736.00
72		3640.57	2785.50
73		3646.53	2808.20

Table 5.1 (continued)

#	^{57}Co	^{49}V	^{166}Er
	E_p (keV)	E_p (keV)	E_n (eV)
74		3659.60	2829.60
75		3667.26	2850.20
76		3671.53	2890.10
77		3675.60	2931.80
78		3677.90	2950.30
79		3680.10	2984.50
80		3693.02	3022.70
81		3697.12	3040.90
82		3700.67	3068.50
83		3702.55	3127.30
84		3711.12	3147.00
85		3727.45	3214.90
86		3736.43	3280.70
87		3743.65	3340.80
88		3749.07	3351.40
89		3753.72	3378.70
90		3761.21	3415.40
91		3772.82	3468.60
92		3778.88	3519.40
93		3781.52	3541.00
94		3792.31	3600.90
95		3796.57	3615.90
96		3798.76	3630.60
97		3802.56	3663.80

Table 5.1 (continued)

#	^{57}Co	^{49}V	^{166}Er
	E_p (keV)	E_p (keV)	E_n (eV)
98		3814.02	3755.00
99		3825.76	3790.70
100		3834.75	3841.50
101		3838.37	3851.30
102		3846.81	3895.00
103			3919.30
104			3982.10
105			4015.90
106			4047.40
107			4110.90
108			4152.70
109			4169.30

[a]Tabulated resonance energies for ^{57}Co and ^{49}V are corrected to constant level density.

Chapter 6

Summary

Extensive use has been made of eigenvalue statistics in the analysis of nuclear data. The common statistics suffer severe limitations if the data are impure or incomplete. Leviandier *et al.* suggested that the Fourier transform would be a useful eigenvalue statistic even for impure and/or incomplete sequences. Prior use of the Fourier transform as an eigenvalue statistic was limited to data sets of many members. A series of modeling calculations was performed on computer-generated sequences to determine how useful the Fourier transform might be as an eigenvalue statistic for nuclear sequences. Two quantitative measures of application of the FT were adopted — the area of the correlation hole and the set of fitting coefficients obtained by fitting the power spectrum curve to a specified functional form. The modeling variables were the number of levels in a sequence, the average level density, the sampling interval, the energy range of the sequence, and the percentage of missing/added levels (in cases of impurity/ incompleteness). In each case, the extreme limits of sequence behavior — GOE statistics and Poisson statistics — were compared.

The Fourier transform, when applied to ensemble-averaged spectra, shows easily identifiable behavior; however, application of a Fourier transform analysis to a

single spectrum yields less definite results. For single sequences of many members, the behavior of the power spectrum is reflective of the statistics of the system. However, for single sequences of few members, the measures obtained from the analysis are subject to considerable uncertainty, diminishing their utility. The behavior of the quantitative measures for superimposed GOE spectra is consistent with earlier work. The modeling results indicate that, although the Fourier transform possesses several desirable features, it is limited in usefulness by the size of the sequence when applied as an eigenvalue statistic using the quantitative measures defined in this work. A data set with $N \gtrsim 100$ that is pure and complete may be confidently characterized by a Fourier transform analysis. However, as the degree of impurity or incompleteness increases, N must increase in order to draw definitive conclusions about the statistical behavior of the data set. Generally, $N \gtrsim 200$ for a Fourier transform based analysis to yield definite results with a high degree of confidence.

Appendix

Calculation of R_{sb}

The modeling results indicate that R_{sb} is approximately equal to the number of levels included in the calculation. This is shown to be the case for a spectrum that is composed of a series of delta functions.

Let f be a function composed of a series of N delta functions, and denote the independent variable by E. Further, suppose the delta functions occur at locations $\{E_i | i = 1, N\}$. The function, f, can be represented in a manner similar to Equation 3.12. Thus,

$$f(E) = \sum_{n=1}^{N} \delta(E - E_n). \tag{A.1}$$

Substituting Equation A.1 into Equation 3.1 yields

$$S(q) = \int_{-\infty}^{\infty} \sum_{n=1}^{N} \delta(E - E_n) \epsilon^{-2\pi i q E} dE = \sum_{n=1}^{N} \int_{-\infty}^{\infty} \delta(E - E_n) \epsilon^{-2\pi i q E} dE = \sum_{n=1}^{N} \epsilon^{-2\pi i q E_n}. \tag{A.2}$$

Therefore,

$$S(q = 0) = N \Longrightarrow |S(q = 0)|^2 = N^2. \tag{A.3}$$

To obtain a value for $S(q)$ in the background region, use the definition of the complex exponential to rewrite Equation A.2:

$$S(q) = \sum_{n=1}^{N} e^{-2\pi i q E_n} = \sum_{n=1}^{N} \cos(2\pi q E_n) - i \sum_{n=1}^{N} \sin(2\pi q E_n). \tag{A.4}$$

Therefore,

$$|S(q)|^2 = \left[\sum_{n=1}^{N} \cos(2\pi q E_n) \right]^2 + \left[\sum_{n=1}^{N} \sin(2\pi q E_n) \right]^2. \tag{A.5}$$

Rewriting the square of the sums as double sums, Equation A.5 becomes

$$|S(q)|^2 = \sum_{n=1}^{N}\sum_{m=1}^{N}\cos(2\pi qE_n)\cos(2\pi qE_m) + \sum_{n=1}^{N}\sum_{m=1}^{N}\sin(2\pi qE_n)\sin(2\pi qE_m). \quad \text{(A.6)}$$

Using a trigonometric identity, Equation A.6 can be rewritten in the form

$$\begin{aligned} |S(q)|^2 &= \frac{1}{2}\sum_{n=1}^{N}\sum_{m=1}^{N}\{\cos[2\pi q(E_n - E_m)] + \cos[2\pi q(E_n + E_m)]\} \\ &\quad + \frac{1}{2}\sum_{n=1}^{N}\sum_{m=1}^{N}\{\cos[2\pi q(E_n - E_m)] - \cos[2\pi q(E_n + E_m)]\}. \end{aligned} \quad \text{(A.7)}$$

Simplifying Equation A.7 yields

$$|S(q)|^2 = \sum_{n=1}^{N}\sum_{m=1}^{N}\cos[2\pi q(E_n - E_m)]. \quad \text{(A.8)}$$

Separating terms with $m = n$ in Equation A.8 and making use of the symmetry of the cosine function yields

$$|S(q)|^2 = N + 2\sum_{n=1}^{N}\sum_{m=n+1}^{N}\cos[2\pi q(E_n - E_m)]. \quad \text{(A.9)}$$

The argument of the cosine function is a random number of both positive and negative sign since the values of $E_n - E_m$ are random numbers. Thus, recalling that $< \cos x >= 0$, Equation A.9 reduces to

$$|S(q)|^2 = N. \quad \text{(A.10)}$$

Therefore, for a background frequency q, the ratio, $|S(q=0)|^2/|S(q)|^2$, from Equations A.3 and A.9 is N, as observed.

Part II

Data Acquisition for Compton-suppressed Spectrometer

Chapter 7

Introduction

The analysis of energy level fluctuation properties in complex systems has been an area of intense activity in recent years. This state of affairs is due principally to a conjecture by Bohigas *et al.* [Boh84] and the increased interest in quantum chaos issues [Rei92]. The conjecture of Bohigas *et al.* states that the quantum analogs of classically chaotic systems obey the Gaussian orthogonal ensemble (GOE) statistics [Bro81] of random matrix theory (RMT). This conjecture is now accepted as generally true, and it is further believed that quantum analogs of classically regular systems obey Poisson statistics. A more extensive discussion of the conjecture of Bohigas *et al.* and its import on statistical nuclear physics is given in Chapters 1 and 2.

Tests of GOE behavior, in light of the conjecture of Bohigas *et al.*, can be taken to be tests of chaotic behavior. As discussed in Chapter 2, these tests are appropriate for the description of a set of quantum states, each of which has the same set of good quantum numbers. Such a set of states, nuclear energy levels in this case, will be termed a *sequence*. Tests for GOE character require that a data set be of extremely high quality, having a minimum number of missing levels and a minimum number of levels with misassigned quantum numbers. Furthermore,

the data set must have a sufficient number of members so that the results are statistically significant. These ideas are discussed at length in Chapter 2.

In general, excellent system resolution is necessary to acquire data sets of sufficient quality for a test of GOE behavior. Experimentally, such a situation is difficult to achieve. Sets of nuclear energy levels have provided the best data for tests of RMT [Shr90]. Brody *et al.* discuss why one might expect resonance data to provide data sufficient for such tests [Bro81]. Both high resolution neutron resonance data and high resolution proton resonance data ([Boh85] and [Haq82]) have been analyzed in this vein. In each case, the data sets are composite well-known sequences of levels from separate nuclei, and agreement with the predictions of RMT is found.

The application of tests of GOE behavior to a sequence formed from a single nuclide is interesting since it would be possible to investigate the fluctuation properties at varying energies and therefore observe any transition in these properties. However, at present, there is only one nuclide for which a nearly pure and complete level scheme exists over a reasonably wide energy range. This nuclide is ^{26}Al, and the level scheme is known to be complete or nearly so from the ground state into the resonance regime. A total of 160 levels from 0 to 8.066 MeV have been identified. Assignments of spin, parity, and isospin have been made to a large number of the states ([End86] and [End88]). The predictions of the nuclear shell model have been used for comparison to obtain an estimate of the completeness of the ^{26}Al data set. The first 100 positive parity states are of extremely high quality; the negative parity states are expected to be of similar quality, but shell model calculations for these states are not available for comparison. The fluctuation properties of this set of ^{26}Al states has been analyzed and found to exhibit "behavior intermediate between GOE and Poisson but apparently favoring GOE." [Shr90]. This result holds throughout the energy region from the ground state to the resonance regime and appears to be independent of isospin (which is expected to be an approximately good quantum number). This result is in agreement with the predictions of Dyson [Dys62] and

Pandey [Pan81] — that the breaking of a symmetry by even a small degree yields fluctuations that would be present in the total absence of that symmetry. Similar behavior has been observed in a study of the role of isospin breaking on fluctuation properties [Guh90b].

It is desirable to apply tests similar to those performed on ^{26}Al to other nuclei, but presently there are no other nuclei with a complete and pure set of energy levels spanning a large energy range. Any candidate nuclide for such a study should possess several characteristics: low proton separation energy, light mass, coexistence of $T = 0$ and $T = 1$ states over the entire energy range, and a sufficient number of levels to be studied statistically. The region just below the proton separation energy presents special difficulty since the levels in this region will be studied by means of γ-decay from resonant states. Since these decays are expected to be weak, it is desirable to restrict this region in size. A low proton separation energy helps to accomplish this. Light mass nuclei have sufficiently low level density that the likelihood of level resolution is increased. Coexistence of isospin states permits the study of symmetry breaking on fluctuation properties throughout the energy range. The odd-odd $N = Z$ nuclei ^{22}Na, ^{26}Al, ^{30}P, ^{34}Cl, and ^{38}K, satisfy these criteria, and ^{26}Al has previously been studied. Of the remaining set, the target for a ^{30}P reaction, ^{29}Si, is the easiest to obtain. Thus, the nuclide ^{30}P was chosen for study.

Several types of experiments are necessary in order to establish a complete and pure level scheme. Direct reactions and γ-decay analyses are useful for investigating the region below the proton separation energy. High resolution proton resonance measurements can be used to study the energy region above the proton separation energy; scattering experiments from resonances usually determine the parity π of the resonant states, while capture measurements often fix the total angular momentum J. The High Resolution Laboratory, located at the Triangle Universities Nuclear Laboratory (TUNL-HRL), provides an excellent venue in which to study proton resonances with high resolution, and the TUNL-HRL group has undertaken

to establish a pure and complete level scheme for ^{30}P by studying the ^{29}Si(p,γ) reaction. The TUNL-HRL, which includes a particle accelerator with associated feedback systems, is capable of excellent beam energy resolution and can selectively populate even closely-lying resonant states. The accelerator, feedback systems, detector system, and data acquisition electronics are discussed in Chapter 8. The data, taken with the TUNL-HRL system, and corresponding analysis for five ^{30}P resonances is shown in Chapter 9. Finally, a summary for this part of this dissertation is given in Chapter 10.

Chapter 8

Equipment

8.1 Introduction

The High Resolution Laboratory located at the Triangle Universities Nuclear Laboratory (TUNL-HRL) houses a model KN Van de Graaff accelerator which has been used for many years in a high resolution mode to study nuclear structure via proton resonance reactions. The accelerator, though originally designed to operate at 3 MV maximum terminal potential, has been modified and upgraded to permit up to 4 MV terminal potential. Together with a high resolution feedback system, this accelerator system provides excellent beam energy resolution, having been recently measured to be $\approx$ 200 eV with a long term drift of $\approx$ 0.1 eV/min. The TUNL-HRL accelerator and associated feedback systems are described in detail elsewhere ([Wes88] and [Wes87]); a brief discussion is given in Section 8.2.

The detector devices used in these past studies have been primarily silicon surface barrier (SSB) detectors — for detection of charged particles — and thallium activated sodium iodide [NaI(Tl)] scintillators — for detection of photons. NaI(Tl) scintillators have excellent timing and efficiency characteristics but relatively poor energy resolution (typically 5-10%). Commonplace now are solid-state

photon detectors that have much better energy resolution (typically 0.1%) than NaI(Tl) scintillators. Thus, when it was decided to perform experiments which required high photon energy resolution, a new state-of-the-art γ-ray detector system was designed, purchased, and placed in operation at the TUNL-HRL. As part of this system, a Compton suppression shield was purchased for one of the solid state photon detectors. This high resolution detector system and associated electronics are complementary to the accelerator system and provide a system well suited to the high resolution study of nuclear structure with proton resonances.

A total of five detectors were used in these experiments: two high-purity germanium (HPGe) detectors, one anti-Compton suppression shield, one NaI scintillator, and one SSB detector. The first three detectors — the two HPGe detectors and the anti-Compton shield — form a unit termed a Compton suppression spectrometer (CSS) system. In Section 8.3 and 8.4.1 the setup and operation of the CSS system and its associated data acquisition electronics will be described. In Section 8.4.2 the data acquisition arrangement for data taken with the SSB detector and the NaI scintillator will be described. In Section 8.5 the software considerations for data acquisition with these five detectors will be briefly discussed. The targets used in these experiments are described in Section 8.6.

8.2 High Resolution Accelerator System

At TUNL, extensive effort has been devoted to the construction of accelerator systems with good beam energy resolution. The primary piece of equipment used by the TUNL-HRL to accomplish this is a homogenizer system. The accelerator system and the various feedback loops (including the homogenizer feedback loops) are shown in Figure 8.1 and discussed below.

The accelerator tank houses a horizontal column which supports, among other equipment, a radio-frequency (RF) ion source which operates at $\approx$ 165 MHz and

Figure 8.1 The control and feedback loops used in the High Resolution Laboratory

High Resolution Lab Control Loops

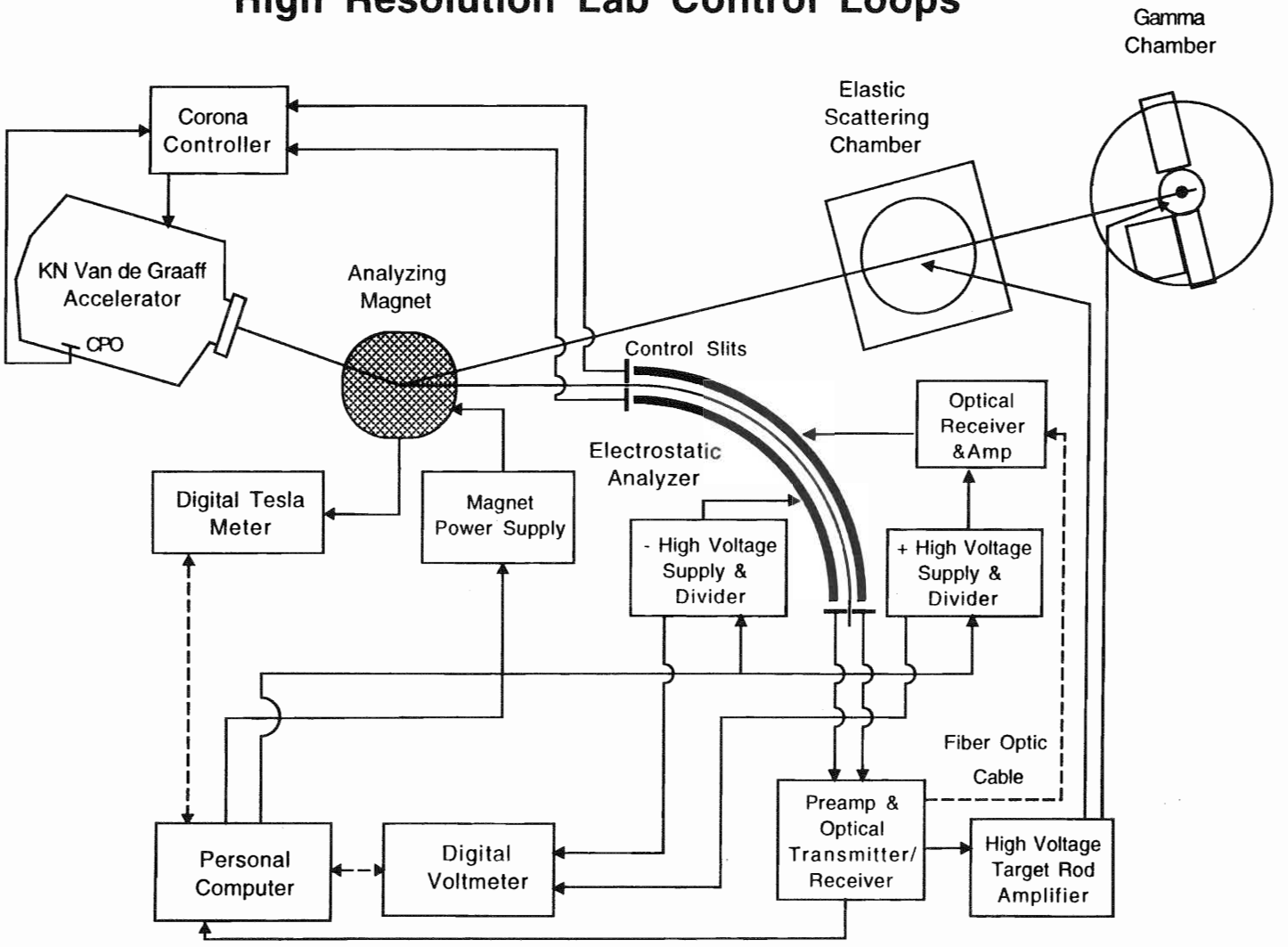

dissociates H_2 gas to produce H^+ ions and HH^+ ions. The dissociation occurs inside a glass bottle into which H_2 gas is slowly admitted by a Pd leak. The positive ions are extracted by a positive high voltage applied at the rear of the source bottle and a negative focus voltage applied at the front of the source bottle. The positive ions exit the source bottle and enter the accelerator tube, across which is maintained the terminal accelerating potential difference. The ions accelerate the length of the tube, pass through a set of electrostatic steerers just outside the tube exit, and enter a region in which a magnetic field is maintained by an analyzing magnet. Due to the mass difference, the H^+ ions and the HH^+ ions are separated, the H^+ ions being deflected $\approx 25°$ left while the HH^+ ions are deflected $\approx 17°$ left.

The H^+ ions (protons) emerge from the analyzing magnet and travel down an evacuated beamline which has a series of steerers and quadrupole focusing magnets to tune the proton beam. The proton beam then enters the target chamber and strikes the target. The targets are held in place by a target rod which is biased at high voltage, for reasons to be discussed shortly. Beyond the target chamber is a Faraday cup which measures the total beam charge that has passed through the target.

The HH^+ beam is used to derive an energy correction signal for the H^+ beam. The HH^+ ions first pass through a pair of slits which serve as both the object slits for the analyzer and the corona control slits. This corona control system is used to remove low frequency beam energy fluctuations. As the beam energy fluctuates, the HH^+ strikes the corona control slits in a different location, resulting in a change in the slit difference signal. The slit difference signal is appropriately amplified, combined with the capacitive pickoff signal (which is a measure of the ac terminal voltage fluctuation), and sent to a vacuum tube which adjusts the corona current to compensate for the beam energy fluctuation. This tube, the corona tube, operates in conjunction with a set of sharp corona needles which are positioned near the terminal dome inside the accelerator tank. A high gradient electric field exists in

the region near the corona needles; this electric field ionizes some of the insulating gas molecules, which are then attracted to the terminal dome where they modulate the voltage fluctuations. Due to the long drift time of the gas ions, only low frequency fluctuations are reduced by corona control.

The HH^+ beam, after passing through the corona control slits, passes through a pair of entrance slits into the electrostatic analyzer (ESA), the central piece of equipment in the TUNL-HRL control and feedback system. The ESA consists of two steel plates, each bent into a 90° arc. The plates have a fixed separation (= 4.57 mm) and have a mean radius of curvature of 101.839 cm. The inner plate is biased at a high negative voltage; the outer plate is biased at the same high positive voltage. Separate programmable power supplies are used to bias the ESA plates. Due to the electrostatic forces from the high voltage plates, the beam travels in a circular arc between the plates. Upon exiting the ESA, the HH^+ beam passes through a set of image slits. The geometry of the ESA is such that the beam energy is 111.34 times the potential difference between the ESA plates. Accordingly, a change in the ESA potential difference of 1 V produces the same additional deflection of the beam as a change in the beam energy of 111.34 eV. Thus the image slit difference signal can be converted to a measure of the energy fluctuation. Any change in beam energy is reflected in a change of slit current difference on the ESA image slits. The image slit difference signal is used in three ways: (1) to center the beam in the ESA by adjusting the outer plate voltage, (2) to apply an energy correction signal to the target rod, and (3) to adjust the analyzing magnet in order to center the beam on the ESA object slits.

The image slit difference signal is sent to the outer ESA plate by a fiber-optic transmitter/receiver; the receiver is located on a high-voltage platform underneath the ESA. This signal determines the adjustment necessary to center the beam in the ESA. The slit difference signal is also amplified (so that it corresponds to beam energy) and applied to the target rod which is floated at +3 kV. Thus, fluctuations

in the proton beam energy (which are the same as the energy fluctuations in the HH^+ beam) are compensated by opposing voltage fluctuations on the target rod. Finally, the slit difference signal can be used in a feedback loop to control the analyzing magnet. Since the ESA image slit difference is a direct measure of beam energy fluctuations, it is possible to correct the magnetic field of the analyzing magnet to center the beam on the ESA object slits. Such a closed loop setup is achieved by reading the ESA slit difference current, scaling it to obtain a magnetic field correction, and adjusting the analyzing magnet power supply accordingly. This is a convenient way to change the beam energy once a good tune is achieved.

The voltage of the ESA plates is controlled by power supplies which are remotely programmed by a personal computer (PC); the PC executes programs written in LabVIEW, a graphical instrumentation language developed by National Instruments. The value sent to the power supplies for determination of the ESA plate voltage is part of a 3-component feedback loop. A LabVIEW program continually polls an RS232 serial port line connected to the VAXstation 3200 over which the desired beam energy (and therefore the voltage on the ESA plates) can be dictated. The potential difference between the ESA plates is read by a Fluke digital voltmeter (DVM), which is also connected to the PC. The LabVIEW program reads the output of the DVM, compares it to the value set by the user from the VAXstation, and outputs a programming voltage to the ESA power supplies such that the beam is centered in the ESA. This feedback loop makes use of a LabVIEW subprogram which accepts an input signal and forms an appropriate output correction signal that maintains the input signal within prescribed bounds. This feedback loop is one way in which data acquisition can be inhibited. The same LabVIEW program raises an inhibit output whenever the ESA potential difference deviates from the set point by 30 eV or more. When the fluctuation is again within acceptable limits, the inhibit status is removed, and data acquisition is begun again.

A second LabVIEW program executes during data taking to control the analyzing magnet power supply (which is remotely programmable). Again, the PC is part of a 3-component feedback loop. The magnetic field is read by a digital Tesla meter (DTM) which is connected to the PC. The LabVIEW program reads the magnetic field value and determines the programming voltage for the power supply. This particular LabVIEW program can be run in one of two modes; the only difference is the manner in which the magnetic field set point is determined. In *manual* mode, the programming voltage is determined by the magnetic field value which the user chooses. This magnetic field value is chosen so that the HH^+ beam is centered in the ESA (as evidenced by a zero image slit difference signal). In *slit* mode, the ESA image slit difference is used directly to determine the programming voltage for the analyzing magnet power supply. In particular, the magnetic field is changed so that the ESA image slit difference signal is driven to zero. In this way, as the beam energy set point is changed by altering the ESA plate voltage, the ESA image slit current changes accordingly, and the magnetic field also changes to center the HH^+ beam in the ESA.

8.3 CSS Detector System

The ideal photon detector produces a signal with a pulse height proportional to the energy of the incident photon. Complications arise when all of the energy of the incident photon is not deposited in the detector. A common example is the occurrence of Compton scattering of the incident photon off a Ge nucleus in the detector. Such situations are not infrequent, as the cross section for Compton scattering from Ge ($Z = 32$) dominates at energies between 0.15 and 9 MeV [Kra88]. Pair production events produce similar complications. Such events are not desirable to record and analyze since the detector output pulse does not correspond to the incident photon energy. The standard method of rejecting such event pulses is to

surround one photon detector with another photon detector and reject those events for which both detectors produce near simultaneous outputs.

The system employed by the HRL to accomplish this rejection consists of a 60%-efficient [compared to a 3 in. by 3 in. NaI(Tl)], high purity germanium (HPGe) detector and a cylindrical anti-coincidence shield made of Bismuth Germanate (which has a chemical composition given by $Bi_4Ge_3O_{12}$ and is symbolized by the abbreviation BGO). Since the object of the anti-coincidence shield is to detect photons that exit the HPGe detector crystal, a desirable property of the anti-coincidence shield is high efficiency. It is desired to detect photons that have escaped from the HPGe detector crystal; therefore, the anti-coincidence shield should have a high efficiency, but not necessarily high energy resolution. The material BGO has the highest detection efficiency of any commonly available scintillator [Kno79]. A top view of the detector arrangement is shown in Figure 8.2. The energy resolution for these HPGe detectors has been measured to be ≈ 1.8 keV for the 1332 keV transition in ^{60}Co. (This transition line is a standard reference for resolution measurements in γ-ray spectroscopy.) This resolution is roughly two orders of magnitude better than a 3 in. by 3 in. NaI(Tl) detector. An HPGe detector slides into a well in the BGO detector, as shown in Figure 8.3. The well in the BGO detector is located such that there is a large fraction of BGO in the direction of forward scattering. Such a configuration increases the likelihood of detection of Compton-scattered photons, which are preferentially forward scattered. The dimensions of the suppression shield were chosen after computer simulations were performed to determine the optimum location of the HPGe detector well within the BGO cylinder [Dra94]. A second, unsuppressed HPGe detector is also used in these measurements.

Figure 8.2 A top view of the CSS system, composed of two HPGe detectors and a BGO anti-coincidence shield for one of them. The large dotted circular plate is a steel plate on which the CSS system rests. The large open circles are the HPGe detector dewars. The small circle in the center of the figure is the scattering chamber. The regions marked with diagonal lines are various plates and support structures for the system.

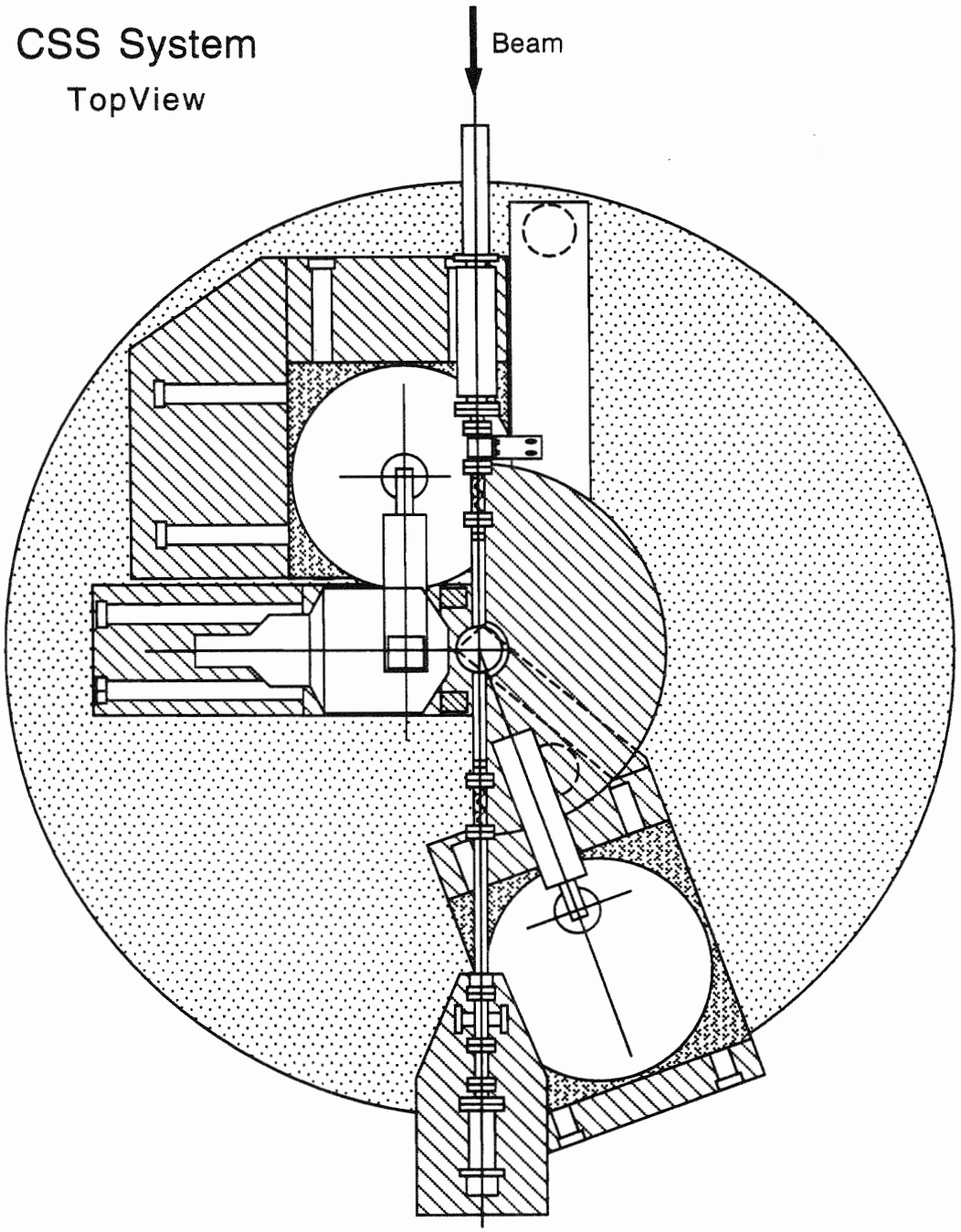
CSS System
TopView
Beam

Figure 8.3 Top cross-sectional view of the suppressed HPGe and the BGO detector.

Top View of HPGe detector within BGO well

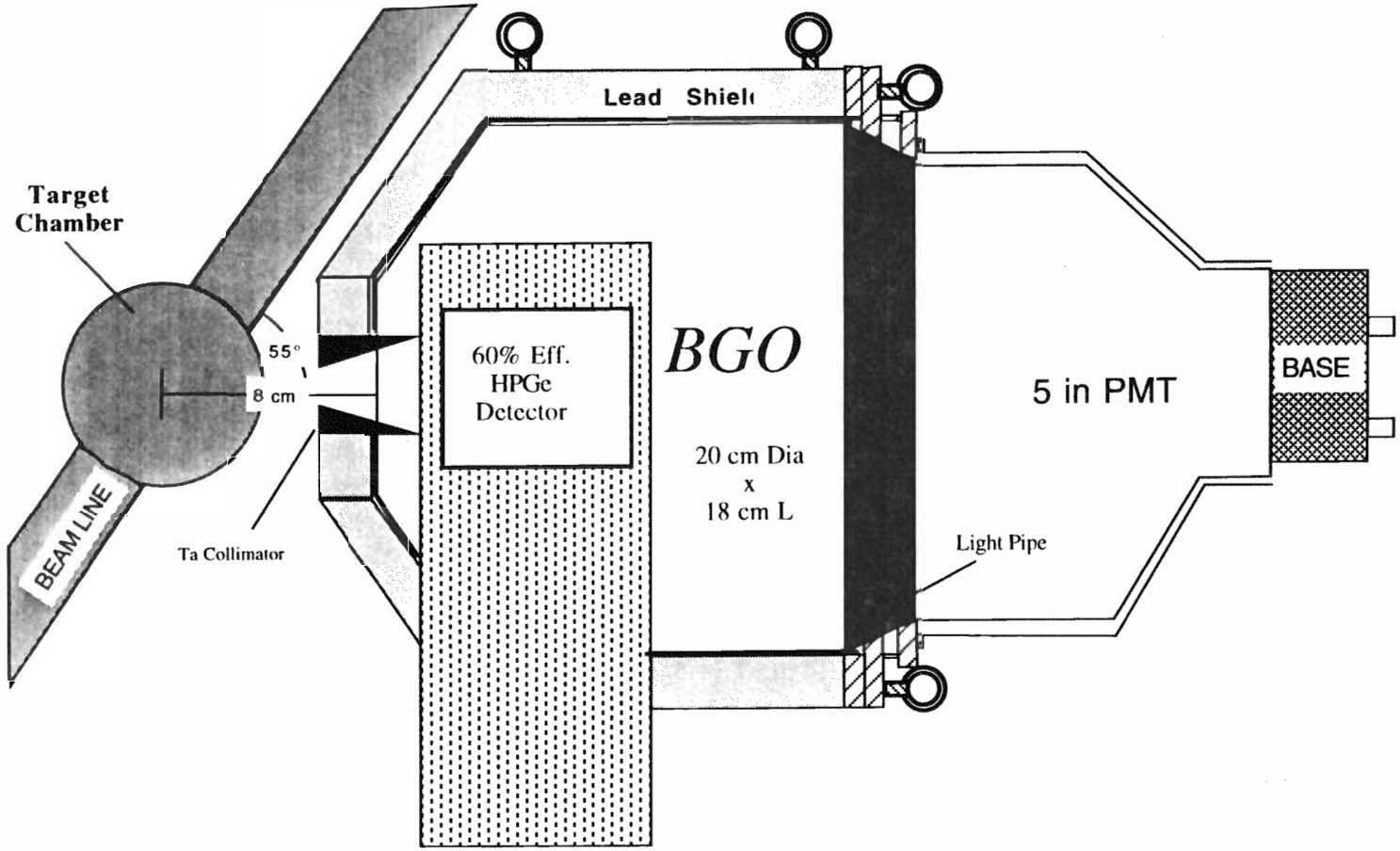

8.4 Data Acquisition Electronics

8.4.1 CSS Data Acquisition Electronics

The electronics for data acquisition through the CSS system and those for data acquisition through the SSB/NaI detectors are largely separate and will be discussed in this section and the following one, respectively. The electronics for acquisition of data from the HPGe detectors must handle two aspects of event detection: photon energy and the time of photon detection. The energy is used to determine the energy of the incident photon, and the timing information is used to determine coincident events both between the two HPGe detectors and between one HPGe detector and its suppression shield. A schematic drawing showing the various electronics modules used in the processing of signals from the HPGe detectors and the BGO detector is shown in Figure 8.4.

Each germanium detector is equipped with a preamplifier that is located in the same housing as the detector crystal. The preamplifier produces two output signals — an energy output and a timing output. For each germanium detector the energy output is sent to a Tennelec TC245 spectroscopy amplifier whose output is then sent to an input of a CAMAC quad ADC which digitizes the signal. These particular spectroscopy amplifiers were chosen because they are equipped with both pulse pileup rejection and ballistic deficit correction circuitry, features desirable for acquisition of high-resolution γ-ray data.

Pileup is the circumstance that occurs when the processing of a signal by an amplifier depends on one or more preceding signals. It is desirable to minimize pileup since it degrades energy resolution. The TC245 amplifier provides a pileup rejected (PUR) output connector which makes available only the shaped signals that are not affected by pileup. In these experiments all energy signals have been taken from the TC245 PUR output connector.

Figure 8.4 The electronics arrangement for use with the CSS system.

Germanium Detector Electronics Setup

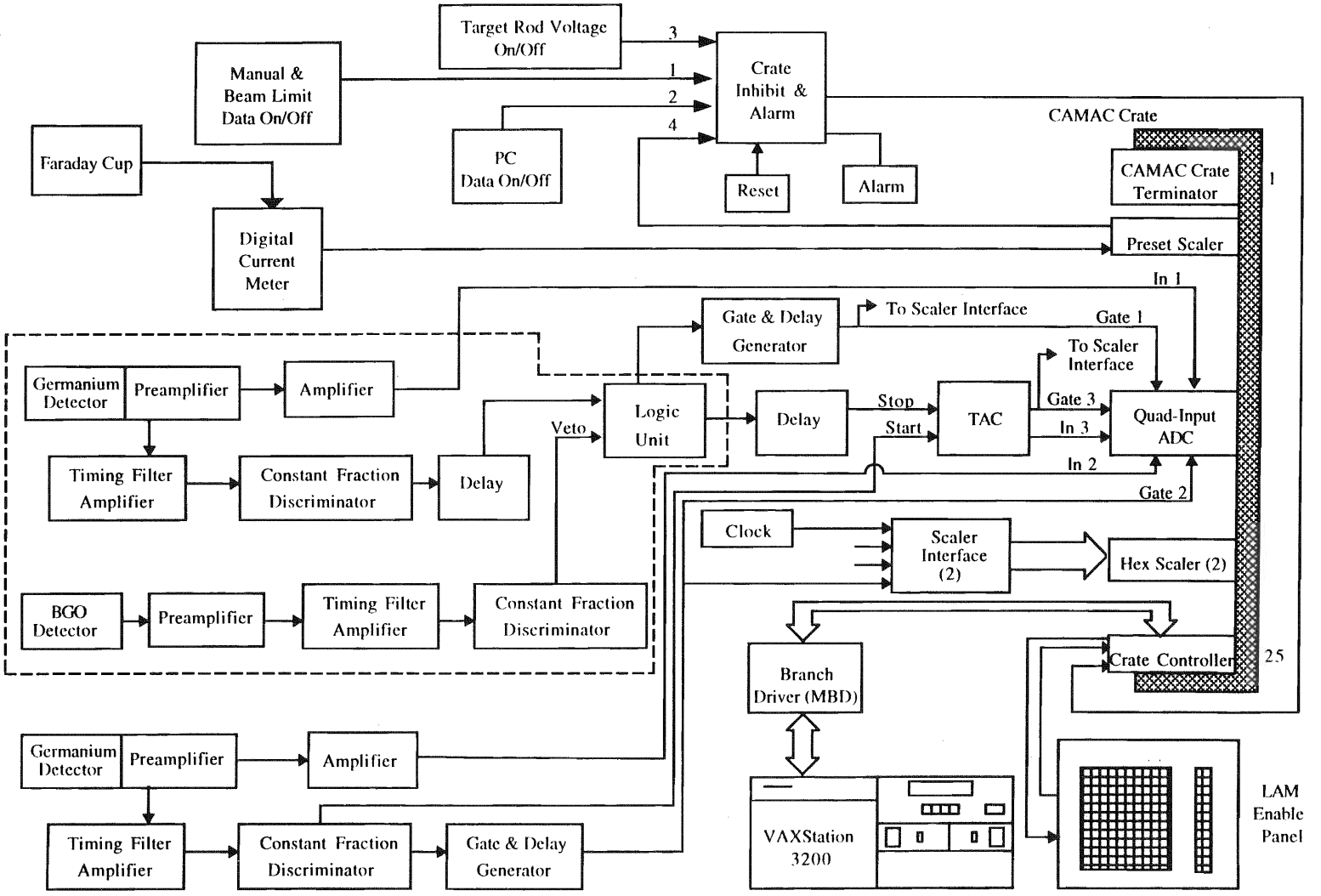

Pulses from HPGe detectors in general and coaxial HPGe detectors in particular are subject to another complication — ballistic deficit. Ballistic deficit occurs when the shaping time of the spectroscopy amplifier is shorter than the time needed for the detector to form an accurate output signal for an event. Since ballistic deficit results in a loss of energy resolution, it should be minimized. The TC245 amplifier can be operated in a mode — called BDC mode — which corrects for ballistic deficit effects and was used throughout these experiments.

Timing considerations related to detection of events are necessary for two separate purposes: rejection of Compton and other undesirable events and recording of coincident events. Many electronics modules for accomplishing these two timing-related tasks are mutually common. The timing outputs from the two HPGe detector preamplifiers as well as the BGO detector preamplifier output are each routed to a Timing Filter Amplifier (TFA) which amplifies and shapes the input signal to produce an output pulse of roughly uniform shape. The TFA output is a variable height fast signal that matches the timing characteristics of the detector and is sent to a Constant Fraction Discriminator (CFD). From its input signal, the CFD associates a definitive time of arrival of the photon into the detector. The CFD output is thus a logic signal which identifies the time of the photon interaction within the detector and thus can be used in subsequent timing measurements.

Near simultaneous outputs from the BGO detector TFA and the corresponding HPGe detector TFA indicate an event which should be rejected. This rejection is performed by a Logic Unit which has a *veto* input and four other standard inputs. If a pulse is detected at the *veto* input, the module produces no output signal regardless of how many acceptable pulses may be present at the other inputs. Thus, the BGO detector CFD output is sent to the logic module *veto* input while the CFD output from the suppressed HPGe detector is delayed 127 ns (to insure that this signal arrives at the Logic Unit after the corresponding veto signal if there is one) and then sent to an input of the Logic Unit. The output from the Logic Unit

represents those events which should be recorded for analysis and is used in three ways: as the *stop* input to a TAC module (to be discussed below), as a scaler for the acceptable events detected within the suppressed HPGe detector, and as a gate for the suppressed HPGe energy signal to the ADC.

Determining the elapsed time between the detection of *good* events in the two HPGe detectors is the next task. A Time-to-Amplitude converter (TAC) module is used to measure the time interval between the photon events. The TAC module accepts two inputs and produces an analog output pulse whose amplitude is proportional to the elapsed time between arrival of the two inputs. The CFD module output for the unsuppressed HPGe detector is used to start the timing sequence; the logic module output corresponding to a suppressed HPGe detector signal, after being delayed 31.5 ns, stops the timing sequence. If the TAC detects a start signal but no stop signal, it resets after a user-selected amount of time (500 μs). The TAC output signal is sent to a different channel of the same ADC as the energy signals for digitization and transfer to the computer. The TAC signal is the signal which identifies a coincident event and is used to direct the software to handle the set of events differently.

Hardware scalers are used to count the number of events of various types. The scalers allow online monitoring of the experiment as well as deadtime corrections to the data. For the electronics setup described in this section, three different events are counted: (1) non-vetoed events detected in the suppressed HPGe detector (the scaler signal is taken from the output of the Logic Unit); (2) events detected in the unsuppressed HPGe detector (the scaler signal is taken from the corresponding output of the CFD); and (3) events corresponding to the number of two-fold coincidences (the scaler signal is taken from the TAC module rear-panel output which indicates a valid conversion). The first two of these signals are first shaped by a gate and delay generator (G&D) before being routed to a scaler interface. The outputs from each scaler interface module are input into a CAMAC Kinetic Systems Hex

Scaler module for transfer to the computer.

The three signals which serve as scaler input signals also serve in another capacity — as coincidence gate signals for the CAMAC ADC. The ADC is operated in gated mode in which analog input signals are converted only if there is an associated coincident gate signal. The energy pulse from the unsuppressed HPGe detector is gated at the ADC by an output pulse from the corresponding CFD, while the energy pulse from the suppressed HPGe detector is gated at the ADC by an output pulse from the Logic Unit. Both gate signals are shaped first by Gate and Delay modules before being sent to the ADC Gate input. In this way, signals from the suppressed HPGe detector which involve Compton scattering or escape of one or more pair-produced photons are not processed, since there will not be a corresponding gate at the ADC. The TAC input to the ADC is gated by a conversion pulse from the TAC module.

The inhibition of data acquisition is desired under certain circumstances. A six-input inhibit module accepts signals from modules which determine inhibit status and output a signal which is used to inhibit the taking of data. There are instances when the user must or should stop data taking, even when no software or other module is signalling an error condition. Such inhibition is accomplished by using a module which outputs an inhibit status signal when a switch is thrown. Returning the switch to the original position lowers the inhibit status. This count/stop module also receives input from a windowed module which allows the user to set acceptable windows around the beam current read at the Faraday cup. If this beam current fluctuates outside the user-set window, data taking is inhibited and is resumed when the beam current is again inside the window. A second criterion used to inhibit data taking is the potential difference between the ESA plates and has been previously discussed. A third criteria for inhibiting data is the absence of a target rod voltage applied to the target rod. In this case, there would be no energy corrections to the H^+ beam and therefore no improvement of the beam energy resolution due to the

homogenizer system. A fourth criterion is software related. When a run is ended, a software inhibit is raised while various run-ending procedures, one of which is often changing the beam energy in preparation for the next run, are accomplished. This inhibit is raised when the system is ready to begin taking data again.

8.4.2 NaI and SSB Data Acquisition Electronics

Signals from the SSB detector and the NaI scintillator are processed differently than those from the CSS system. The principal difference is that the timing of these signals need not be considered; no rejection of events is explicitly performed nor are coincidence events an issue. A schematic showing the electronics configuration used in acquiring data from these two detectors is shown in Figure 8.5. The signals, whether from the SSB detector or from the NaI scintillator, are processed basically the same way; each is treated as an energy signal and processed by the same type of electronics modules, though an extra test is performed in the processing chain for signals from the SSB detector.

The output signal from each detector is preamplified and sent to a spectroscopy amplifier which integrates the input signal and shapes the resulting pulse. The amplifier provides two output signals for each conversion — one with unipolar shape and one with bipolar shape. The unipolar output pulse is used to associate an energy with the detected particle or photon; it is delayed 900 ns (plus 2 μs internal delay) and sent to a gated multiplexer module. Operating the multiplexer in coincidence gated mode allows undesirable events to be discarded and not recorded.

The generation of a gate signal for the multiplexer is accomplished using the bipolar amplifier signal. The bipolar signal is sent to both a Timing Single Channel Analyzer (TSCA) and a delay module. The TSCA has a window set to enclose signals arising from elastic scattering off carbon. (As discussed in Section 8.3, the targets that are used in the HRL are deposited onto carbon foils. Thus, in any

Figure 8.5 The electronics modules used with the SSB detector and the NaI scintillator.

Data Acquisition Electronics Setup

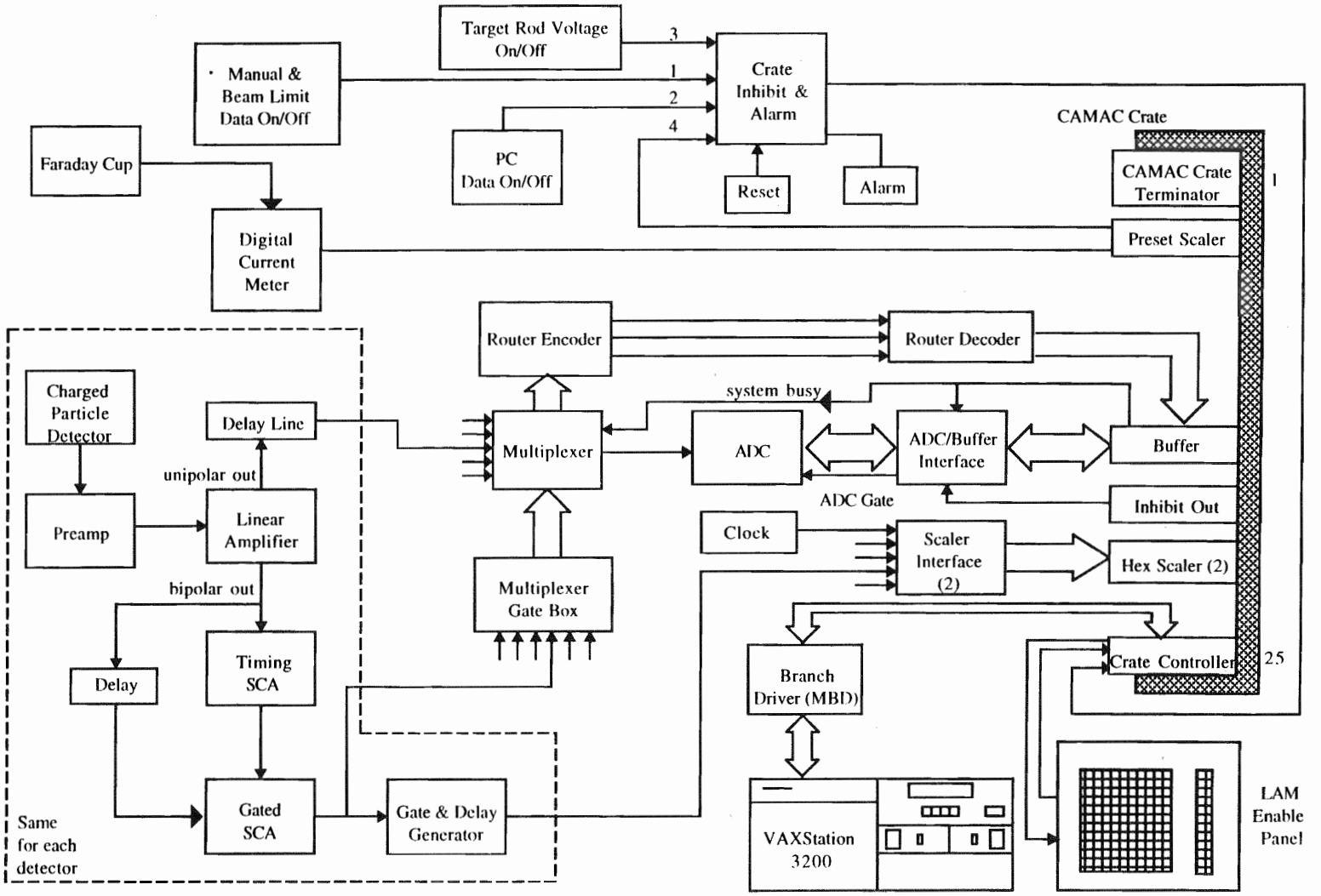

experiment there will be many events arising from elastic scattering of protons off carbon; their result is pileup and increased deadtime.) This is the only difference between accumulating spectra from a SSB detector versus a NaI scintillator: the window on the TSCA is set for zero width for NaI spectra since there are no carbon peaks to be gated out. The delayed bipolar output signal is input into a Single Channel Analyzer (SCA) which also serves as a discriminator. The TSCA output signal is sent to an inhibit input of the SCA; a signal detected at this input results in no output from the module. In this way, the SCA produces an output signal only for an amplifier output pulse with an amplitude in the acceptable range set on the SCA, excluding signals resulting from scattering off carbon. The SCA output is then used to gate the multiplexer. The multiplexer output is sent to a Northern Scientific ADC for digitization.

Since the multiplexer passes the signals to the ADC independent of the detector source, some mechanism is necessary to distinguish the origin of signals so that proper sorting of the data by the computer is accomplished. Routing signals from the multiplexer are used for this purpose, indicating with which detector the pulse should be associated. These routing signals are used to gate open a CAMAC Borer buffer module, which outputs a signal that is used to produce a gate signal for the Northern ADC. After conversion, the data are sent to the same Borer module where the data are combined with the multiplexer routing signals and await transfer to the computer.

Recently, the HRL has purchased another CAMAC ADC, similar to the one used for acquisition of data from the CSS system. This second ADC can be used to acquire data from the NaI detector and the SSB detector. In this setup, the signals from the amplifier are sent directly to the ADC which is gated with signals from the corresponding SCA. Thus, events arising from elastic scattering off carbon are not digitized since there is no associated enable gate at the ADC. Some of the data for this dissertation was acquired in this mode.

As with the Ge detectors, hardware scalers are also monitored for the SSB detector and the NaI scintillator. Two types of events are counted: (1) the events detected in the SSB detector and (2) the events detected in the NaI scintillator. In each case the scaler is taken from the corresponding SCA output. The signals are handled similarly to those in the CSS electronics setup in that they are sent to a G&D module for shaping before input into a scaler interface module.

Another data acquisition component that is used in these experiments is the preset scaler module; it is used to indicate the end of a data-taking run. Proton beam current is collected on a Faraday cup that is located downstream from the target; this current is integrated by a Digital Current Integrator (DCI) and sent to a CAMAC preset scaler module which decrements an internal counter by its input signal. The user loads the preset scaler module with a number related to the amount of beam desired to pass through the target for a run. When the preset scaler counter reaches zero, the run is ended, and the CAMAC crate is inhibited, halting data acquisition.

8.5 Data Acquisition Software

Both digitized amplitudes and scalers are transferred from CAMAC modules to a VAXstation 3200 computer for storage, analysis, and display. The mechanism for data transfer uses a CAMAC crate controller and a Microprogrammable Branch Driver (MBD) which performs DMA operations to the computer. The XSYS data acquisition and analysis package ([Sod87] and [Kin81]) directs this transfer of data to the VAXstation computer by way of programs executing continually to accomplish this task. XSYS programs were written to direct the specifics of this transfer of data. Several XSYS programs have been modified to suit the specific needs of the HRL; a description of the changes is given elsewhere [Bul89].

Energy signals from the CSS system may be classified into two categories. If

both HPGe detectors signal an event and the BGO suppressor does not, there are three signals to be transferred to the computer for that event: two energy signals and one TAC signal. In this case, the singles, coincident, and TAC spectra are incremented. Additionally, the spectra which display all γ-rays in coincidence with a given γ-ray are incremented if the user has set the appropriate gates. If only one of the HPGe detectors signals a *good* event, there is only one signal to transfer to the computer: the corresponding energy signal. In this case, the appropriate singles spectrum is incremented. Data from the NaI detector and the SSB detector is simpler; each event is sorted into the proper spectrum corresponding to the prepended multiplexer routing signal. Additionally, scaler information is transferred to the computer by the same XSYS mechanism.

Data are sorted by XSYS subprocesses into arrays, called data areas, which the user allocates to contain specific kinds of data. A listing of the data areas used with the CSS system are shown in Table 8.1. A brief comment description indicates the criteria which allows a count to be sorted into a given data area. The CSS data acquisition system can also write event mode data in which a record of each event is separately written to a file on disk for offline replay and extended analysis. This option is extremely useful for analyzing coincidence events.

The process of accumulating data sometimes involves many successive short data runs. When the preset scaler signals that a run is ended, several tasks are automatically performed by various computer processes. The CAMAC crate is inhibited; experiment parameters, such as the beam energy and various data acquisition counters, are changed; data from the previous run are written to disk for offline analysis; online data acquisition information, such as scalers and certain data areas, is updated; and finally the crate inhibit is removed so that data acquisition can begin again. This sequence of events is automated to increase the efficiency of data acquisition.

An important task to be performed in the experiment is the transfer of the data

from disk to a storage medium. A program was written to accomplish this task. It executes as the data are taken, reading the data from files written to disk at the end of each run and transferring the data to 8 mm cassette. This procedure continues until the experiment is completed. Many experimental circumstances are handled by this program: the possibility of no files on disk, many files on disk, and experimental changes to filenames. The program was written to interfere minimally with the data acquisition processes executing concurrently — it uses its own set of data areas and uses only a small amount of computer resources. Additionally, the program produces a log file which contains a record of what files have been transferred to tape.

TABLE 8.1. Data areas used with the CSS system.

Number	Name	Description
1	NAI	Singles spectrum from NaI
2	PART	Particle data spectrum
3	SSNG	Singles spectrum from suppressed Ge
4	USNG	Singles spectrum from unsuppressed Ge
5	TAC	TAC spectrum
6	SCON	Spectrum produced from suppressed Ge when TAC is present
7	UCON	Spectrum produced from unsuppressed Ge when TAC is present
101	CSG1	Spectrum from suppressed Ge when TAC is within gate 1 and the event in the unsuppressed Ge falls inside gate 1
102	CSG2	Spectrum from suppressed Ge when TAC is within gate 1 and the event in the unsuppressed Ge falls inside gate 2
103	UG1	Spectrum from unsuppressed Ge when TAC is within gate 1 and the event in the suppressed Ge falls inside gate 1
104	UG2	Spectrum from unsuppressed Ge when TAC is within gate 1 and the event in the suppressed Ge falls inside gate 2

8.6 Targetry

8.6.1 ^{29}Si Targets

Thin ^{29}Si targets were used to study the ^{30}P nuclide via the reaction ^{29}Si(p,γ). These targets consisted of thin films of ^{29}Si evaporated to a thickness of 1.5 - 3.0 μg/cm^2 onto carbon foils. The foils were $\approx$ 5.0 μg/cm^2 thick and were obtained from the Arizona Carbon Foil Company on glass slides. Distilled water was used to float the foils off the slides and onto stainless steel target rings. The isotope was obtained from the Oak Ridge National Laboratory in the form of SiO_2 enriched to $\approx$ 95% ^{29}Si. A 0.005 in. Ta closed boat was filled with isotope and Ta powder in the ratio 7-8:1 and placed under high vacuum; the targets were positioned above the Ta boat. A current of 85 A was then run through the boat in order to raise it to a temperature of $\approx$ 1100° C. At this temperature the boat outgassed; the purpose of this step was to insure that water was not present during evaporation. Since this temperature is below the melting point for SiO_2, no ^{29}Si was deposited on the carbon foils. After the boat was outgassed, the vacuum was allowed to improve, and the evaporation procedure was begun. At a current of 115 A, the boat reached a temperature of 1450° C, which is above the melting point of SiO_2. The Ta powder is a reducing agent for the SiO_2, and the reduction reaction (which occurs at this temperature) leaves SiO and Si which is subsequently evaporated onto the carbon foils.

A Maxtek TM-100R Thickness Monitor displays the thickness of the material deposited on the targets. A quartz crystal is exposed to the boat and collects material as it evaporates. This added mass decreases the vibrational frequency of the crystal, and the monitor converts this change to a thickness value. Since the monitor reads the total accumulation of mass onto the targets, all contaminants are included in the final thickness value; therefore, only a relative measure of the

thickness is obtained. A monitor reading of 0.07 kÅ corresponded to 1.5 $\mu g/cm^2$, and 0.13 kÅ corresponded to 3.0 $\mu g/cm^2$. The target thickness values were actually measured by comparing elastic proton scattering with Coulomb scattering.

8.6.2 ^{27}Al Targets

The preparation of ^{27}Al targets was similar in many ways to the preparation of ^{29}Si targets. The carbon foils were identical to those used for the ^{29}Si case, as was the evaporating chamber and setup. Prior to the Al evaporation, a small amount of Vicatwet was placed in a 0.005 in. Ta open boat and evaporated at a current of 10 A for $\approx$ 3 minutes; this material coats the inside of the bell jar and facilitates later cleaning of the vacuum chamber. A 0.75 cm segment of Ultrapure Al wire, originally obtained in wire form with a diameter $\approx$ 0.040 in., was placed into a 0.005 in. Ta open boat. The current through the boat was slowly increased to 50 A, at which point the Al melted and began to evaporate onto the carbon foils. The evaporation continued until the thickness monitor displayed a reading of $\approx$ 0.350 Å, which corresponded to a target thickness of $\approx$ 10 $\mu g/cm^2$.

Chapter 9

Data and Analysis

9.1 Introduction

The mode of nuclear deexcitation with which we are concerned in these studies is nuclear γ-decay, a transition between two nuclear states accompanied by the simultaneous emission of a γ-ray. In particular, the capture reaction ^{29}Si(p,γ) has been used to study the structure of the ^{30}P nuclide. A general discussion of γ-decay is presented in Section 9.2. A discussion of the recommended upper limit (RUL) concept of Endt is also given. In our studies, γ-rays with energies up to $\approx$ 8 MeV are detected and used to determine the properties of nuclear excited states of interest. A calibration procedure that accurately determines the energy and the intensity of the detected γ-rays is necessary. In Section 9.3 our energy calibration and efficiency calibration procedures are described; the resulting calibrations used to analyze the ^{30}P data are presented and discussed. The data, analysis, and results for five ^{29}Si(p,γ) resonances are presented and discussed in Sections 9.4 - 9.8.

9.2 Nuclear Gamma Decay

A nucleus in an excited state often may decay by a number of different processes [Bla91]. Generally, the number of possible decay modes increases with increasing excitation energy E_x . Two particular decay processes that occur frequently in the reactions induced in the TUNL-HRL are proton emission and γ-emission. Where particle emission is possible, it is usually the preferred decay mode. A critical number for proton emission is the proton separation energy S_p , which is the amount of energy needed to remove a proton from a nucleus. A nucleus with $E_x \geq S_p$ may decay by emitting a proton, while a nucleus with $E_x < S_p$ is energetically forbidden from proton emission. For ^{30}P, $S_p = 5.5945$ MeV. Though resonance states may decay by proton emission, it may take a long time (by nuclear standards) for the excess energy of the ^{30}P compound nucleus to be concentrated on one proton, leading to its ejection. In such cases, the nucleus most often decays by γ-emission. Decay by γ-emission is a frequent deexcitation mechanism for states with $E_x < S_p$ (bound states) and for states with $E_x \geq S_p$ (resonance states). Proton emission is the only particle emission process to consider in our energy range ($E_p = 0$ - 4 MeV) since the neutron separation energy for ^{30}P is 11.328 MeV.

Gamma-emission involves an interaction between a nucleus and an external electromagnetic field. Transitions between the nuclear states are governed by certain conservation laws. The nuclear states are identified by a set of good quantum numbers (such as E, J, π, and T) that specify the eigenvalues of a particular operator when applied to the nuclear wavefunction. (See Sections 2.1 and 2.2 for a more complete discussion.) It is well known that electromagnetic radiation can be analyzed in terms of a multipole expansion of its source distribution; this procedure can be done for either static or dynamic electromagnetic fields. In the nucleus the electromagnetic sources are the various charges and currents. It is convenient and useful to consider the radiation in γ-decay in terms of multipoles. Extensive

details in the development of γ-decay from electromagnetism are given by [Bla91] and [Jac75].

Consider a decay from the nuclear state $E_x = \mathrm{E}_i$ to the state $E_x = \mathrm{E}_f < E_i$ by γ-emission. Two quantities associated with the emitted radiation are of specific interest in our studies involving γ-decay: the energy and the angular momentum. The photon energy is given by $E_\gamma = E_i - E_f$ and represents the difference in energy between the two nuclear states. The angular momentum, with quantum number L, has magnitude $\sqrt{L(L+1)}\hbar$ and defines the multipolarity of the emitted radiation. The value of L also characterizes the multipole order λ $(= 2^L)$ of the radiation. The total angular momentum is conserved. Denoting the nuclear angular momentum by $\vec{I}$, this conservation is expressed as $\vec{I}_i = \vec{I}_f + \vec{L}$. These two quantities — E_γ and L — alone, however, are not sufficient to uniquely characterize the emitted radiation since electromagnetic radiation may be of two types: electric and magnetic. Both electric L-pole radiation and magnetic L-pole radiation carry identical angular momentum: however, the electromagnetic field patterns are not identical since there is a phase difference between them. Symmetry properties of the transition matrix elements relate the parities of the nuclear states to the possible electromagnetic radiation types. If the parity of the initial nuclear state is (is not) equal to the parity of the final nuclear state in the γ-decay process, the emitted radiation may consist of even electric (magnetic) or odd magnetic (electric) multipole radiation or some mixture thereof. This parity restriction together with the requirement of angular momentum conservation specifies what multipolarities are allowed for transition between two nuclear states. A knowledge of the excitation energy and parity of the initial and final nuclear states and the multipolarity of the emitted radiation fully specifies the radiation characteristics. Our goal is to use pieces of this information to infer the quantum numbers of the initial or the final nuclear state.

In addition to the energy and angular momentum, a quantity which reveals much

information about a particular γ-decay is the transition probability T_{fi} [Rin80] for a γ-transition between the initial nuclear state $|i>$ and the final nuclear state $<f|$:

$$T_{fi}(\Lambda, L) = \frac{\Gamma_\gamma}{\hbar} = \frac{8\pi(L+1)}{L\hbar[(2L+1)!!]^2}\left(\frac{E_\gamma}{\hbar c}\right)^{2L+1} B(\Lambda L, I_i \rightarrow I_f), \tag{9.1}$$

where Γ_γ = the partial γ-decay width, Λ = E(M) for electric (magnetic) multipole radiation, L = multipolarity of the radiation, and B(ΛL) = the reduced transition probability, which manifests the connection with the nuclear states. Expressing the reduced transition probability in terms of widths is convenient since the widths are often known experimentally. The reduced transition probability is given by

$$B(\Lambda L, I_i \rightarrow I_f) = \frac{1}{2I_i+1}\left|< f|\hat{M}(\Lambda)|i >\right|^2. \tag{9.2}$$

where $\hat{M}$ is the electric (magnetic) multipole operator if Λ = E (M). The multipole operators are discussed in detail by Ring [Rin80]. By making use of some simplifying assumptions, Weisskopf derived estimates for B(ΛL) for a nucleus with $N+Z=A$:

$$B_W(EL) = \frac{(1.2)^{2L}}{4\pi}\left(\frac{3}{L+3}\right)^2 A^{2L/3} \quad \mathrm{e^2\ fm^{2L}} \tag{9.3}$$

and

$$B_W(ML) = \frac{10}{\pi}(1.2)^{2L-2}\left(\frac{3}{L+3}\right)^2 A^{(2L-2)/3} \quad \mu_N^2\ \mathrm{fm^{2L-2}}. \tag{9.4}$$

These estimates assume a single proton transition and are referred to as single particle estimates. They are used as units to express the magnitude of the reduced transition probability and are termed Weisskopf units (W.u.). The corresponding width that is obtained using the Weisskopf estimate for the reduced transition probability is symbolized by Γ_W and is used extensively in the following analyses. These estimates indicate that the probability of E(L) radiation is roughly a factor of 100 larger than the probability of M(L) radiation, though the two cannot occur simultaneously because of parity restrictions. Furthermore, the probability for radiation of a given multipolarity is larger by a factor of $\sim 10^5$ than the same radiation type of multipolarity L + 1 [Sie87]. From Equations 9.3 and 9.4. M($L+1$) radiation

cannot compete with E(L) radiation in transition probability, but E($L+1$) often does compete favorably with M(L) in transition probability. Thus, a mixture of radiation types M(L) and E($L+1$) in a given transition is frequent. Also, from Equations 9.3, 9.4, and 9.1, T_{fi} is a rapidly decreasing function of L. Thus, in any given γ-decay, usually only the lowest two multipoles contribute significantly.

The reduced transition probability for a given transition is given theoretically by Equation 9.2 and can be determined experimentally by using Equation 9.1 if Γ_γ is known. In addition to the conservation requirements mentioned earlier, the reduced transition probability provides another way to accept or reject transition assignments. After considering a large number of γ-decay transitions in the low mass range, Endt has suggested a set of recommended upper limits (RUL) for the reduced transition probabilities [End93]. In the analysis process, one considers assignment possibilities for a given state based on the levels to which it decays. The RUL for each of the set of possible assignments sometimes can be used to eliminate certain of the possibilities; if the given transition strength exceeds the RUL (Endt suggests by at least a factor of 2), the possible transition is extremely unlikely, and the possible assignment can be ruled out. Endt's RUL values for isoscalar and isovector E1 - E3, M1, and M2 character transitions are shown in Table 9.1. As mentioned previously, a given transition may have components of different character; particularly, transitions mixing M(L) with E(L + 1) radiation are common. For all such instances, regardless of what specific radiation types are being mixed, the calculation of the partial γ-ray widths requires that the mixing ratios of the components be known. For two-component mixing, the mixing ratio $\delta_{\overline{L}L}$ is defined as

$$\delta_{\overline{L}L} = \frac{\sqrt{\Gamma_L}}{\sqrt{\Gamma_{\overline{L}}}} \tag{9.5}$$

where $\overline{L} < L$. If the mixing ratio is known, the partial width can be split into the two components, and the reduced transition probability can be determined for each

TABLE 9.1. Recommended upper limits for reduced transition probabilities in the mass range A = 21 - 44.

Transition Type[a]	RUL (W. u.)[b]
$E1_{IS}$	0.002
$E1_{IV}$	0.1
$E2_{IS}$	100
$E2_{IV}$	5
$E3_{IS}$	50
$M1_{IS}$	0.05
$M1_{IV}$	5
$M2_{IS}$	0.2
$M2_{IV}$	5

[a]IS (IV) indicates isoscalar (isovector) transitions.

[b]RUL values taken from [End93].

component. However, if the mixing ratio for a transition is unknown, the partial γ-ray decay width cannot be so divided, and only an upper limit on the reduced transition probability can be deduced in such cases.

9.3 Calibration

In any experiment it is important to calibrate the measuring instruments that are used. In these γ-ray studies, both the photon energy and the strength of the corresponding transition are used in the analysis procedure. The energy is assigned as the centroid of the peak in the data spectrum, while the strength is related to the area under the peak. It is essential, then, that an energy calibration be performed to relate channel number (centroid position) with photon energy; our procedure for energy calibration is discussed in Section 9.3.1.

The response function for a γ-ray detector is complicated, consisting of contributions from many different physical processes [Kno79]. An important consequence of the response function behavior is that the detection efficiency is energy-dependent. Thus, the probability of detecting a specific energy γ-ray is not equal to the probability of detecting a γ-ray of a different energy even if all other quantities are equal. Clearly, this fact affects the area under a spectrum peak, and an efficiency calibration is necessary to unfold these energy dependent effects. Our efficiency calibration procedure is described in Section 9.3.2.

9.3.1 Energy Calibration

The basic procedure in our energy calibration is to formulate an expression which determines the energy E as a function of channel number x. The means of accomplishing this task involves determining the channel numbers corresponding to a set of well-known γ-rays. Ideally, the γ-rays used for calibration should be

strong since identification is then easier. With such a set of coordinate pairs (E,x), a fitting procedure can be used to fix a set of parameters in a known functional form. In these experiments, a large energy range (0 - 8 MeV) is spanned by the ^{30}P γ-rays. Since it is difficult to obtain a single γ-ray source with well-known γ-ray energies covering this large an energy range, we decided to use two γ-ray sources for calibration purposes — one providing the calibration at lower energies and one providing the calibration at higher energies.

A standard source that produces low energy γ-rays whose energies are well known is ^{152}Eu. The γ-rays from ^{152}Eu range in energy from 121 to 1408 keV. A list of the thirteen ^{152}Eu γ-ray lines used in our energy calibration is shown in Table 9.2. Columns 1 and 2 display the accepted γ-ray energies and corresponding uncertainties; columns 3 and 4 display the accepted γ-ray relative intensities and corresponding uncertainties.

The ^{152}Eu data were collected prior to the accumulation of ^{30}P data by placing a 10 μCi source in a target position in the CSS chamber and accumulating data for two hours. It is necessary to place the ^{152}Eu source in a target position so that the configuration is as similar as possible to that for the actual ^{30}P data accumulation. The region of the ^{152}Eu spectrum from 0 to $\approx$ 1.5 MeV is shown in Figure 9.1. The γ-rays listed in Table 9.2 are clearly visible.

Extracting an energy calibration from the data shown in Figure 9.1 consists of two distinct parts — determining the centroids of the peaks of interest (in this case, those listed in Table 9.2) and forming a function which yields the γ-ray energy E_γ as a function of channel number x. Both steps are accomplished by using various codes in the GELIFT package, a set of FORTRAN programs developed and written by D. C. Radford at Chalk River. The codes are primarily designed for the analysis of γ-ray spectra that result from Ge detectors. There are several factors which determine a γ-ray line shape, and the GELIFT fitting algorithm utilizes a functional form which properly takes these various factors into account [Rad89]. GELIFT performs

TABLE 9.2. ^{152}Eu Calibration γ-ray Energies[a]

E_γ (keV)	E_γ Error (keV)	Relative Intensity	Relative Intensity Error
244.692	0.002	3580.	60.
295.939	0.008	211.	5.
344.275	0.004	12750.	190.
367.789	0.005	405.	8.
411.115	0.005	1070.	10.
488.661	0.039	195.	2.
688.678	0.006	400.	8.
778.903	0.006	6190.	80.
867.388	0.008	1990.	40.
964.131	0.009	6920.	90.
1212.950	0.012	670.	8.
1299.124	0.012	780.	10.
1408.011	0.014	10000.	30.

[a]Information taken from [Led78].

Figure 9.1 ^{152}Eu calibration data. The portion of the ^{152}Eu spectrum covering channels 0 to 2000 is shown. (Top) Spectrum from unsuppressed HPGe. (Bottom) Spectrum from suppressed HPGe.

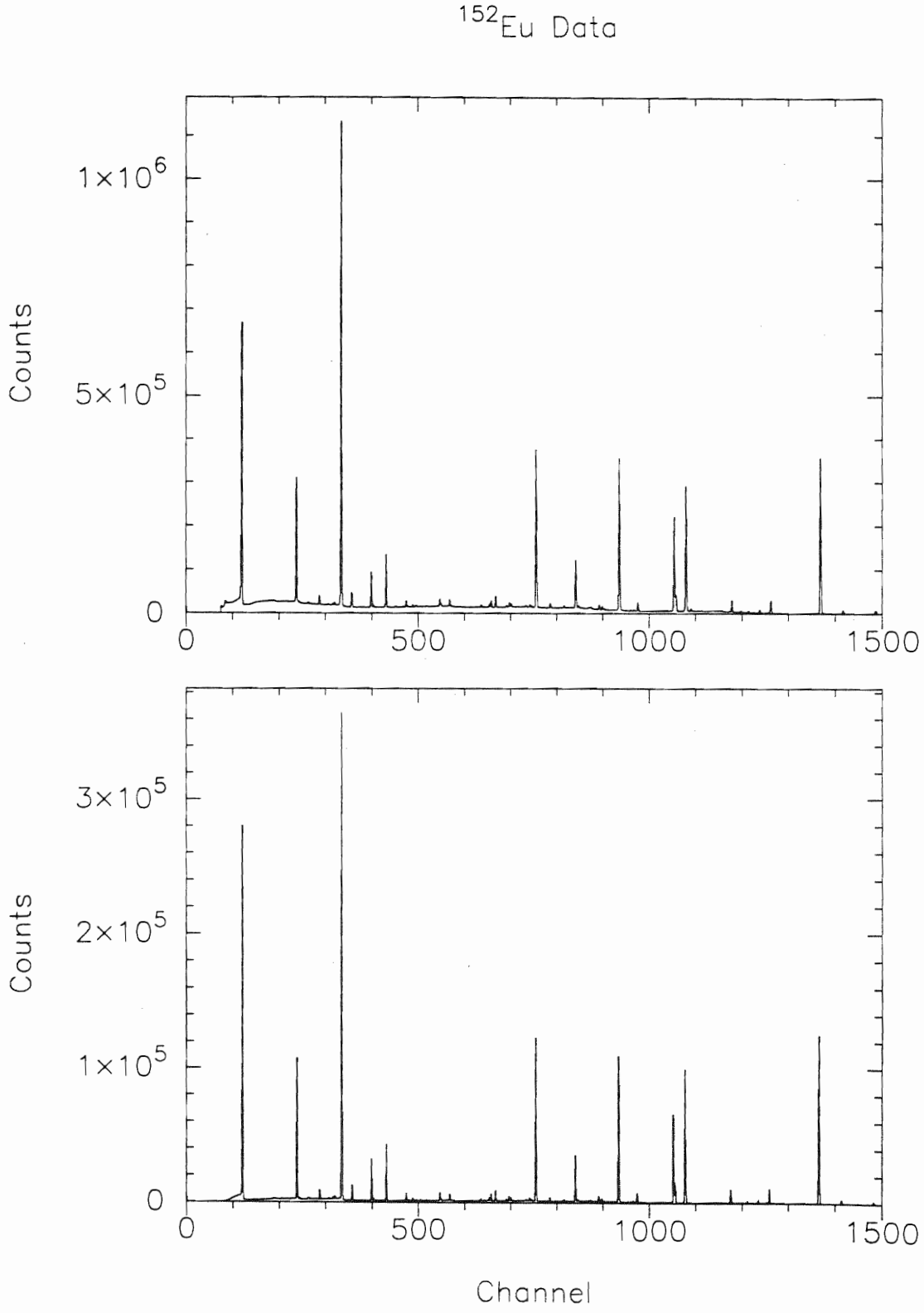
^{152}Eu Data
Counts
1×10^6
5×10^5
0
0
500
1000
1500
Counts
3×10^5
2×10^5
1×10^5
0
0
500
1000
1500
Channel

a nonlinear χ^2 minimization of the functional form to the peak shape and returns the set of parameters that best describe the peak shape. For an energy calibration, the centroid of the peak is the principal quantity of interest, but other quantities are also returned. The ^{152}Eu peaks of interest are fit using GELIFT, and the results are stored in a file (STO file) which contains the energies and areas of the fit peaks.

The formation of the function which expresses the γ-ray energy as a function of the channel number is also a fitting procedure. A second GELIFT program SOURCE is run, which outputs a source intensity (SIN) file that contains the measured intensities of the particular γ-ray source. A third GELIFT program ENCAL uses the output of SOURCE and performs a linear least squares fit of a polynomial (with constant coefficients to be determined by the fit) of order n to the data. The polynomial fitting function can be expressed as:

$$E = \sum_{i=0}^{n} a_i x^i \tag{9.6}$$

where x = channel number. The order n is chosen by the user to yield the best fit of the polynomial to the data. This procedure is followed for both HPGe detectors to yield an energy calibration function for each. A polynomial of fifth order fits the ^{152}Eu data for each detector; the fitting coefficients obtained from the ^{152}Eu data are shown in the first and third columns of Table 9.3. The data points, the energy determined from Equation 9.6 with appropriate coefficients, and the difference between the data points and the energies are displayed in Figure 9.2 for the low energy region of the suppressed HPGe detector. A quantity that we use as a rough indication of the goodness of fit is the mean square deviation of the fit about zero. This quantity is denoted as $\sqrt{<\Delta^2>}$ and is calculated using the expression,

$$\sqrt{<\Delta^2>} = \sqrt{\sum_{j=1}^{N} (E_j - f(x_j))^2} \tag{9.7}$$

TABLE 9.3. ^{152}Eu Energy Calibration Parameters[a]

	Suppressed HPGe		Unsuppressed HPGe	
Order[b]	Low Energy	High Energy	Low Energy	High Energy
0	-0.4417×10^{1}	0.4127×10^{1}	-0.3907×10^{1}	0.8229×10^{1}
1	0.1058×10^{1}	0.1031×10^{1}	0.1059×10^{1}	0.1024×10^{1}
2	-0.5972×10^{-4}	-0.2325×10^{-5}	-0.7325×10^{-4}	-0.1418×10^{-6}
3	0.7303×10^{-7}	0.6013×10^{-9}	0.9377×10^{-7}	0.3542×10^{-10}
4	-0.4457×10^{-10}	-0.6936×10^{-13}	-0.5963×10^{-10}	
5	0.1020×10^{-13}	0.3234×10^{-17}	0.1427×10^{-13}	

[a]The units on each parameter are keV/(channel number)^{i}.

[b]The order i corresponds to the exponent in Equation 9.6.

Figure 9.2 Suppressed HPGe energy calibration fit for ^{152}Eu. (Top) The data points and fit are shown. (Bottom) The difference between the data points and the fit are shown.

^{152}Eu Energy Calibration for Suppressed HPGe

$\langle \Delta^2 \rangle^{1/2} = 0.024$ keV

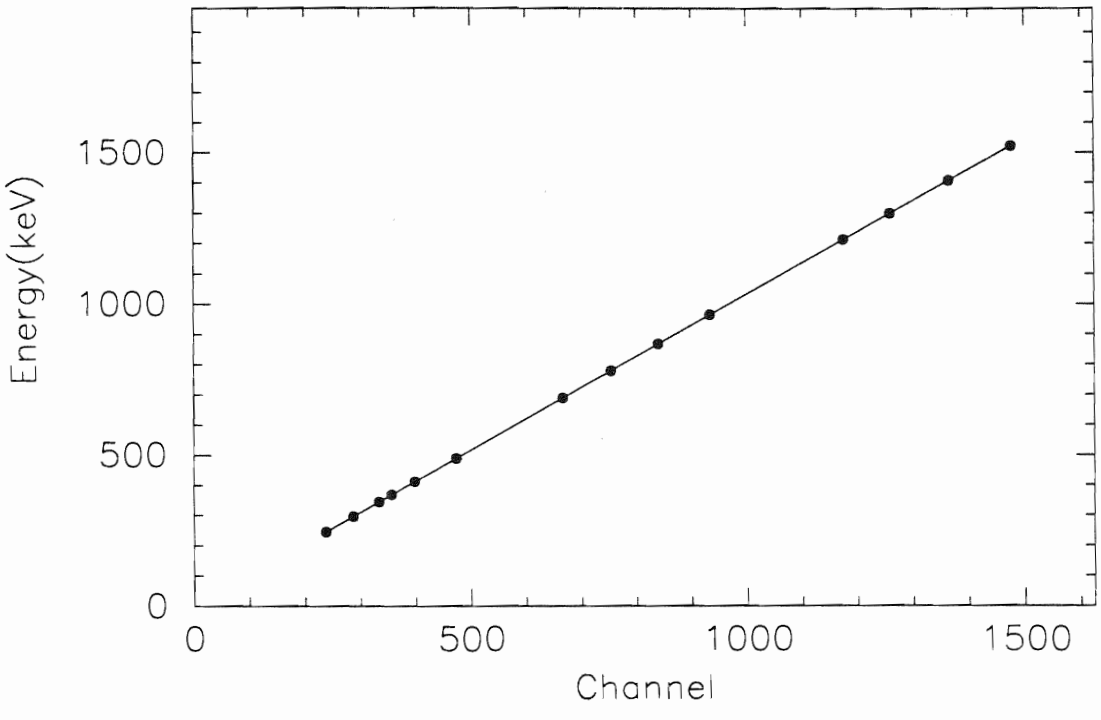

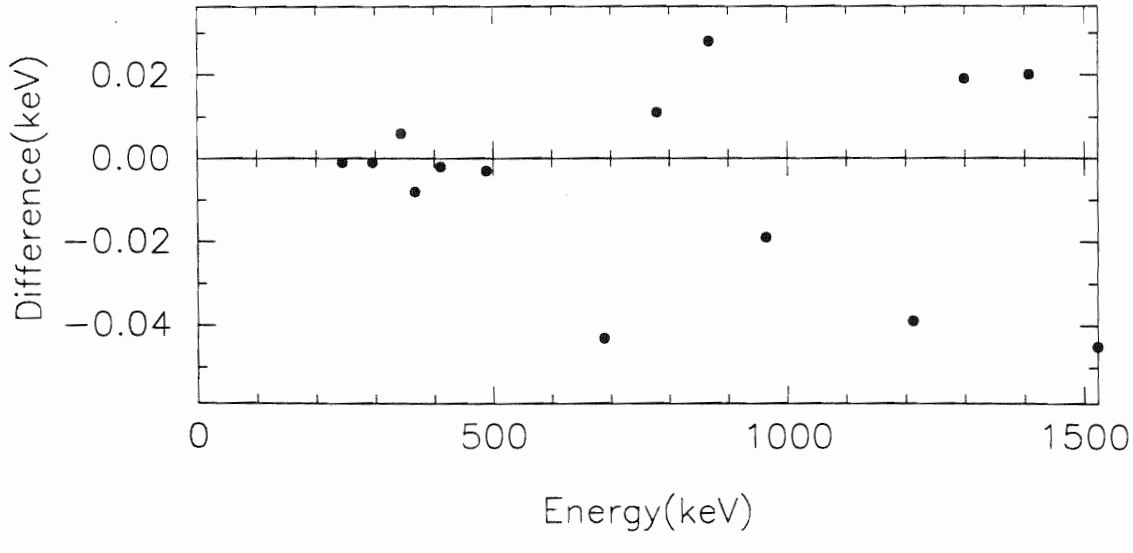

where N = the number of data points, E_j = accepted γ-ray energy, and f(x) = the fitting function evaluated at x. A small value of $\sqrt{<\Delta^2>}$ is desirable since it provides an estimate of the uncertainty on the γ-ray energies.

It is necessary that one have an energy calibration that covers the entire energy range to be studied. The energy calibration from the ^{152}Eu data is used to calibrate up to E_γ = 1522 keV (this number is explained below). For higher energies, another calibration source is needed. No easily obtainable permanent source is available that yields γ-rays of energies up to 8000 keV; therefore, a calibration source for this energy region is produced by an online nuclear reaction. The ^{27}Al(p,γ) reaction has been extensively studied, and the target is easily fabricated. In the decay of the E_p = 0.99186 MeV resonance in ^{27}Al(p,γ), there is a set of γ-rays which are well known and cover a large energy range [End90b]. The γ-rays from the decay of this resonance are used to determine an energy calibration at energies above 1522 keV. In Table 9.4 are listed the γ-ray lines from the decay of ^{28}Si that we use to determine a calibration at high energies. To obtain the ^{27}Al(p,γ) data for an energy calibration, we accumulated data from the ^{27}Al(p,γ) resonance until a total of 10,000 μC of charge had been collected on the Faraday cup. The data are displayed in Figure 9.3 for the high energy region of the suppressed HPGe detector. A procedure similar to that described for the ^{152}Eu calibration analysis is followed. The peaks corresponding to the γ-ray energies listed in Table 9.4 are fit using GELIFT. The program SOURCE is run, followed by ENCAL, which fits the source intensity data to Equation 9.6. The energy calibration fitting coefficients for the ^{28}Si data are listed in columns two and four of Table 9.3, and the calibration fit is shown in Figure 9.4. The energy calibration fit for the suppressed HPGe detector is fifth order; the fit for the unsuppressed HPGe detector is third order. The ^{152}Eu data and the E_p = 0.99186 ^{28}Si resonance data for the unsuppressed HPGe detector are shown in the top portion of Figure 9.1 and in Figure 9.5, respectively. The corresponding energy calibration fits are displayed in Figures 9.6 and 9.7 for the

TABLE 9.4. ^{28}Si Calibration γ-ray Energies[a]

E_γ (keV)	E_γ Error (keV)	Relative Intensity	Relative Intensity Error
1522.81	0.11	2787.	94.
1658.34	0.08	610.	16.
1779.030	0.011	94766.	4.
1873.26	0.19	288.	9.
2838.83	0.04	5598.	4.
3061.82	0.18	1110.	40.
3124.14	0.20	790.	30.
4497.17	0.07	4563.	26.
4607.86	0.17	3960.	120.
4742.30	0.17	8500.	300.
4799.31	0.15	287.	11.
5662.52	0.16	700.	20.
6019.98	0.09	5634.	94.
6265.11	0.16	2150.	70.
6878.79	0.08	498.	8.
7923.45	0.15	4090.	120.
7933.45	0.10	3309.	60.

[a]Information taken from [End90b].

Figure 9.3 Suppressed HPGe ^{28}Si energy calibration data. The data are shown on a logarithmic vertical scale. (Top) The region of the spectrum from channels 1000 to 3400. (Center) The region of the spectrum from channels 3400 to 5800. (Bottom) The region of the spectrum from channels 5800 to 8200.

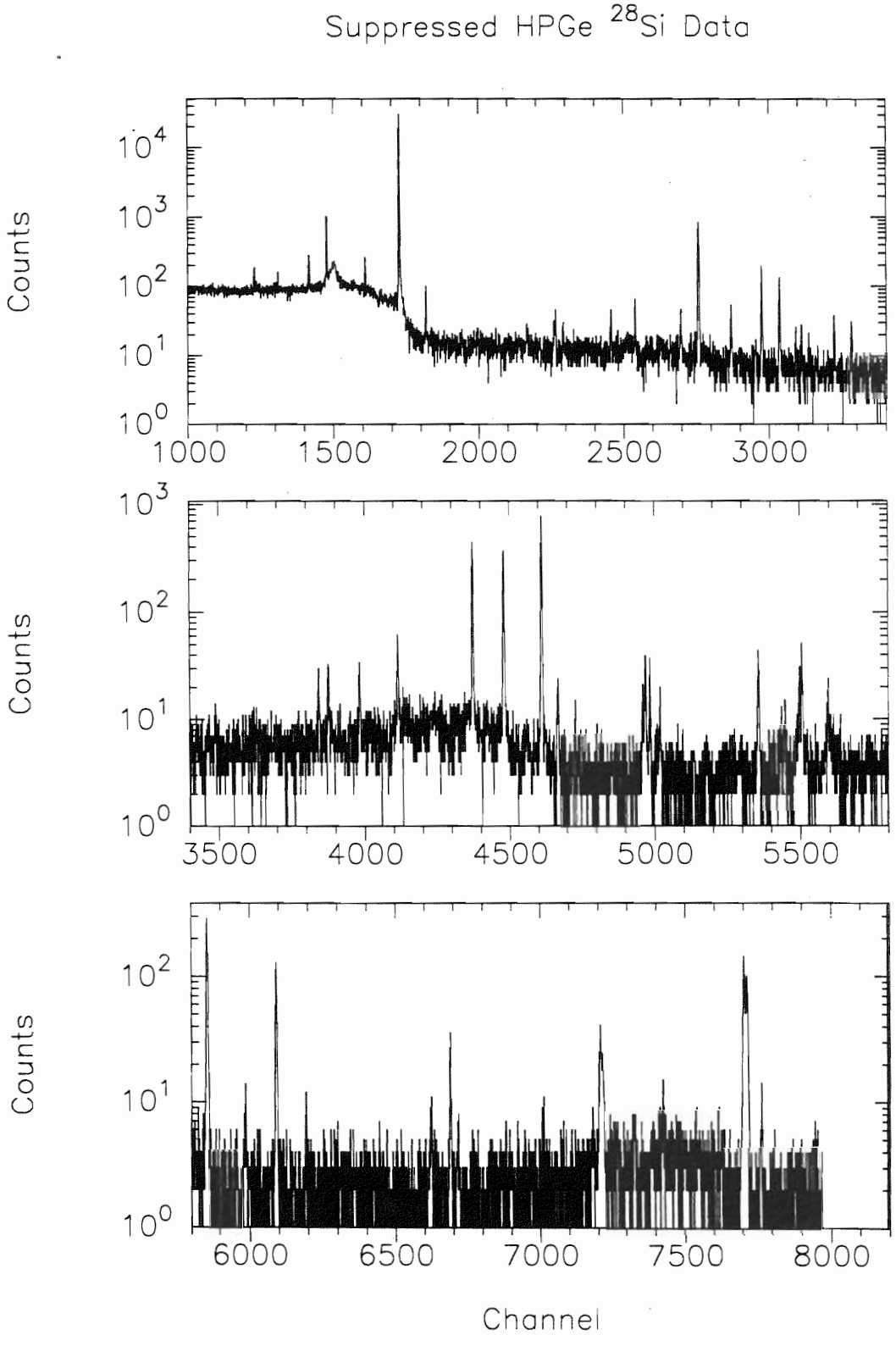
Suppressed HPGe ^{28}Si Data
Counts
10^4
10^3
10^2
10^1
10^0
1000
1500
2000
2500
3000
Counts
10^3
10^2
10^1
10^0
3500
4000
4500
5000
5500
Counts
10^2
10^1
10^0
6000
6500
7000
7500
8000
Channel

Figure 9.4 Suppressed HPGe energy calibration fit for ^{28}Si. (Top) The data points and fit are shown. (Bottom) The difference between the data points and the fit are shown.

^{28}Si Energy Calibration for Suppressed HPGe

$\langle \Delta^2 \rangle^{1/2}$ = 0.209 keV

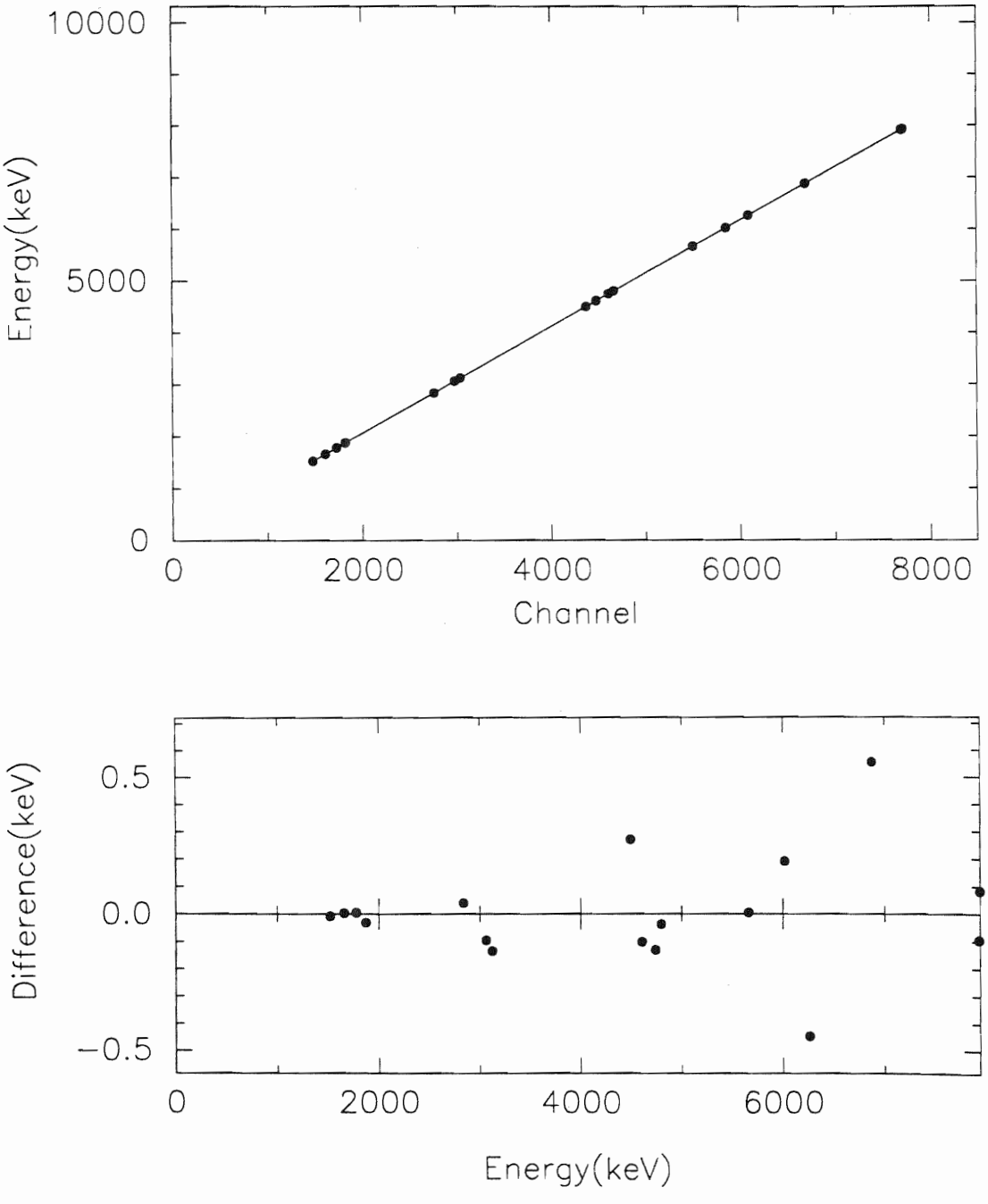

Figure 9.5 Unsuppressed HPGe ^{28}Si energy calibration data. The data are shown on a logarithmic vertical scale. (Top) The region of the spectrum from channels 1000 to 3400. (Center) The region of the spectrum from channels 3400 to 5800. (Bottom) The region of the spectrum from channels 5800 to 8200.

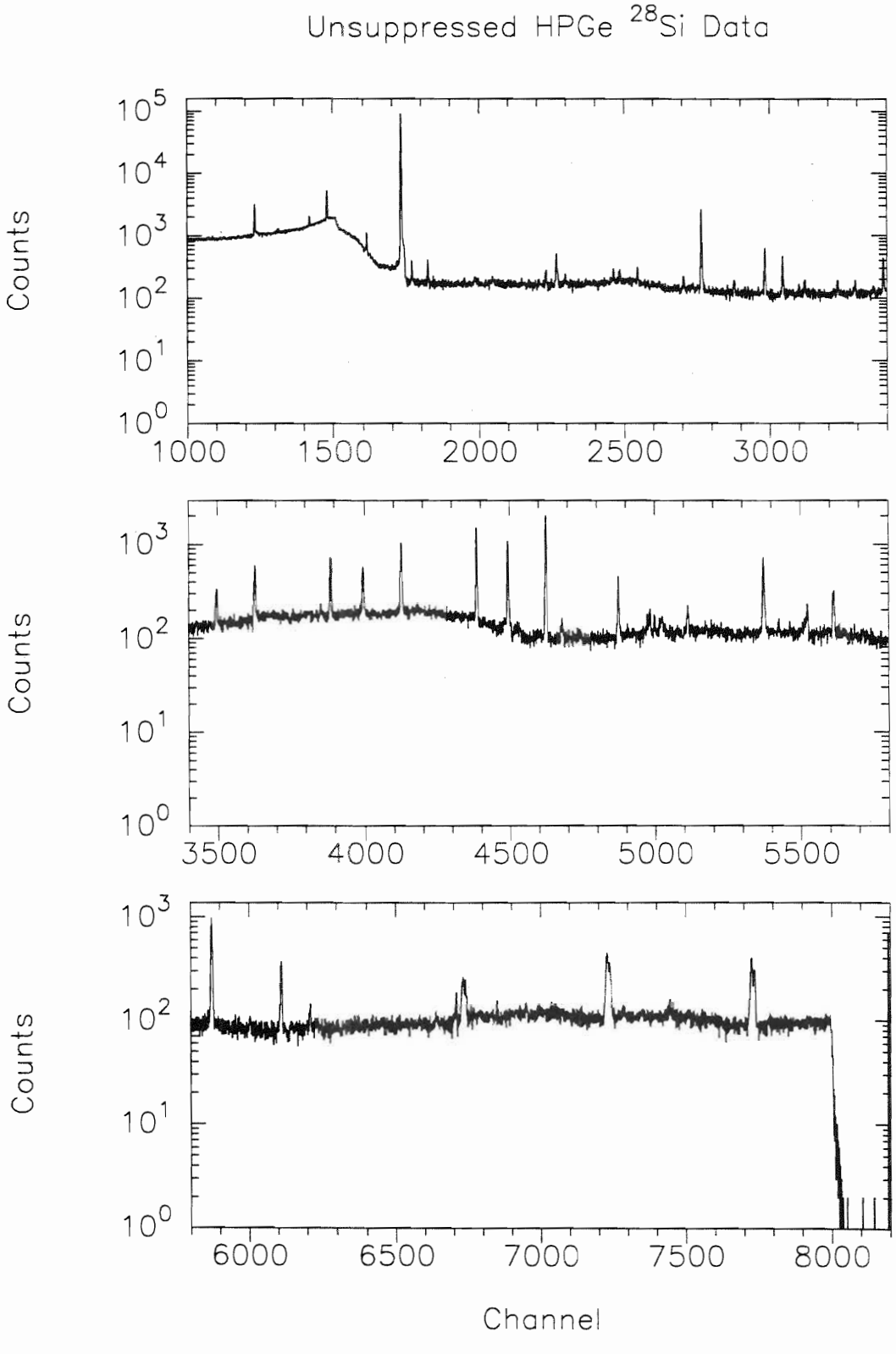
Unsuppressed HPGe ^{28}Si Data
Counts
10^5
10^4
10^3
10^2
10^1
10^0
1000
1500
2000
2500
3000
Counts
10^3
10^2
10^1
10^0
3500
4000
4500
5000
5500
Counts
10^3
10^2
10^1
10^0
6000
6500
7000
7500
8000
Channel

Figure 9.6 Unsuppressed HPGe energy calibration fit for ^{152}Eu. (Top) The data points and fit are shown. (Bottom) The difference between the data points and the fit are shown.

^{152}Eu Energy Calibration for Unsuppressed HPGe

$\langle \Delta^2 \rangle^{1/2} = 0.037$ keV

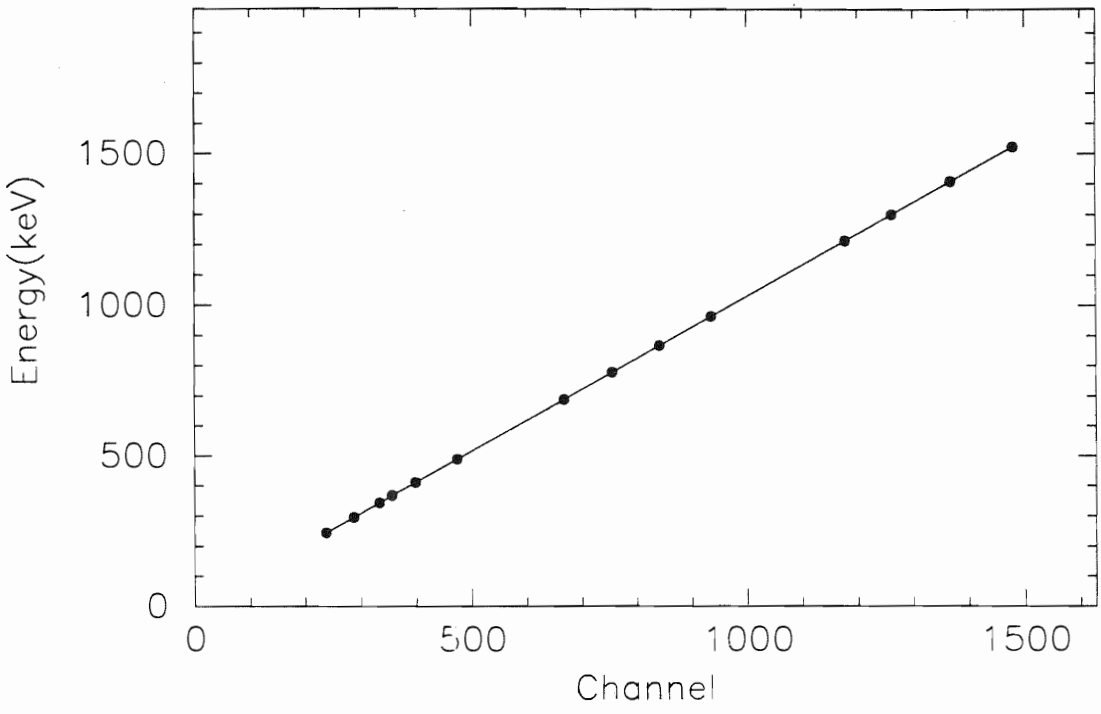

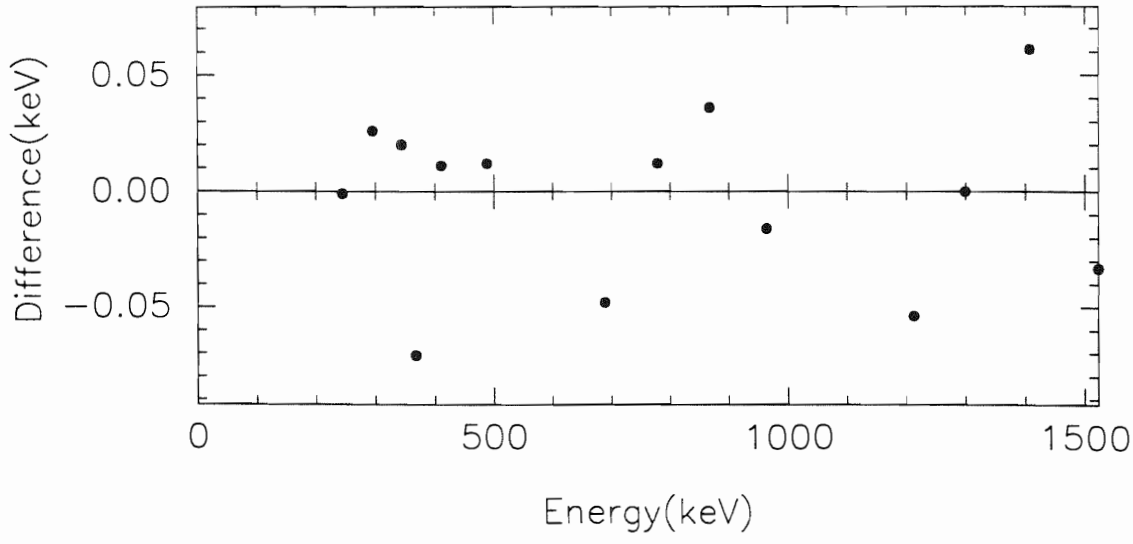

Figure 9.7 Unsuppressed HPGe energy calibration fit for ^{28}Si. (Top) The data points and fit are shown. (Bottom) The difference between the data points and the fit are shown.

^{28}Si Energy Calibration for Unsuppressed HPGe

$\langle \Delta^2 \rangle^{1/2} = 0.162$ keV

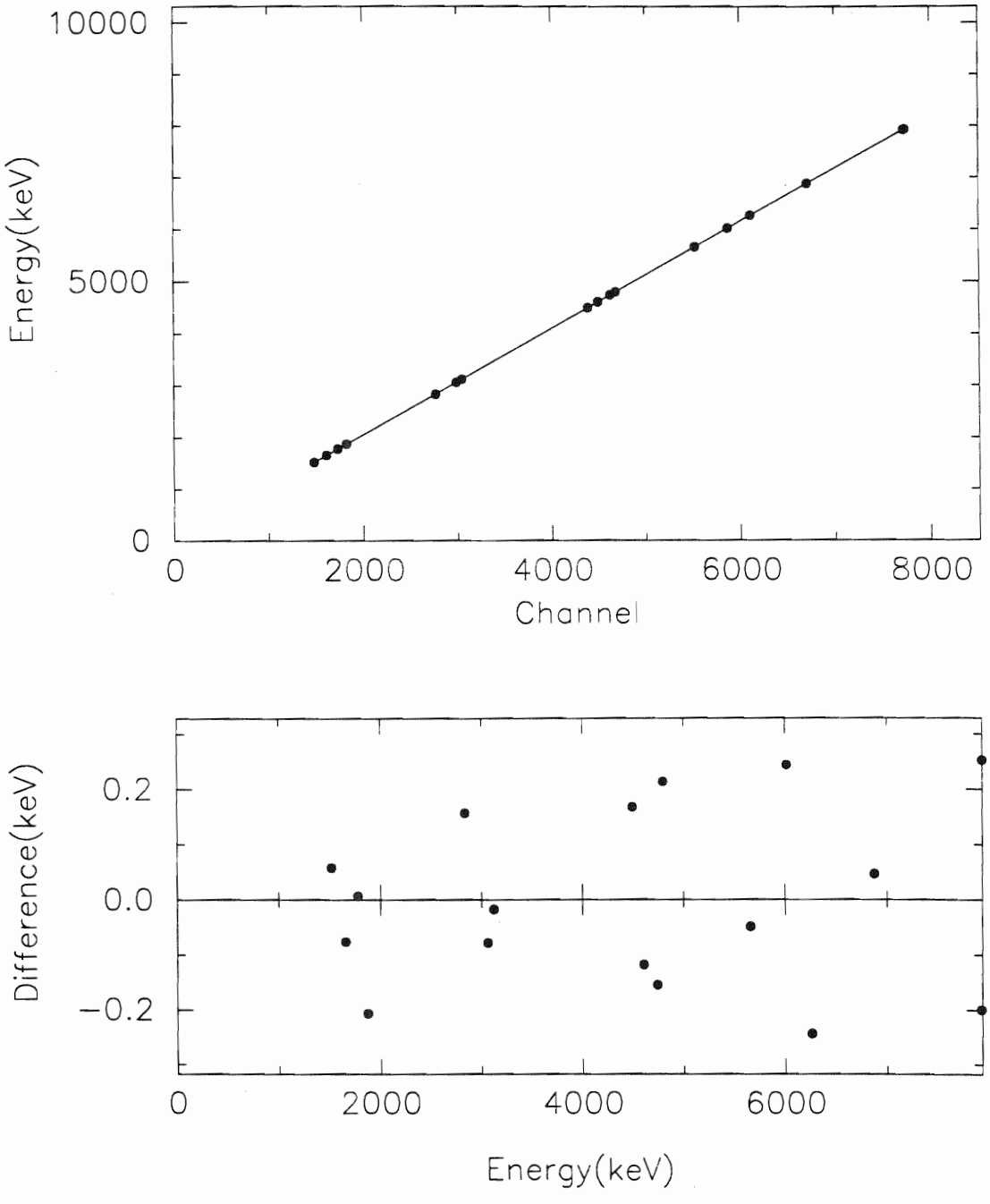

low and high energy regions of the unsuppressed HPGe detector.

The values of $\sqrt{<\Delta^2>}$ indicate that the two separate energy calibrations well characterize their respective regions — ^{152}Eu for $E_\gamma < 1522$ keV and the $E_p = 0.99186$ ^{27}Al(p,γ) resonance for $E_\gamma > 1522$ keV. As shown in Tables 9.2 and 9.4, the highest energy γ-ray used from the ^{152}Eu source is 1408 keV, and the lowest energy γ-ray used from the $E_p = 0.99186$ ^{27}Al(p,γ) resonance is 1522 keV. There is a region between these energies in which it is unclear what the calibration parameters should be. We chose to form the calibration for this region by requiring that the known energy calibration functions for the two regions must meet in such a way to produce a small error on the energies in this middle region. The method which we adopted to accomplish this was to add the first point from the ^{28}Si data set to the ^{152}Eu data set and perform the energy calibration with the modified ^{152}Eu data set. This procedure forced the two fitting functions to approach smoothly the data point with energy 1522 keV and satisfied the requirement. As a check of the procedure, the calibration from both the ^{152}Eu data and the ^{28}Si data was used to determine the energy of both the 1408 keV peak and the 1522 keV peak. The resulting energies, as determined from each calibration, should be close to one another and close to the accepted value. For the 1408 keV γ-ray in ^{152}Eu, this modified calibration procedure yields, for the suppressed (unsuppressed) HPGe detector, γ-ray energies that differ from the accepted value by $\leq$ 76 eV (450 eV) and differ from one another by $\leq$ 60 eV (390 eV). For the 1522 keV γ-ray in ^{152}Eu, this modified calibration procedure yields, for the suppressed (unsuppressed) HPGe detector, γ-ray energies that differ from the accepted value by $\leq$ 45 eV (59 eV) and differ from one another by $\leq$ 40 eV (90 eV). Agreement of $<$ 100 eV is considered satisfactory. The only questionable energy determination is the 1408 keV γ-ray energy as measured using the high energy calibration; the difference is too large, being $\approx$ 450 eV. This circumstance was considered acceptable since the ^{28}Si calibration covers the region $1522 < E_\gamma < 8000$ keV; therefore, the 1408 keV γ-ray

line would never be determined using the high energy calibration.

9.3.2 Efficiency Calibration

The efficiency calibration is performed by using EFFIT, another program in the GELIFT package. EFFIT performs a fit of the data contained in a SIN file to a specified functional form which mimics the behavior of the detector efficiency ξ as a function of energy E_γ. An accepted form for the functional variation of efficiency as a function of energy for Ge detectors is

$$\ln \xi = \left\{ [A + Bu + Cu^2]^{-G} + [D + Ev + Fv^2]^{-G} \right\}^{\frac{-1}{G}} \tag{9.8}$$

where u $= \ln\left(\frac{E_\gamma}{100}\right)$, v $= \ln\left(\frac{E_\gamma}{1000}\right)$, and E_γ is expressed in keV. A discussion of Equation 9.8 and the parameters in it is given by Radford [Rad89]. The seven parameters A - G are determined by performing a nonlinear least squares fit of Equation 9.8 to the data points in the SIN file. Although the data for the efficiency calibration is taken in two parts (like the energy calibration), a single efficiency calibration function is formed to cover the entire range. The ^{152}Eu data used for the energy calibration is combined with a set of ^{28}Si data (100,000 μC beam collected on the Faraday cup) taken with the suppressed HPGe detector positioned at 55° with respect to the beam direction. Since this was the orientation of the suppressed HPGe detector for the accumulation of the ^{30}P data, it is necessary that the efficiency calibration be performed with the detector in the same orientation. The unsuppressed HPGe detector was positioned at 90° throughout these experiments as well as all calibration measurements. The efficiency calibration parameters for both HPGe detectors are shown in Table 9.5. The efficiency fits are shown for both HPGe detectors in Figures 9.8 and 9.9. The value of the average deviation is used (as for the energy calibration) to indicate the goodness of fit; a value less than 5% is considered acceptable.

TABLE 9.5. Efficiency calibration parameters

Parameter[a]	Suppressed HPGe	Unsuppressed HPGe
A	1.188	6.015
B	3.669	3.699
C[b]	0.000	0.000
D	3.553	4.919
E	−0.571	−0.775
F	−0.137	−0.107
G	10.000[b]	2.561

[a]Parameter labels follow the designation of Equation 9.5.

[b]Parameter value is held fixed.

Figure 9.8 Suppressed HPGe efficiency calibration fit. (Top) The data points and fit are shown. (Bottom) The difference between the data points and the fit are shown.

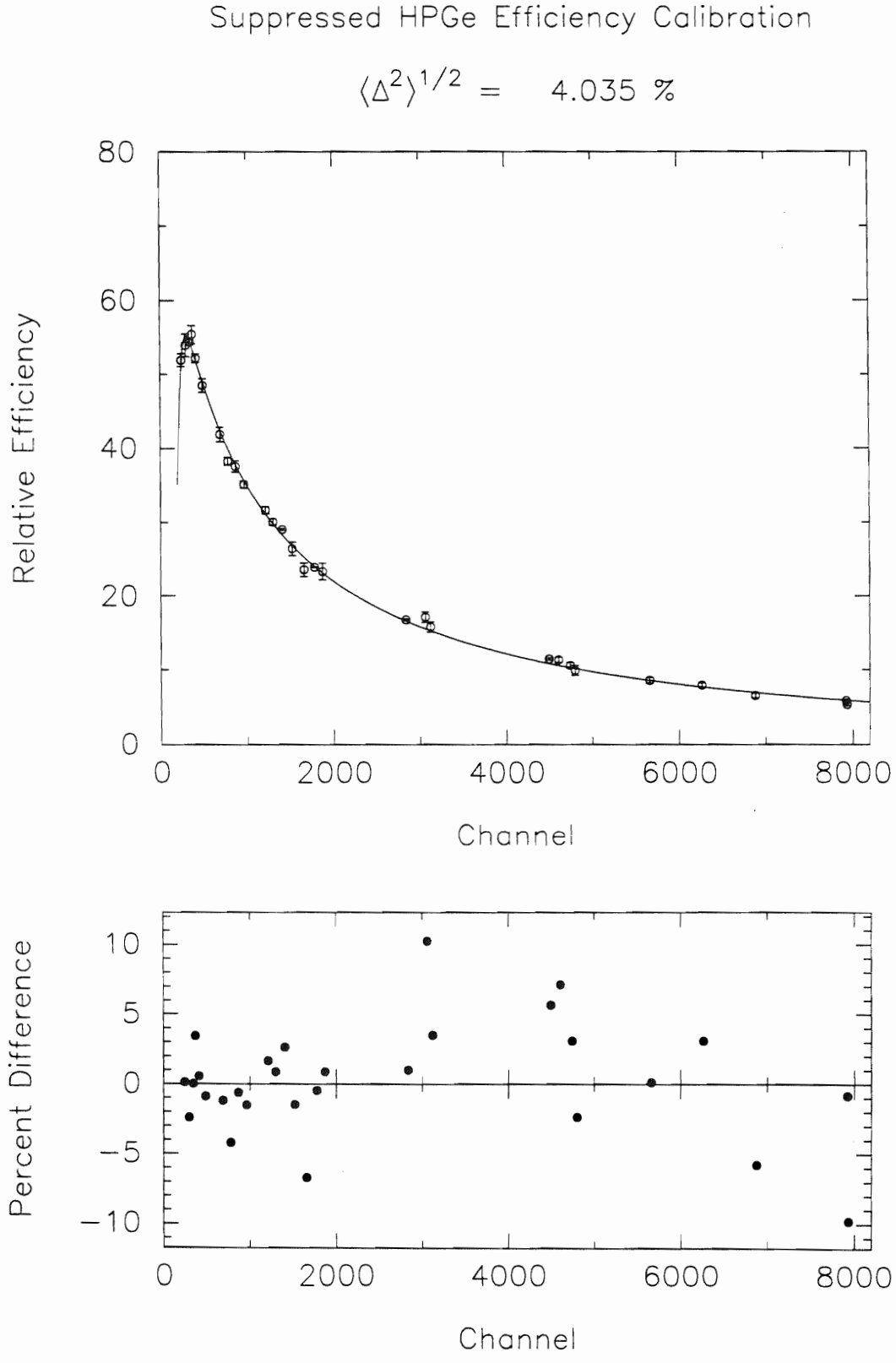
Suppressed HPGe Efficiency Calibration
$\langle \Delta^2 \rangle^{1/2}$ = 4.035 %
Relative Efficiency
0
20
40
60
80
0
2000
4000
6000
8000
Channel
Percent Difference
10
5
0
−5
−10
0
2000
4000
6000
8000
Channel

Figure 9.9 Unsuppressed HPGe efficiency calibration fit. (Top) The data points and fit are shown. (Bottom) The difference between the data points and the fit are shown.

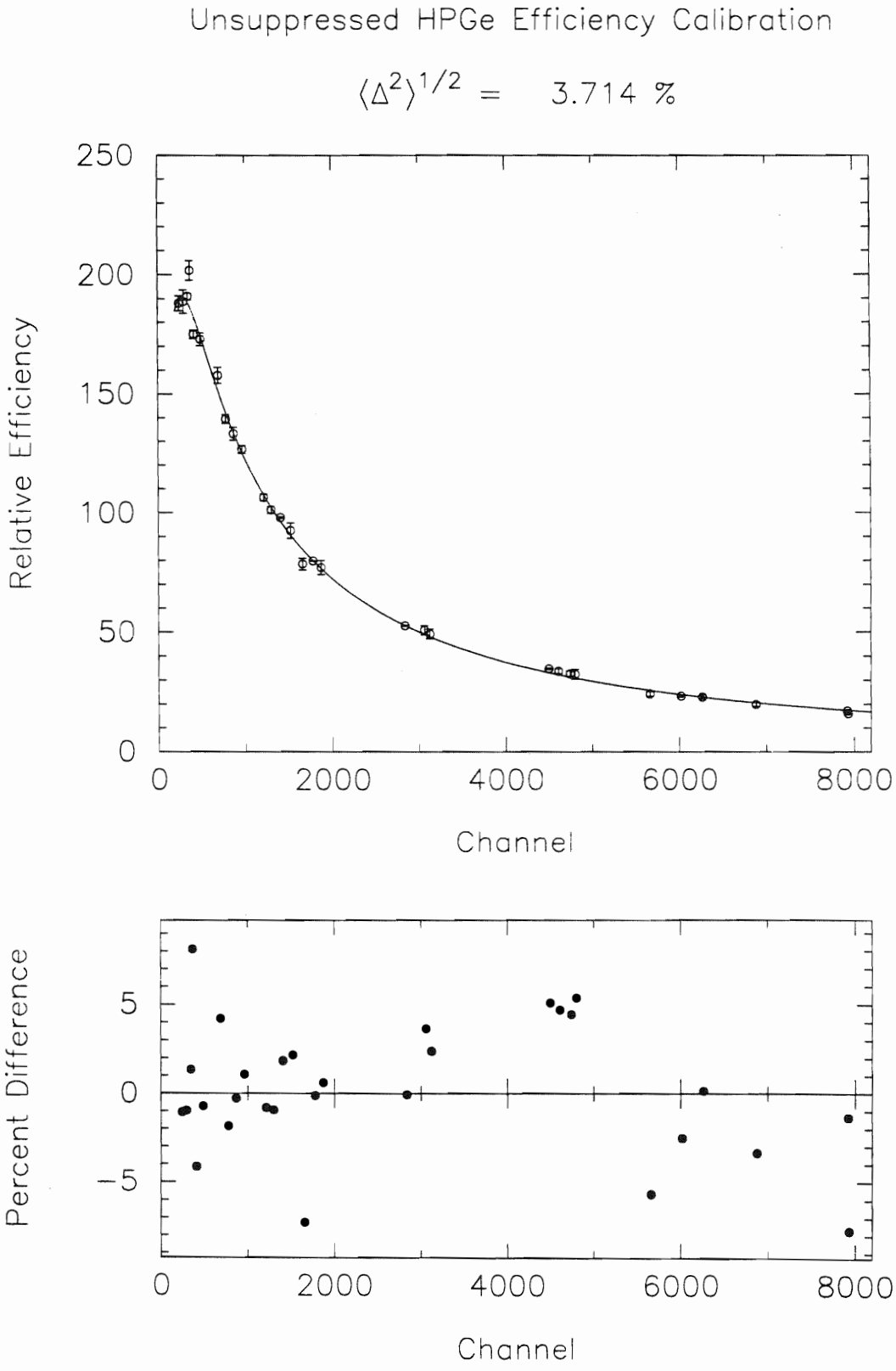
Unsuppressed HPGe Efficiency Calibration
$\langle \Delta^2 \rangle^{1/2}$ = 3.714 %
Relative Efficiency
250
200
150
100
50
0
0
2000
4000
6000
8000
Channel
Percent Difference
5
0
−5
0
2000
4000
6000
8000
Channel

9.4 E_x = 7752.7 keV ^{30}P Resonance Analysis

After the calibration measurements were completed, data were taken on selected resonances in ^{30}P. Background data were taken in order to permit identification of γ-rays not originating from population of the ^{30}P resonance. The HPGe detectors were positioned as in Figure 8.2, with the suppressed detector and suppressor at 55° with respect to the beam direction and the unsuppressed detector at 90° with respect to the beam direction. All ^{30}P data were taken with the HPGe detectors oriented in this configuration. In each case, GELIFT was used to fit the resulting γ-ray peaks in the suppressed HPGe detector. Subsequently, the peaks in the unsuppressed HPGe detector that correspond to those in the suppressed detector were fit. The former information yields intensity information; the latter yields energy information. Since $\theta = 55°$ is a zero of $P_2(\cos\theta)$, which is generally the largest non-constant term in the functional variation of the angular distribution, the undesirable angular distribution effects are minimized. Whenever possible, the energy of a particular γ-ray was taken from the unsuppressed HPGe detector since there is no Doppler shift at 90°.

One of the resonances studied was quoted previously as having excitation energy $E_x = 7759.6$ keV, $J^\pi = (3-5)^+$, and $T = 1$ [Fra91]. Data were collected both on-resonance and off-resonance until 220.000 μC of charge were accumulated; the off-resonance data were taken 2 keV higher than the resonance energy. The data accumulated in the suppressed and the unsuppressed HPGe detectors are shown in Figures 9.10 and 9.11, respectively. The γ-ray lines in the resulting spectra were fit with GELIFT, using the appropriate energy calibration. Based on the presence of the γ-ray (room background, off-resonance, or on-resonance), its energy, and its intensity, assignments were made as to the source of the γ-ray. One quantity which is useful in the determination of the correctness of γ-ray assignments is the intensity balance for a given level. The sum of the intensities of all γ-rays which feed a level

Figure 9.10 Suppressed HPGe $E_x = 7752.7$ keV ^{30}P data

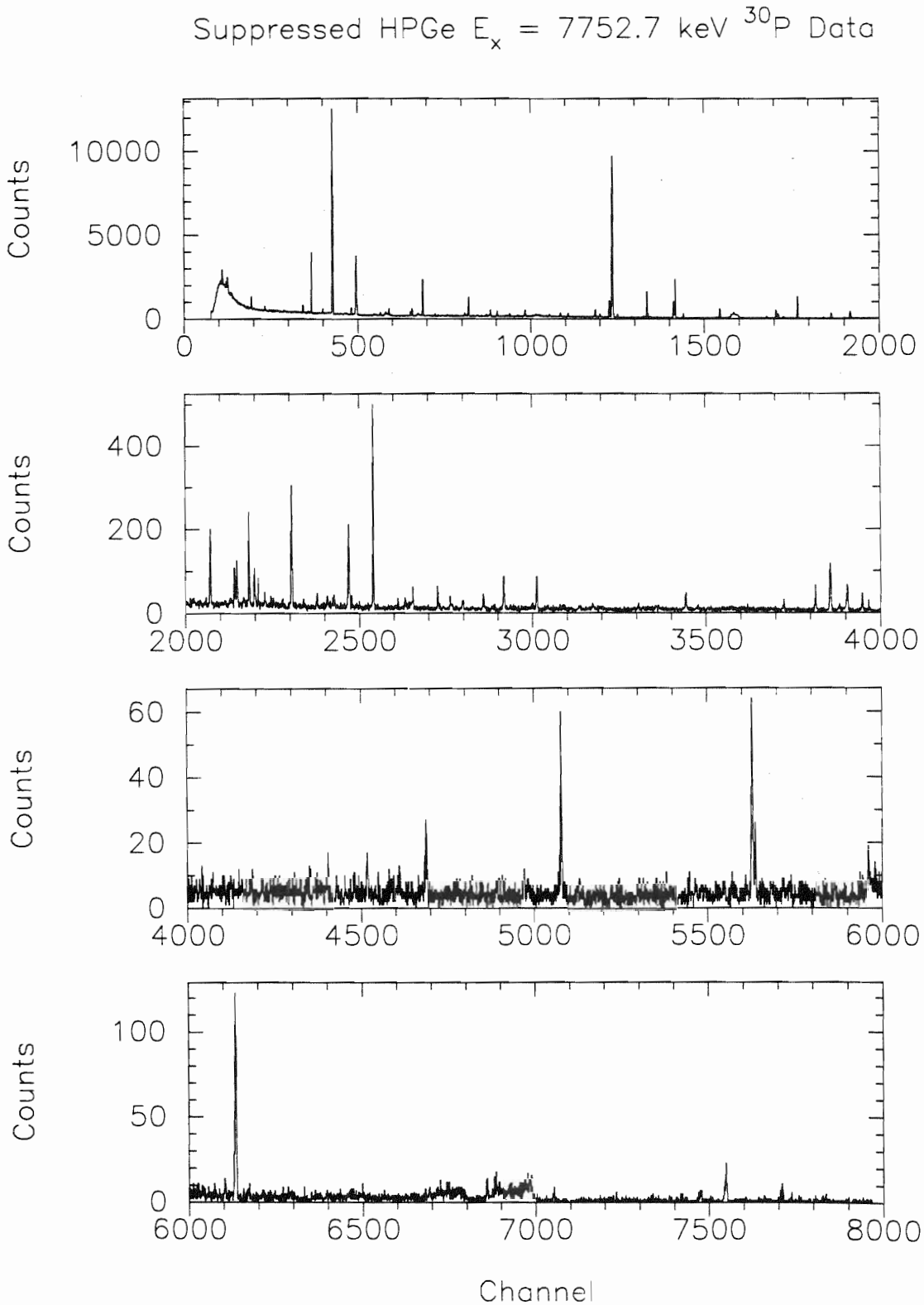
Suppressed HPGe E_x = 7752.7 keV ^{30}P Data
Counts
10000
5000
0
0
500
1000
1500
2000
Counts
400
200
0
2000
2500
3000
3500
4000
Counts
60
40
20
0
4000
4500
5000
5500
6000
Counts
100
50
0
6000
6500
7000
7500
8000
Channel

Figure 9.11 Unsuppressed HPGe $E_x = 7752.7$ keV ^{30}P data

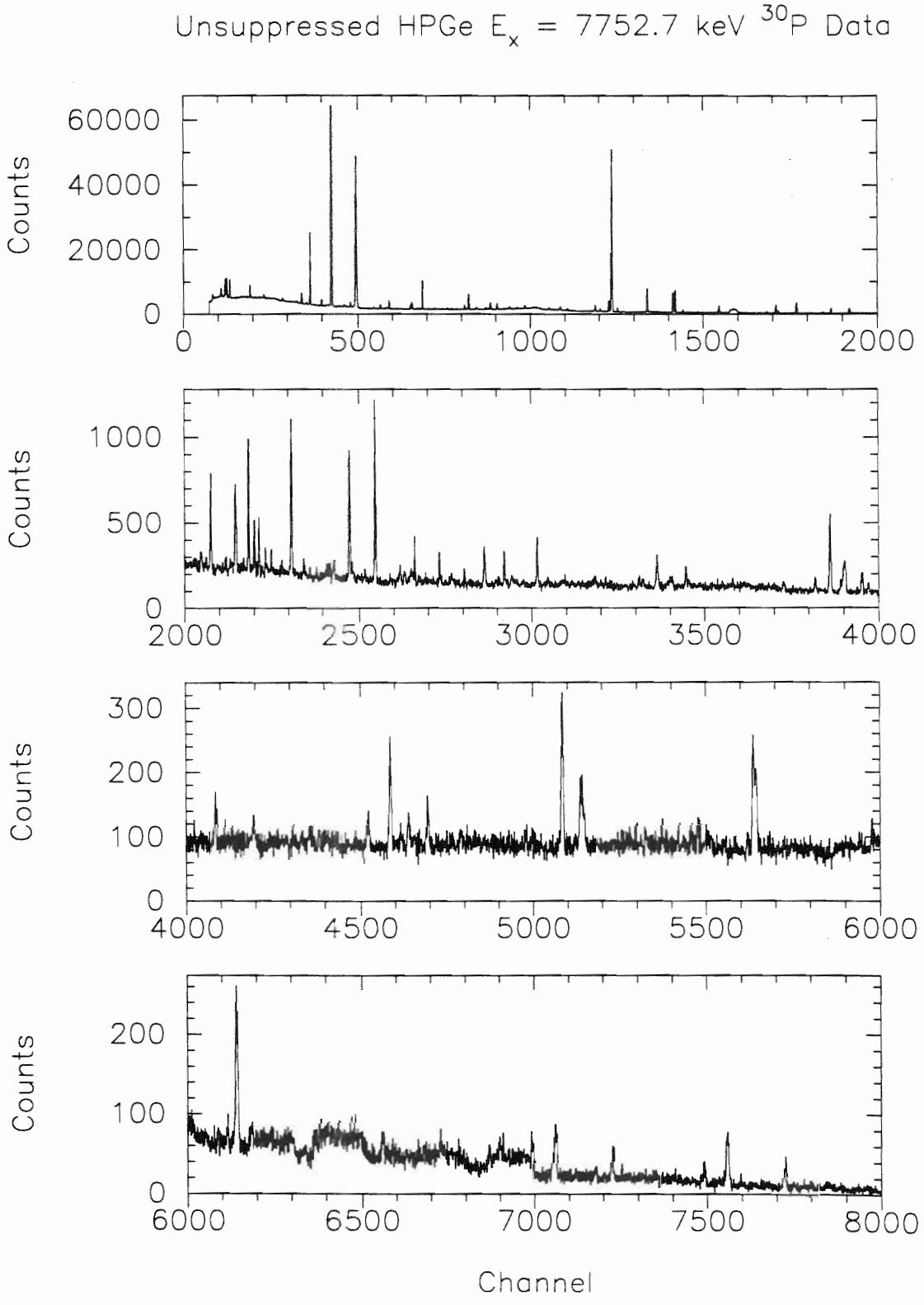
Unsuppressed HPGe E_x = 7752.7 keV ^{30}P Data
Counts
60000
40000
20000
0
0
500
1000
1500
2000
Counts
1000
500
0
2000
2500
3000
3500
4000
Counts
300
200
100
0
4000
4500
5000
5500
6000
Counts
200
100
0
6000
6500
7000
7500
8000
Channel

should equal the sum of the intensities of all γ-rays which decay from the same level. An intensity balance significantly different from zero signifies a questionable γ-ray assignment. In Table 9.6 is shown the γ-ray information that was obtained from fitting the various peaks in Figures 9.10 and 9.11; this table is included as an illustration of the information obtained from a single resonance. Assignments are listed if they are known. Based on the energy calibrations (Figures 9.6 and 9.7), the error on E_γ is estimated to be 0.2 keV (0.4 keV) if $E_\gamma < (>)$ 1522 keV. The intensity I_γ for a given gamma-ray is obtained in a two step process. When the peak is fit, an area A_γ and corresponding statistical uncertainty σ_{A_γ} are determined by GELIFT. The γ-ray intensity shown in Table 9.6 is obtained by scaling each individual area by the largest area A_L; the uncertainty on the γ-ray intensity is also obtained by scaling the statistical uncertainty by A_L. The γ-ray peak with the largest area is from the ^{29}Si(p,pγ)^{29}Si reaction. Thus, $I_\gamma = 100\frac{A_\gamma}{A_L}$, and $\sigma_{I_\gamma} = 100\frac{\sigma_{A_\gamma}}{A_L}$.

The region of channels from 6000 to 7000, in both the suppressed and unsuppressed HPGe detectors, is highly irregular. The strange spectrum behavior is due to contamination from fluorine; similar spectra have been seen in other studies [Bar94]. Fluorine is used in several stages of the production of the carbon foils on which our targets are deposited. It is believed that no information for this resonance has been lost due to the fluorine contamination.

A transition from the resonance level to another level ($E_x = E_L$) is termed a primary transition, and a transition from E_L to a lower state is termed a secondary transition. A total of ten primary transitions were identified from the analysis of the data from the $E_x = 7752.7$ keV resonance. The energies in ^{30}P determined from this study and the corresponding energies quoted from Endt [End90a] are shown in Table 9.7 for comparison. The decay from a given level reaches the state $E_x = 0$ by a number of transition paths, say k in number; from these paths, a set of k energies and uncertainties for the level can be calculated. The level energies quoted in the left column of Table 9.7 are obtained by averaging the resulting k values of energy.

TABLE 9.6. $E_x = 7752.7$ keV ^{30}P γ-ray information

E_γ[a] (keV)	I_γ	σ_{I_γ}	E_i (keV)	E_f (keV)	Assigned Nucleus
109.9	20.3	1.7	109.9	0.0	^{19}F
122.0[b]	9.6	1.3			
126.3	18.8	1.2	127.2	0.0	^{56}Fe
197.1	3.26	0.17	197.2	0.0	^{19}F
238.5	0.740	0.086	238.6	0.0	^{212}Bi
295.1	0.36	0.10	295.2	0.0	^{214}Bi
352.0	1.273	0.091	351.9	0.0	^{214}Bi
377.4	9.05	0.16	377.9	0.0	^{52}Cr
411.3[c]	0.831	0.083			
439.7	46.43	0.35	439.9	0.0	^{23}Na
495.0	1.129	0.085	495.3	0.0	^{17}F
563.9	0.310	0.067	564.1	0.0	^{53}Cr
569.0	0.46	0.10	569.65	0.0	^{207}Pb
582.9	0.556	0.073	3197.7	2614.5	^{208}Pb
599.1[c]	1.60	0.14			
604.6[c]	0.69	0.12			
608.9	1.337	0.088	609.3	0.0	^{214}Bi
673.1	0.770	0.076	673.4	0.0	^{57}Co
676.9	1.567	0.092	677.29	0.0	^{30}P
708.6	8.44	0.18	709.02	0.0	^{30}P
745.1	0.42	0.21	1454.67	709.02	^{30}P
754.9[c]	0.192	0.072			
768.1	0.171	0.066	1377.68	609.3	^{214}Bi
783.1[c]	0.401	0.089			
834.5[b]	0.590	0.082			

Table 9.6 (continued)

E_γ[a] (keV)	I_γ	σ_{I_γ}	E_i (keV)	E_f (keV)	Assigned Nucleus
843.9	0.726	0.069	843.8	0.0	^{27}Al
846.4	4.40	0.14	846.8	0.0	^{56}Fe
860.9	0.177	0.072	3475.0	2614.5	^{208}Tl
870.0	0.71	0.11	870.8	0.0	^{17}O
897.8	0.622	0.064	3835.9	2937.87	^{30}P
906.2[d]	0.473	0.060			
911.3	1.950	0.098	968.8	57.8	^{228}Ac
931.1	1.472	0.085	931.3	0.0	^{55}Fe
959.6[d]	0.255	0.064			
964.1	0.221	0.073	1022.4	57.8	^{228}Ac
968.8	0.701	0.082	968.8	0.0	^{228}Ac
990.8	0.380	0.083	3928.9	2937.87	^{30}P
1014.1	2.25	0.12	1014.4	0.0	^{27}Al
1037.8[c]	0.287	0.091			
1046.3[c]	0.59	0.12			
1087.6	0.521	0.080	3122.9	2085.03	^{56}Fe
1118.4	1.38	0.11	1729.61	609.31	^{214}Bi
1140.7[d]	1.015	0.095			
1223.3	2.12	0.12	1224.0	0.0	^{56}Fe
1237.5	0.951	0.092	1847.4	609.31	^{214}Bi
1264.2	7.60	0.20	1973.62	709.02	^{30}P
1272.7	100.00	0.66	1273.3	0.0	^{29}Si
1289.0	1.179	0.095	1289.7	0.0	^{53}Mn
1368.8	0.584	0.083	1368.7	0.0	^{23}Na

Table 9.6 (continued)

E_γ[a] (keV)	I_γ	σ_{I_γ}	E_i (keV)	E_f (keV)	Assigned Nucleus
1377.0	9.39	0.22	1377.68	0.0	^{56}Fe
1384.5	0.271	0.057	2839.9	1454.67	^{30}P
1454.0	8.48	0.22	1454.67	0.0	^{30}P
1460.3	15.16	0.28	1460.8	0.0	^{40}K
1482.8	1.59	0.11	2937.87	1454.67	^{30}P
1508.0	0.252	0.072	2118.55	609.31	^{214}Bi
1528.8[c]	0.231	0.063			
1590.0	4.41	0.17	5933.6	4343.6	^{30}P
1625.2[c]	2.69	0.42			
1632.8	6.43	0.35	1633.8	0.0	^{20}Ne
1640.1[c]	4.62	0.23			
1730.1	0.821	0.088	1729.61	0.0	^{214}Bi
1757.3	4.05	0.16	1757.6	0.0	^{56}Fe
1764.2	2.10	0.12	1764.51	0.0	^{214}Bi
1779.2	0.828	0.086	1778.8	0.0	^{28}Si
1818.1	11.14	0.25	7752.7	5933.6	^{30}P
1896.9	0.768	0.088	1897.4	0.0	^{56}Fe
1919.2	3.34	0.15	1919.6	0.0	^{56}Fe
1958.2[c]	0.300	0.076			
1964.8[d]	0.211	0.063			
1973.3	5.42	0.19	1973.62	0.0	^{30}P
1998.5[d]	0.154	0.053			
2011.2[d]	0.116	0.050			
2028.3	0.199	0.057	2539.03	0.0	^{30}P

Table 9.6 (continued)

E_γ[a] (keV)	I_γ	σ_{I_γ}	E_i (keV)	E_f (keV)	Assigned Nucleus
2117.9	0.107	0.051	2118.55	0.0	^{214}Bi
2132.3	1.194	0.057	2839.9	709.02	^{30}P
2205.0	0.900	0.095	2204.09	0.0	^{214}Bi
2211.4[d]	1.19	0.11			
2228.5	0.195	0.073	2937.87	709.02	^{30}P
2243.6	2.26	0.13	7752.7	5508.6	^{30}P
2260.2	1.21	0.11	2937.87	677.29	^{30}P
2274.1	0.593	0.082	2273.8	0.0	^{52}Cr
2293.1	0.351	0.075	2293.4	0.0	^{214}Bi
2310.6	0.173	0.059	2686.5	377.9	^{52}Cr
2318.8[d]	0.145	0.051			
2341.9[d]	0.178	0.060			
2370.3	4.64	0.19	4343.6	1973.62	^{30}P
2384.3	0.101	0.053	3835.9	1454.67	^{30}P
2406.9	0.203	0.057	2407.0	0.0	^{52}Cr
2447.3	0.375	0.075	2447.72	0.0	^{214}Bi
2476.9	0.366	0.079	2478.2	0.0	^{56}Fe
2496.7	0.51	0.10	2875.6	377.8	^{52}Cr
2538.8	3.62	0.17	2539.03	0.0	^{30}P
2546.5[d]	0.259	0.064			
2614.2	6.29	0.22	2614.6	0.0	^{208}Tl
2687.1	0.262	0.067	2686.5	0.0	^{52}Cr
2709.3[c]	0.452	0.072			
2719.5	0.180	0.045	3096.9	377.9	^{52}Cr

Table 9.6 (continued)

E_γ[a] (keV)	I_γ	σ_{I_γ}	E_i (keV)	E_f (keV)	Assigned Nucleus
2728.1[c]	0.57	0.10			
2730.7	0.464	0.076	2730.9	0.0	^{56}Fe
2804.1	0.631	0.088	3181.9	377.9	^{52}Cr
2812.0[c]	0.092	0.041			
2821.4[c]	0.186	0.075			
2840.2	0.303	0.088	2839.9	0.0	^{30}P
2846.6[c]	0.33	0.11			
2878.5	0.437	0.085	2879.1	0.0	^{56}Fe
2937.7	0.724	0.097	2937.87	0.0	^{30}P
2996.4	1.51	0.13	5933.6	2937.87	^{30}P
3087.3[d]	0.140	0.056			
3094.4	1.40	0.13	5933.6	2839.9	^{30}P
3131.6	0.208	0.066	3835.9	709.02	^{30}P
3226.4[c]	0.265	0.088			
3265.4[d]	0.306	0.085			
3395.8	0.212	0.070	5933.6	2539.03	^{30}P
3534.9	0.91	0.11	5508.6	1973.62	^{30}P
3577.5[d]	0.108	0.051			
3615.0[d]	0.173	0.063			
3823.5	0.426	0.085	7752.7	3928.9	^{30}P
3916.7	1.26	0.13	7752.7	3835.9	^{30}P
3960.4	3.24	0.19	5933.6	1973.62	^{30}P
3991.5	0.329	0.070	3990.8	0.0	^{56}Fe
4004.3[d]	0.34	0.10			

Table 9.6 (continued)

E_γ[a] (keV)	I_γ	σ_{I_γ}	E_i (keV)	E_f (keV)	Assigned Nucleus
4016.4[c]	1.60	0.15			
4053.4	0.87	0.12	5508.6	1454.67	^{30}P
4072.3[d]	0.401	0.078			
4530.2[c]	0.178	0.064			
4637.3[d]	0.440	0.095			
4813.3	0.83	0.13	7752.7	2937.87	^{30}P
5213.3	1.79	0.17	7752.7	2539.03	^{30}P
5787.3[e]	0.58	0.12	7752.7	1454.67	^{30}P
5788.2	2.55	0.22	7752.7	1973.62	^{30}P
6128.6	0.46	0.12	6130.4	0.0	^{16}O
6270.5[c]	0.341	0.099			
6297.6	5.88	0.32	7752.7	1454.67	^{30}P
7043.8	0.44	0.11	7752.7	709.02	^{30}P
7240.8[e]	0.329	0.094	7752.7	0.0	^{30}P
7682.2[c]	0.56	0.13			
7751.7	1.53	0.19	7752.7	0.0	^{30}P
7879.6[c]	0.155	0.064			
7923.9[c]	0.77	0.14			

[a]Uncertainty on $E_\gamma = 0.2$ keV for $E_\gamma \leq 1522$ keV and 0.4 keV for $E_\gamma > 1522$ keV

[b]Present in room background

[c]Present off resonance

[d]Present on resonance

[e]Escape Peak

TABLE 9.7. Final states populated by decay of the $E_x = 7752.7$ keV resonance

Present Work		Endt[a]	
Energy (keV)	Uncertainty (keV)	Energy (keV)	Uncertainty (keV)
676.90	0.20	677.29	0.07
708.60	0.20	709.02	0.06
1453.90	0.16	1454.67	0.07
1972.97	0.23	1973.62	0.11
2538.80	0.40	2539.03	0.11
2839.30	0.20	2839.9	0.2
2937.03	0.18	2937.87	0.06
3836.68	0.20	3835.9	0.2
3927.83	0.27	3928.9	0.3
4343.27	0.46	4343.6	0.5
5507.56	0.32	5508.6	0.4
5933.6	0.22	5929.	4.
7752.7	0.14	7762.	3.

[a]Energies taken from [End90a].

The corresponding uncertainty on each level energy is obtained by propagating the k uncertainty values using standard methods of error propagation. All of the level energies as determined from this study agree well with previous studies except the two highest in energy, which will be discussed further. In Figure 9.12 is shown the decay scheme for the $E_x = 7752.7$ keV resonance state; the width of the lines is proportional to the intensity of the transition. Branching ratios for transitions from a level are useful for understanding the decay scheme from a nuclide. Branching ratios for this resonance had not been previously measured. The branching ratios for the primary transitions were determined by dividing each individual primary decay intensity by the sum of the primary decay intensities. Given the uncertainties on the intensities, which were discussed earlier, a statistical uncertainty on the branching ratios was calculated by standard error propagation. Since the detector efficiency is a factor in determining the peak area (Equation 9.8), the uncertainty on the efficiency should be factored into the uncertainty on the branching ratios. The total uncertainty on the branching ratio was obtained by adding the statistical uncertainty in quadrature with a global efficiency uncertainty of 6%. The branching ratios for the decay of the $E_x = 7752.7$ keV resonance are listed in Table 9.8.

The quantum numbers associated with the resonance state were not uniquely assigned based on previous studies. Although the previous uncertainty in the resonance energy was large (See Table 9.7), the value obtained in the present study is far outside the error limits. The excitation energy listed by Endt [End90a] was apparently derived by adding S_p to the proton resonance energy. Since the value for S_p used by Endt is 6.9 keV higher than the currently accepted value, the value he quotes for E_x is also high by about 6.9 keV. Taking this fact into account lowers the expected excitation energy and makes the value obtained from the present study fall within the error limits quoted by Endt.

Figure 9.12 Decay scheme for the $E_x = 7752.7$ keV resonance

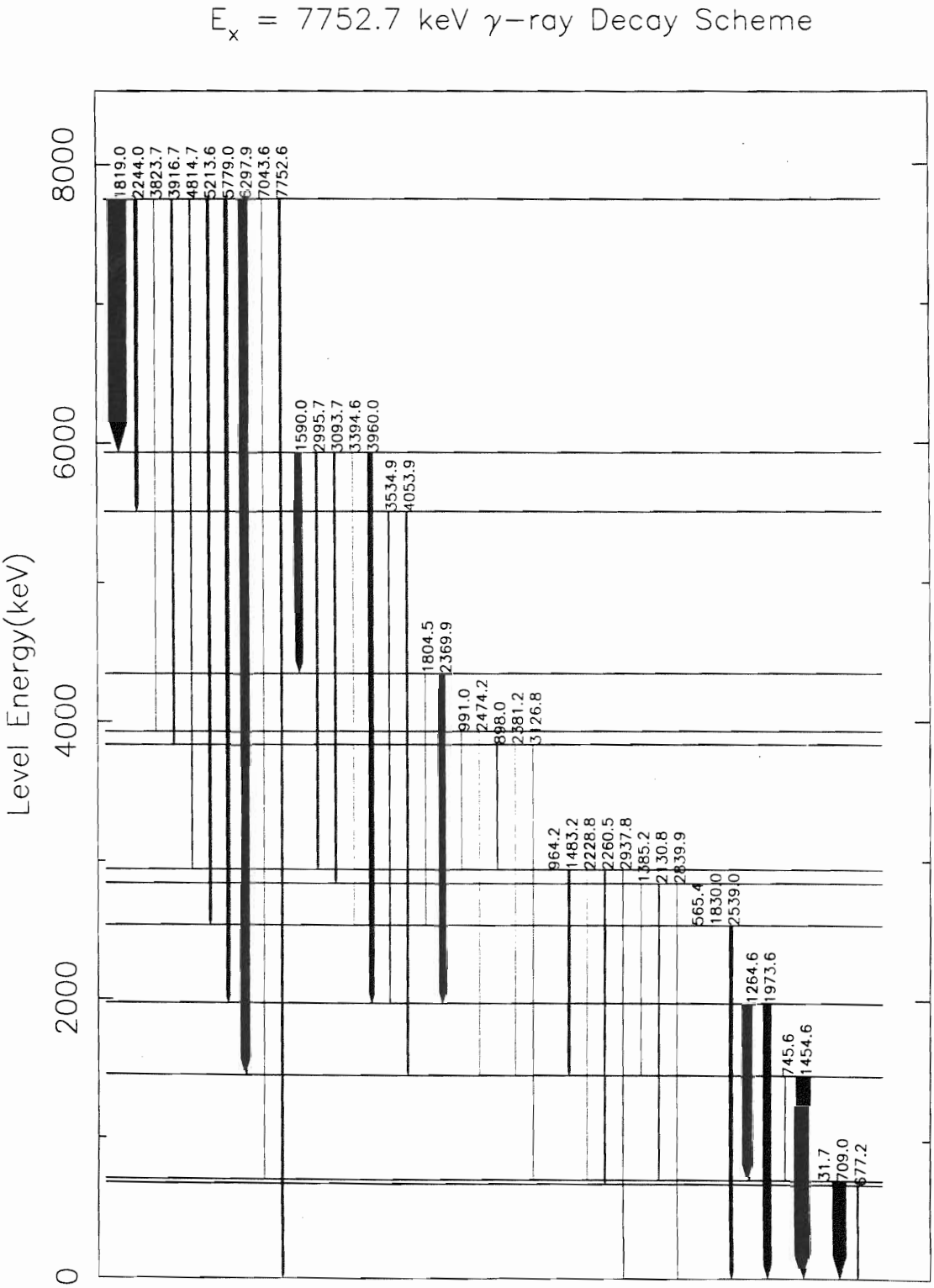
E_x = 7752.7 keV γ−ray Decay Scheme
Level Energy(keV)
0
2000
4000
6000
8000
1819.0
2244.0
3823.7
3916.7
4814.7
5213.6
5779.0
6297.9
7043.6
7752.6
1590.0
2995.7
3093.7
3394.6
3960.0
3534.9
4053.9
1804.5
2369.9
991.0
2474.2
898.0
2381.2
3126.8
964.2
1483.2
2228.8
2260.5
2937.8
1385.2
2130.8
2839.9
565.4
1830.0
2539.0
1264.6
1973.6
745.6
1454.6
31.7
709.0
677.2

TABLE 9.8. Branching ratios for decay from the $E_x = 7752.7$ keV resonance.

E_f (keV)	Branching Ratio (%)
0.0	5.4 ± 0.8
709.02	1.6 ± 0.4
1454.67	21. ± 2.
1973.62	9. ± 1.
2539.03	6.4 ± 0.7
2937.87	3.0 ± 0.5
3835.9	4.5 ± 0.5
3928.9	1.5 ± 0.3
5508.6	8.0 ± 0.7
5933.6	40. ± 3.

Another interesting feature of the decay of the $E_x = 7752.7$ keV level is the strong transition to the $E_x = 5933.6$ keV state. This is the first clear evidence in these studies of γ-decay through an unbound state. Although the excitation energy of the level at $E_x = 5933.6$ keV was previously known, the other quantum numbers were not. Endt [End90a] quotes the value at 5929 ± 4 keV. The relatively large uncertainty derives from the fact that this level was identified previously in a pickup reaction, ^{31}P(t,α) [van74]. For $E_x = 7752.7$ keV, decay to a level at $E_x = 5933.6$ keV is strongly favored in the present study since eight unassigned γ-rays are then placed, and the intensity balance for the entire decay scheme is made much more plausible by this assignment. Determining the level energy in a manner similar to that just discussed for $E_x = 7752.7$ keV leads to an excitation energy of $E_x = 5933.6$ keV, approximately 4 keV higher than the value quoted by Endt. Since little information was previously known about this level, any additional information will be a plus. In particular, for the level at $E_x = 5933.6$ keV, branching ratios and possible ranges of the quantum numbers can be obtained from the decays observed in this level. The branching ratios for the $E_x = 5933.6$ keV level obtained from this study are listed in Table 9.9. The ranges for obtained quantum numbers will be discussed in conjunction with the further analysis of the state at $E_x = 7752.7$ keV.

The conservation of angular momentum discussed in Section 9.2 places limits on the possible values of J for the resonance state. If one knew J^π for the final state and the radiation type ΛL, a small set of possible values for J^π for the decaying state could be formed. In these studies, neither Λ nor L are measured. The set of known information consists of the quantum numbers for the levels as determined in previous studies. Since the probability of emission of ΛL radiation decreases rapidly with L (See Section 9.2), our approach is to assume initially that the transitions are ΛL = E1, M1, E2, M2, or E3 and determine the possible quantum numbers of the decaying state by combining the initial state properties with these possibilities. For the $E_x = 7752.7$ keV resonance, decay to the various final states permits $J^\pi =$

TABLE 9.9. Branching ratios for decay from the $E_x = 5933.6$ keV resonance.

E_f (keV)	Branching Ratio (%)
1973.62	30. ± 3.
2539.03	2.0 ± 0.7
2839.9	13. ± 1.
2937.87	14. ± 2.
4343.6	41. ± 3.

$0^-, 1^\pm, 2^\pm, 3^\pm$, and 4^-. An analysis of the transition strength may further eliminate some of these possibilities. The transition $E_x = 7752.$ keV $\longrightarrow$ $E_x = 2937.87$ keV is possibly a mixed M2/E3 transition with unknown mixing ratio, if $E_x = 7752.7$ keV is $4^-;1$. If it is pure M2, B(M2) = 2.45 W.u., which exceeds the M2IS RUL. If it is pure E3, B(E3) = 747 W.u., which exceeds the E3IS RUL. Therefore, neither pure transition type is permitted. Furthermore, no degree of mixing produces a mixing ratio that is physically permissible. Thus, the $J^\pi = 4^-;1$ possibility is eliminated. If $E_x = 7752.7$ keV is $4^-;0$, the transition to $E_x = 1454.67$ keV may also be a mixture of M2 and E3 character, with an unknown mixing ratio. If the transition is pure M2, B(M2) = 4.48 W.u., which exceeds the M2IS RUL. If it pure E3, B(E3) = 798 W.u., which exceeds the E3IS RUL. No degree of mixing results in a value for $\delta_{M2/E3}$ such the transition can occur. Therefore, the $J^\pi = 4^-;0$ possibility is also eliminated. If $E_x = 7752.7$ keV is $0^-;1$, the transition to $E_x = 2937.87$ keV is an M2IS transition with B(M2) = 2.45 W.u. Since the M2IS RUL is 0.2 W.u., $0^-;1$ must be eliminated. Similarly, if $E_x = 7752.7$ keV is $0^-;0$, the transition to $E_x =$ 1973.62 keV is an E3IS transition with B(E3) = 624.4 W.u. Since the E3IS RUL is 50 W.u., $0^-;0$ must be eliminated. If $E_x = 7752.7$ keV is $1^-;0$, the transitions to the $E_x = 1973$, 2539, and 3928 keV levels are also possible mixed M2/E3 transitions with unknown mixing ratios. The B(M2) and B(E3) values exceed the RUL in each case; therefore, the possibility $1^-;0$ is eliminated. Therefore, from this study, the remaining possibilities for $E_x = 7752.7$ keV are $J^\pi;T = 1^-;1$, $J^\pi = 1^+$, $J = 2$, and $J = 3$. Previous studies permit J^π values of $3^+, 4^+$, or 5^+. The only common element to these two sets of possibilities is $J^\pi = 3^+$; T remains ambiguous.

The decay $E_x = 7752.7$ keV to $E_x = 5933.6$ keV provides an opportunity to determine a range for the quantum numbers for the final state, for which nothing is currently known except the excitation energy. The final states and branching ratios for decays from $E_x = 5933.6$ keV are listed in Table 9.9. Final states of these decays are to levels with $J^\pi = 3^+$ (1973, 2539, 2840 keV), 2^+ (2938 keV), and 5^+

(4343 keV). Assuming transitions to order E3 results in the possibilities 2^-, 3, 4, and 5^-. Since the strength of this resonance has not been measured, an RUL analysis for decays from this state cannot be performed. However, an RUL analysis for decays from known higher states to this state can be performed. Since the resonance state $E_x = 7752.7$ keV is 3^+, decay to $E_x = 5933$ keV of 5^- may be a mixed M2/E3 isoscalar or isovector transition; both the M2 and the E3 RUL's are far exceeded for either isospin assignment. Thus, the possibility of 5^- is eliminated. Therefore, the remaining possibilities for $E_x = 5933.6$ keV are 2^-, 3, and 4. Additionally, $2^-; 1$ is eliminated if $E_x = 7752.7$ keV is $3^+; 1$ since B(E1) = 0.00319 W.u., which exceeds the E1IS RUL (albeit by only a factor of 1.6). However, since T is not known for $E_x = 7752.7$ keV, this possibility must remain for $E_x = 5933.6$ keV.

9.5 $E_x = 7749.3$ keV ^{30}P Resonance Analysis

The second ^{30}P resonance which we studied is $E_x = 7749.3$ keV. Data were accumulated both on- and off-resonance until a total of 225.000 μC of charge had been collected on the Faraday cup at each energy: the off-resonance data were taken at an energy 5 keV lower than the resonance energy. The spectra taken with the suppressed HPGe and unsuppressed HPGe detectors on the $E_x = 7749.3$ keV resonance are shown in Figures 9.13 and 9.14. The previously mentioned fluorine contamination is clearly visible in these spectra as well. The same energy and efficiency calibrations are valid for these data as for the $E_x = 7752.7$ keV data since neither the electronics nor the physical orientation of the detectors was changed. The data were fit using GELIFT, and the information was stored in a STO file. Based on the room background spectrum, the off-resonance spectrum, and the known ^{30}P decay scheme, the γ-rays were assigned.

Nine primary γ-rays are assigned for the $E_x = 7749.3$ keV resonance from this study. Previously, Reinecke had assigned five primary branches [Rei85]. The

Figure 9.13 Suppressed HPGe $E_x = 7749.3$ keV ^{30}P data

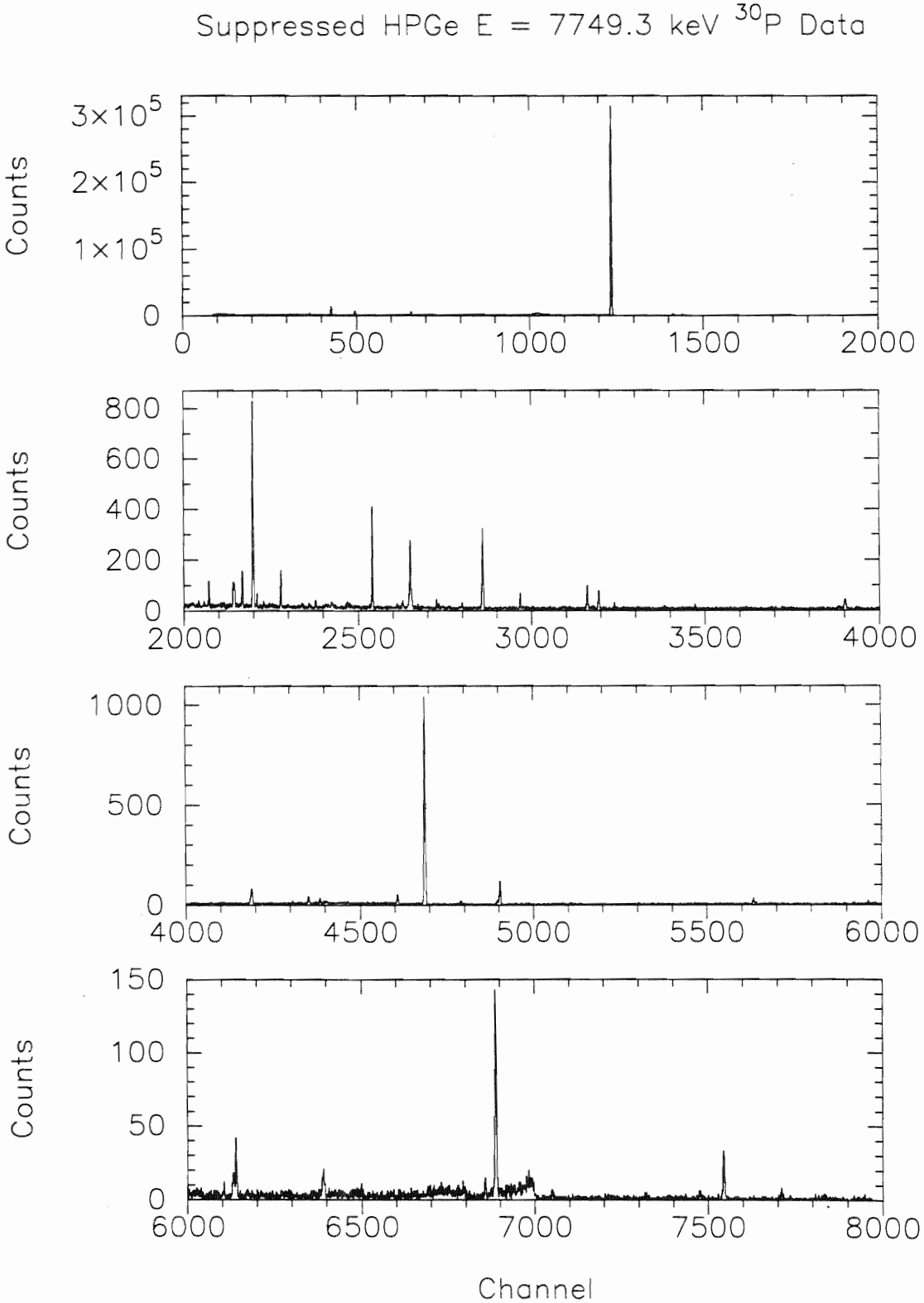
Suppressed HPGe E = 7749.3 keV ^{30}P Data
Counts
3×10^5
2×10^5
1×10^5
0
0
500
1000
1500
2000
Counts
800
600
400
200
0
2000
2500
3000
3500
4000
Counts
1000
500
0
4000
4500
5000
5500
6000
Counts
150
100
50
0
6000
6500
7000
7500
8000
Channel

Figure 9.14 Unsuppressed HPGe $E_x = 7749.3$ keV ^{30}P data

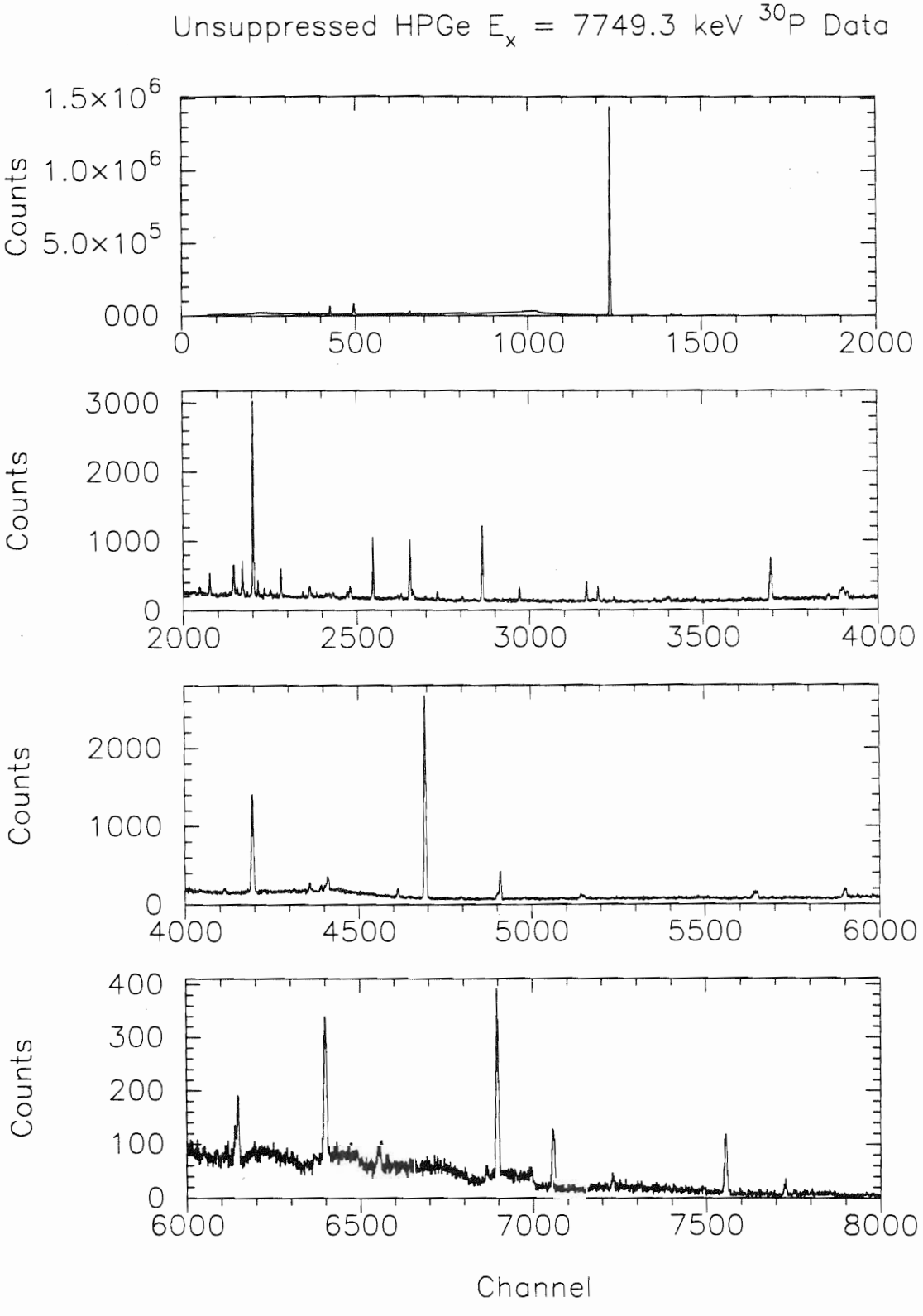
Unsuppressed HPGe E_x = 7749.3 keV ^{30}P Data
Counts
1.5×10^6
1.0×10^6
5.0×10^5
000
0
500
1000
1500
2000
Counts
3000
2000
1000
0
2000
2500
3000
3500
4000
Counts
2000
1000
0
4000
4500
5000
5500
6000
Counts
400
300
200
100
0
6000
6500
7000
7500
8000
Channel

branching ratios obtained from this work and those from Reinecke are listed in Table 9.10. Except for the branching ratio for the decay to the $E_x = 677.29$ keV level, the branching ratios obtained from this work agree well with Reinecke's for those cases where he has a value. Since the previous value has no quoted uncertainty, it is not known how well that value is determined. Clearly, there are several more branches observed in this study; therefore, there must be a discrepancy in at least one branching ratio. The 677.29 keV branch is the only one which differs substantially. The decay scheme for the $E_x = 7749.3$ keV resonance, with the assignments made in this study, is shown in Figure 9.15.

With the γ-ray assignments made, an analysis of this resonance was done in hopes of verifying the previous assignment of $J^\pi; T = 1^+; (0)$ [Fra91]. Primaries to final states with $J^\pi = 0^+, 1^+$, and 2^+ are observed. Considering transitions of order up to E3, the set of possibilities for $E_x = 7749.3$ keV is 1, 2, and 3^-. If $E_x = 7749.3$ keV is $1^-; 1$, the transition to $E_x = 2937$ keV $(2^+; 1)$ yields B(E1) = 0.00371 W.u., which exceeds the E1IS RUL by a factor of 1.9. If $E_x = 7749.3$ keV is $2^-; 0$, the transition to $E_x = 4468$ keV $(0^+; 1)$ yields B(M2) = 175.9 W.u., which exceeds the M2IV RUL by a factor of 35. If $E_x = 7749.3$ keV is $2^-; 1$, the transition to $E_x = 677$ keV $(0^+; 1)$ yields B(M2) = 22.7 W.u., which exceeds the M2IS RUL by a factor of 113. If $E_x = 7749.3$ keV is $3^-; 0$, the transition to $E_x = 3019$ keV $(1^+; 0)$ is possibly a mixed M2/E3 transition with unknown mixing ratio. If it is pure M2, B(M2) = 32.8, which exceeds the M2IS RUL by a factor of 164; the minimum value of $\delta_{M2/E3}$ which could permit this B(M2) is 12.8. If it is pure E3, B(E3) = 10358, which exceeds the E3IS RUL by a factor of 207; the maximum value of $\delta_{M2/E3}$ which could permit this B(E3) is 0.07. Thus, no degree of mixing could result in allowed reduced transition probabilities, and $3^-; 0$ must be eliminated. If $E_x = 7749.3$ keV is $3^-; 1$, the transition to $E_x = 677$ keV $(0^+; 1)$ yields B(E3) = 3207 W.u., which exceeds the E3IS RUL by a factor of 64. Thus, $J^\pi; T = 1^-; 1$, $J^\pi; T = 2^+; 0$, $J^\pi = 2^-$, and $J^\pi = 3^-$ must be eliminated as possibilities. The

TABLE 9.10. Branching ratios for decay from the $E_x = 7749.3$ keV resonance.

Present Work		Previous Work[a]	
E_f (keV)	Branching Ratio (%)	E_f (keV)	Branching Ratio (%)
0.0	4.3 ± 0.5	0.0	4.1
677.29	15. ± 1.	677.29	22.
709.02	1.0 ± 0.3		
1454.67	2.0 ± 0.3		
2723.96	1.6 ± 0.3		
2937.87	68. ± 4.	2937.87	68.
3019.39	2.9 ± 0.3	3019.39	2.8
4468.33	2.5 ± 0.3		
4502.32	3.4 ± 0.3	4502.32	3.1

[a]Branching ratios taken from [Rei85].

Figure 9.15 Decay scheme for the $E_x = 7749.3$ keV resonance

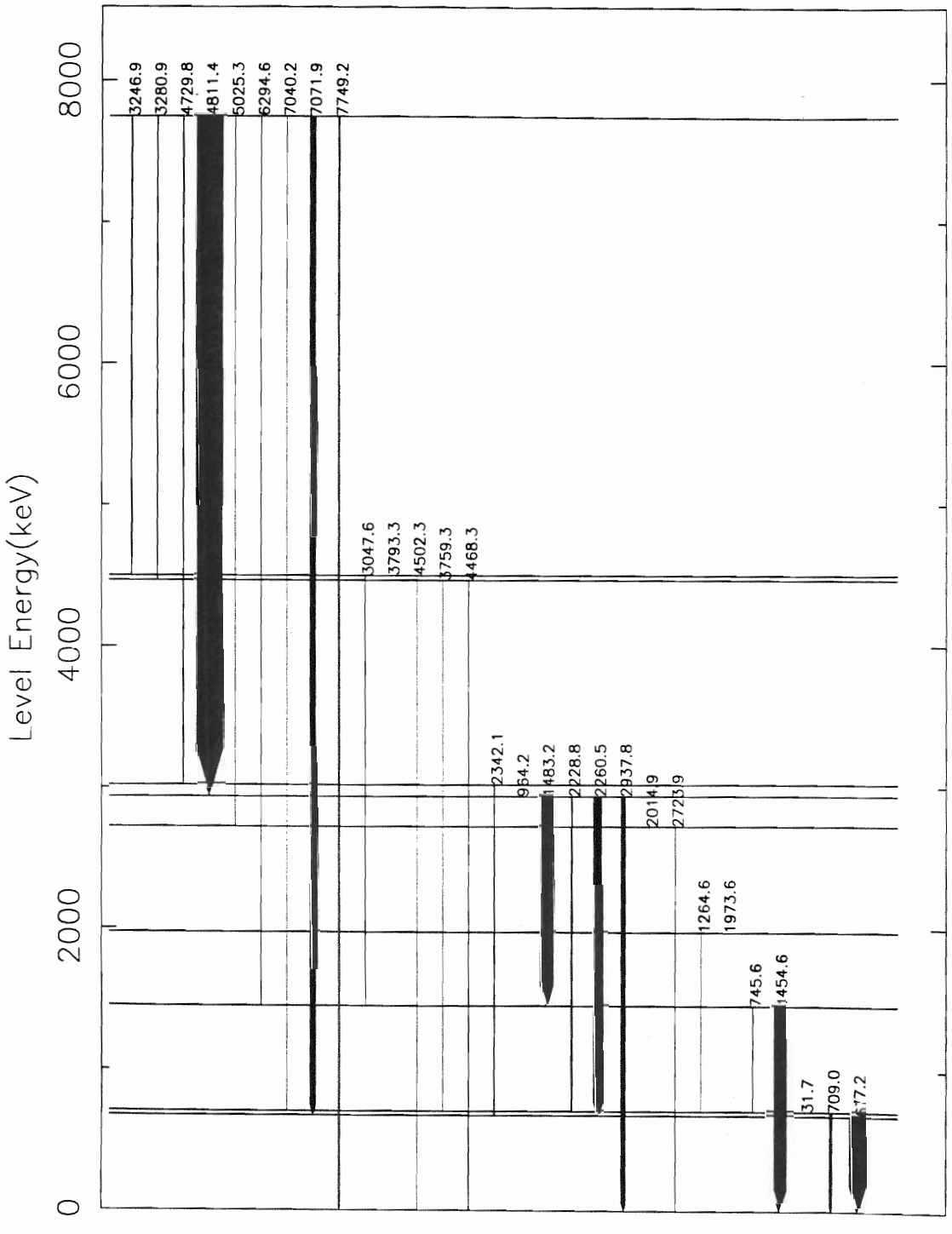
E_x = 7749.3 keV γ−ray Decay Scheme
Level Energy(keV)
0
2000
4000
6000
8000
3246.9
3280.9
4729.8
4811.4
5025.3
6294.6
7040.2
7071.9
7749.2
3047.6
3793.3
4502.3
3759.3
4468.3
2342.1
964.2
1483.2
2228.8
2260.5
2937.8
2014.9
2723.9
1264.6
1973.6
745.6
1454.6
31.7
709.0
417.2

remaining set of allowable quantum numbers for $E_x = 7749.3$ keV is then $J^\pi = 1^+$, $J^\pi; T = 1^-; 0$, and $J^\pi = 2^+$. Some of these remaining possibilities could perhaps be eliminated if further information on certain transitions were known.

Decays of $E_x = 7749.3$ keV to three states reveal interesting possibilities for the quantum numbers of the initial state. Decays to the final states of 2937.87 keV $(2^+; 1)$ and 4502.32 keV $(1^+; 1)$ are both possible mixed M1/E2 transitions with unknown $\delta_{M1/E2}$ and place limitations on the mixing ratio for decays to those states. If $E_x = 7749.3$ keV is $1^+; 0$ or $2^+; 0$, a pure E2 transition to $E_x = 2937.87$ keV yields B(E2) = 22.44 W.u., which requires $\delta_{M2/E3} < 0.54$. If $E_x = 7749.3$ keV is $1^+; 1$ or $2^+; 1$, a pure M1 transition to $E_x = 2937.87$ keV yields B(M1) = 0.11 W.u., which requires $\delta_{M2/E3} > 1.11$. Therefore, if $\delta_{M1/E2}\,(7749.3 \longrightarrow 2937.87) < 0.54$, $1^+; 1$ and $2^+; 1$ must be eliminated as possibilities for $E_x = 7749.3$ keV, and if $\delta_{M1/E2}\,(7749.3 \longrightarrow 2937.87) > 1.11$, $1^+; 0$ and $2^+; 0$ must be eliminated as possibilities for $E_x = 7749.3$ keV. Also, If $E_x = 7749.3$ keV is $1^+; 0$ or $2^+; 0$, a pure E2 transition to $E_x = 4502.32$ keV yields B(E2) = 8.02 W.u., which requires $\delta_{M2/E3} < 1.29$. Thus, if $\delta_{M1/E2}\,(7749.3 \longrightarrow 4502.32) > 1.29$, $1^+; 0$ and $2^+; 0$ can be eliminated. Since these mixing ratios are not known, the set $J^\pi = 1^+$, $J^\pi; T = 1^-; 0$, and $J^\pi = 2^+$ remain as possibilities. This experiment is similar to an earlier experiment which resulted in a tentative isospin assignment of $T = 0$: however, the current experiment does not eliminate $T = 1$. Isospin is not assigned for this state. Determination of mixing ratios in a future measurement should determine T.

9.6 $E_x = 7742.0$ keV ^{30}P Resonance Analysis

The third ^{30}P resonance that we studied during the course of these experiments is $E_x = 7742.0$ keV, previously quoted as having $E_x = 7749 \pm 3$ keV with $J^\pi = 1^-$ [End90a]. This resonance has a proton width of 52 keV [Fra91]; therefore,

an off-resonance background spectrum would be of limited usefulness. Thus, no off-resonance data were taken for this resonance. Additionally, the value of Γ_γ for this resonance is unknown. Our procedure for data collection for this resonance was to initially accumulate data for a lengthy period of time. Subsequently, if appropriate ^{30}P γ-ray lines appear in the spectrum, the resonance apparently has a non-zero gamma width, and additional data on the resonance would be accumulated. Conversely, if no appropriate ^{30}P γ-ray lines appear in the spectrum, the gamma width must be extremely small, and no additional data for this resonance would be accumulated due to the extensive time requirement. Initially, data were collected until 190.000 μC of charge had been collected on the Faraday cup. Some ^{30}P γ-ray lines were present in the spectrum; however, since there were other resonances with known gamma widths to be studied in this data-taking run, we proceeded to accumulate data on another resonance, $E_x = 7688.2$ keV. After accumulating a sufficient amount of data on $E_x = 7688.2$ keV, we collected more data on the $E_x = 7742.0$ keV resonance until another 200.000 μC of charge had been collected on the Faraday cup.

Since this resonance is broad and has not been previously observed in the (p,γ) reaction, any ^{30}P γ-rays are expected to be weak. In order to assist in assigning the ^{30}P γ-rays, data were taken the second time 2 keV lower in energy. Thus, all primary γ-rays observed during the second data collection should shift downward by 2 keV, while all other ^{30}P γ-rays should remain unshifted. To carry out this analysis means that the spectra from each data collection run were separately fit. Then, comparison of the separate STO files revealed which γ-rays were primaries. Subsequently, the γ-ray intensities from the separate STO files were added to obtain the final intensity. The data taken with the suppressed HPGe detector during the first and second collections are shown in Figures 9.16 and 9.17, respectively. The effects of the fluorine contamination discussed earlier is clearly visible between channels 6000 and 7000. Gamma-ray assignments were made based on previous assignments of

Figure 9.16 Suppressed HPGe $E_x = 7742.0$ keV ^{30}P data taken at resonance energy.

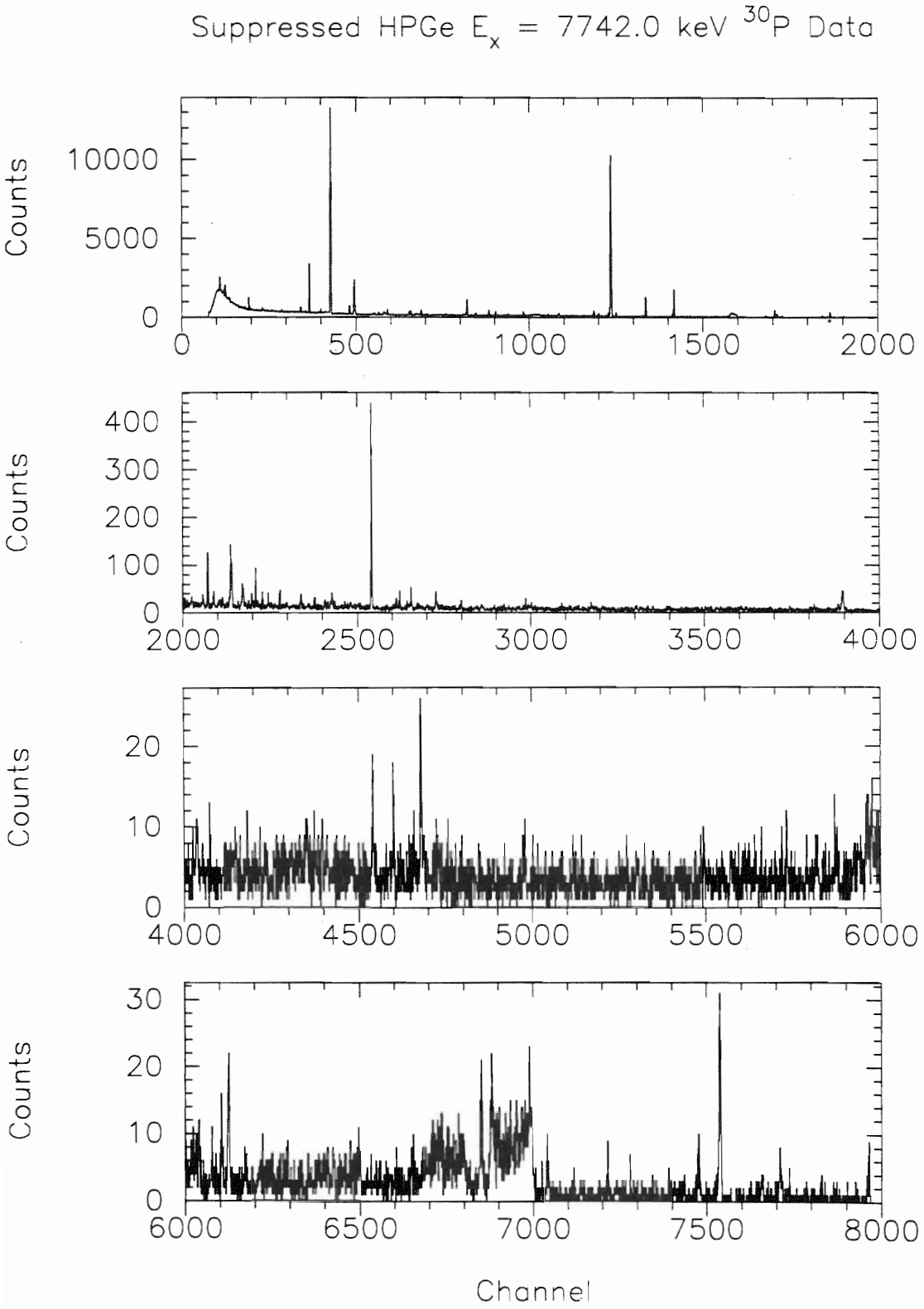
Suppressed HPGe E_x = 7742.0 keV ^{30}P Data
Counts
10000
5000
0
0
500
1000
1500
2000
Counts
400
300
200
100
0
2000
2500
3000
3500
4000
Counts
20
10
0
4000
4500
5000
5500
6000
Counts
30
20
10
0
6000
6500
7000
7500
8000
Channel

Figure 9.17 Suppressed HPGe $E_x = 7742.0$ keV ^{30}P data taken 2 keV lower than resonance energy.

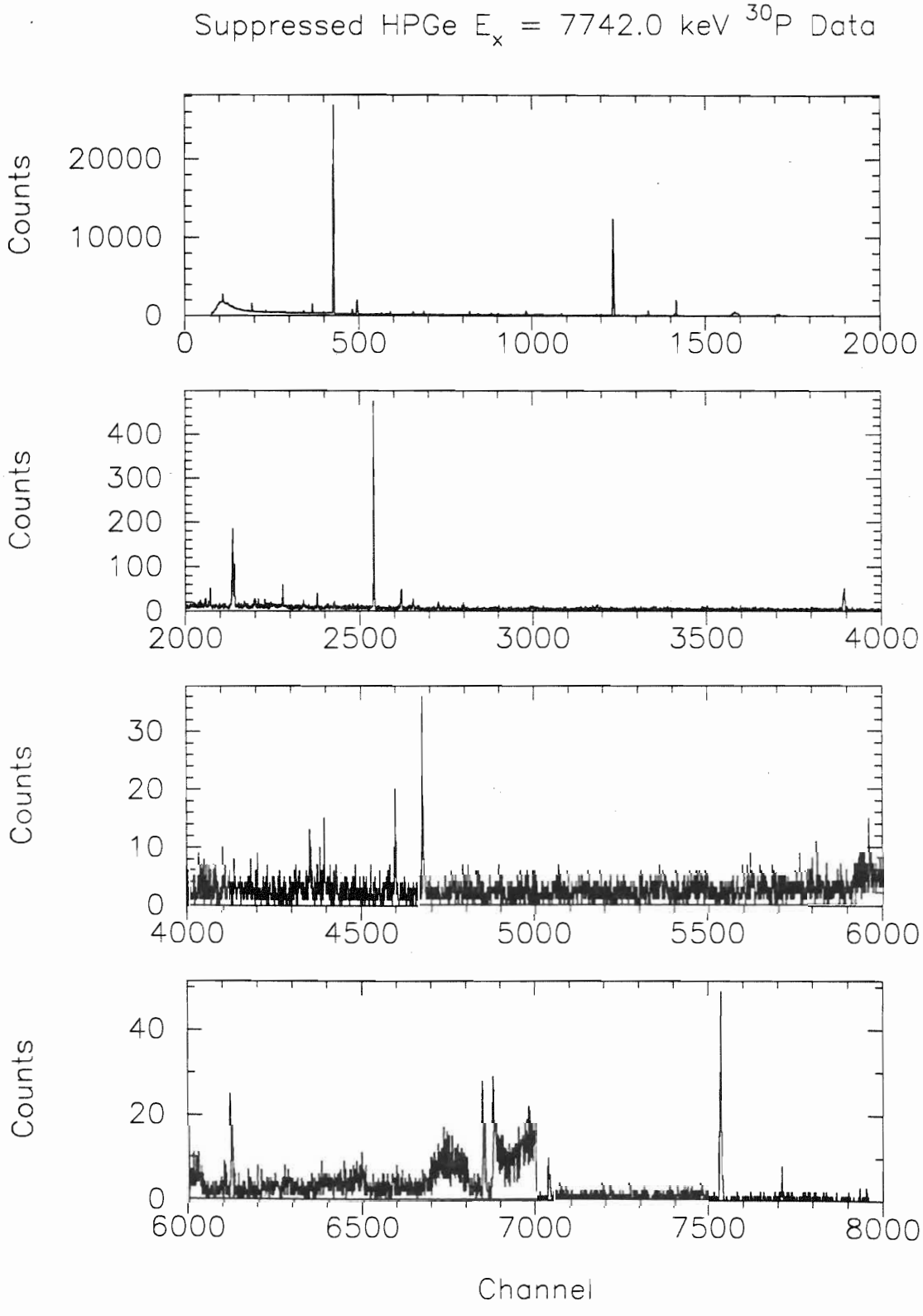
Suppressed HPGe E_x = 7742.0 keV ^{30}P Data
Counts
20000
10000
0
0
500
1000
1500
2000
Counts
400
300
200
100
0
2000
2500
3000
3500
4000
Counts
30
20
10
0
4000
4500
5000
5500
6000
Counts
40
20
0
6000
6500
7000
7500
8000
Channel

contaminants, whether γ-ray energy shifted, and previous assignments of transitions in ^{30}P. There are many γ-rays that are present in only one of the data collection runs. These are likely not ^{30}P γ-rays and are left unassigned. There are also several γ-rays that are present in both data collection runs but do not fit in the ^{30}P decay scheme; these are also left unassigned.

No previous decay information was known for this resonance. From this study, it is found that $E_x = 7742.0$ keV, compared with $E_x = 7749 \pm 3$ keV quoted earlier by Endt [End90a]. Adjusting the proton separation energy as discussed in Section 9.4 yields a value in agreement with the current study. Based on the present work, a total of six primaries have been assigned for the $E_x = 7742.0$ keV resonance. These primaries and the corresponding branching ratios are listed in Table 9.11. The uncertainties are calculated in the same manner as those in Table 9.8. A decay scheme for $E_x = 7742.0$ keV, based on this work, is shown in Figure 9.18. The quantum numbers of the final states are well known, and, assuming transitions to order E3, the corresponding possibilities for the initial state are $1, 2$, and 3^-. Since the strength for this resonance is unknown, the partial widths are not available, and an RUL analysis is not possible. The previous assignment of 1^- is a subset of the possibilities and is the adopted value.

TABLE 9.11. Branching ratios for decay from the $E_x = 7742.0$ keV resonance.

E_f (keV)	Branching Ratio (%)
0.0	37. ± 3.
677.29	13. ± 2.
709.02	19. ± 2.
1454.67	15. ± 2.
2937.87	11. ± 1.
3019.39	4.3 ± 0.6

Figure 9.18 Decay scheme for the $E_x = 7742.0$ keV resonance

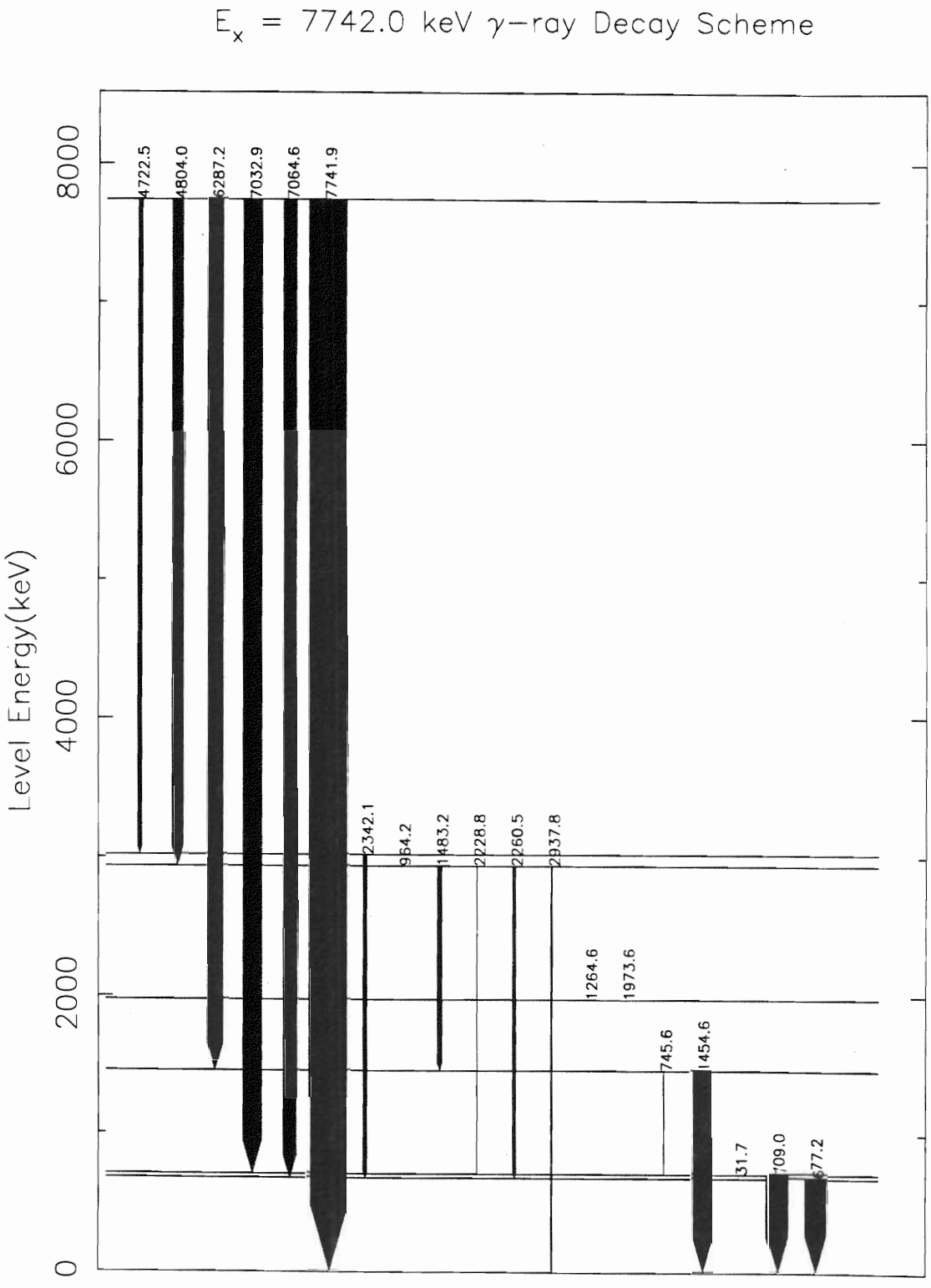
E_x = 7742.0 keV γ−ray Decay Scheme
Level Energy(keV)
0
2000
4000
6000
8000
4722.5
4804.0
6287.2
7032.9
7064.6
7741.9
2342.1
954.2
1483.2
2228.8
2260.5
2937.8
1264.6
1973.6
745.6
1454.6
31.7
109.0
677.2

9.7 E_x = 7688.2 keV ^{30}P Resonance Analysis

Data were also taken in these studies on the ^{30}P resonance previously quoted at E_x = 7694.2 keV [Fra91]; the corresponding set of quantum numbers is $J^\pi = 3^+$. Both on- and off-resonance data were collected on this resonance until 200,000 μC of charge had been collected on the Faraday cup downstream from the target. The data taken with the suppressed HPGe detector and the unsuppressed HPGe detector are shown in Figures 9.19 and 9.20. The γ-rays were assigned based on their presence in the room background spectrum, the off-resonance spectrum, and the on-resonance spectrum.

A total of eight primaries are assigned as decays of the E_x = 7688.2 keV resonance. The decay scheme for E_x = 7688.2 keV resulting from these assignments is shown in Figure 9.21. The branching ratios from the resonance state and the previous set of branching ratios [Rei85] are shown in Table 9.12. With the exception of the branch to the ground state, the branching ratios compare favorably with those of Reinecke, where there are values with which to compare. The one major difference is the branch to the ground state, which is observed to be much weaker than the previously observed branching ratio would suggest. In this study, however, four new primaries were assigned.

Allowing transitions of order up to E3, the set of possible quantum numbers for E_x = 7688.2 keV is $2^-, 3$, and 4^-. The observed reduced transition probabilities eliminate some of these possibilities. If E_x = 7688.2 keV is $2^-;0$, the transition to E_x = 4298.1 keV $(4^-;0)$ is possibly mixed M2/E3 with unknown mixing ratio. If it is pure M2, B(M2) exceeds the M2IS RUL by a factor of 358 and requires that $\delta_{M2/E3} > 18.9$. If the transition is pure E3, B(E3) exceeds the E3IS RUL by a factor of 882 and requires that $\delta_{M2/E3} < 0.03$. Such a situation is impossible, and $2^-;0$ must be removed as a possibility. The possibility of $2^-;1$ must also be eliminated since the reduced transition probability B(E3) for the transition to

Figure 9.19 Suppressed HPGe $E_x = 7688.2$ keV ^{30}P data

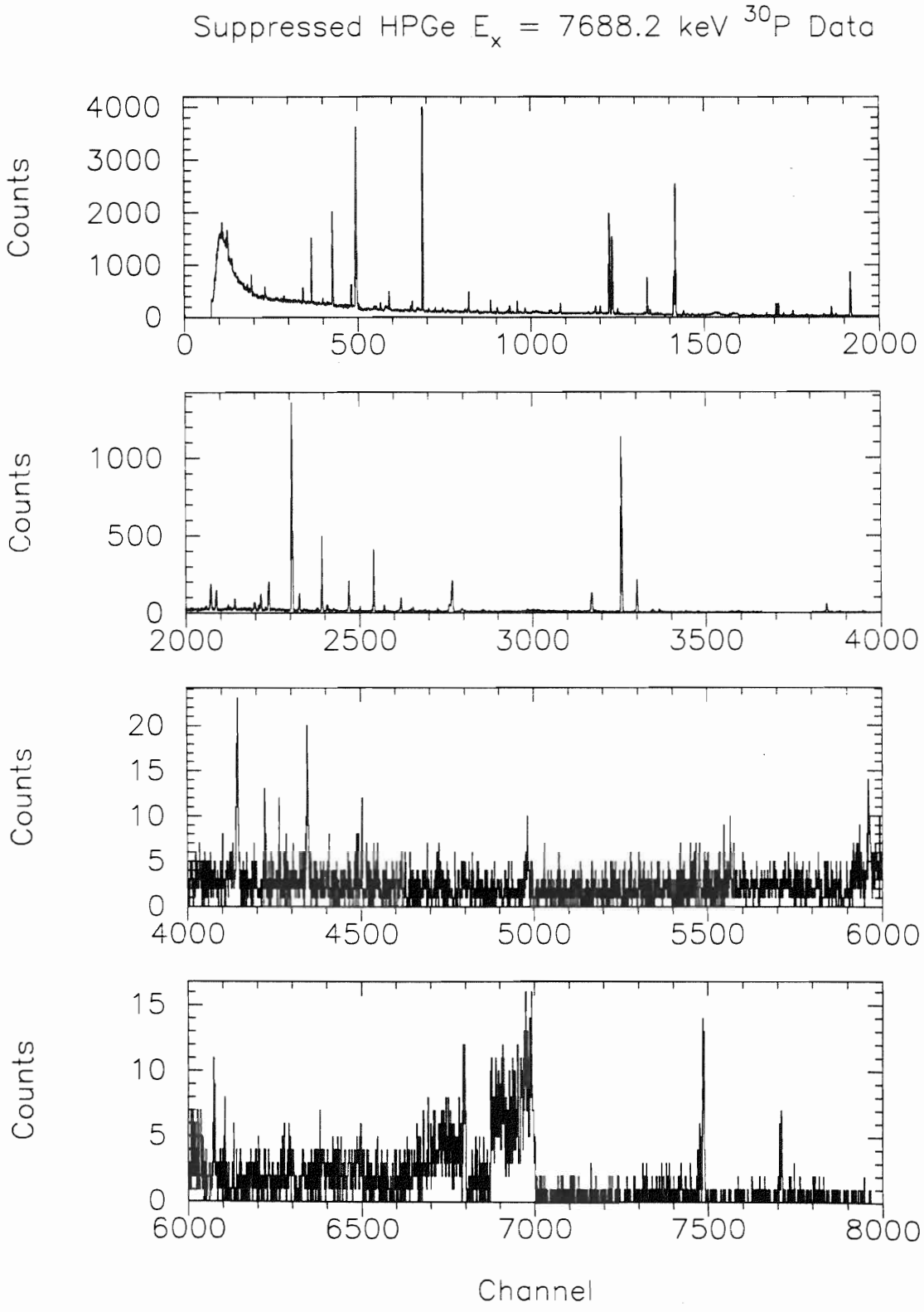
Suppressed HPGe E_x = 7688.2 keV ^{30}P Data
Counts
4000
3000
2000
1000
0
0
500
1000
1500
2000
Counts
1000
500
0
2000
2500
3000
3500
4000
Counts
20
15
10
5
0
4000
4500
5000
5500
6000
Counts
15
10
5
0
6000
6500
7000
7500
8000
Channel

Figure 9.20 Unsuppressed HPGe $E_x = 7688.2$ keV ^{30}P data

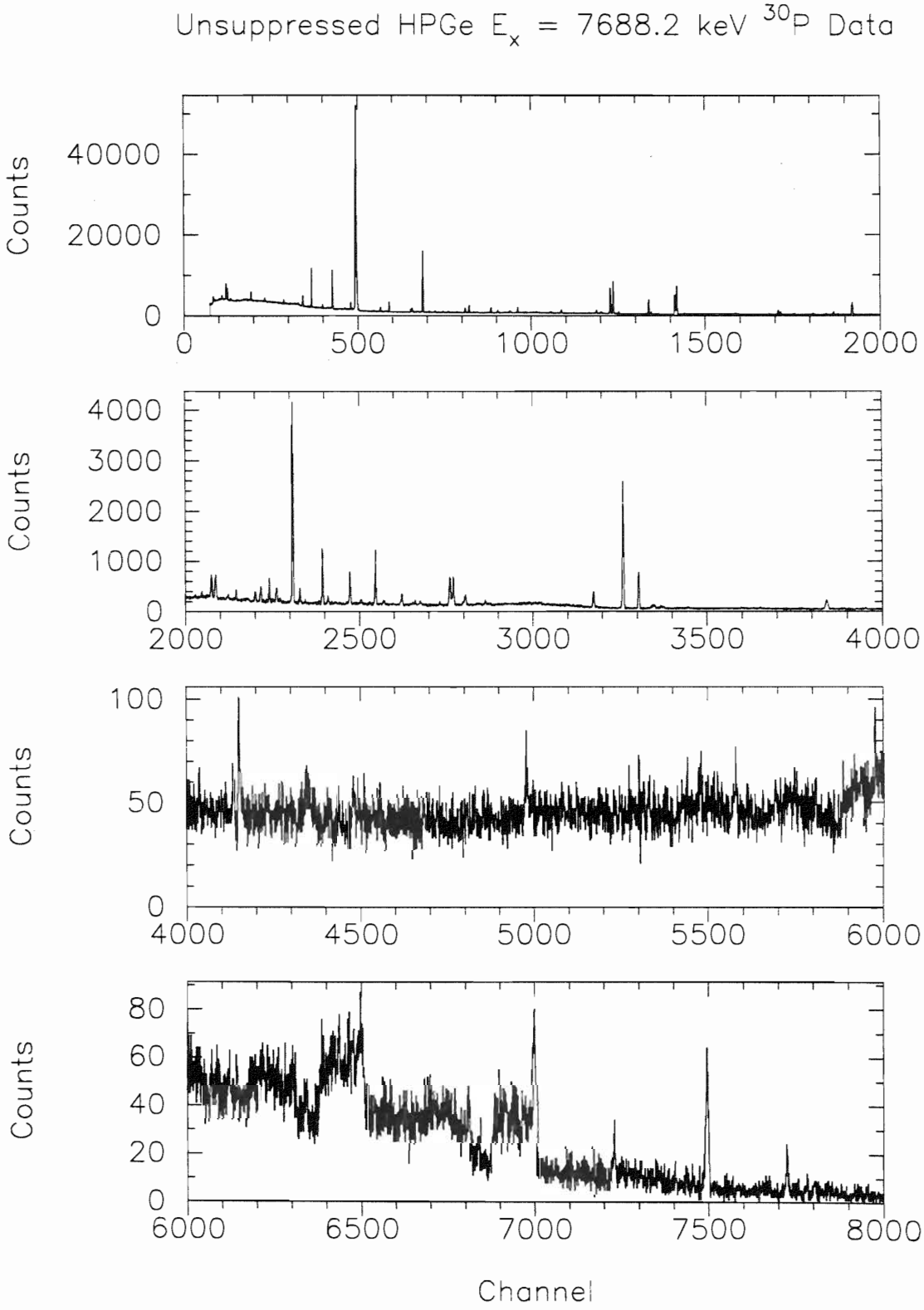
Unsuppressed HPGe E_x = 7688.2 keV ^{30}P Data
Counts
40000
20000
0
0
500
1000
1500
2000
Counts
4000
3000
2000
1000
0
2000
2500
3000
3500
4000
Counts
100
50
0
4000
4500
5000
5500
6000
Counts
80
60
40
20
0
6000
6500
7000
7500
8000
Channel

Figure 9.21 Decay scheme for the $E_x = 7688.2$ keV resonance

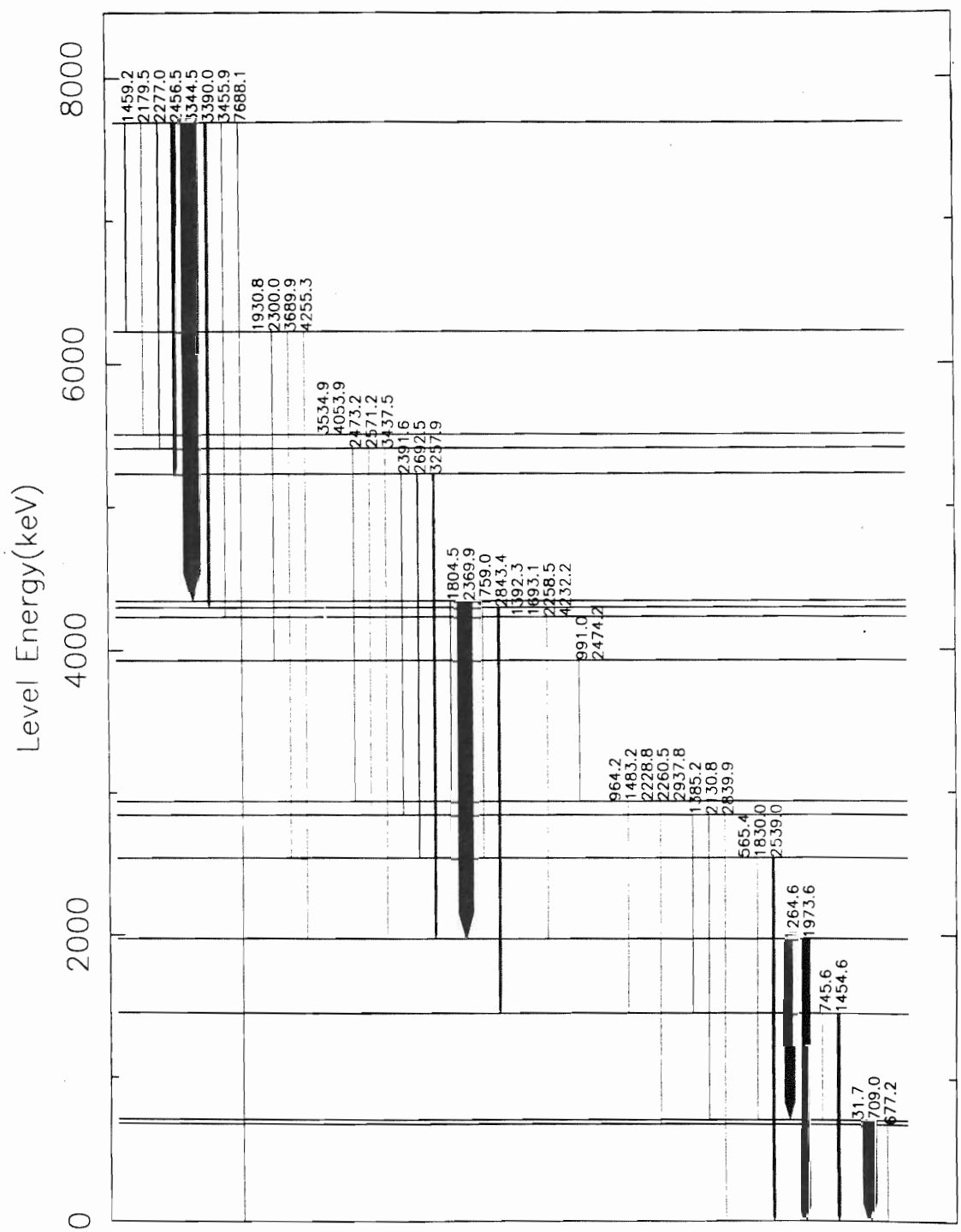
E_x = 7688.2 keV γ−ray Decay Scheme
Level Energy(keV)
0
2000
4000
6000
8000
1459.2
2179.5
2277.0
2456.5
3344.5
3390.0
3455.9
7688.1
1930.8
2300.0
3689.9
4255.3
3534.9
4053.9
2473.2
2571.2
3437.5
2391.6
2692.5
3257.9
1804.5
2369.9
1759.0
2843.4
1392.3
1693.1
2258.5
4232.2
991.0
2474.2
964.2
1483.2
2228.8
2260.5
2937.8
1885.2
2130.8
2839.9
565.4
1830.0
2539.0
1264.6
1973.6
745.6
1454.6
31.7
709.0
677.2

TABLE 9.12. Branching ratios for decay from the $E_x = 7688.2$ keV resonance.

Present Work		Previous Work[a]	
E_f (keV)	Branching Ratio (%)	E_f (keV)	Branching Ratio (%)
0.0	2.5 ± 0.4	0.0	14.
4232.2	0.9 ± 0.2		
4298.1	11.4 ± 0.9	4298.1	10.
4343.6	60. ± 4.	4343.6	62.
5231.6	17. ± 1.	5231.6	14.
5416.	3.8 ± 0.4		
5508.6	0.7 ± 0.2		
6235.	3.7 ± 0.5		

[a]Energies and branching ratios taken from [End90a].

$E_x = 4343.6$ keV $(5^+;0) > 255000$ W.u., which is unreasonably large. Similarly, if $E_x = 7688.2$ keV is 3^-, the possible mixed M2/E3 transition to $E_x = 4343.6$ keV yields B(M2) and B(E3) which exceed both the isoscalar and isovector RUL values by large factors. Therefore, 3^- must be eliminated as a possibility. Finally, $3^+;1$ can be discarded since B(E2) for the transition to $E_x = 4343.6$ keV exceeds the E2IV RUL by a factor of 2.5. If the initial state is $4^-;1$, the transition to the ground state is an E3 transition with B(E3) = 31.4 W.u. Since this value is unreasonably large, the $J^\pi;T = 4^-;1$ possibility is eliminated. Therefore, the allowed values of the quantum numbers for $E_x = 7688.2$ keV based on this study are $J^\pi;T = 3^+;0$ and $J^\pi;T = 4^-;0$. Although Frankle assigns $J^\pi = 3^+$ [Fra91] based on scattering results, it is not clear why. Apparently the state was not observed in scattering in that study. Therefore, both of the above possibilities are retained. Based on this work, there is a definite isospin assignment of $T = 0$.

This resonance, much like $E_x = 7752.7$ keV, is observed to have an interesting decay scheme since the final states of two of the primary decays are states for which all of the quantum numbers are not definitely known. Specifically, the $E_x = 6229.0$ keV state was previously quoted by Endt [End90a] to be 6235 ± 3 keV. His value for E_x was taken from the work of Ramstein [Ram81] which utilized a $(^3He,\tau)$ transfer reaction. The uncertainty on the final state energies is larger for these experiments. The value obtained from the present study lies outside the error range of Endt; however, the present assignment places six γ-rays and improves the intensity balance of the decay scheme. Therefore, a primary transition from $E_x = 7688.2$ keV to $E_x = 6229.0$ keV is assigned. Three branches from the $E_x = 6229.0$ keV state are assigned from this work; a listing of the primary branches and the branching ratios are given in Table 9.13. The primary decays of $E_x = 6229.0$ keV combined with the feeding by $E_x = 7688.2$ keV restrict the set of quantum numbers for $E_x = 6229.0$ keV to $J^\pi = 1^-$ or 6^- and $J = 2, 3, 4$, or 5; transitions to order E3 are considered in obtaining this set of possibilities. Since no strength is known for

TABLE 9.13. Branching ratios for decay from the $E_x = 6229.0$ keV resonance.

E_f (keV)	Branching Ratio (%)
1973.62	18. ± 3.
2539.03	6. ± 2.
3928.9	64. ± 5.
4298.1	11. ± 2.

this resonance, an RUL analysis for decays from this state is not possible. However, since the resonance state is $J^\pi;T = 3^+;0$ or $J^\pi;T = 4^-;0$, the transition from the resonance state to $E_x = 6229.0$ keV eliminates some possibilities. If $E_x = 6229.0$ keV is $6^-;1$, the transition from $E_x = 7688.2$ keV is either an E3IV transition or an E2IV transition. For the E2 transition case, B(E2) = 50 W.u. and exceeds the E2IV RUL by a factor of 10. For the E3 transition case, B(E3) is unreasonably large. Thus, $J^\pi = 6^-;1$ is eliminated. If $E_x = 6229.0$ keV is 1^-, the transition from $E_x = 7688.2$ keV is possibly mixed M2/E3 with unknown mixing ratio. If the transition is pure M2, B(M2) = 1575 W.u., which exceeds both the M2IS and the M2IV RUL's by a large factor. If the transition is pure E3, B(E3) is unreasonably large. Furthermore, no mixing ratio can yield this transition permissible. Thus, $J^\pi = 1^-$ is eliminated. Additionally, if $E_x = 6229.0$ keV is $2^+;1, 3^+;1$, or $4^+;1$ and $E_x = 7688.2$ keV is $3^+;0$, the transition from $E_x = 7688.2$ keV is possibly mixed M1/E2 with unknown mixing ratio. In each case, it is required that $\delta_{M1/E2} < 0.33$. Since $\delta_{M1/E2}$ is unknown for this transition, these possibilities have been retained. If $E_x = 7688.2$ keV is $3^+;0$, the possibility of $J^\pi;T = 6^-;1$ for $E_x = 6229.0$ keV is eliminated since the transition would be an E3IS transition that exceeds the E3IS RUL by a large factor. The set of possibilities from this work for $E_x = 6229.0$ keV is $J = 2, 3, 4$, or 5, and $J^\pi;T = 6^-;0$. Previously, this resonance was quoted to have $J^\pi = 3^+$ or 5^+. The intersection of these sets is the adopted set of possible quantum numbers for this resonance.

An assignment has also been made of a decay from $E_x = 7688.2$ keV to $E_x = 5508.6$ keV, a state quoted by Endt to be (2,3);1 [End90a] and Frankle [Fra91] to be (1^+-3);1. The decay to this state accounts for three γ-rays and improves the intensity balance for lower-lying states. Two branches are known from previous work [End90a]. These two were also observed in this study, and a comparison of the values is shown in Table 9.14. The branching ratios are quite different, but there is a large uncertainty on both Endt's measurements and those of this study. The

transition is observed weakly in this study, and the statistics are such that there is a large inherent uncertainty. Considering transitions to order E3, the observed feeding to and the observed decaying from $E_x = 5508.6$ keV yields possibilities of $J = 1, 2, 3$, and $J^\pi = 0^-, 4^-$.

However, an analysis of the strength of the transitions eliminates some of these possibilities. If $E_x = 5508.6$ keV is 0^-, the transition to $E_x = 1454.67$ keV is an M2 transition with B(M2) = 169 W.u. This reduced transition probability exceeds the M2IS RUL by a factor of ≈ 850 and exceeds the M2IV RUL by a factor of ≈ 34. Therefore, 0^- is eliminated. If $E_x = 5508.6$ keV is $1^-; 0$, the transition to $E_x = 1973.62$ keV is possibly mixed M2/E3. If it is pure M2, B(M2) = 224 W.u., which exceeds the M2IS RUL by over three orders of magnitude, and it is required that $\delta_{M2/E3} > 33.4$. If the transition is pure E3, B(E3) $> 10^5$ W.u., which is extremely large. Thus, this possibility is eliminated. If $E_x = 5508.6$ keV is $1^-; 1$, a similar situation exists. The transition to $E_x = 1973.62$ keV is possibly mixed M2/E3, and the corresponding M2IV RUL is exceeded by a large factor. The B(E3) value is also very large for the E3IV transition. Thus, 1^- is eliminated as a possibility for the $E_x = 5508.6$ keV resonance. If $E_x = 5508.6$ keV is $4^-; 0$, the transition to $E_x = 1454.67$ keV is possibly mixed M2/E3. If it is pure M2, B(M2) = 169 W.u., which exceeds the M2IS RUL by almost three orders of magnitude, and it is required that $\delta_{M2/E3} > 29.1$. If the transition is pure E3, B(E3) > 70000 W.u., and it is required that $\delta_{M2/E3} < 0.03$. No such $\delta_{M2/E3}$ exists, and $4^-; 0$ is eliminated. If $E_x = 5508.6$ keV is $4^-; 1$, the transition to $E_x = 1454.67$ keV is possibly mixed M2/E3, and the M2IV RUL is exceeded by a factor of 34. If the transition is pure E3, B(E3) > 70000 W.u. and surely is unreasonably large. Therefore, 4^- must be eliminated as a possibility for $E_x = 5508.6$ keV. The remaining set of possibilities is $1^+, 2$, and 3. Both T values are retained as possibilities; it is unclear why Endt assigns $T = 1$. Additionally, if $E_x = 5508.6$ keV is $2^+; 1$ or $3^+; 1$, the decay to $E_x = 1973.62$ keV is mixed M1/E2, and it is required that $\delta_{M1/E2} < 1.54$. With no

knowledge of this mixing ratio, the possibilities for $E_x = 5508.6$ keV must remain.

A transition from $E_x = 7688.2$ keV to the state previously quoted to be $E_x = 5416 \pm 3$ keV is also observed. This state has possible quantum numbers of 0^- or 2^- according to Frankle [Fra91]. No decays from this state were previously known. In this study, three decays from $E_x = 5416$ keV are observed. Calculating the energy of the state from this study yields $E_x = 5411.1 \pm 0.3$ keV, which is slightly outside the error limits set previously by Endt [End90a]. However, four γ-rays are placed with this assignment. The branching ratios for $E_x = 5411.1$ keV are listed in Table 9.15. The observed decays restrict the set of quantum numbers for $E_x = 5411.1$ keV to $0^-, 1, 2, 3, 4$, and 5^-. Since no γ-width is known for this state, an RUL analysis using final states cannot be performed. However, since the state at $E_x = 7688.2$ keV has $J^\pi; T = 3^+; 0$ or $J^\pi; T = 4^-; 0$, an RUL analysis using this transition eliminates some of the possibilities. If $E_x = 5411.1$ keV is 0^-, the transition from 7688.2 keV is an E3 or an E4 transition. The reduced transition probability B(E3) or B(E4) is greater than 230000 W.u., exceeds the appropriate existing RUL values, and is unreasonably large. Thus, $J^\pi = 0^-$ is eliminated as a possibility. If $E_x = 5411.1$ keV is 1^-, the transition $E_x = 7688.2$ keV $\longrightarrow E_x = 5411.1$ keV is possibly mixed M2/E3 in the lowest multipolarity case, for which $E_x = 7688.2$ keV is $J^\pi; T = 3^+; 0$. If the transition is pure M2, B(M2) = 175 W.u., which exceeds both the M2IS and the M2IV RUL's by a large factor. Furthermore, no mixing ratio exists which can permit this transition. If the transition is pure E3, B(E3) exceeds the E3IS RUL by a factor of roughly 40000 and requires $\delta_{M2/E3} < 0.01$. If the transition is isovector, B(E3) is unreasonably large. Thus, $J^\pi = 1^-$ must be eliminated. There are additional limits placed on the quantum numbers based on the mixing ratios. If $E_x = 7688.2$ keV is $3^+; 0$ and $E_x = 5411.1$ keV is $4^+; 1, 3^+; 1$, or $2^+; 1$, the transition is possibly mixed M1/E2, and it is required that $\delta_{M1/E2} < 2.99$. Since $\delta_{M1/E2}$ is unknown for this transition, these possibilities must remain. The set of possibilities of quantum numbers for $E_x = 5411.1$ keV from this work is $J^\pi = 1^+$ and $J = 2, 3, 4$,

and 5^-. From previous work, the set of possibilities is $J^\pi = 0^-$, or 2^-. The adopted value is $J^\pi = 2^-$ since it is the only member of both sets.

TABLE 9.14. Branching ratios for decay from the $E_x = 5508.6$ keV resonance.

Present Work		Previous Work[a]	
E_f (keV)	Branching Ratio (%)	E_f (keV)	Branching Ratio (%)
1454.67	40 ± 20	1454.67	60 ± 10
1973.62	60 ± 20	1973.62	40 ± 10

[a]Branching ratios taken from [End90a].

TABLE 9.15. Branching ratios for decay from the $E_x = 5411.1$ keV resonance.

E_f (keV)	Branching Ratio (%)
1973.62	28 ± 8
2839.9	41 ± 9
2937.87	31 ± 9

9.8 E_x = 6876.3 keV ^{30}P Resonance Analysis

The lowest energy resonance analyzed in these studies was previously tabulated to have $E_x = 6883.6$ keV with $J^\pi = 2^-$. Equipment problems restricted the amount of data collected for this resonance. Both on- and off-resonance data were collected until 48,000 μC of charge had been collected on the Faraday cup, significantly less than we would have preferred. The off-resonance data were taken at 10 keV lower in energy than the on-resonance data. The spectra taken with the suppressed and unsuppressed HPGe detectors are shown in Figures 9.22 and 9.23, respectively.

A total of nine primaries are assigned for this resonance based on this study. These primaries and the associated branching ratios are listed in Table 9.16; the observed decay scheme for this resonance is shown in Figure 9.24. There is generally good agreement between the previous branching ratios [Rei85] and those obtained in this study. The resonance to ground state transition accounts for at least 75% of all resonance decays. The other branches, whether in this study or previous ones, are weak. Reinecke quotes a 1.2% branch to $E_x = 4143.67$ keV which is not seen in this study. Two branches, a 2.7% branch to $E_x = 2937.87$ keV and a 0.4% branch to $E_x = 1973.62$ keV, are observed in this study but not in the previous measurement. Some of the intensities are quite weak due to the small amount of data collected on this resonance; more data would likely clear up some of these questions related to primaries. The assignments were made based on intensity balances and observed transitions.

The observed primary transitions restrict the resonance state quantum numbers to $0^-, 1, 2, 3$, and 4^-, assuming transitions to order E3. The observed primary transition to $E_x = 2723.96$ keV eliminates both $J^\pi = 0^-$ possibilities; B(M2) far exceeds both the isoscalar and the isovector RUL's. The observed transition to $E_x = 2839.9$ keV eliminates both $J^\pi = 1^-$ possibilities. The transition is possibly mixed M2/E3 with unknown mixing ratio. The B(M2) value exceeds the M2 RUL,

Figure 9.22 Suppressed HPGe $E_x = 6876.3$ keV ^{30}P data

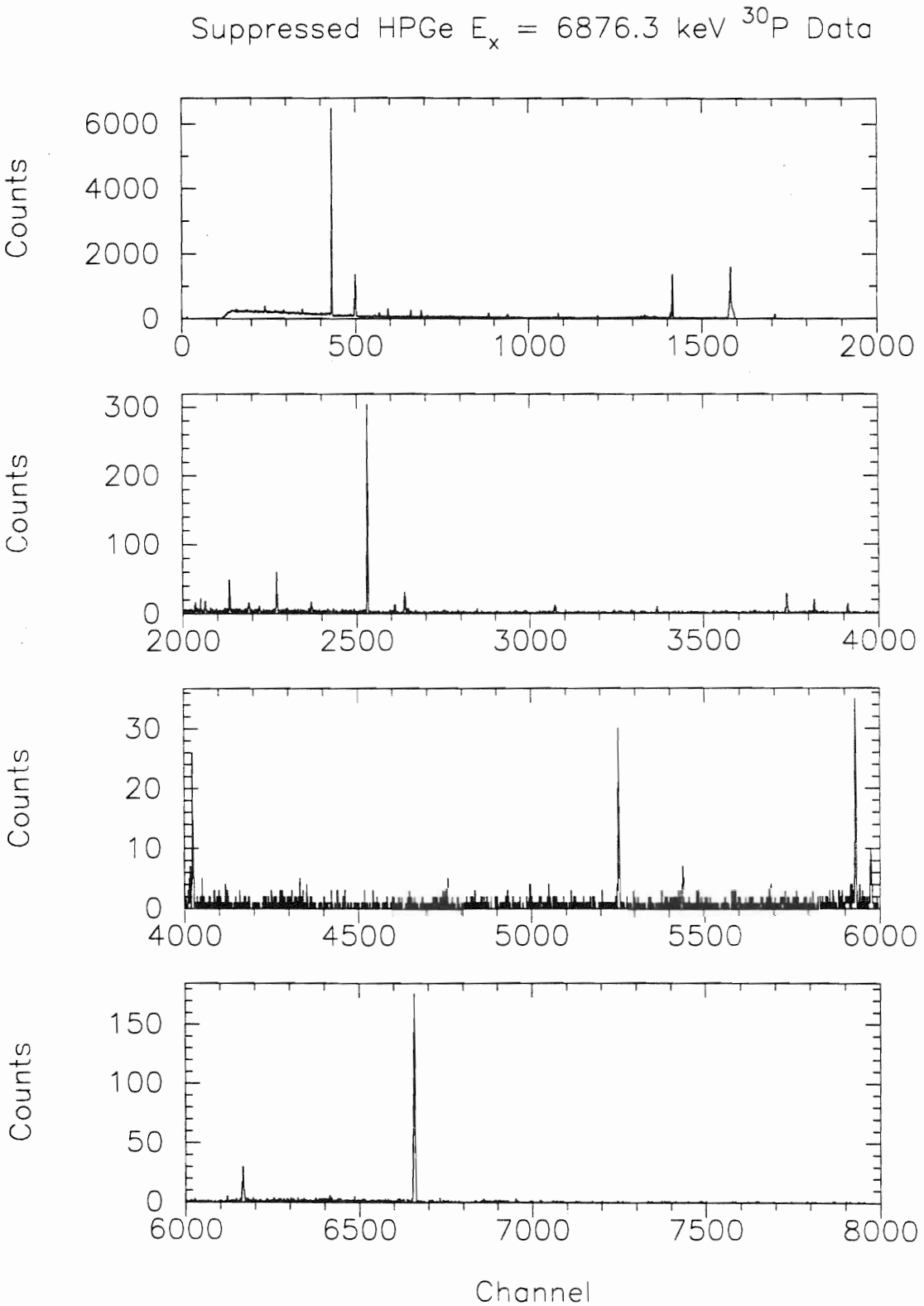
Suppressed HPGe E_x = 6876.3 keV ^{30}P Data
Counts
6000
4000
2000
0
0
500
1000
1500
2000
Counts
300
200
100
0
2000
2500
3000
3500
4000
Counts
30
20
10
0
4000
4500
5000
5500
6000
Counts
150
100
50
0
6000
6500
7000
7500
8000
Channel

Figure 9.23 Unsuppressed HPGe $E_x = 6876.3$ keV ^{30}P data

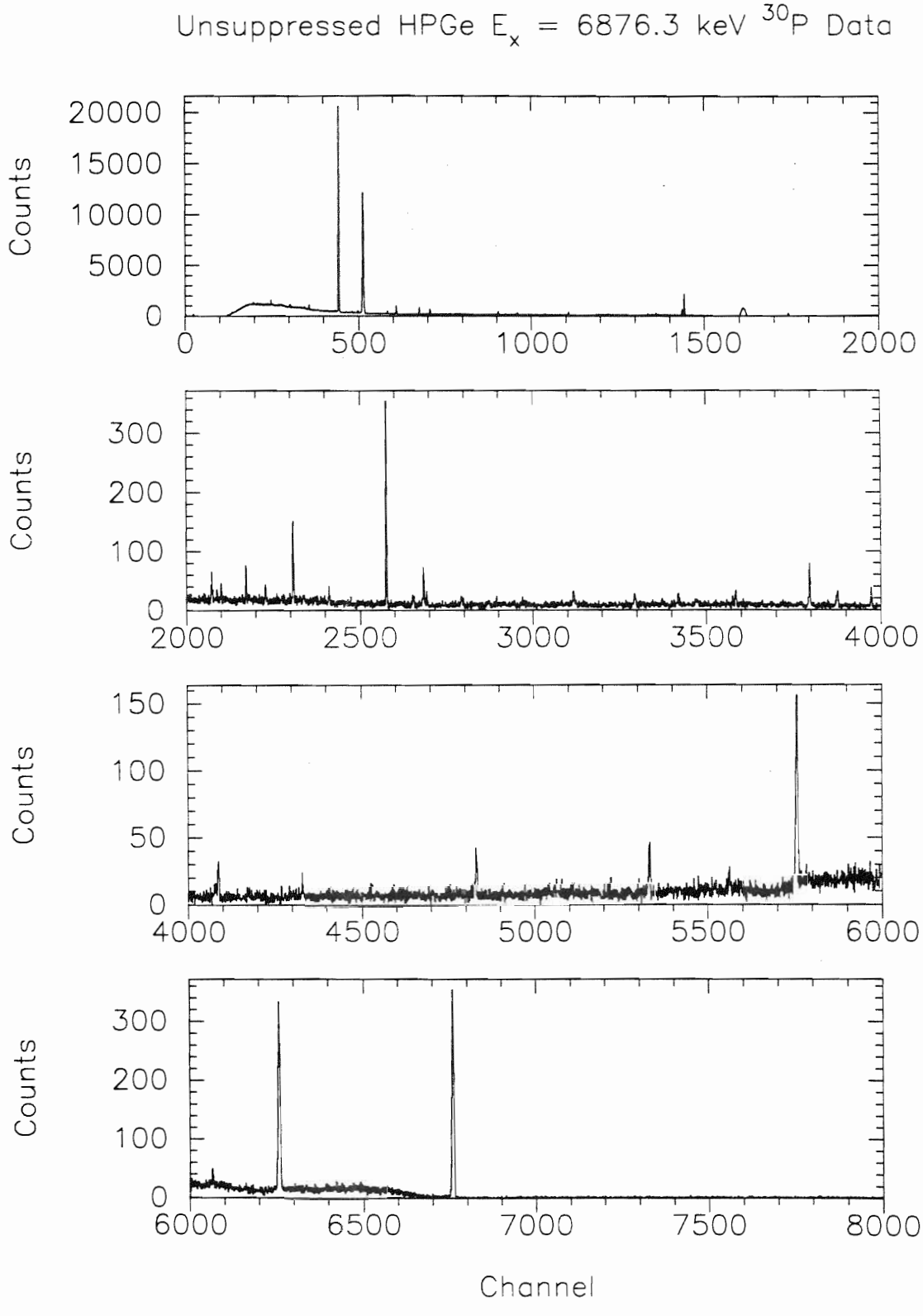
Unsuppressed HPGe E_x = 6876.3 keV ^{30}P Data
Counts
20000
15000
10000
5000
0
0
500
1000
1500
2000
Counts
300
200
100
0
2000
2500
3000
3500
4000
Counts
150
100
50
0
4000
4500
5000
5500
6000
Counts
300
200
100
0
6000
6500
7000
7500
8000
Channel

Figure 9.24 Decay scheme for the $E_x = 6876.3$ keV resonance

E_x = 6876.3 keV γ−ray Decay Scheme

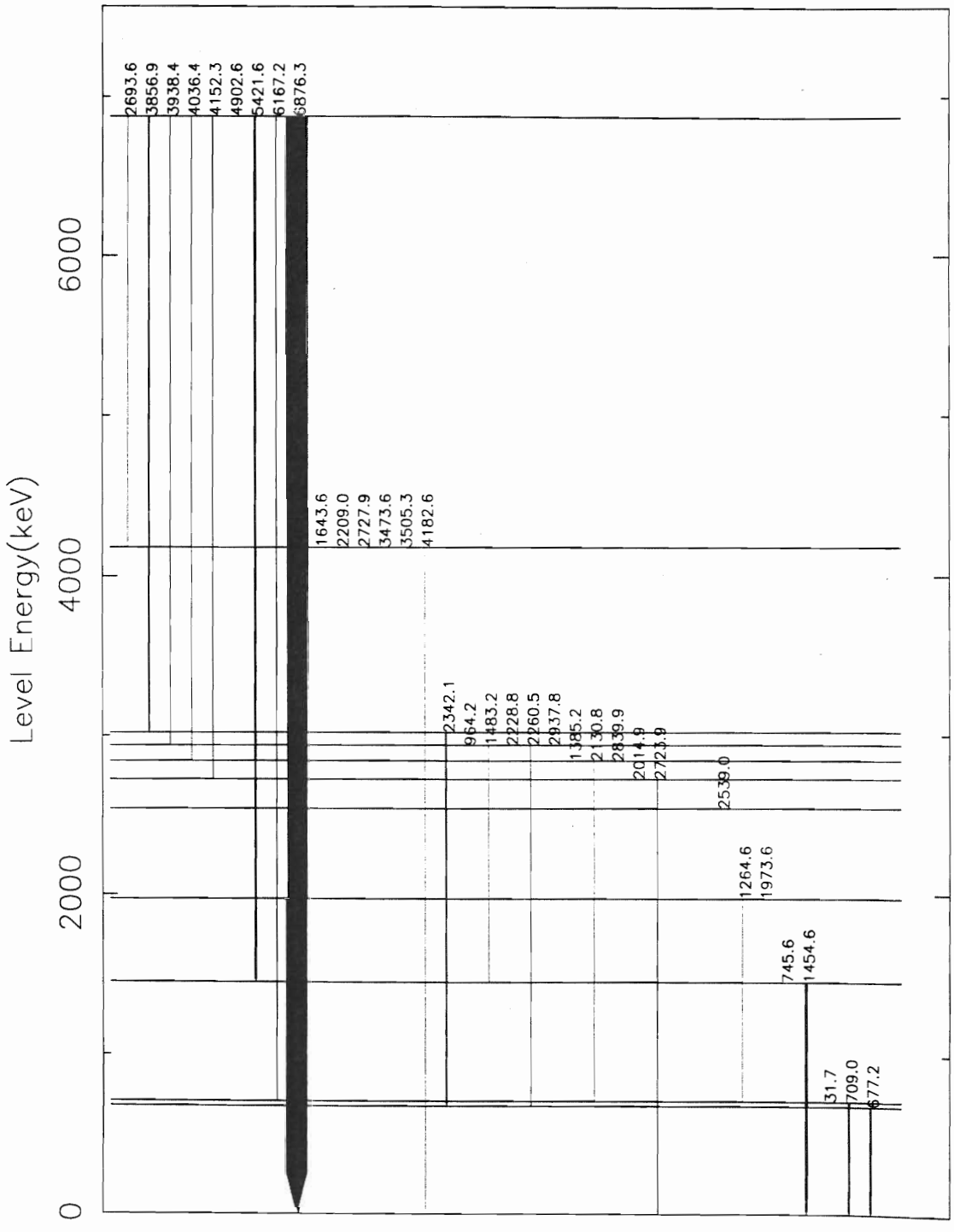

TABLE 9.16. Branching ratios for decay from the $E_x = 6876.3$ keV resonance.

Present Work		Previous Work[a]	
E_f (keV)	Branching Ratio (%)	E_f (keV)	Branching Ratio (%)
0.0	74. ± 5.	0.0	83
709.02	3.2 ± 0.7	709.02	2.1
1454.67	8. ± 1.	1454.67	4.0
1973.62	0.4 ± 0.2		
2723.96	3.4 ± 0.6	2723.96	2.8
2839.9	2.3 ± 0.5	2839.9	2.1
2937.87	2.7 ± 0.5		
3019.39	5.4 ± 0.7	3019.39	4.0
		4143.67	1.2
4182.65	1.4 ± 0.3	4182.65	0.8

[a]Values taken from [Rei85].

while the B(E3) value exceeds the corresponding E3 RUL; both isoscalar and isovector RUL's are exceeded. Therefore, $J^\pi = 1^-$ must be eliminated. The resonance to ground state primary transition eliminates 3^- and 4^- as possibilities. If the resonance state is 3^-, this transition is possibly mixed M2/E3 in character. In this case, both the isoscalar and isovector M2 and E3 RUL's are exceeded. If the resonance state is 4^-, this transition is an E3 transition and exceeds the E3IS RUL. Though there is no E3IV RUL, the B(E3) value, being 2253 W.u., is sufficiently large to insure that the transition is not allowed. Additionally, the $E_x = 6876.3$ keV $\longrightarrow E_x = 4182.65$ keV transition requires a possibly mixed M2/E3 transition. It is required that $\delta_{M1/E2} < 0.94$ if the resonance state is $1^+;0.\ 2^+;0.$ or $3^+;0$. This mixing ratio is not known, and those possibilities are retained. Thus, the possibilities from this study are $J^\pi = 1^+, 2^+, 2^-$, and 3^+ with either isospin. The previously quoted values for the quantum numbers [Fra91] are a subset of those which are possible based on this study.

A total of five ^{30}P resonance states were studied in this work. Primary decays populated an additional four states which were not well known. The adopted values of the quantum numbers for each of these resonances are shown in Table 9.17 for easy reference. In some cases, the set of possible values is equal to the previously known set. However, if this study has eliminated some of the possibilities, the reduced set is listed in the table.

TABLE 9.17. Quantum numbers assigned to states studied in this work[a]

E_x (keV)	This Work	Previous Assignment[b]	Adopted Assignment[b]
7752.7	$[1^-;1],[1^+],[2],[3]$	$[3^+],[4^+],[5^+]$	$[3^+]$
7749.3	$[1^+],[2^+],[1^-;0]$	$[1^+;(0)]$	$[1^+]$
7742.0	$[1],[2],[3^-]$	$[1^-]$	$[1^-]$
7688.2	$[3^+;0],[4^-;0]$	$[3^+]$	$[3^+;0],[4^-;0]$
6876.3	$[1^+],[2^+],[2^-],[3^+]$	$[2^-]$	$[2^-]$
6229.0	$[2],[3],[4],[5],[6^-:0]$	$[3^+],[5^+]$	$[3^+],[5^+]$
5933.6	$[2^-],[3],[4]$		$[2^-],[3],[4]$
5508.6	$[1^+],[2],[3]$	$[1^+;1],[2;1],[3;1]$	$[1^+],[2],[3]$
5411.1	$[1^+],[2],[3],[4],[5^-]$	$[0^-],[2^-]$	$[2^-]$

[a]Brackets are used to delimit a single set of quantum numbers. All values for a given quantum number are allowed unless explicitly specified.

[b]Isospin values in parentheses are tentatively assigned based on comparison with the ^{30}Si level scheme listed in [End90a].

Chapter 10

Summary

At the TUNL-HRL a new Compton-suppressed spectrometer (CSS) has been recently put into operation. This detector system, together with the high resolution accelerator system, permits a high resolution γ-ray study of the decay of nuclear resonances. The first nuclide to be studied using this new detector system is ^{30}P. The goal of this study is to establish a pure and complete level scheme for ^{30}P: the energy level fluctuations can then be analyzed to determine if signatures of chaos appear in the nucleus.

In addition to the detectors, new electronics were purchased to process the signals from the detector system. We are interested not only in individual γ-rays, but also in coincidence measurements of two γ-rays. Therefore, in addition to the γ-ray energy, the time between detection of γ-rays is important. The electronics components of the data acquisition system were set up to enable the measurement of the required quantities. Extensive software modification also was necessary in order to acquire data from the CSS detector system and properly store it for future analysis and use.

Prior to accumulating data on ^{30}P resonances, a calibration procedure was performed. A standard ^{152}Eu γ-ray source was used to provide calibration energy at

lower energies. The reaction ^{27}Al(p,γ)^{28}Si was used to populate a well-known resonance at $E_x = 12541.31$ keV. The decay of this resonance was used to establish a calibration at high energies.

A set of five ^{30}P resonances were studied using the CSS detector system. For each resonance, assignments of the observed γ-rays were made. Many of the γ-rays were identified as coming from the decay of contaminant nuclei. A decay scheme for the resonance under study was constructed from the observed γ-rays energies. In three instances. the final states of the all of the primary transitions are bound states; the other two resonances studied decay through at least one unbound state. Primaries from two resonances populate four states for which there was little previously known information. Thus, a total of nine states in ^{30}P were analyzed either directly or indirectly from the population of five resonance states.

Conservation laws of γ-decay permit the restriction of the quantum numbers for a level based on the observed decay. The set of possibilities is further restricted by comparing the observed reduced transition probability for the decay with the recommended upper limit for that particular decay type. These constraints were used to ascertain a final set of allowed quantum numbers for the nine states studied in this work. In some instances. the constraints on the quantum numbers for some levels placed in previous studies were relaxed. These instances occur when earlier work is not clear on why certain quantum numbers are eliminated. Based on this work, a definite J value was assigned for one resonance state, and, for a different resonance state, a definite value of T was assigned, completing the set of J, π, and T. The set of possible quantum numbers was verified or further restricted for six other bound and unbound states in ^{30}P. One of the states populated by a primary transition was previously without restrictions on J, π, or T; a set of allowed quantum numbers has now been established for this state. In Table 9.17 the assigned quantum numbers are summarized.

References

[Bar94] P. H. Barker, "Aligning a Ge Detector Using the $^{19}F(p,\alpha\gamma)$ Reaction", Nucl. Instrum. Methods **A345**, 445 (1994).

[Ber77] M. V. Berry and M. Tabor, "Level Clustering in the Regular Spectrum", Proc. R. Soc. London, Ser. A **356**, 375 (1977).

[Bla91] J. M. Blatt and V. F. Weisskopf, *Theoretical Nuclear Physics*, Dover Publications, Mineola, 1991.

[Ble94] C. Blecken, Y. Chen, and K. A. Muttalib, "Transitions in Spectral Statistics", J. Phys. A **27**, L563 (1994).

[Boh69] A. Bohr and B. R. Mottelson, *Nuclear Structure*, W. A. Benjamin, New York, 1969, Two volume set.

[Boh84] O. Bohigas, M. J. Giannoni, and C. Schmidt, "Characterization of Chaotic Quantum Spectra and Universality of Level Fluctuation Laws", Phys. Rev. Lett. **52**, 1 (1984).

[Boh85] O. Bohigas, R. U. Haq, and A. Pandey, "Higher-Order Correlations in Spectra of Complex Systems", Phys. Rev. Lett. **54**, 1645 (1985).

[Bra78] R. Bracewell, *The Fourier Transform and its Applications*, McGraw-Hill Book Co., New York, 1978.

[Bri74] O. Brigham, *The Fast Fourier Transform*, Prentice-Hall, New Jersey, 1974.

[Bro73] T. A. Brody, "A Statistical Measure for the Repulsion of Energy Levels", Lett. Nuovo Cimento **7**, 482 (1973).

[Bro81] T. A. Brody et al., "Random-matrix fluctuations: spectrum and strength fluctuations", Rev. Mod. Phys. **53**, 385 (1981).

[Bul89] J. S. Bull, *Entrance Channel Correlations in* ^{40}Ca, Ph.D. thesis, Duke University, 1989.

[Del87] D. Delande and J. C. Gay, "Scars of Symmetries in Quantum Chaos", Phys. Rev. Lett. **59**, 1809 (1987).

[Del91] A. Delon, R. Jost, and M. Lombardi, "NO_2 Jet Cooled Visible Excitation Spectrum: Vibronic Chaos Induced by the $\tilde{X}^2A_1 - \tilde{A}^2B_2$ Interaction", J. Chem. Phys. **95**, 5701 (1991).

[Dra94] J. M. Drake, *Resonance Tests of Detailed Balance and Design of a Compton Suppression Spectrometer*, Ph.D. thesis, North Carolina State University, 1994.

[Dys62] F. J. Dyson, "A Brownian-Motion Model for the Eigenvalues of a Random Matrix", J. Math. Phys. **3**, 1191 (1962).

[Dys63] F. J. Dyson and M. L. Mehta, "Statistical Theory of the Energy Levels of Complex Systems. IV", J. Math. Phys. **4**, 701 (1963).

[End86] P. M. Endt, P. de Wit, and C. Alderliesten, "The ^{25}Mg(p,γ)^{26}Al and ^{25}Mg(p,p') Resonances for $E_p = 0.31 - 1.84$ MeV", Nucl. Phys. **A459**, 61 (1986).

[End88] P. M. Endt, P. de Wit, and C. Alderliesten, "The ^{25}Mg(p,γ)^{26}Al Reaction: Branchings, Energies, and Lifetimes", Nucl. Phys. **A476**, 333 (1988).

[End90a] P. M. Endt, "Energy Levels of A = 21 - 44 Nuclei (VII)", Nucl. Phys. **A521**, 1 (1990).

[End90b] P. M. Endt, "Spectroscopic Information on ^{24}Mg and ^{28}Si from Proton Capture", Nucl. Phys. **A510**, 209 (1990).

[End93] P. M. Endt. "Strengths of Gamma-Ray Transitions in A = 5 - 44 Nuclei.IV", Atomic Data and Nuclear Data Tables **55**, 171 (1993).

[Fra91] S. C. Frankle, *Nuclear Resonance Spectroscopy in* ^{30}P, Ph.D. thesis, North Carolina State University, 1991.

[Guh90a] T. Guhr, 1990, private communication.

[Guh90b] T. Guhr and H. A. Weidenmüller, "Isospin Mixing and Spectral Fluctuation Properties", Ann. Phys. **199**, 412 (1990).

[Haq82] R. U. Haq, A. Pandey, and O. Bohigas, "Fluctuation Properties of Nuclear Energy Levels: Do Theory and Experiment Agree?", Phys. Rev. Lett. **48**, 1086 (1982).

[Hol87] A. Holle et al., "Hydrogenic Rydberg Atoms in Strong Magnetic Fields: Theoretical and Experimental Spectra in the Transition Region from Regularity to Irregularity", Z. Phys. D **5**, 279 (1987).

[Iu89] C. Iu, G. R. Welch, M. M. Kash, L. Hsu, and D. Kleppner, "Orderly Structure in the Positive-Energy Spectrum of a Diamagnetic Rydberg Atom", Phys. Rev. Lett. **63**, 1133 (1989).

[Jac75] J. D. Jackson. *Classical Electrodynamics*, John Wiley and Sons, New York, second edition, 1975.

[Jos86] R. Jost and M. Lombardi, "Survey of Correlation Properties of Polyatomic Molecules Vibrational Energy Levels Using F.T. Analysis", in *Proceedings of the Second International Conference on Quantum Chaos and the Fourth International Conference on Statistical Nuclear Physics*, edited by T. H. Seligman and H. Nishioka, 1986, Springer-Verlag, Berlin, p. 72.

[Kin81] S. E. King, Y. C. Lau, and C. R. Gould, "Data Acquisition with a VAX 11/780 and MBD Branch Driver", IEEE Trans. Nucl. Sci. **NS-28**, 3822 (1981).

[Kno79] G. F. Knoll, *Radiation Detection and Measurement*, John Wiley & Sons, New York, second edition, 1979.

[Kra88] K. Krane, *Introductory Nuclear Physics*, John Wiley and Sons, New York, 1988.

[Led78] C. M. Lederer and V. S. Shirley, editors, *Table of Isotopes*, John Wiley and Sons, New York, seventh edition, 1978.

[Lev86] L. Leviandier, M. Lombardi, R. Jost, and J. Pique, "Fourier Transform: A Tool to Measure Statistical Level Properties in Very Complex Spectra", Phys. Rev. Lett. **56**, 2449 (1986).

[Li90] J. Li, *Level Density Studies in* ^{49}V, Ph.D. thesis, Duke University, 1990.

[Li91] J. Li, E. G. Bilpuch, C. R. Westerfeldt, G. E. Mitchell, and F. Yang, "Test of Level Densities with Proton Resonances", Phys. Rev. C **44**, 345 (1991).

[Lio72] H. I. Liou et al., "Neutron-Resonance Spectroscopy. VIII The Separated Isotopes of Erbium: Evidence for Dyson's Theory Concerning Level Spacings", Phys. Rev. C **5**, 974 (1972).

[Lom90] M. Lombardi, 1990, private communication.

[Meh91] M. L. Mehta, *Random Matrices*, Academic Press, New York, second edition, 1991.

[Mit85] G. E. Mitchell, E. G. Bilpuch, J. F. Shriner, Jr., and A. M. Lane, "Amplitude Correlations in Nuclear Resonance Spectroscopy", Phys. Rep. **117**, 1 (1985).

[Pan79] A. Pandey, "Statistical Properties of Many-Particle Spectra III. Ergodic Behavior in Random-Matrix Ensembles", Ann. Phys. (N.Y.) **119**, 170 (1979).

[Pan81] A. Pandey, "Statistical Properties of Many-Particle Spectra. IV. New Ensembles by Stieltjes Transform Methods". Ann. Phys. **134**, 110 (1981).

[Piq87] J. P. Pique, Y. Chen, R. W. Field, and J. L. Kinsey, "Chaos and Dynamics on 0.5–300-ps Time Scales in Vibrationally Excited Acetylene: Fourier Transform of Stimulated-Emission Pumping Spectrum". Phys. Rev. Lett. **58**, 475 (1987).

[Piq90] J. P. Pique, "Molecular Dynamics and Quantum Chaos in Small Polyatomic Molecules (CS_2, C_2H_2) through Stimulated-Emission Pumping Experiments and Statistical Fourier-transform Analysis". J. Opt. Soc. Am. B **7**, 1816 (1990).

[Pre92] W. Press, B. Flannery, S. Teukolsky, and W. Vetterling, *Numerical Recipes in Fortran: The Art of Scientific Computing*, Cambridge University Press, Cambridge, second edition, 1992.

[Rad89] D. C. Radford, *GELIFT Reference Manual*, Argonne National Laboratory, 1989.

[Ram81] B. Ramstein, L. H. Rosier, and R. J. De Meijer, "Investigation of States in ^{30}P via the ^{30}Si(^{3}He,t)^{30}P Reaction at 30 MeV", Nucl. Phys. **A363**, 110 (1981).

[Rei85] J. P. L. Reinecke et al., "The Energy Levels of ^{30}P", Nucl. Phys. **A435**, 333 (1985).

[Rei92] L. E. Reichl, *The Transition to Chaos in Conservative Classical Systems: Quantum Manifestations*, Springer-Verlag, New York, 1992.

[Rin80] P. Ring and P. Schuck, *The Nuclear Many-Body Problem*, Springer-Verlag, New York, 1980.

[Sel85] T. H. Seligman, J. J. M. Verbaarschot, and M. R. Zirnbauer, "Fluctuations of Quantum Spectra and Their Semiclassical Limit in the Transition between Order and Chaos", J. Phys. A **18**, 2227 (1985).

[Shr87] J. F. Shriner, Jr., E. G. Bilpuch, and G. E. Mitchell, "New Test of the Reduced-Width-Amplitude Distribution", Phys. Rev. Lett. **59**, 435 (1987), **59**, 1492(E) (1987).

[Shr89] J. F. Shriner, Jr., E. G. Bilpuch, and G. E. Mitchell, "Tests of the Reduced-Width-Amplitude Distribution with Proton Resonance Data", Z. Phys. A **332**, 45 (1989).

[Shr90] J. F. Shriner, Jr., E. G. Bilpuch, P. M. Endt, and G. E. Mitchell, "Fluctuation Properties of States in ^{26}Al", Z. Phys. A **335**, 393 (1990).

[Shr92] J. F. Shriner, Jr. and G. E. Mitchell, "Small Sample Size Effects in Statistical Analyses of Eigenvalue Distributions", Z. Phys. A **342**, 53 (1992).

[Sie87] P. J. Siemens and A. S. Jensen, *Elements of Nuclei: Many-Body Physics with the Strong Interaction*, Addison-Wesley, New York, 1987.

[Sit94] G. Sitja and J. P. Pique, "Transition to Soft Chaos in the Vibrational Spectrum of the CS_2 Molecule", Phys. Rev. Lett. **73**, 232 (1994).

[Sod87] J. P. Soderstrum, M. A. Boyd, C. R. Gould, and N. R. Roberson, *XSYS Reference Manual*, Triangle Universities Nuclear Laboratory, Durham, NC, sixth edition, 1987.

[van74] J. J. M. van Gasteren, A. J. L. Verhage, and A. Van der Steld, "Investigation of the ^{31}P(t,α)^{30}P Reaction at $E_x = 15$ MeV", Nucl. Phys. **A231**, 425 (1974).

[Wat80] W. A. Watson III, *A High Resolution Study of Proton Resonances in ^{57}Co*, Ph.D. thesis, Duke University, 1980.

[Wat81] W. A. Watson III, E. G. Bilpuch, and G. E. Mitchell, "High Resolution Measurement of Proton Resonances in ^{57}Co", Phys. Rev. C **24**, 1992 (1981).

[Wel89] G. R. Welch, M. M. Kash, C. Iu, L. Hsu, and D. Kleppner, "Experimental Study of Energy-Level Statistics in a Regime of Regular Classical Motion", Phys. Rev. Lett. **62**, 893 (1989).

[Wes87] C. R. Westerfeldt, R. O. Nelson, E. G. Bilpuch, and G. E. Mitchell. *The TUNL High Resolution Laboratory System and Operating Procedures*, Triangle Universities Nuclear Laboratory, Durham, NC, second edition, 1987.

[Wes88] C. R. Westerfeldt, R. O. Nelson, E. G. Bilpuch, and G. E. Mitchell, "A Microcomputer-Based System for Measuring Excitation Functions with Good Energy Resolution", Nucl. Instrum. Methods **A270**, 467 (1988).

[Wig57a] E. P. Wigner, "Results and Theory of Resonance Absorption", in *Conference on Neutron Physics by Time-of-Flight*, 1957, Oak Ridge National Laboratory, Gatlinburg, TN, p. 59.

[Wig57b] E. P. Wigner, "Statistical Properties of Real Symmetric Matrices with Many Dimensions", Can. Math. Congr. Proc. (1957).

[Won86] S. S. M. Wong, *Nuclear Statistical Spectroscopy*, Oxford University Press, New York, 1986.